

ANDRÉ KHALIL

**ANALYSE STRUCTURELLE DE L'HYDROGÈNE NEUTRE DANS LA
VOIE LACTÉE**

Thèse présentée
à la Faculté des études supérieures de l'Université Laval
dans le cadre du programme de doctorat sur mesure en Mathématiques-Astrophysique
pour l'obtention du grade de Philosophiae Doctor (Ph.D.)

FACULTÉ DES ÉTUDES SUPÉRIEURES
UNIVERSITÉ LAVAL
QUÉBEC

NOVEMBRE 2004

© André Khalil, 2004

Résumé

Les étoiles vivent et meurent en rejetant de la matière dans le milieu interstellaire (MIS) et elles naissent à l'intérieur de celui-ci. Nous avons analysé la composante d'hydrogène neutre du MIS. Nos données proviennent de la partie canadienne de l'International Galactic Plane Survey qui vise l'imagerie spectroscopique de l'hydrogène neutre du plan de notre galaxie. Nous avons utilisé deux outils mathématiques d'analyse d'images: la technique d'Espaces Métriques (TEM) et la méthode des Maxima du Module de la Transformée en Ondelettes (MMTO).

La TEM est un formalisme mathématique d'analyse d'images qui permet de comparer quantitativement la complexité des objets étudiés. Nous avons amélioré l'outil aux niveaux mathématique et technique avant de l'utiliser pour caractériser la complexité de 28 régions d'hydrogène neutre. Après avoir classé les 28 objets, nous avons trouvé des corrélations entre ce classement et les propriétés physiques des objets sous-jacents, dont: (1) Plus le flux des photons UV est élevé, plus la région de H I photodissociée est complexe; et (2) la complexité des régions H I augmente avec l'âge des restes de supernovae auxquels elles sont associées.

La méthode MMTO est un formalisme multifractal basé sur la transformée en ondelettes. Nos résultats obtenus à partir de cette méthode concernent les propriétés multifractales et anisotropes de l'hydrogène neutre dans notre galaxie. Les nuages terrestres exhibent des propriétés multifractales. Nous avons démontré que l'hydrogène neutre du disque de notre galaxie est monofractal. En analysant séparément les bras spiraux et les milieux inter-bras, nous avons découvert une signature anisotrope et que les structures horizontales sont plus complexes que les structures verticales. Cette anisotropie est indépendante de l'échelle pour les inter-bras tandis qu'elle est dépendante de l'échelle pour les bras spiraux. Les hypothèses investiguées pour obtenir une explication physique sont: le gradient de distribution en z (“scale-height gradient”), l'onde de densité, l'activité de formation d'étoiles, la photo-lévitation de nuages poussiéreux, les mouvements aléatoires de nuages H I, la corrugation et la turbulence.

Abstract

Stars live and die by rejecting matter in the interstellar medium (ISM), where they were born. We have analyzed the neutral hydrogen component of the ISM. The data come from the Canadian portion of the International Galactic Plane Survey which aims the spectroscopic imaging of the neutral hydrogen from our Galaxy. We have used two mathematical image analysis tools: Metric Space Technique (MST) and the Wavelet Transform Modulus Maxima (WTMM) method.

The MST is an image analysis mathematical formalism that allows one to quantitatively compare the complexity of the studied objects. We have improved the tool mathematically and technically before using it to characterize the complexity of 28 neutral hydrogen regions. After classifying the 28 objects, we have found some correlations between this ranking and the physical properties of the underlying objects, for example: (1) The complexity of the photodissociated neutral hydrogen regions increases with the flux of UV photons; and (2) the complexity of neutral hydrogen regions increases with the age of the supernovae remnants to which they are associated.

The WTMM method is a multifractal formalism based on the wavelet transform. The results we obtain from this method concern the multifractal and anisotropic properties of neutral hydrogen in our Galaxy. Earth clouds exhibit multifractal properties. We have shown that the neutral hydrogen from our galactic disk is monofractal. By analyzing separately spiral arms and the inter-arm regions, we have discovered an anisotropic signature and that the horizontal structures are more complex than the vertical structures. This anisotropy is independent of scale for the inter-arms while it is dependent of scale for the spiral arms. The investigated hypotheses to obtain some physical explanations are: the scale-height gradient, the density wave, star formation activity, photo-levitation of dusty clouds, random motions of neutral hydrogen clouds, corrugation and turbulence.

Avant-propos

Les deux chapitres substantiels de cette thèse sont des articles, le premier, publié dans *Astrophysical Journal* en janvier 2004 (Khalil, Joncas & Nekka, 2004), et le deuxième, soumis à *Astrophysical Journal* en septembre 2004 (Khalil et al., 2004). Je suis l'auteur principal de ces deux articles et je les ai rédigés à $\approx 95\%$. Pour le premier article (chapitre 2), les auteurs sont André Khalil, Gilles Joncas, et Fahima Nekka. Deux autres collaborateurs se sont ajoutés à notre groupe pour le deuxième article (Khalil et al. (2004), chapitre 3): Alain Arneodo, directeur de recherche au CNRS au Laboratoire de Physique de l'École Normale Supérieure de Lyon et inventeur principal de la méthode d'analyse multifractale qui est utilisée dans le chapitre 3 et Pierre Kestener, ancien étudiant du Dr Arneodo. Cette collaboration avait d'ailleurs débuté en juin 2002 lorsque j'ai fait un stage avec l'équipe du Dr Arneodo alors qu'elle était au Centre de Recherche Paul-Pascal, à Bordeaux (le déménagement de l'équipe pour Lyon s'est fait en septembre 2003).

L'inclusion de Khalil, Joncas & Nekka (2004) dans le chapitre 2 est quasi intégrale mis à part quelques corrections très mineures.

Quelques ajouts accompagnent l'article Khalil et al. (2004) dans le chapitre 3:

- Exemples: Deux exemples accompagnés de plusieurs figures, insérés avec des modifications mineures à partir de Arneodo, Decoster & Roux (2000) ont été ajoutés à la §3.9.1.
- Mise en algorithmie numérique: La marche à suivre numérique pour la méthode a été insérée dans la §3.9.2 à partir de Arneodo, Decoster & Roux (2000).

Ces deux items ne sont pas inclus dans la version de l'article Khalil et al. (2004) soumis à *Astrophysical Journal* en septembre 2004.

Deux personnes sont en partie responsables de la réussite de cette thèse. L'arrivée de Hubert “Ti-Bubu” en décembre 2003 m'aura permis de générer toute l'énergie requise

pour mettre ce projet à terme. La remise en contexte quotidienne créée par le moindre sourire ou ricanement aura été parmi les plus grandes utilités. Et que dire que Lyne “Wonder-Woman” Guimond? Encourageante, inépuisable, compréhensive, solidaire et... enseignante, étudiante et mère! Nous sommes fier de vous avoir dans notre organisation...

Est-ce que j'aurais fait un doctorat si mon père n'avait pas passé par là? Difficile à dire... Je remercie chaleureusement Nicole et Michel pour tout ce qu'ils ont fait pour moi. Je remercie aussi mes deux frères Louis et Jean-François ainsi que tous les membres de ma famille et mes amis pour leurs encouragements et leurs marques de confiance en ma réussite.

C'est en sortant d'une rencontre courte et décevante (mais sans aucune conséquence sur mon moral) avec un membre de la direction du département de physique concernant la possibilité (qui semblait plus être, l'impossibilité) qu'un mathématicien puisse faire un doctorat en physique que j'ai rencontré Gilles Joncas. “Assieds-toi, je cherche justement un spécialiste des fractales”, fut la réponse de Gilles à la question “Bonjour Monsieur, est-ce que vous connaissez un professeur qui aimerait travailler avec un spécialiste des fractales?” Près de cinq ans plus tard, je remercie Gilles de m'avoir très majoritairement traité comme un collègue et rarement (mais parfois essentiellement!) comme un étudiant gradué.

Ce ne fut pas facile de trouver “Celle qui comprend bien”. C'est après une recherche de quelques mois que j'ai enfin rencontré Fahima. Elle est devenue une bonne amie qui a souvent eu l'occasion de jouer le rôle de la sage grande soeur. Je la remercie grandement pour ses encouragements réguliers.

Un merci très spécial s'adresse à mes deux collègues français Alain et Pierre. Ce fut un honneur de travailler avec le grand Alain Arneodo, pour qui intensité, rigueur, ténacité et exigence sont aussi importants que enthousiasme, disponibilité, encouragements et... sens de l'humour. C'est un très grand plaisir pour moi de pouvoir poursuivre cette collaboration dans le futur immédiat dans le domaine de l'imagerie médicale. Un merci très chaleureux à Pierre Kestener, pour qui la taille des problèmes est proportionnelle à son appétit de les solutionner.

Merci aux gens du Centre de Recherche Paul-Pascal (CRPP) qui m'ont accueilli à Bordeaux lors de mon stage avec Alain et Pierre. Qui aurait cru que ce séjour me permettrait de faire partie de l'équipe de basket-ball du CRPP (gagnante par un point!).

Je tiens aussi à saluer tous mes collègues du groupe d'astrophysique de l'Université Laval. Le seul fait de pouvoir considérer autant les étudiants que les professeurs dans ce même groupe d'amis est une indication de la forte cohésion qui unit les membres du groupe. Je vous salue tous chaleureusement. Merci aussi à mon ami Mike Todaro qui a participé, de façon bénévole, à l'amélioration du texte du chapitre 2.

Toute lecture de ce document devrait adéquatement être précédée d'au moins une écoute de *Interstellar Overdrive* de Pink Floyd (1967), pièce que j'ai découverte une douzaine d'années avant le début de ce projet de recherche et qui s'inscrit dans le grand schème évolutif du cycle de vie... des étoiles. Merci donc au psychédélisme de Syd "Crazy Diamond" Barrett.

Table des matières

Résumé	i
Abstract	ii
Avant-propos	iii
Table des matières	vi
Liste des figures	xv
Liste des tableaux	xxi
1 Introduction	1
1.1 MISE EN SITUATION	1
1.2 LE MILIEU INTERSTELLAIRE	3
1.2.1 L'hydrogène neutre	4

1.2.1.1	CNM vs WNM	5
1.3	OUTILS MATHÉMATIQUES	6
1.3.1	Les analyses fractales	7
1.3.1.1	Comptage de boîtes	8
1.3.1.2	Relation aire-périmètre	9
1.3.1.3	Autres techniques fractales	10
1.3.2	Les analyses multifractales	10
1.3.2.1	Formalisme multifractal de comptage de boîtes	11
1.3.3	Fonction de corrélation	14
1.3.4	Arbres statistiques	15
1.3.5	Caractérisation de la turbulence	15
1.3.6	Technique d’Espaces Métriques	19
1.3.7	Formalisme multifractal basé sur la transformée en ondelettes	19
2	Metric Space Technique	21
	RÉSUMÉ	21
2.1	INTRODUCTION	22

2.2 DATA	23
2.2.1 Object Parameters: Age, Area, Distance, Flux, H I Mass, & z	24
2.3 THE TOOL: METRIC SPACE TECHNIQUE	26
2.3.1 Output Functions	27
2.3.1.1 Distribution of Density	28
2.3.1.2 Distribution of Volume	28
2.3.1.3 Distribution of Topological Components	30
2.3.1.4 Distribution of Filaments	30
2.3.2 Metrics	32
2.3.3 Coordinates	33
2.4 IMPROVEMENTS	34
2.4.1 p=1	34
2.4.2 Two New Output Functions	34
2.4.2.1 Distribution of Pixel Values	34
2.4.2.2 Average H I Spectrum	35
2.4.3 Complexity Classification Scheme	36
2.4.3.1 Positional Rank	36

2.4.3.2 Normalization – Average Coordinate	37
2.4.3.3 Normalization – Maximal Coordinate	38
2.4.4 Distance Effects: Revised Components and Pixels Distributions . .	38
2.5 RESULTS AND ANALYSIS	40
2.5.1 Complex Classification	42
2.5.2 WR140	44
2.5.3 G109.1-1.0	45
2.5.4 The Most Complex H II Regions	45
2.5.5 Correlations	46
2.5.5.1 Complexity vs Age	48
2.5.5.2 Complexity vs Area	48
2.5.5.3 Complexity vs Distance	48
2.5.5.4 Complexity vs Flux	49
2.5.5.5 Complexity vs H I Mass	49
2.5.5.6 Complexity vs $ z $	49
2.5.5.7 Complexity vs Stellar Wind Speed	49

2.5.5.8 Complexity, Physical Parameters vs Fractal Dimension: One Correlation	50
2.6 DISCUSSION	51
2.7 CONCLUSION	53
2.8 ACKNOWLEDGEMENTS	54
2.9 APPENDICES	54
2.9.1 MINOR FAULT CONCERNING THE FILAMENT INDEX OF NON-CONVEX COMPONENTS	54
2.9.2 REVISITING THE MATHEMATICAL FORMALISM: IMPROVE- MENTS	56
3 2D Wavelet-Transform Modulus Maxima Method	58
RÉSUMÉ	58
3.1 INTRODUCTION	59
3.1.1 Fractals & Multifractals	59
3.1.2 The Wavelet Transform	61
3.1.3 The WTMM Method	62
3.1.4 Application of the 2D WTMM Method to H 1	64
3.2 DATA	64

3.3 THE 2D WAVELET-TRANSFORM MODULUS MAXIMA METHOD	67
3.3.1 Description of the 2D WTMM Method	68
3.3.1.1 The Wavelet Transform and the Analyzing Wavelets	68
3.3.1.2 Global and Local Regularity Properties of Rough Surfaces: Hurst and Hölder Exponents	69
3.3.1.3 The 2D WTMM Method	71
3.3.1.4 Probability Density Functions	75
3.4 TEST APPLICATIONS OF THE 2D WTMM METHOD	76
3.4.1 Isotropic Fractional Brownian Surfaces	77
3.4.1.1 Fourier Analysis	79
3.4.1.2 Wavelet Analysis	79
3.4.1.3 Numerical Computation of the $\tau(q)$ and $D(h)$ spectra . .	81
3.4.1.4 Probability Density Functions	82
3.4.2 Multifractal Rough Surfaces	86
3.4.2.1 Fourier Analysis	87
3.4.2.2 Wavelet Analysis	87
3.4.2.3 Numerical Computation of the $\tau(q)$ and $D(h)$ spectra . .	88

3.4.2.4	Probability Density Functions	91
3.4.3	Anisotropic Surfaces	93
3.4.3.1	Fourier Analysis	94
3.4.3.2	Wavelet Analysis	96
3.4.3.3	Numerical Computation of the $\tau(q)$ and $D(h)$ spectra . .	97
3.4.3.4	Probability Density Functions	98
3.4.3.5	Sensitivity test	101
3.5	RESULTS	113
3.5.1	Noise Analysis and Filtering	113
3.5.1.1	Noise Analysis from the DRAO Empty Channels	114
3.5.1.2	Filtering	120
3.5.2	The Three Spiral Arms	122
3.5.2.1	Fourier Analysis	122
3.5.2.2	Wavelet Analysis	125
3.5.2.3	Numerical Computation of the $\tau(q)$ and $D(h)$ spectra . .	129
3.5.2.4	Probability Density Functions	133
3.5.3	The Two Inter-Arms	143

3.5.3.1	Fourier Analysis	143
3.5.3.2	Wavelet Analysis	146
3.5.3.3	Numerical Computation of the $\tau(q)$ and $D(h)$ spectra . .	146
3.5.3.4	Probability Density Functions	151
3.6	ANALYSIS AND DISCUSSION	156
3.6.1	Spiral vs Inter Arms	157
3.6.2	Astrophysical Discussion	159
3.6.2.1	Scale-Height Relation	159
3.6.2.2	Anisotropy	160
3.6.2.3	Turbulence	163
3.7	CONCLUSION	164
3.7.1	The Galactic H I	164
3.7.2	Future Work	166
3.8	ACKNOWLEDGEMENTS	166
3.9	APPENDICES	166
3.9.1	Examples	167
3.9.2	Numerical Implementation	174

<i>TABLE DES MATIÈRES</i>	xiv
4 Conclusion	178
4.1 TECHNIQUE D'ESPACES MÉTRIQUES	179
4.2 MÉTHODE DES MAXIMA DU MODULE DE LA TRANSFORMÉE EN ONDELETTES	179
4.3 AUTO-CRITIQUE ET TRAVAUX FUTURS	180
4.3.1 TEM	180
4.3.2 Méthode MMTO	182
Bibliographie	184

Liste des figures

2.1	Column density map of the sample H I feature associated with S134.	27
2.2	Density distribution of the sample H I feature S134.	29
2.3	Volume distribution of the sample H I feature S134.	29
2.4	Components distribution of the sample H I feature S134.	30
2.5	Filament index distribution of the sample H I feature S134.	31
2.6	Pixel distribution of the sample H I feature S134.	35
2.7	Number of H I features according to complexity ranks.	42
2.8	Bar chart representing the overall complexity classification with respect to the analyzed H I features.	44
2.9	<i>A</i> and <i>B</i> have the same diameter and the same area and therefore, the same filament index, even though their structure is quite different.	55
3.1	The mosaics Local, Inter I, Perseus, Inter II, and Outer.	66
3.2	The first and third-order analyzing wavelets.	69

3.3 FBm surfaces generated with the Fourier transform filtering synthesis method. a) $H = 0.2$; b) $H = 0.5$; c) $H = 0.8$	78
3.4 Fourier analysis of the 512×512 central part of a fBm surface $B_{H=0.2}(\mathbf{x})$	79
3.5 2D wavelet transform analysis of $B_{H=0.2}(\mathbf{x})$	80
3.6 Wavelet transform skeleton of an isotropic 2D fBm surface.	81
3.7 Determination of the $\tau(q)$ and $D(h)$ spectra of 2D fBm with the 2D WTMM method.	83
3.8 Pdfs of the WTMM coefficients of $B_{H=0.2}(\mathbf{x})$	84
3.9 Pdfs of the WTMM coefficients of $B_{H=0.2}(\mathbf{x})$	85
3.10 Fourier analysis of the 512×512 central part of a multifractal surface.	88
3.11 2D wavelet transform analysis of a multifractal rough surface.	89
3.12 Determination of the $\tau(q)$ and $D(h)$ spectra of multifractal rough surfaces.	90
3.13 Pdfs of the WTMM coefficients of synthetic multifractal rough surfaces.	92
3.14 Fourier analysis of the 512×512 central part of the simulated anisotropic surfaces $B_{H_x=0.10, H_y=0.50}(\mathbf{x})$	95
3.15 2D wavelet transform analysis of $B_{H_x=0.10, H_y=0.50}(\mathbf{x})$	96
3.16 One-dimensional cuts taken from one realization of $B_{H_x=0.10, H_y=0.50}(\mathbf{x})$	97
3.17 Determination of the $\tau(q)$ and $D(h)$ spectra of the fBs $B_{H_x=0.10, H_y=0.50}(\mathbf{x})$	99

3.18 Pdfs of the WTMMM coefficients of $B_{H_x=0.10, H_y=0.50}(\mathbf{x})$.	100
3.19 Pdfs of the x and y components of the WTMMM coefficients of the surfaces $B_{H_x=0.10, H_y=0.50}(\mathbf{x})$.	101
3.20 Fourier analysis of the 512×512 central part of the simulated anisotropic surfaces $B_{H_x=0.41, H_y=0.44}(\mathbf{x})$.	103
3.21 Fourier analysis of the 512×512 central part of the simulated anisotropic surfaces $B_{H_x=0.45, H_y=0.52}(\mathbf{x})$.	104
3.22 2D wavelet transform analysis of $B_{H_x=0.41, H_y=0.44}(\mathbf{x})$.	105
3.23 2D wavelet transform analysis of $B_{H_x=0.45, H_y=0.52}(\mathbf{x})$.	106
3.24 Determination of the $\tau(q)$ and $D(h)$ spectra of the fBs $B_{H_x=0.41, H_y=0.44}(\mathbf{x})$ with the 2D WTMM method.	107
3.25 Determination of the $\tau(q)$ and $D(h)$ spectra of the fBs $B_{H_x=0.45, H_y=0.52}(\mathbf{x})$ with the 2D WTMM method.	108
3.26 Pdfs of the WTMMM coefficients of $B_{H_x=0.41, H_y=0.44}(\mathbf{x})$.	109
3.27 Pdfs of the WTMMM coefficients of $B_{H_x=0.45, H_y=0.52}(\mathbf{x})$.	109
3.28 Pdfs of the x and y components of the WTMMM coefficients of the surfaces $B_{H_x=0.41, H_y=0.44}(\mathbf{x})$.	110
3.29 Pdfs of the x and y components of the WTMMM coefficients of the surfaces $B_{H_x=0.45, H_y=0.52}(\mathbf{x})$.	111
3.30 Rescaled pdfs of the x components of the WTMMM coefficients of the surfaces $B_{H_x=0.41, H_y=0.44}(\mathbf{x})$.	112

3.31 512 × 512 sample noise images.	114
3.32 Fourier analysis of the 512×512 central part of the DRAO (\diamond) and synthetic (\bullet) noise surfaces.	116
3.33 Determination of the $\tau(q)$ and $D(h)$ spectra of the DRAO (\diamond) and synthetic (\bullet) noise mosaics with the 2D WTMM method.	117
3.34 Pdfs of the WTMM coefficients of the DRAO noise surfaces.	118
3.35 Effects of the filtering algorithm.	120
3.36 Comparisons between the filtered (\diamond) and unfiltered (full line) mosaics on the expectation values $h(q, a)$ and Fourier analysis for the Local arm subregions.	121
3.37 Fourier analysis of the Local arm subregions.	122
3.38 Fourier analysis of the Perseus arm subregions.	123
3.39 Fourier analysis of the Outer arm subregions.	124
3.40 2D wavelet transform analysis of one Local arm subregion.	126
3.41 2D wavelet transform analysis of one Perseus arm subregion.	127
3.42 2D wavelet transform analysis of one Outer arm subregion.	128
3.43 Determination of the $\tau(q)$ and $D(h)$ spectra of the Local arm subregions with the 2D WTMM method.	130
3.44 Determination of the $\tau(q)$ and $D(h)$ spectra of the Perseus arm subregions with the 2D WTMM method.	131

3.45 Determination of the $\tau(q)$ and $D(h)$ spectra of the Outer subregions with the 2D WTMM method.	132
3.46 Pdfs of the WTMM coefficients of the Local arm subregions.	134
3.47 Pdfs of the WTMM coefficients of the Perseus arm subregions.	135
3.48 Pdfs of the WTMM coefficients of the Outer arm subregions.	136
3.49 Pdfs of the x and y components of the WTMM coefficients of the Local arm subregions.	137
3.50 Pdfs of the x and y components of the WTMM coefficients of the Perseus arm subregions.	138
3.51 Pdfs of the x and y components of the WTMM coefficients of the Outer arm subregions.	139
3.52 Pdfs of the x and y components of the WTMM coefficients of the Local arm subregions.	140
3.53 Rescaled pdfs of the x components of the WTMM coefficients of the Local arm subregions.	141
3.54 Pdfs of the WTMM coefficients for the Local arm mosaic.	143
3.55 Fourier analysis of the Inter I subregions.	144
3.56 Fourier analysis of the Inter II subregions.	145
3.57 2D wavelet transform analysis of one Inter I subregion.	147
3.58 2D wavelet transform analysis of one Inter II subregion.	148

3.59 Determination of the $\tau(q)$ and $D(h)$ spectra of the Inter I subregions with the 2D WTMM method.	149
3.60 Determination of the $\tau(q)$ and $D(h)$ spectra of the Inter II subregions with the 2D WTMM method.	150
3.61 Pdfs of the WTMM coefficients of the Inter I subregions.	152
3.62 Pdfs of the WTMM coefficients of the Inter II subregions.	153
3.63 Pdfs of the x and y components of the WTMM coefficients of the Inter I subregions.	154
3.64 Pdfs of the x and y components of the WTMM coefficients of the Inter II subregions.	155
3.65 Schematic view of the Galactic plane.	161
3.66 Three-dimensional representation of the function $f_1(\mathbf{x}) = Ae^{-(\mathbf{x}-\mathbf{x}_1)^2/2\sigma^2} + B \mathbf{x} - \mathbf{x}_0 ^{0.3}$	167
3.67 Wavelet transform of the function f_1 shown in Figure 3.66.	168
3.68 Maxima chains defined by the WTMM of the function f_1 (Fig. 3.66). . .	170
3.69 Three-dimensional representation of the topological evolution of the WTMM chains of f_1 in the space-scale half-hyperplane.	171
3.70 Evolution of $\mathcal{M}_\psi(f_1)$ and $\mathcal{A}_\psi(f_1)$	172
3.71 WTMM analysis of the function $f_2(\mathbf{x})$	173
3.72 Evolution of $\mathcal{M}_\psi(f_2)$ and $\mathcal{A}_\psi(f_2)$	174

Liste des tableaux

2.1	Characteristics of the 28 H I Features	25
2.2	Complexity Ranking: Standard and Revised Components Distribution . .	40
2.3	28 H I Features, Ordered According to Their Complexity, From Least to Most Complex. Also Shown is the Fractal Dimension for Every Object. .	41
2.4	Correlation Between the Complexity of H I Features and Physical Parameters, if $\geq 80\%$ in absolute value.	47
3.1	Five H I mosaics	67
3.2	Hurst Exponents for the Five H I mosaics	156
3.3	Power Spectral Indices for the Five H I mosaics	158

Chapitre 1

Introduction

1.1 MISE EN SITUATION

Un consortium international de radioastronomes s'est formé en 1994 sous l'égide d'un groupe de chercheurs canadiens afin de produire un relevé panoramique multispectral du plan de notre galaxie. Cette approche permet l'étude des trois composantes gazeuses et de la composante solide (grains de poussière) qui peuplent le milieu entre les étoiles. Le but ultime de cette entreprise est d'établir les relations entre les composantes et de déterminer les processus physiques qui les façonnent afin d'obtenir une vision globale de l'écosystème galactique.

Le professeur Gilles Joncas coordonne un groupe pluridisciplinaire qui utilise plusieurs outils mathématiques comme les statistiques, la topologie, la géométrie fractale, la vision numérique, la logique floue, les réseaux de neurones et les ondelettes pour caractériser et classifier les structures du gaz d'hydrogène neutre ($H\ 1$) du milieu interstellaire (MIS). À l'intérieur de ce groupe, nous visons à construire un scénario évolutif du MIS et pour ce, nous tentons de répondre aux questions suivantes: 1) Peut-on associer à chaque structure $H\ 1$ un processus de création connu? 2) Comment la matière y est-elle distribuée? 3) Comment les structures atomiques se débarassent-elles de leur énergie pour passer de

l'atome à la molécule?

L'objectif de cette thèse interdisciplinaire est d'apporter une expertise mathématique à la compréhension, l'amélioration et l'utilisation, en astrophysique, d'outils d'analyse d'images fondés sur des notions mathématiques et ce, dans le cadre d'un doctorat sur mesure en mathématiques-astrophysique. Le contexte astrophysique se situe donc au niveau de l'étude du MIS, plus précisément de la composante atomique du MIS: le H I. Le H I constitue une des phases du MIS les plus compliquées. Il s'agit de structures chaotiques complexes, diffuses, imbriquées les unes dans les autres, et donc difficiles à décortiquer. Depuis plusieurs décennies, la difficulté majeure à laquelle les radioastronomes se sont heurtés est l'interprétation de la structure globale du H I dans la Galaxie. Et jusqu'à tout récemment, aucun outil quantitatif n'était disponible pour analyser le H I de façon globale.

Pour la première fois depuis la découverte de la raie à 21 cm, il y a plus de 50 ans, un relevé unique et détaillé sur le H I est maintenant disponible: le Canadian Galactic Plane Survey (CGPS) (Taylor et al., 2003). Vue l'ampleur de ce relevé et de la qualité inégalée de sa résolution, de nouveaux outils d'analyse doivent être utilisés pour en assurer une bonne exploitation. Contrairement à l'étude des nuages moléculaires, qui sont des objets isolés bien définis, le H I, beaucoup plus diffus, est présent dans tout le plan galactique. Il faut donc utiliser des méthodes objectives pour l'étudier.

L'omniprésence du H I en fait un traceur de structure dans la Galaxie. Notre premier objectif était donc d'analyser les structures H I (provenant du CGPS) associées à des objets ponctuels “connus” (régions H II, restes de supernova et étoiles Wolf-Rayet) à l'aide de nouveaux outils d'analyse morphologique. Ce type d'analyse est présenté au chapitre 2.

Une partie importante de la recherche d'outils mathématiques était concentrée du côté des formalismes fractals et multifractals. Cette recherche nous a amenés à découvrir une méthode objective très puissante qui permet d'analyser les structures à grande échelle du plan galactique. Cette analyse est présentée au chapitre 3.

1.2 LE MILIEU INTERSTELLAIRE

C'est au dix-huitième siècle que les télescopes sont devenus assez puissants pour découvrir, entre autres par William Herschel, des régions diffuses de lumière alors appelées “nébuleuses” (nebulae, du latin pour nuage). Aucune observation précédente ne pouvait indiquer la présence de matière interstellaire. Et avant l'étude des spectres de ces objets par William Huggins dans les années 1860, ces premières observations étaient interprétées comme étant des amas d'étoiles de faible intensité. Huggins a montré que ces nébuleuses brillantes étaient composées de gaz chaud, comme l'hydrogène. Les travaux de Slipher, Wolf, Barnard, Hartmann et Trumpler entre les années 1910 et 1930 ont mis en évidence la présence de la poussière interstellaire (nuages sombres), de par l'extinction interstellaire que celle-ci causait sur les observations d'étoiles. Mais il s'agit toujours d'objets considérés comme discrets. Aucune observation ne permettait de dire qu'une matière diffuse était omniprésente dans le milieu interstellaire. La détection de la raie d'hydrogène neutre ($H\ I$) à 21 cm en 1951 a confirmé la présence d'une telle composante.

Le MIS sert d'ingrédient pour la formation de nouvelles étoiles et ces dernières rejettent leur matière dans le MIS sous forme de vents stellaires et lors de leur mort. L'analyse du MIS permet, par exemple, de tracer la rotation de la Galaxie, d'étudier le taux de création de nouveaux éléments et de déterminer la masse de galaxies spirales distantes.

Les spécialistes du MIS ont divisé le gaz interstellaire en quatre classes: le milieu neutre froid (*cold neutral medium*, CNM), le milieu neutre chaud (*warm neutral medium*, WNM), le milieu ionisé chaud (*warm ionized medium*, WIM) et le milieu ionisé très chaud (*hot ionized medium*, HIM). Cependant, Wynn-Williams (1992) présente une classification en trois grandes catégories suivant l'histoire du gaz, ce qui permet une compréhension plus intuitive du cycle de vie du MIS. Chacune de ces catégories peut ensuite être classifiée selon la température du gaz.

La première de ces trois grandes catégories est *le gaz récemment éjecté des étoiles*. Selon la température, les trois sous-catégories sont: 1) les coquilles circumstellaires, qui sont générées par les vents provenant de la surface d'étoiles géantes rouges; 2) les nébuleuses planétaires, qui sont formées lorsque le gaz circumstellaire est ionisé par le

cadavre stellaire qu'il entoure; et 3) les restes de supernova, qui résultent de l'explosion d'une étoile massive devenue instable.

La deuxième grande catégorie est *le gaz associé à la naissance des étoiles*. Les trois sous-catégories sont les nuages moléculaires denses ayant des température d'environ 15 K (mais pouvant atteindre 50 K près des limites du nuage ou bien près des étoiles récemment formées), les régions d'hydrogène ionisé (régions H II) se trouvant autour de nouvelles étoiles massives (O-B) où la température se situe entre 8000 – 10000 K ainsi que le H I photodissocié, provenant de molécules d'hydrogène qui ont été dissociées.

La troisième grande catégorie est *le gaz diffus du MIS*, où la première des trois sous-catégories concerne les nuages “froids”, ayant des températures d'environ 80 K et une densité de l'ordre de 10 à 100 atomes cm⁻³. Il y a deux types de gaz dans les nuages froids: le gaz moléculaire, détecté par les raies d'absorption dans le domaine ultra-violet et le gaz H I, détecté par son émission à la raie de 21 cm (et aussi par les raies d'absorption dans le domaine ultra-violet). La deuxième sous-catégorie de gaz diffus est le gaz “chaud”, ayant une température d'environ 8000 K et une densité d'environ 0.1 atomes cm⁻³, qui est composé d'un mélange de gaz H I et de gaz ionisé. La troisième sous-catégorie est le gaz coronal, ayant une température pouvant atteindre le million de Kelvin et une densité plus petite que 10⁻² atomes cm⁻³ et qui est majoritairement détecté par l'émission de rayons-X ainsi que par l'observation des raies UV d'atomes très ionisés (e.g. OVI).

1.2.1 L'hydrogène neutre

Les raies spectrales observées par les astronomes se comptent par milliers, mais la raie à 21 cm se distingue nettement de par son importance au niveau physique ainsi que pour l'étude du MIS. Les lois de la mécanique quantique permettent les états parallèle et anti-parallèle de l'atome d'hydrogène. L'état parallèle se situe à un niveau d'énergie légèrement supérieur à celui de l'état anti-parallèle: une différence de 6×10^{-6} eV, qui correspond à un photon ayant une longueur d'onde de 21 cm. La raie à 21 cm est très importante en astronomie, étant la seule pouvant être émise par l'hydrogène neutre sous des conditions interstellaires “normales”. Toute autre raie spectrale de l'hydrogène

nécessite un saut au niveau $n \geq 2$, ce qui requiert au moins 10.2 eV par atome, donc environ un million de fois plus d'énergie que la raie à 21 cm.

La raie à 21 cm est une des plus “interdites”. Un atome d'hydrogène laissé à lui-même dans l'état parallèle restera dans cet état pendant environ 10^7 années avant de changer d'état et d'émettre un photon à 21 cm. Malgré la faible densité du H I dans le MIS, les collisions entre atomes d'hydrogène se produisent aux environs de tous les 1000 ans. Ces collisions sont responsables du changement de transition entre les deux états. La mécanique quantique nous dit ensuite que le nombre de photons à 21 cm émis par seconde d'une région H I dépend seulement de la quantité totale d'hydrogène neutre dans cette région.

Une des raisons pour laquelle la raie à 21 cm est si importante en astronomie est la quasi-absence d'absorption. Par contre, à ce grand avantage est associé un inconvénient: comme le photon à 21 cm ne subit que très peu d'absorption, il est très difficile de déterminer sa provenance (i.e. sa distance sur la ligne de visée). La mesure de l'effet Doppler, lors de l'observation de la raie à 21 cm, nous informe sur la vitesse de l'atome d'où provient le photon, ce qui nous permet de situer grossièrement la structure H I dans la Galaxie. C'est d'ailleurs en analysant la relation entre l'intensité du signal et sa vitesse que nous pouvons situer les structures H I qui nous intéressent (bras spiraux, etc).

1.2.1.1 CNM vs WNM

Les deux phases les plus importantes de l'hydrogène neutre sont le milieu neutre froid (*cold neutral medium*, CNM) et le milieu neutre chaud (*warm neutral medium*, WNM). Ce qui suit est une description comparative de ces deux phases, basée sur les résultats présentés dans Dickey et al. (2001), Lequeux (2002) et Miville-Deschénes et al. (2003).

Le CNM est évidemment beaucoup plus froid que le WNM, avec des températures de 60 – 100 K pour le premier et 3000 – 8000 K pour le second. Et bien que la masse totale des deux dans la Galaxie soit similaire, i.e. $1.5 \times 10^9 M_\odot$, leur densité est différente. Comme la température du CNM est beaucoup plus petite que celle du WNM, la densité

de ce dernier est très faible, i.e. $0.1 - 0.3 \text{ cm}^{-3}$, tandis que la densité du CNM est de $20 - 30 \text{ cm}^{-3}$. À grande échelle, le WNM occupe un disque plus épais que le CNM. Par exemple, autour du Soleil les demi-épaisseurs sont de 186 et 105 pc respectivement. La raie à 21 cm peut se manifester également en absorption devant une source de continuum radio ou devant la raie à 21 cm émise par du gaz plus chaud. Donc, pour le CNM, la densité de colonne ne peut être déduite des observations en absorption seules. En général, le CNM a des structures plus complexes (notamment dans les enveloppes des nuages moléculaires) que le WNM, qui est distribué plus uniformément dans la Galaxie.

Selon Dickey et al. (2001), le CNM et le WNM sont dans deux régimes de turbulence fondamentalement différents. Pour le CNM, les processus actifs sont dominés par les fluctuations en vitesse tandis que pour le WNM, les processus qui dominent sont les fluctuations en densité (la pente du spectre de puissance augmente avec l'épaisseur des régions analysées). Les objets analysés dans cette thèse font donc partie du WNM. Les objets ou bien les sous-régions H I appartenant au CNM (sources en absorption, par exemple) ont été évités ou bien rejetés, selon le cas.

1.3 OUTILS MATHÉMATIQUES

Le MIS est un lieu où plusieurs processus dynamiques plus ou moins organisés sont actifs: champs magnétiques, ondes de chocs de supernovae, vents stellaires, collisions et turbulence. Tel que décrit dans Dickey et al. (2001), la structure du gaz H I de la Galaxie peut être considérée comme une combinaison de deux états: déterministe et stochastique. Dans le premier cas, il s'agit de structures plus ou moins bien connues comme des coquilles, des bulles, des cheminées, des nuages et des courants (*streams*). Dans le second cas, il s'agit de structures pouvant être caractérisée de façon statistique. Comme les deux processus seraient reliés (Dickey et al., 2001), il est extrêmement important, et de surcroît, délicat d'en analyser les structures de façon objective et quantitative.

L'époque des analyses qualitatives, par inspection visuelle par exemple, ou sommaire via des paramètres globaux, doit s'effacer si on veut réaliser des profits substantiels. La puissance sans cesse croissante des ordinateurs permet d'innover grandement dans le

domaine de l'analyse d'image.

Les outils d'analyse utilisés ici sont basés sur des fondements mathématiques. La technique d'Espaces Métriques (TEM, chapitre 2) est basée sur des notions de l'analyse réelle et fonctionnelle tandis que la méthode des Maxima du Module de la Transformée en Ondelettes (méthode MMTO, chapitre 3) est construite en toute analogie avec la thermodynamique.

En 1992, Adams présentait une approche “topologique / géométrique” pour l'étude des images astrophysiques (Adams, 1992). La justification d'une telle approche dans le contexte de l'époque était de trouver une méthode pouvant différencier, de façon quantitative, deux images astrophysiques distinctes. Même si cette époque ne date que d'une dizaine d'années, il faut bien prendre note qu'il s'agit d'une période où plusieurs outils d'analyse *objective* ont fait leur apparition. Nous allons maintenant nous attarder de façon détaillée à ces outils avant d'introduire la TEM et la méthode MMTO.

1.3.1 Les analyses fractales

C'est Mandelbrot qui a proposé l'adjectif *fractal* pour décrire la géométrie des objets pouvant être caractérisés par une dimension non-entière (Mandelbrot, 1977, 1982). Une des propriétés fondamentales de ces objets *fractals* est la présence d'une autosimilarité qui se résume par le fait qu'il existe des transformations impliquant des dilatations qui laissent l'objet invariant (éventuellement dans un sens statistique). En astrophysique, les exemples les plus connus sont la distribution des galaxies (Gaite & Maurubia (2002), par exemple), les grains de poussières (Fogel & Leung, 1998), et bien évidemment, les structures gazeuses du milieu interstellaire.

Les objets fractals ont l'originalité de présenter des détails à toutes les échelles de longueur, ce qui explique les difficultés rencontrées pour les caractériser. Un des grands mérites de Mandelbrot est d'avoir su reconnaître que de nombreuses structures ou dynamiques complexes multi-échelles observées dans de nombreux domaines des sciences fondamentales et appliquées, pouvaient être appréhendées au sein d'un cadre fédérateur

basé sur les notions de fractale et d'invariance d'échelle. Le succès de ses différents ouvrages a donné un nouvel élan expérimental à de nombreuses branches de la physique, de la chimie, de la biologie, de la géologie, de la météorologie, de la science des matériaux, de l'astronomie, ainsi qu'en mathématiques.

Un objet *monofractal* est un objet invariant par des transformations géométriques de dilatation: sans plus d'information sur l'objet, on est incapable de distinguer l'objet lui-même de l'un de ses détails, convenablement dilaté, comme des flocons de neige, naturels ou mathématiques, ou les trajectoires du mouvement Brownien (dans un sens statistique). Un objet *multifractal* est plus complexe dans le sens où il est toujours invariant par dilatation, mais le facteur de dilatation nécessaire pour ne pouvoir distinguer le détail de l'objet entier dépend du détail observé. En mathématiques, les exemples concernent la théorie de la mesure, où l'invariance par dilatation est exacte, tandis que sur le plan expérimental en géophysique, en turbulence, en électrochimie ou en astrophysique, l'invariance est vraie dans un sens statistique.

1.3.1.1 Comptage de boîtes

L'utilisation la plus répandue des concepts fractals en astrophysique est sans aucun doute la dimension fractale. Le fait que deux objets aient des dimensions fractales similaires ou différentes peut habituellement indiquer des liens ou des différences, au niveau, par exemple, de la physique, de la composition chimique, ou de la structure des deux objets. Par contre, il est très important de tenir compte du fait que la dimension fractale est dégénérée en ce sens que deux processus extrêmement différents peuvent avoir la même dimension fractale.

La technique dite de comptage de boîtes est probablement la plus simple et la plus répandue pour estimer la dimension fractale. À une échelle de longueur donnée, ϵ , il s'agit de recouvrir l'objet étudié par des "boîtes"¹. Le nombre de boîtes requis pour recouvrir l'objet, $N(\epsilon)$, se comporte en loi de puissance de la façon suivante: $N(\epsilon) \sim \epsilon^{-D}$, où D est

¹En théorie, ces boîtes n'ont pas de structure pré-définie, il pourrait s'agir de cercles, de triangles, ou toute autre forme géométrique simple.

la dimension fractale de l'objet (Mandelbrot, 1977, 1982; Falconer, 1990; Barnsley, 1993). Pour une discussion mathématique détaillée sur la technique de comptage de boîtes, voir Khalil (1998).

Comme nous le verrons au chapitre 3, la dimension fractale est en fait une sous-estimation de la dimension de Hausdorff. Cette dernière est calculée d'une façon similaire, à l'exception du fait très important que les boîtes de recouvrement doivent circonscrire la partie de l'objet qu'elles recouvrent. L'échelle de longueur donnée ϵ n'est alors que le minimum de toutes les boîtes utilisées, ce qui rend la mise en algorithme impossible². Par contre, le meilleur rapprochement consiste à utiliser des boîtes adaptables et oscillantes, i.e. des ondelettes (chapitre 3).

Pour l'étude du MIS, la technique de comptage de boîtes a été utilisée entre autres par Stanimirovic et al. (1998); Westpfahl et al. (1999); Datta (2003). Westpfahl et al. (1999) ont analysé le gaz H I de plusieurs galaxies membres du groupe M81, où ils trouvent $1.2 \leq D \leq 1.5$. Le fait que D soit non-entière est en soi une confirmation que les structures H I analysées sont détaillées à toutes les échelles (il n'existe pas d'échelle privilégiée). Comme les structures fractales ont une surface beaucoup plus grande que des structures lisses, les échanges de température et de matériel se font beaucoup plus rapidement. D'ailleurs, les nouveaux modèles du MIS comportent maintenant des propriétés fractales, ce qui les rend beaucoup plus réalistes (voir les références de Westpfahl et al. (1999)).

1.3.1.2 Relation aire-périmètre

Concept introduit par Mandelbrot (1977) et initialement utilisé pour l'étude des nuages terrestres (Lovejoy, 1982), la relation entre l'aire, A , et le périmètre, P , d'un objet est exprimée de la façon suivante: $A^{1/2} \sim P^{1/D}$, où D est toujours la dimension fractale. Cette relation simple a été grandement utilisée pour l'analyse des nuages moléculaires (Bazell & Désert, 1988; Dickman, Horwath & Margulis, 1990; Scalo, 1990; Falgarone, Phillips & Walker, 1991) ainsi que pour le H I (Vogelaar & Wakker, 1994). Pour ces études aussi, les valeurs estimées pour D sont dans l'intervalle $\approx [1.2, 1.5]$. Nous y re-

²Notons qu'une nouvelle méthode vient de voir le jour (Li, Arneodo & Nekka, 2004).

viendrons dans quelques paragraphes.

1.3.1.3 Autres techniques fractales

Gill & Henriksen (1990) et Gill (1993) sont les premiers à avoir utilisé la transformée en ondelettes dans le cadre d'une analyse multi-échelle de nuages moléculaires. Les auteurs présentent une relation entre la transformée en ondelettes et son facteur d'échelle pour calculer la dimension fractale. Ils obtiennent des résultats similaires aux autres études des nuages moléculaires, i.e. $\approx 2.35^3$.

Stutzki et al. (1998) présentent une nouvelle méthode, qu'ils appellent “ Δ -variance”. En utilisant cette méthode sur des nuages moléculaires, la dimension fractale qu'ils dérivent est $D \approx 1.6$ et est donc plus élevée que celle des autres études.

1.3.2 Les analyses multifractales

La dimension fractale est une information quantitative qui peut aider à déterminer la complexité des structures. La majorité des études mentionnées ici présentent des résultats pour D dans l'intervalle $\approx [1.2, 1.5]$ (Bazell & Désert, 1988; Gill & Henriksen, 1990; Scalo, 1990; Falgarone, Phillips & Walker, 1991; Gill, 1993; Vogelaar & Wakker, 1994; Elmegreen & Falgarone, 1996; Stanimirovic et al., 1998; Westpfahl et al., 1999) (Stutzki et al. (1998) obtiennent ≈ 1.6). Le fait que D soit universelle (et similaire aux résultats obtenus sur des nuages terrestres (Lovejoy, 1982; Rys & Waldvogel, 1986)) peut nous informer sur les processus physiques sous-jacents qui sculptent le gaz. Par exemple, certains auteurs trouvent “une analogie avec l'exposant $4/3$ qui est associé à la caractérisation de la dépendance de la variance des fluctuations de pression avec séparation spatiale dans une atmosphère obéissant à la théorie de Kolmogorov sur la turbulence incompressible, homogène et isotrope” (Dickman, Horwath & Margulis, 1990). La turbulence serait donc un processus physique majeur responsable de la structure des nuages interstellaires

³Notons que ce résultat correspond à la dimension véritable des nuages en 3D, contrairement aux autres études, qui présentent la dimension fractale des objets projetés en 2D.

(Scalo, 1987; Falgarone, 1989; Falgarone & Phillips, 1990). D'autres auteurs déduisent une relation entre la dimension fractale et la pente de la fonction de masse initiale de Salpeter (1955), i.e. ~ 1.35 , ce qui suggèrerait que la masse des "grumeaux" (clumps) des nuages moléculaires (structures hiérarchiques) suit la même loi de puissance que les étoiles qu'ils vont éventuellement former.

L'universalité de D peut être interprétée de deux façons diamétralement opposées. D'une part, une D universelle peut suggérer des parallèles entre l'hydrodynamique des nuages galactiques et les courants atmosphériques qui sculptent les nuages terrestres. D'autre part, comme la dimension fractale est dégénérée, il est très possible que l'universalité ne soit en fait que coïncidence. Et de plus, si les surfaces analysées ont des propriétés multifractales, alors les méthodes mentionnées jusqu'ici ne pourraient pas les détecter. Donc, il se pourrait très bien que les spectres d'exposants qui caractérisent les objets multifractals soient, eux aussi, universels, ou bien très différents selon le type de nuages analysés (moléculaire, H I, ou terrestre). D'ailleurs, l'analyse multifractale des nuages terrestres à l'aide de la méthode MMTO a démontré la présence d'une signature multifractale (Roux, Arneodo & Decoster, 2000), tandis que, comme nous le verrons au chapitre 3, les structures H I que nous avons analysées exhibent des propriétés monofractales.

1.3.2.1 Formalisme multifractal de comptage de boîtes

En reconnaissant la dégénérence de la dimension fractale, Scalo et Chappell ont décidé d'utiliser le formalisme multifractal de comptage de boîtes. Une signature multifractale consiste en un spectre de dimensions, ce qui rend cette approche moins dégénérée que l'approche mono-fractale. De plus, un processus multifractal peut être mathématiquement relié au concept de cascade multiplicative (dont nous reparlerons aux sections 3.1 et 3.4.2; voir aussi Meneveau & Sreenivasan (1987) et Chappell & Scalo (2001)), ce qui en fait l'outil idéal pour étudier les structures hiérarchiques⁴, ce qu'ont fait Chappell et Scalo sur des nuages moléculaires (Chappell & Scalo, 2001).

⁴Un processus multiplicatif dans une surface 2D se traduit par l'intensité en un point donné comme étant le résultat de multiplications successives le long d'une lignée hiérarchique.

L'approche multifractale présentée par Chappell & Scalo (2001) était tout à fait novatrice pour les experts du MIS et il est fort à parier que leur étude constitue une solide référence pour les approches similaires dans le futur. C'est pourquoi nous profiterons de cette introduction pour en discuter plus amplement.

En plus de la discussion sur la caractérisation des phénomènes multiplicatifs pouvant être associés aux structures hiérarchiques, les auteurs vantent les avantages de leur approche (avec raison) qui tient compte de tous les points des surfaces, et non simplement les points compris dans les courbes disjointes des isocontours utilisées pour la technique de la relation aire-périmètre. Ils mentionnent tout de même que la dimension obtenue par cette dernière technique est un outil utile en soi qui est complémentaire aux autres outils descriptifs. De plus, ils ne se contentent pas d'utiliser le formalisme multifractal comme une simple généralisation des concepts monofractals. Chappell & Scalo (2001) présentent les types de comportements multifractals pouvant être associés à certains phénomènes physiques, comme la turbulence incompressible pleinement développée (Muzy, Bacry & Arneodo, 1991) (dont nous reparlerons au chapitre 3), qui exhibe une signature multifractale universelle.

Nous pouvons donc dire que tout indique que les auteurs sont bien préparés pour interpréter adéquatement les résultats que leur analyse produira. Malheureusement, à cette excellente préparation interprétative n'est pas associée une préparation méthodique adéquate. Les formalismes multifractals sont loin d'être des boîtes noires auxquelles on peut fournir aveuglément de l'information (signaux, images, etc). Le problème est que si on agit ainsi, des résultats seront tout de même produits par la boîte noire. Il est donc très important de calibrer la méthodologie, ce que Chappell & Scalo (2001) semblent avoir omis de faire⁵.

Comme nous le verrons au chapitre 3, le paramètre q est un paramètre libre, réel qui, pour des valeurs entières positives, caractérise les moments des valeurs d'une fonction

⁵A. Arneodo, inventeur principal de la méthode MMTO et co-auteur de l'article qui constitue le chapitre 3 de cette thèse, qui a donc régulièrement servi d'arbitre scientifique pour des publications en relation avec les notions de fractales / multifractales, constate que ce genre d'erreur est assez répandu dans plusieurs domaines scientifiques, et ce, nonobstant le degré de notoriété des auteurs qui soumettent ces publications (communication privée).

de partition. Dans le cadre d'une analyse multifractale, la caractérisation ne passe pas par la détermination d'un seul nombre (la dimension fractale), mais un spectre continu de dimensions indiquées par q . Le paramètre q permet donc d'examiner les différentes *phases d'autosimilarité* de la fonction (image, surface) considérée: en faisant varier q de $+\infty$ à $-\infty$, on caractérise successivement les régions les plus concentrées jusqu'aux régions les plus raréfiées. La fonction $\tau(q)$, obtenue à partir du comportement en loi de puissance d'une fonction de partition, est linéaire en fonction de q pour une signature monofractale (homogène), et non-linéaire pour une signature multifractale (hétérogène) et ce, pour n'importe quel formalisme multifractal (par comptage de boîtes ou bien basé sur la transformée en ondelettes). Un des buts de la calibration est donc de déterminer sur quel intervalle de q l'analyse peut être faite. Par exemple, pour la méthode MMTO, Arneodo, Decoster & Roux (2000) ont démontré (empiriquement) que les valeurs de q ne pouvaient être plus petites que $q \approx -6$ et plus grandes que $q \approx 8$ et ce, pour une analyse dont les résultats sont moyennés sur 32 images 1024×1024 . Comme nous le verrons au chapitre 3 pour l'analyse des bras spiraux et des inter-bras, le fait d'utiliser moins de 32 images, pour lesquelles l'accès aux plus petites échelles est interdit (à cause du bruit) nous restreint à utiliser des valeurs de q dans l'intervalle $[-1, 3]$. De plus, la méthodologie de Arneodo, Decoster & Roux (2000) met en évidence une relation tenant compte du paramètre q et qui est obtenue à partir des propriétés d'auto-similarité des surfaces monofractales. Cette relation, que nous utiliserons au chapitre 3, permet de valider le choix de l'intervalle des valeurs de q .

En analysant plusieurs images prises séparément, Chappell & Scalo (2001) ont de toute évidence accès à (relativement) très peu de pixels. Pourtant, ils utilisent des valeurs de q allant jusqu'à 20. Et bien qu'ils ne puissent justifier un tel choix, n'ayant pas calibré leur méthodologie en analysant des surfaces simulées ou bien en utilisant une relation d'auto-similarité tenant compte du paramètre q , tout porte à croire que ce choix ($q = 20$) est trop élevé⁶. Par conséquent, que les propriétés des surfaces qu'ils analysent soient monofractales ou multifractales, les incertitudes sur les valeurs associées au choix de $q = 20$ pourraient être telles que leurs résultats soient basés sur des phénomènes artificiels. En effet, le fait de considérer des valeurs de q trop élevées peut facilement donner une fonction $\tau(q)$ ayant un comportement non-linéaire alors que la structure

⁶Il serait difficile de calculer combien d'images seraient nécessaires pour pouvoir utiliser $q = 20$ et quelles grandeurs devraient avoir ces images.

analysée est monofractale.

Un problème supplémentaire est qu'une bonne partie de l'interprétation astrophysique présentée par Chappell & Scalo (2001) soit basée sur les valeurs obtenues à partir du comportement de la fonction de partition pour $q = 20$.

Enfin, leurs résultats démontrent que les images analysées (densité de colonne de nuages moléculaires à partir de données IRAS) ont toutes des propriétés multifractales. Il est bien possible que ce soit effectivement le cas. Et le choix de $q = 20$ est peut-être adéquat après tout. Mais sans une calibration et une validation de leur méthodologie, nous ne pouvons que comparer l'utilisation de $q = 20$ à d'autres analyses similaires et conclure qu'il est peu probable que les résultats soient totalement réels.

1.3.3 Fonction de corrélation

Au début des années 1990, Scalo et Houlahan ont présenté une étude en deux parties sur la caractérisation et la reconnaissance des structures interstellaires hiérarchiques. La seconde partie, qui sera traitée à la section suivante, traite des arbres statistiques. La première partie (Houlahan & Scalo, 1990) présente une discussion sur l'utilité de la fonction de corrélation (à deux points) pour l'étude d'une multitude de modèles analytiques. L'objectif des auteurs est de trouver les conditions à partir desquelles la fonction de corrélation peut reconnaître et caractériser les structures hiérarchiques pouvant exister dans les régions de formation d'étoiles, dans l'espoir de contribuer à l'élaboration des modèles physiques de fragmentation. Les auteurs concluent que la domination des effets de taille finie et les effets de bord, causée par les plus grandes structures (une petite quantité de grands nuages dont la surface occupe une fraction importante de l'image) contrôle la forme de la fonction de corrélation. Ce comportement reflète donc la présence des gradients et des séparations des grands nuages, qui ne sont pas nécessairement importants au niveau statistique et qui peuvent donc être mieux étudiés par une inspection visuelle des images originales, ce qui ajoute de fortes contraintes à la méthode. Par contre, elle peut être utilisée pour caractériser les amas de sources ponctuelles, mais sur des échelles beaucoup plus petites que la taille de l'image, ainsi que pour la détection de

faibles gradients.

1.3.4 Arbres statistiques

Bien qu'elle soit présentée comme une méthode pour la quantification des images complexes du MIS, l'analyse des “arbres de structures” (Houlihan & Scalo, 1992) est mieux adaptée à l'étude des nuages moléculaires que celle des images H I⁷. L'idée, simple et originale, consiste à faire une représentation hiérarchique de la partition des nuages et des sous-nuages en ne tenant compte que de la position des centroïdes, à partir des iso-contours de ces derniers. Comme les relations spatiales des nuages et sous-nuages sont considérées, une “lignée” de descendants peut être caractérisée. Le formalisme distingue très bien les structures (simulées) hiérarchiques des structures aléatoires et même des structures combinant les deux (hiérarchiques et aléatoires). Le formalisme est testé sur une région du nuage moléculaire Taurus (données IRAS) où une structure hiérarchique est effectivement détectée, ce qui confirme que les processus de formation d'étoiles se réalisent étape par étape et non en un seul effondrement gravitationnel.

Ce qui affaiblit ce formalisme pour l'analyse potentielle du H I réside dans l'énorme perte statistique occasionnée par la seule considération de centroïdes, qui eux sont obtenus à partir d'iso-contours. Par contre, tel que constaté par Scalo lui-même⁸, cet outil ne fournit qu'un seul type d'information et devrait donc être utilisé en conjonction avec d'autres méthodes.

1.3.5 Caractérisation de la turbulence

La turbulence hydrodynamique constitue incontestablement l'un des problèmes majeurs de la physique moderne, ce qui explique et justifie les efforts, aussi bien au niveau

⁷Les nuages moléculaires sont des objets ayant des frontières généralement bien définies et possèdent une structure hiérarchique. Par contre, le H I est diffus et ne possède pas nécessairement de structure hiérarchique.

⁸Communication privée

théorique qu’expérimental, qui ont été effectués depuis la deuxième moitié du vingtième siècle. L’étude du MIS n’y fait pas exception. La grande majorité des spécialistes du MIS parlent de phénomènes turbulents à toutes les échelles observables, que ce soit la turbulence pleinement développée en milieu incompressible, en milieu compressible, ou bien la fameuse turbulence magnéto-hydrodynamique. Comme le sujet de la turbulence n’est pas abordé de façon détaillée dans cette thèse, mais fera partie de l’interprétation des résultats du chapitre 3, nous jugeons qu’il est adéquat de profiter de cette introduction pour en discuter convenablement.

C'est en 1922 que Richardson propose la notion de cascade d'énergie pour décrire la turbulence pleinement développée (Richardson, 1922), un scénario selon lequel les tourbillons à une certaine échelle résultent de la désstabilisation de tourbillons à plus grande échelle, et ce, de l'échelle intégrale (injection de l'énergie) jusqu'à l'échelle de dissipation. La théorie statistique de la turbulence énoncée par Kolmogorov (1941) dit que, à des échelles suffisamment petites, les propriétés d'invariance des équations de Navier-Stokes sont restaurées statistiquement. La théorie de Kolmogorov prédit le résultat important suivant: lorsque le nombre de Reynolds (Re)⁹ est suffisamment élevé, le champ de vitesse est statistiquement homogène et donc caractérisé par un exposant unique. L'exposant β , qui est extrait à partir du comportement en loi de puissance du spectre de puissance en fonction du module du vecteur d'onde $\mathbf{k} = (k, \theta)$: $S(k) = \frac{1}{2\pi} \int d\theta |\hat{f}(k, \theta)|^2 \sim k^\beta$ est donc $\beta = -5/3$. Il s'agit de la fameuse "loi en $k^{-5/3}$ " de Kolmogorov (en 1D). Une relation similaire existe avec les fonctions de structure d'ordre p , $S_p(l) = |\delta v_l|^p$, qui se comportent en $S_p(l) \sim l^{\zeta_p=p/3}$, où les δv_l sont les moments de la distribution des incrément de vitesse ($\delta v_l(x) = v(x + l) - v(x)$ est un incrément du signal enregistré sur une distance l). D'ailleurs, la valeur $\zeta_2 = 2/3$ peut être reliée à l'exposant β par la relation $\beta = 1 + \zeta_2$. En termes de fractalité, le comportement homogène prédit par Kolmogorov implique une signature mono-fractale.

Ce sont les premières expériences de Batchelor et Townsend qui ont révélé les imperfections de la théorie de Kolmogorov et principalement son incapacité à rendre compte du phénomène d'intermittence aux petites échelles (Batchelor & Townsend, 1949). Ce phénomène contredit les hypothèses d'homogénéité et d'invariance d'échelle globale qui

⁹ $Re = \frac{\rho U L}{\mu}$, où ρ est la densité du fluide, U est une vitesse caractéristique, L est une échelle de longueur caractéristique et μ est un coefficient de viscosité.

sont au cœur de la théorie de Kolmogorov. Les expériences de Anselmet et al. (1984) ont effectivement confirmé que le spectre des exposants ζ_p définis ci-dessus n'est pas une fonction linéaire de p . Les valeurs qu'ils trouvent pour ζ_p s'écartent indubitablement de la droite $\zeta_p = p/3$ pour les grandes valeurs de p .

En 1985, Frisch et Parisi proposent une description alternative de la nature intermittente de la turbulence (Parisi & Frisch, 1985). Ces auteurs sont en fait les premiers à proposer le terme multifractale pour caractériser un signal dont le degré de régularité fluctue spatialement. Pour ces auteurs, la nature intermittente de la turbulence s'exprime par un spectre de singularités, $D(h)$ (qui sera défini au chapitre 3), qui n'est pas concentré en un seul point, contrairement à ce que prédit Kolmogorov. Pour caractériser la multifractalité de la turbulence à l'aide de $D(h)$, ils utilisent les fonctions de structure.

Plusieurs analyses du MIS à l'aide du spectre de puissance et de la fonction de structure ont été effectuées depuis les 40 dernières années (voir respectivement Miville-Deschénes et al. (2003) et Padoan et al. (2003) et les références qui y sont mentionnées). Deux études de l'hydrogène neutre par analyse du spectre de puissance ont retenu notre attention: celles de Dickey et al. (2001) et Miville-Deschénes et al. (2003). Dans les deux cas, un compte-rendu détaillé des études précédentes similaires (par exemple Gautier et al. (1992) et Green (1993)), est inclus.

L'analyse présentée dans Dickey et al. (2001) concerne les données H I du *Southern Galactic Plane Survey* (SGPS), où les auteurs mesurent le spectre de puissance spatial de l'hydrogène neutre dans le quatrième quadrant de la Galaxie. Leurs résultats sont similaires aux études précédentes dans le deuxième quadrant ainsi que pour les nuages de Magellan, c'est-à-dire une pente linéaire caractérisée par un exposant β de ~ 3 . Les auteurs trouvent une différence entre le gaz chaud (WNM) et le gaz froid (CNM). Pour le gaz chaud, la pente du spectre de puissance est accentuée, de -3 à -4 lorsque la moyenne sur les cubes H I est prise sur des intervalles plus grands que la dispersion de vitesse à petite échelle. Pour le gaz froid, la pente demeure stable, ce qui suggère aux auteurs que ces deux phases du MIS sont dans deux régimes de turbulence différents.

Un point soulevé par Dickey et al. (2001) et bien repris par Miville-Deschénes et al. (2003) est le fait que la gaz optiquement mince puisse être caractérisé par une pente du

spectre de puissance significativement différente de celle du gaz optiquement épais. Et c'est justement en analysant des cirrus en haute latitude galactique que Miville-Deschénes et al. (2003) ont pu vérifier cette affirmation en analysant une région H I optiquement mince.

Deux points extrêmement importants sont à retenir ici avant de continuer car ils pourraient très bien constituer les bases de la justification d'une étude à grande échelle comme celle que nous présentons au chapitre 3. D'une part, Dickey et al. (2001) mentionnent très clairement que leur étude n'est pas nécessairement représentative de la Voie Lactée. En effet, ils n'ont analysé que deux petites régions de 128×128 pixels¹⁰. Ces auteurs concluent que seule une étude détaillée de plusieurs degrés carrés (tout le SGPS) pourrait démontrer à quel point le comportement du spectre de puissance peut être diversifié. D'autre part, Miville-Deschénes et al. (2003) qui, eux aussi, n'analysent qu'une petite quantité de données (une seule région d'environ 400×250 pixels) évoquent le besoin de faire une analyse anisotrope. En effet, la structure allongée des cirrus suggère que la turbulence puisse imposer une structure anisotrope au gaz H I. Pour répondre à ces deux points, une caractérisation (entre autres) anisotrope à grande échelle des mosaïques H I est présentée au chapitre 3.

Nous savons que l'approche de l'analyse du spectre de puissance est génériquement réservée aux phénomènes homogènes tandis que la fonction de structure permet une caractérisation de phénomènes hétérogènes. Par contre, comme nous en reparlerons au chapitre 3, la fonction de structure comporte deux faiblesses importantes. De par sa définition, la fonction de structure ne peut détecter les singularités de faible intensité. Plus important encore, les valeurs négatives de p ne sont pas accessibles, ce qui veut dire que seule une partie du spectre $D(h)$ sera disponible. Ces faiblesses sont absentes du formalisme multifractal basé sur la transformée en ondelettes qui sera utilisé dans cette thèse. En effet, comme le comportement des fonctions de structure ne reflète que très partiellement la structure singulière de la turbulence, les arguments de Frisch et Parisi pour estimer le spectre $D(h)$ des singularités de la turbulence ont été réexprimés à l'intérieur du cadre rigoureux qu'est la méthode des Maxima du Module de la Transformée en Ondelettes (Arneodo, Bacry & Muzy, 1991; Muzy, Bacry & Arneodo, 1993).

¹⁰Nous verrons au chapitre 3 que notre analyse à grande échelle est de loin supérieure statistiquement, avec des mosaïques ayant en moyenne une douzaine de sous-régions de 512×512 pixels.

1.3.6 Technique d’Espaces Métriques

Lors de la prise de connaissance des capacités d’analyse limitées de chacun de ces outils et/ou de leur dégénérescence, une des idées de la fin des années 90 consiste à utiliser plusieurs de ces outils simultanément, où chacun apporte une interprétation physique différente et complémentaire. Le but ici est d’obtenir de meilleurs résultats à partir de la somme de plusieurs outils simultanément au lieu d’analyses individuelles. Nous verrons au chapitre 2 que, par sa définition, la TEM permettait déjà de faire ce type d’analyse “multi-facettes”, où plusieurs caractéristiques physiques peuvent être analysées simultanément. C’est donc dire que la vision de Adams au début des années 90 aura été garante de succès. En effet, la TEM est définie de telle sorte qu’un nombre quasi-infini de caractéristiques physiques peuvent être analysées.

Adams & Wiseman ont donc écrit trois articles (Adams, 1992; Adams & Wiseman, 1994; Wiseman & Adams, 1994) dans lesquels ils présentent la TEM de façon détaillée avant de l’utiliser pour l’analyse de nuages moléculaires. Ils concluent qu’ils peuvent quantifier la différence en complexité des nuages. Ils ont analysé cinq nuages moléculaires provenant de données IRAS. Les auteurs ont classé ces régions de formation d’étoiles selon leur complexité et ont trouvé une forte corrélation entre la complexité des nuages et leur masse. De plus, en analysant les jeunes objets stellaires dans ces nuages, ils ont pu appuyer la “...conjecture disant que les étoiles plus massives ont tendance à se former dans des environnements plus complexes.”

1.3.7 Formalisme multifractal basé sur la transformée en ondelettes

Les concepts fractals et multifractals qui nous intéressent dans cette thèse concernent les outils de l’analyse multifractale basée sur la transformée en ondelettes: la méthode des Maxima du Module de la Transformée en Ondelettes (MMTO). La transformée en ondelettes (Grossmann & Morlet, 1984; Goupillaud, Grossmann, & Morlet, 1984; Grossmann & Morlet, 1985; Combes, Grossmann, & Tchamitchian, 1989; Meyer, 1990;

Lemarié, 1990; Meyer, 1992; Daubechies, 1992; Ruskai et al., 1992; Chui, 1992; Meyer & Roques, 1993; Arneodo et al., 1995a; Erlebacher, Hussaini, & Jameson, 1996; Holschneider, 1996; Mallat, 1998; Torresani, 1998; Flandrin, 1998) est un outil mathématique apparu dans les années 80 en analyse du signal. Introduite par Morlet et Grossmann (Grossmann & Morlet, 1984; Goupillaud, Grossmann, & Morlet, 1984) dans le cadre de l'analyse de signaux sismiques, elle consiste à décomposer un signal sur un ensemble de fonctions caractérisées par un paramètre de position et un paramètre d'échelle. Véritable microscope mathématique (Arneodo et al., 1995a), la transformée en ondelettes est particulièrement adaptée pour analyser les propriétés d'invariance d'échelles des objets fractals. Comme nous le verrons au chapitre 3, son utilisation est au cœur de la méthode MMTO, qui permet de caractériser la complexité des objets *monofractals* et *multifractals*, à l'aide de spectres d'exposants jouant un rôle équivalent aux potentiels thermodynamiques en mécanique statistique.

Plusieurs facettes contribuent à l'originalité de cette thèse. Dans un premier lieu, aucune des deux techniques n'avaient été utilisées sur des données H 1. De plus, chacun de ces outils d'analyse a été amélioré: pour la TEM, les améliorations sont autant du côté mathématique que technique, tandis que pour la méthode MMTO, l'innovation vient de la caractérisation de structures anisotropes ayant des exposants de Hurst directionnels dans l'intervalle [0, 1]. Enfin, nous avons espoir que la présentation détaillée de la méthode MMTO pourra mettre en valeur sa puissance d'analyse, tout en démontrant la forte sensibilité, souvent mal connue, associée aux formalismes fractals et multifractals.

Chapitre 2

Metric Space Technique

RÉSUMÉ

La technique d’Espaces Métriques (TEM), développée par Adams et Wiseman, est un formalisme mathématique d’analyse d’image utilisé pour classifier, de façon quantitative, des images astronomiques selon leur complexité. Au lieu de comparer les images de pixel à pixel, il s’agit de comparer les “fonctions de sortie” unidimensionnelles caractérisant différents aspects morphologiques/physiques des images. L’outil est utilisé pour analyser 28 régions H I dont les origines sont connues, prises à partir du relevé canadien du plan galactique (Canadian Galactic Plane Survey) où les images font 18 secondes d’arc par pixel (résolution de $1 \csc \delta$ arcmin). Des améliorations techniques et mathématiques au formalisme sont présentées. Après avoir classifié les 28 images selon leur complexité, nous avons cherché des corrélations entre ce classement et d’autres aspects quantifiables des régions H I: l’âge, l’aire, la distance, le flux des étoiles ionisantes, la dimension fractale, la masse du H I et $|z|$ (la valeur absolue de la hauteur des objects par rapport au plan galactique). Les corrélations les plus intéressantes sont (1) plus le flux des photons UV est élevé, plus la région de H I photodissociée est complexe, et (2) la complexité des régions H I augmente avec l’âge des restes de supernovae auxquels elles sont associées.

2.1 INTRODUCTION

The abundance of atomic hydrogen gas (H I) makes it an important tracer of structure in the interstellar medium (ISM). The discovery of the 21-cm line half a century ago has greatly improved our understanding of the different phases of the ISM and of the whole life cycle of stars and galaxies in the Universe. Although H I is distributed throughout the disk of the Galaxy, we consider this distribution at two levels: small and large scales. At small scales, H I can be found near star forming regions. The atomic hydrogen gas results from the dissociation of hydrogen molecules, provoked by the UV emission from newly-formed stars, starting from early B's (Roger & Dewdney, 1992). Also at small scales, the H I is pushed around by stellar winds and supernovae. At a larger scale, the study of the morphology of the H I in the spiral arms (where the density of H I is relatively high) as well as in the inter-arm region (where the H I is more diffuse) can help us understand which physical processes are morphing the ISM, in what proportion, and how they accomplish this.

The general study of the atomic hydrogen has led us to explore mathematical tools that provide a quantitative description of the distribution of matter in H I structures. One wishes to determine if there are differences (that the tools can discriminate) in these structures and thereby verify them. If so, what are the causes? What physical processes are responsible for creating these differences? More generally, our goal is to understand the evolutionary scenario of H I structures in the Galaxy. For example, the diffuse H I gas is pushed by the shock front from supernovae. After the passage of this shock front the gas rids itself of thermal energy to form molecules. Can the structural change of an H I feature as it becomes a molecular cloud be observed? If so, a kinematical analysis of the H I features will provide insight on the effects of turbulence and magnetic fields on the process.

Adams & Wiseman wrote three papers (Adams, 1992; Adams & Wiseman, 1994; Wiseman & Adams, 1994) (henceforth A, AW and WA) in which they first presented a detailed formalism of “metric space techniques” (A & AW) and then used the formalism to study molecular clouds (WA). They concluded that their method could quantify the complexity of the clouds. They analyzed IRAS maps of 5 different molecular clouds.

They were able to order these star-forming regions according to their complexity and found a strong correlation between the complexity of the clouds and their masses. Furthermore, by analyzing young stellar objects in these clouds, they were able to support the “...conjecture that more massive stars tend to form in more complex environments.” In this paper (paper I), we analyze the small scale structure of the 21-cm line H I data taken from the Canadian Galactic Plane Survey (CGPS). Our goal is to quantitatively differentiate H I features which are associated to specific physical entities (SNRs, WRs, and H II regions) with respect to physical characteristics of these features: age, area, distance, flux of the ionizing stars, H I mass, and $|z|$. We verify how the complexity of the H I structures is correlated with these parameters.

After the explosion of applications of fractal geometry in almost every area of natural sciences, one can safely say that the most utilized tool has been the fractal dimension. However, the fractal dimension is degenerate since an infinite number of sets or images having very different structures can have the same fractal dimension; for example, earth clouds and molecular clouds (Lovejoy, 1982; Bazell & Désert, 1988; Falgarone, Phillips & Walker, 1991). Although the multifractal formalism (which is discussed in Paper II) is one of the answers to palliate this degeneracy, a lack of correlation between the complexity classification of H I features presented here and the respective fractal dimension of these features could show that the Metric Space Technique can discriminate structural differences where the fractal dimension cannot.

In §2.2, the data obtained from the CGPS are briefly described. The description of the tool, “Metric Space Technique,” is reviewed in §2.3. Mathematical and technical improvements are listed in §2.4. In §2.5 we present the results and analysis, and the discussion and conclusion are in §2.6 and §2.7 respectively.

2.2 DATA

All of the data come from the CGPS. The observations were taken with the Dominion Radio Astrophysical Observatory (DRAO) telescopes (Landecker et al., 2000). The survey consists of a mosaic of 193 synthesis fields and covers Galactic longitudes from

$l=74.2$ to 147.3 degrees and latitudes from $b=-3.6$ to $+5.6$ degrees. The observations yield H I cubes with 256 channels giving a velocity resolution of 1.2 km s^{-1} . A detailed description of the CGPS is given in Taylor et al. (2003).

We have analyzed a total of 28 H I features which fall into three categories: H I features associated to H II regions (20), supernova remnants (4), and Wolf-Rayet stars (4) (Table 2.1). The subcubes containing the relevant H I data were compressed (channel summation) in order to work with column density maps. Whatever the sophistication level of a tool, the introduction of spurious data is to be avoided. Therefore the maps were filtered so that only pixels above the 3σ RMS noise level were kept.

This sample of objects was chosen with great care. First, the catalogs of Blitz, Fich & Stark (1982), van der Hucht (2001), and Green¹ were overlapped with the CGPS mosaics. Then, an extensive review of the literature for the SNRs and WR stars was made to choose only H I features with confirmed physical association. The same was done for H II regions in order to select the velocity range corresponding to the associated molecular cloud only. This latter information was completed using the FCRAO CO survey (Heyer et al., 1998) when the literature search turned out empty. The manner by which these images were constructed leads to unavoidable spurious data. By integrating along the line of sight, we are aware that a relatively small quantity of H I emission may not come from the region under study. Ideally, the background emission should be subtracted. Moreover, for computing purposes the images have a rectangular shape, which implies that all objects were oversampled in size since most of them seem to have a circular or irregular shape (from a visual inspection).

2.2.1 Object Parameters: Age, Area, Distance, Flux, H I Mass, & z

The distance to all objects, and the age and area of some have been found in the literature. For some H I features, z was given in the literature; for others, they were calculated from the known distance and galactic latitude. The warp of the Galactic disk

¹See A Catalogue of Supernova Remnants at <http://www.mrao.cam.ac.uk/snrs>.

Table 2.1: Characteristics of the 28 H I Features

H I Feature	Vel. Range (km s ⁻¹)	d (kpc)	Ionizing Stars (type)	Age (yr)	Area (pc ²)	H I Mass (M _⊙)	z (pc)	Ref
H II (Perseus Arm):								
S139	[-42.69, -49.28]	3.2	O9, B2	48.32	...	452	7.1×10^3	-9
S142	[-36.92, -50.11]	3.2	2O6, O9	49.57	2.5×10^6	693	1.1×10^4	-53
S158	[-53.40, -60.00]	2.5	O7, O9.5	48.93	...	52	2.8×10^3	38
S159	[-54.23, -60.00]	3.6	O8.5	48.45	...	88	7.4×10^2	34
S162	[-42.69, -58.35]	3.4	O6.5	49.02	3.5×10^5	1301	4.4×10^4	13
S168&169	[-36.92, -44.34]	3.8	O9.5, B0.5	48.08	...	150	5.0×10^3	-100
S170	[-39.39, -51.76]	2.3	O9.5	48.08	...	562	3.2×10^3	91
S173	[-27.85, -40.21]	2.7	O9, B3	48.32	...	437	1.1×10^4	-40
S181	[-34.44, -39.39]	2.6	B0	47.63	...	119	7.5×10^2	117
S199	[-33.62, -45.16]	2.1	2O7, 2O8	49.35	...	4220	4.4×10^4	57
H II (Local Arm):								
S112	[-0.64, -9.71]	1.74	O7	48.86	...	43	1.1×10^3	99
S131	[4.31, -9.71]	0.75	O6.5, 4B3	49.02	5.0×10^6	1028	1.7×10^4	56
S134	[-13.01, -20.43]	0.8	O6	49.24	...	1379	4.1×10^3	34
S135	[-16.30, -25.37]	1.7	O9.5	48.08	...	29	1.2×10^3	34
S154	[-5.59, -12.18]	1.4	B0	47.63	...	468	4.2×10^3	36
S155	[-3.94, -17.13]	0.73	3O8.5, O6.5	49.28	6.0×10^6	637	4.3×10^3	33
S165	[-28.67, -37.74]	1.6	B0	47.63	...	17	5.1×10^2	4
S187	[-12.18, -18.78]	1	B0	47.63	1.5×10^5	22	1.1×10^2	-13
H II (Outside Arm):								
S141	[-63.30, -68.24]	7	O8	48.59	...	74	3.8×10^3	389
S151	[-50.93, -62.47]	4.8	O8	48.59	...	769	2.6×10^4	-247
SNRs:								
G109.1-1.0	[-41.01, -57.53]	3	3.0×10^3	400	1.8×10^5	-52
G78.2+2.1	[16.67, -8.88]	1.5	1.4×10^4	538	4.8×10^4	55
G85.4+0.7	[-7.23, -20.43]	3.8	6.3×10^3	7854	3.8×10^4	46
G89.0+4.7	[2.66, -11.36]	0.8	1.9×10^4	588	2.8×10^4	66
WRs:								
WR140	[6.78, -25.37]	1.1	6.5×10^4	80
WR149	[-39.39, -54.23]	4.0	3.5×10^6	10207	6.9×10^5	45
WR4	[-39.39, -50.93]	2.44	2.6×10^4	-127
WR5	[-9.71, -20.43]	1.91	1.1×10^4	-72

a. Log of number of photons s⁻¹

Refs: (1) Avedisova & Palous 1989; (2) Fich & Blitz 1984; (3) Panagia 1973; (4) Moreno & Chavania-K. 1986; (5) Lebron et al. 2001; (6) Pismis et al. 1983; (7) Blitz et al. 1982; (8) Hunter & Massey 1990B; (9) Landecker et al. 1992; (10) Lahulla 1985; (11) Weikand et al. 1996; (12) Sargent 1998; (13) Sargent 1977; (14) Kothes et al. 2002; (15) Uchiyama et al. 2002; (16) Kothes et al. 2001; (17) Koo et al. 2001; (18) Williams et al. 1997; (19) van der Hucht 2001; (20) Cappa et al. 1996.

was not taken into account for these calculations. We are aware that the $b = 0$ latitude represents the position of the average intensity peaks so that it is possible for some values of $|z|$ to be over or underestimated. However, given the uncertainties on the distances to many objects and the lack of a precise, quantitative understanding of the effects of the warp, it would be difficult to add this variable to the calculation. Moreover, all of the estimations of $|z|$ that were found in the literature were calculated from the estimated distances and the latitudes of the objects. To the best of our knowledge, for the objects presented here, no author has considered any quantitative effects of the Galactic warp. The H I mass is given by

$$M_H = 1.23 \times 10^{-3} \int \int \Delta \overline{T}_b \, dv \, d\Omega_{am^2} \, d_{kpc}^2 \, M_\odot,$$

where d_{kpc} is the distance to the object in kpc, dv is the velocity increment in km s^{-1} , and $\Delta \overline{T}_b$ is the temperature difference between the feature and the background. The quantity $d\Omega_{am^2}$ is the incremental surface area, in square arc minutes. For the total flux of ionizing photons (for H II regions), the quantification of the spectral types of the exciting stars was used (Panagia, 1973). For example, the flux of an O6V is quantified by 49.24 units² while a B3V is 43.91. We have assumed that all the stars from the 20 H I features associated to H II regions are dwarves (type V). If an H II region has more than one ionizing star, we simply took the sum of the corresponding fluxes. References are given for each object in Table 2.1.

2.3 THE TOOL: METRIC SPACE TECHNIQUE

The technique is based on the work of Adams and Wiseman (A, AW and WA). It uses a mathematical formalism which is rigorously described in their papers. It is supported by many theorems and formal mathematical definitions, which create a very strong foundation for this form description tool. To explain how the formalism works, we will consider one of the H I images, S134 (Fig. 2.1), and describe how the technique works in a step-by-step manner³. Moreover, to help the reader who may wish to refer to

²The log of the number of ionizing photons s^{-1} provided by Panagia's model

³All 28 objects can be seen at <http://www.astro.phy.ulaval.ca/akhalil/28HI.html>

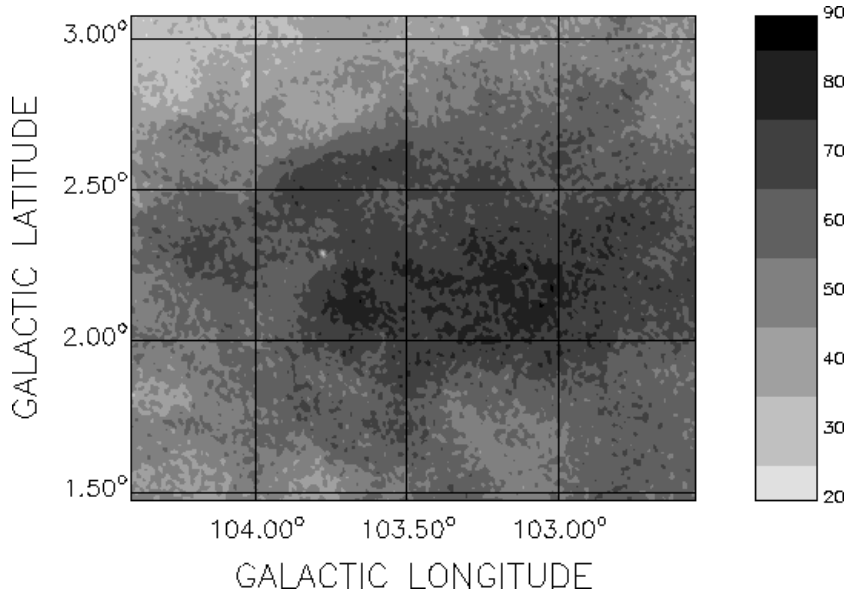


Figure 2.1: Column density map of the sample H I feature associated with S134. Its characteristics are in Table 2.1. Units are in K km s^{-1} .

the articles for more insight, the mathematical notation will follow that of A, AW and WA.

The formalism has been developed with the aim of comparing any two different astrophysical maps. Here, any given map will always be compared to a uniform map (a map where all pixels have the same integrated brightness temperature value). This way, instead of comparing two different maps, both of them are separately compared to a uniform map, giving us information on “how far” (in the metric sense) both fall from uniformity, thus giving quantitative information on the complexity of each of the maps.

2.3.1 Output Functions

Instead of comparing maps on a pixel-to-pixel basis, information is extracted from the maps in the form of *output functions*. An output function is a one-dimensional function representing a profile of some physically-meaningful quantity. Its independent variable

is the pixel values (integrated brightness temperature), called the *threshold value* Σ . In practice, we have to discretize the pixel values and in fact, the range from minimal to maximal threshold values is divided into 125 bins.

Six output functions are used for each map (four from the work of Adams and Wiseman, described below and two new ones, described in §2.4), each of them associated to a physical characteristic of interest. These are then compared to the output functions of the uniform map. In the next subsections, σ denotes an arbitrary H I map.

2.3.1.1 Distribution of Density

This output function characterizes “the fraction m of material at column densities higher than the reference (threshold) value Σ ”:

$$m(\sigma; \Sigma) = \frac{\int \sigma(x) \Theta[\sigma(x) - \Sigma] d^2x}{\int \sigma(x) d^2x} \quad (2.1)$$

where Θ is a step function and the integrals are taken over a bounded domain, i.e., from the minimal to maximal threshold values (Fig. 2.2).

2.3.1.2 Distribution of Volume

Obviously related to the distribution of density, the distribution of volume characterizes “the volume fraction v of material at densities higher than the reference (threshold) value Σ ”:

$$v(\sigma; \Sigma) = \frac{\int \Theta[\sigma(x) - \Sigma] d^2x}{\int d^2x} \quad (2.2)$$

where, again, Θ is a step function and the integrals are taken over a bounded domain (Fig. 2.3). Note that we use the term “volume” even though we are dealing with 2-dimensional images. Technically, this output function should be called “distribution of area”, but since one of the physical parameters used to compare the complexity of the features is the actual area of the objects, we called it distribution of volume.

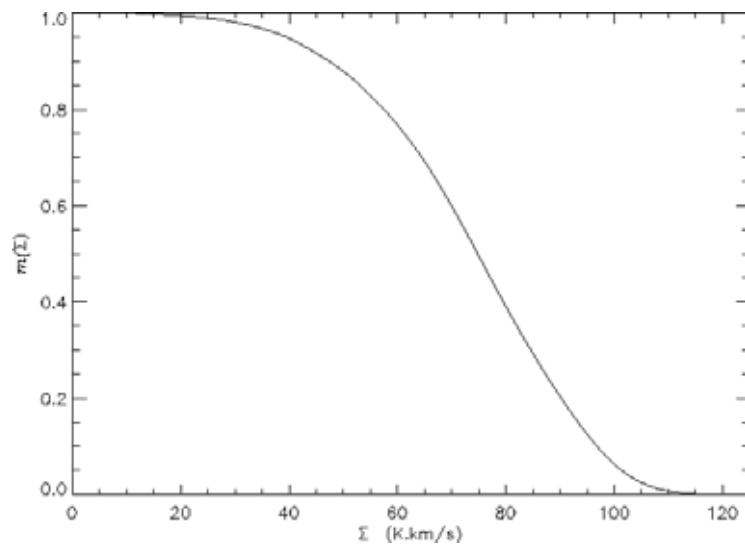


Figure 2.2: Density distribution of the sample H I feature S134.

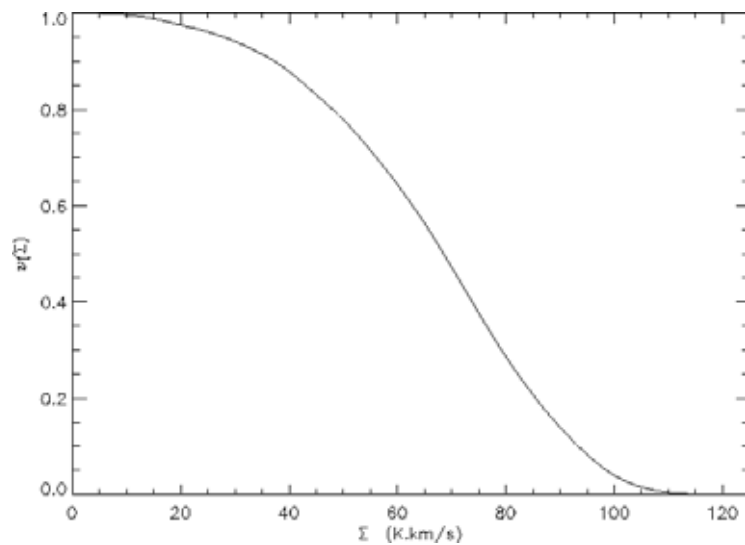


Figure 2.3: Volume distribution of the sample H I feature S134.

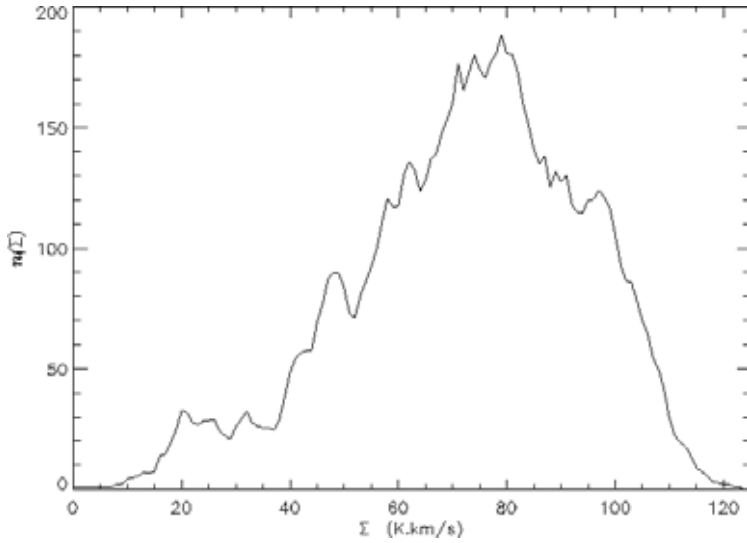


Figure 2.4: Components distribution of the sample H I feature S134.

2.3.1.3 Distribution of Topological Components

A topological component is a set of connected pixels for a fixed threshold value. We use the notation $n(\sigma; \Sigma)$ to denote the distribution of components (the number of components as a function of the threshold value) (Fig. 2.4).

2.3.1.4 Distribution of Filaments

Each component can be associated to a filament index, F , which characterizes the filamentary structure of the component. F is defined in the following way:

$$F = \frac{\pi D^2}{4A}, \quad (2.3)$$

where D and A are the diameter and the area of the component, respectively. Here, we use the standard definition of a diameter, i.e., for an arbitrary set S (for example, a component), the diameter of the set S is $D(S) = \max_{x,y \in S} \{|x - y|\}$. The diameter of a unit square is $\sqrt{2}$, while for an ellipse, D is twice the semi-major axis.

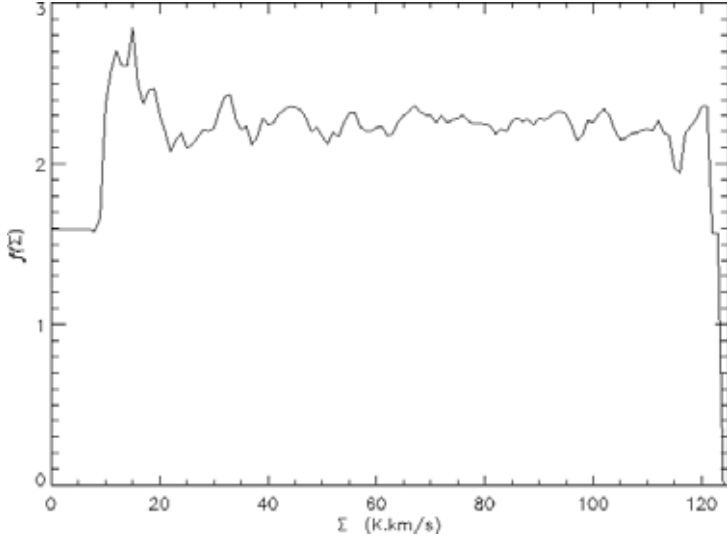


Figure 2.5: Filament index distribution of the sample H I feature S134.

We are interested in the distribution of the filament indices

$$f(\sigma; \Sigma) = \frac{1}{n(\sigma; \Sigma)} \sum_j F_j, \quad (2.4)$$

where $j = 1, 2, \dots, n(\sigma; \Sigma)$.

From the definition of the filament index, we can readily see that a circle has index 1 and that a square has index $F = \pi/2$. This information can be significant: if an image has a distribution of filaments with indices close to $F = \pi/2$, one has to verify if edge-effects are altering the results by artificially “squaring” an object which is larger than the image. In fact, this behavior is expected for small pixel values of the distribution since, at a low pixel threshold, the number of components is very small. The components at these low pixel thresholds most likely represent real objects that are larger than the image, and which are thus squared by the edges of the image, inferring a filament index that is close to the filament index of a square, i.e. $F = \pi/2$ (Fig. 2.5).

On the other hand, one has to be scrupulously careful, since an ellipse having an eccentricity of $e = 0.77$ also has a filament index of $F \approx \pi/2$. Thus, a blind interpretation of the distribution of filament indices can be unquestionably misleading. (See also Appendix 1 in §2.9.1).

It is easy to show that there is an analytic relationship between e and F : we have either

$$F = \sqrt{\frac{1}{1 - e^2}} \quad (2.5)$$

where $0 \leq e < 1$, or

$$e = \frac{\sqrt{F^2 - 1}}{F} \quad (2.6)$$

where $F = a/b \geq 1$ by definition (a and b are the semi-major and semi-minor axis of the ellipse). For an arbitrary H I feature, like S134, the filament index distribution can have a maximum value between 2.5 and 3.0, which could be the signature of an elliptic structure with eccentricity between 0.92 and 0.94.

In Appendix 1 (§2.9.1) we discuss a minor shortcoming in the definition of the filament index. When dealing with non-convex components, we show that the estimated filament index is always an underestimate of the true value of the filament index.

2.3.2 Metrics

A *metric space* (X, d) is a set X together with a distance function $d : X \times X \rightarrow \mathbf{R}$, called a *metric* if, for any $x, y, z \in X$, we have

$$d(x, y) = 0 \Rightarrow x = y \quad (2.7a)$$

$$x = y \Rightarrow d(x, y) = 0 \quad (2.7b)$$

$$d(x, y) = d(y, x) \quad (2.7c)$$

$$d(x, y) \leq d(x, z) + d(y, z) \quad (2.7d)$$

If equation (2.7a) is not satisfied, then d is a *pseudometric*. In this paper, the term “metric” is used even though we are often dealing with pseudometrics. This mathematical distinction will not affect our results.

An example of a metric space is the 2-dimensional real Euclidean metric space (\mathbf{R}^2, d_E) , where d_E is the Euclidean metric: for any $(x_1, y_1), (x_2, y_2) \in \mathbf{R}^2$, we have

$$d_E(x, y) = \left(|x_2 - x_1|^2 + |y_2 - y_1|^2 \right)^{1/2}. \quad (2.8)$$

A generalization of the real Euclidean space is the functional Euclidean space (L^p, d_E) . Here, d_E is defined in the following way: for any functions $f, g \in L^p$, we have

$$d_E(f, g) = \left(\int |f(x) - g(x)|^p dx \right)^{1/p}, \quad (2.9)$$

where p is usually chosen to be 2. We will see in §2.4.1 that $p = 1$ is more adequate than $p = 2$ for the analysis presented here. Note that other metrics could be used. In Appendix 2 (§2.9.2) mathematical arguments are presented, showing how output functions could be considered as sequences of points instead of functions.

2.3.3 Coordinates

Coordinates are used to quantify the complexity of each H I feature. To each output function g , its coordinate η_g is calculated in the following way.

$$\eta_g = \min\{d_E(g_\sigma, g_{\sigma_o}) \mid \sigma_o \text{ is a uniform image}\} \quad (2.10)$$

where the Euclidean metric $d_E : \sigma \rightarrow \mathbf{R}$ is used

$$d_E(g_\sigma, g_{\sigma_o}) = \left(\int |g_\sigma(x) - g_{\sigma_o}(x)|^p dx \right)^{1/p}, \quad (2.11)$$

where $g_\sigma \in L^p$ is an output function associated to $\sigma \subset \mathbf{R} \times \mathbf{R}$, the image (H I feature) under study, and x is the threshold level, which goes from the minimum pixel value to the maximum pixel value of the image. Thus η_g gives a quantitative information as to “how far” σ is from uniformity. Clearly, if $\sigma = \sigma_o$, then $\eta_g = 0$. And the larger the value η_g is, the “farther” σ is from σ_o , and hence the more complex it is.

Coordinates are calculated for each of the four output functions of the H I feature. Using the output functions m, v, n and f , a 4-dimensional vector is derived

$$\vec{\eta} = \{\eta_m, \eta_v, \eta_n, \eta_f\} \quad (2.12)$$

corresponding to the coordinates of the 4 output functions. This 4-dimensional vector is associated with each image. This way, one can classify the H I features according to their vectors, which can be seen as coordinates in the 4-D “complexity space”. Furthermore, one can easily see that using a fifth, sixth, or many more output functions will not be a problem.

2.4 IMPROVEMENTS

We have found a mathematical alteration which improves the distinction of different maps in terms of coordinates (§2.4.1). In contrast, the formalism is extremely adaptable in the sense that different analyses will warrant different types of output functions. The more output functions one uses, the more resolution one obtains with the coordinates. Therefore, we propose two new output functions for the analysis of H 1 features (§2.4.2). In §2.4.3, we present the complexity classification scheme used. And finally in §2.4.4, a major alteration in the components and pixels output functions is presented. Although quite simple, this change of definition greatly minimizes the effects of distance on the computed complexity ranking.

2.4.1 p=1

In the calculation of the coordinates by means of the Euclidean metric (Eq. 2.11), we have compared the use of $p = 1$ and $p = 2$. Although the overall complexity rankings obtained by using $p = 1$ and $p = 2$ are 99.9% correlated, using $p = 1$ provides the largest dynamic range in coordinates. An even better resolution would probably be obtained if a value of p closer to 0 were used. But then, the metric definition (Eq. 2.7d) would not be satisfied, where the condition $p \geq 1$ is necessary to verify the so-called triangle inequality.

2.4.2 Two New Output Functions

2.4.2.1 Distribution of Pixel Values

We use the distribution of pixel values, j , as an additional output function. It consists of a histogram where the number of pixels is counted, for each 125 bins of threshold values.

$$j(\sigma; \Sigma) = \#\{\Theta[\sigma(x) - \Sigma]\} \quad (2.13)$$

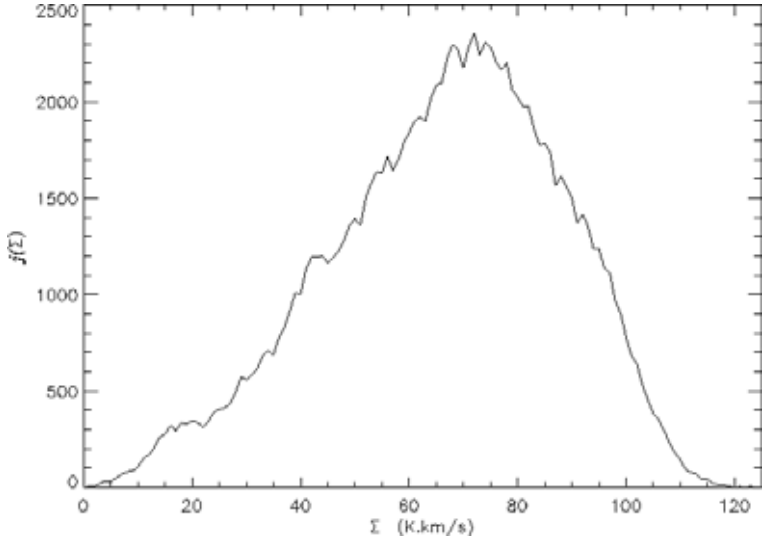


Figure 2.6: Pixel distribution of the sample H I feature S134.

where Θ is a step function and where $\#\{S\}$ denotes the cardinality of the set S (Fig. 2.6). This choice is based on the hypothesis (Joncas & Mashchenko, 1999) that such distributions have different shapes depending on the physical process that creates the H I structure. Note that this histogram (even a cumulative, normalized version of it) is not equivalent to the distribution of volume. In fact, the distributions of volume and density are more closely related to each other than to the distribution of pixels.

2.4.2.2 Average H I Spectrum

We take the H I spectrum averaged over the area and limited to the velocity range of the cloud as a new output function. This supplies a coarse estimate of the kinematics of the gas. We call this output function “Average Spectrum” (a), and denote its corresponding coordinate η_a . The H I features were all obtained by the collapse of a number of velocity channels. Our numerical calculations show that finite-size effects cause η_a to be extremely correlated ($> 99.9\%$) with the number of velocity channels used to construct each object. Therefore, for each image, the average spectrum was normalized by dividing the coordinate η_a by the number of velocity channels corresponding to the H I feature.

Simple calculations and the fact that $p = 1$ is used with the Euclidean metric (see §2.4.1) show that, with this normalization, η_a is nothing but the average value of the pixels in the collapsed H I feature.

Thus Eq. (2.12) becomes

$$\vec{\eta} = \{\eta_m, \eta_v, \eta_n, \eta_f, \eta_j, \eta_a\}. \quad (2.14)$$

2.4.3 Complexity Classification Scheme

As mentioned in §2.3.3, since the coordinates are dimensionless, there is a need for a uniform classification scheme where all the coordinates are considered at a unique scale. For the sample feature S134, $\vec{\eta} = \{27896, 24170, 34002, 27894, 23907, 58.1\}$. These ranges have to be rescaled to give the coordinates equal weights. WA did not need to establish a classification scheme since they were only dealing with 5 images and it was easy to see the relationships between the image coordinates. Since the present study deals with 28 images, there is a need for an automated classification method as such. Three classification schemes are presented in the following three subsections.

2.4.3.1 Positional Rank

For each output function, the HI features are sorted and ranked according to the value of each of their coordinates. We take the sum of these ranks, call it R and associate each feature to its value of R . A feature having the lowest coordinate values for the density, volume, components, pixel and average spectrum distributions and the second lowest for the filament index distribution would have $R = 1 + 1 + 1 + 1 + 1 + 2 = 7$. Since we have 28 images and 6 coordinates, $R \in \{6, 7, 8, \dots, 168\}$. Hence, of all the 28 H I features, the one with R closest to 6 will be the most homogeneous, and the one with R closest to 168 will be the most complex.

Using the “positional rank” classification scheme has the advantage of simplicity, giv-

ing equal weight to each coordinate. Its major drawback is its incapacity in discriminating by what factors our images differ from each other. For example, supposing images A, B, and C, have coordinates, 0.05, 0.15 and 2.80 respectively for a given output function. Then this classification scheme would not inform us about the “closeness” of images A and B compared to image C. It would simply give $R = 1$ for image A, $R = 2$ and $R = 3$ for images B and C respectively. This classification scheme was thus rejected.

2.4.3.2 Normalization – Average Coordinate

To take into account the difference factor between images, one can normalize the coordinates by dividing the value of each of them by the average value of the 28 images for that coordinate.

Consider again the above example, i.e., where the output function is the distribution of density, image A has coordinate 0.05, image B has 0.15 and image C, 2.80, where the average is 1.00, and the standard deviation is 1.56. Then, this classification scheme would tell us that $R = 0.05/1.00 = 0.05$ for image A, $R = 0.15/1.00 = 0.15$ for image B and $R = 2.80/1.00 = 2.80$ for image C. One can readily see that the “closeness” of images A and B compared to image C will then be well quantified. On the other hand, suppose one has for coordinates, 0.525, 0.575 and 1.90, where the output function is the distribution of filament indices. The average is also 1, but the standard deviation is now 0.78. Then, $R = 0.525$, $R = 0.575$ and $R = 1.90$, respectively. Now, since $1.90 < 2.80$, image C will have less “filament index weight” than “density weight”. Since the averages were the same, the standard deviation is to blame. Thus, the standard deviations associated to each of the 6 averages, corresponding to our 6 output function coordinates, will play a role in giving unequal weights to different coordinates. This classification scheme was also rejected.

2.4.3.3 Normalization – Maximal Coordinate

Here, we simply divide each coordinate by the value of the maximum coordinate value for each of the six output functions.

In this case, we are certain that each of the 6 coordinates representing each image will have equal weight. In fact, these coordinates will all be in the interval $(0, 1]$ (where the sup of the interval, 1, is attained each time). The possible fault associated to this classification scheme lies in the fact that many calculations (i.e. the division of each coordinates by the maximal coordinate) depend on the value of one (maximal) coordinate. There could be a large uncertainty associated to this maximal coordinate since the division relies on a single “observation” which suffers from an inherent uncertainty. This is the classification scheme used here.

Therefore, for each output function, the H I features are sorted and ranked according to the value of each of their coordinates. We take the sum of these ranks. To take into account the difference factor between images, the coordinates are normalized by dividing them by the value of the maximum coordinate from the 28 images for each output function. Doing so ensures that equal weights are given to the six output functions.

2.4.4 Distance Effects: Revised Components and Pixels Distributions

Using a test image, WR140, a 512×512 pixel square image, and degrading its resolution by averaging four pixels to one, a new 256×256 image is obtained, which could be considered as being twice as far as the original. Repeating this process twice gives us four different images (512^2 , 256^2 , 128^2 , and 64^2 pixels) to perform tests and verify the effect varying distances has on the output functions. This is called “box averaging”. We find that complexity increases with the number of pixels, meaning that *complexity decreases with distance as expected* (Table 2.2, upper part, columns 2 and 5). This is not surprising at all since two of the output functions (the components and the newly

defined pixels distributions) will produce coordinates which are clearly dependent on the number of pixels in the analyzed image as defined in WA.

However, the beauty of the metric space technique is that we can correct for the effect distance has on the output functions (smoothing and diminishing image size). The definitions of the components and pixel distributions output functions were revised

$$n'(\sigma; \Sigma) = \frac{n(\sigma; \Sigma)}{N} \quad (2.15)$$

and

$$j'(\sigma; \Sigma) = \frac{j(\sigma; \Sigma)}{N} = \frac{\#\{\Theta[\sigma(x) - \Sigma]\}}{N}, \quad (2.16)$$

where N is the total number of pixels in the image σ . Equation (2.14) now becomes

$$\vec{\eta} = \{\eta_m, \eta_v, \eta_{n'}, \eta_f, \eta_{j'}, \eta_a\}. \quad (2.17)$$

No revision was required for the density, filaments, volume distributions and the average spectrum since these output functions were already “normalized” by definition. The effects of the revision on the complexity ranking are shown in the top part of Table 2.2, column 3. The correction for distance effects was tested on the four test images (WR140 with 512^2 , 256^2 , 128^2 , and 64^2 pixels). Also included is the complexity ranking from Wiseman & Adams’s “A resolution study”, using the Taurus molecular cloud map and degrading its resolution four times (Appendix A of WA). In order to make a compatible comparison with WA’s results, the pixels distribution and average spectrum are not included in the complexity ranking, and $p = 2$ is used. Normalizing the output functions enables the comparison of clouds at different spatial resolutions.

The above statement being so important, we tested the revised output functions with another smoothing tool. We convolved the original image three times to new beam sizes, the integral of image intensities over the image being preserved. The convolution was done by applying a filter to the $u - v$ transform of the image. These results are shown in the bottom part of Table 2.2, where all output functions were used except the filament distribution. This is because using this convolution method, where each smoothed image is the same size (in pixels) as the original, yields much less components

Table 2.2: Complexity Ranking: Standard and Revised Components Distribution

Test Image	Rank (Standard)	Rank (Revised)	WA Test Image	Rank WA (Standard)
Box Averaging:				
WR140 “512x512”	3.96	3.96	Taurus “400x400”	4.00
WR140 “256x256”	3.43	3.94	Taurus “200x200”	3.59
WR140 “128x128”	3.08	3.91	Taurus “100x100”	3.07
WR140 “64x64”	2.95	3.91	Taurus “50x50”	2.61
Smoothing by Convolution:				
WR140 “512x512”	5.00	5.00		
WR140 “512x512”smooth 1	4.75	4.98		
WR140 “512x512”smooth 2	4.31	4.95		
WR140 “512x512”smooth 3	4.00	4.91		

in the smoothed images than in the original. But although they are in smaller numbers, these components are very large and also very detailed (a consequence of having so many pixels for a convolved image). Therefore, the filament output function associated to these components can reach artificially high values since the large scales dominate.

We can conclude from our simulations that complexity decreases only very slightly with increasing distance for our revised scheme compared to the WA (standard) scheme. There is a maximum of 2% change in complexity rank for a distance factor of 8. This is a major improvement to the technique. Since the distances to the objects under study are all within the same order of magnitude, these new revised components and pixels distributions are used with no further corrections for distance.

2.5 RESULTS AND ANALYSIS

Table 2.3 presents the classification of the 28 H I features according to their complexity, ordered according to the maximal coordinate normalization classification scheme (§2.4.3). The fractal dimension for each feature is also shown for later analysis. A histogram representing the number of objects classified by binned complexity ranks is presented in Figure 2.7.

Table 2.3: 28 H I Features, Ordered According to Their Complexity, From Least to Most Complex. Also Shown is the Fractal Dimension for Every Object.

H I Feature	Components	Density	Filaments	Pixels	Volume	Avg Spectrum	Complexity Rank	F. Dim.
S181	14918	12758	18261	14926	12759	27.0	2.04	2.42
S170	18008	15346	20558	18012	14941	37.6	2.47	2.46
WR4	19070	17800	20315	19072	17835	33.9	2.62	2.39
S159	21622	19498	20675	21636	19448	64.8	3.16	1.90
S165	22584	19930	24964	22589	19588	51.9	3.17	2.44
S187	23101	20488	21851	23105	20616	56.0	3.21	2.43
WR149	22201	19915	26186	22195	19946	54.6	3.21	2.37
WR5	23350	20774	26969	23362	20705	46.7	3.24	2.52
S151	24588	21616	28202	24581	21594	45.7	3.36	2.38
S155	26450	23758	29589	26454	23758	57.2	3.71	2.40
S131	27170	24367	30320	27172	24358	58.9	3.81	2.35
G109.1-1.0	26361	24080	26710	26351	24104	71.6	3.82	2.41
S134	27896	24170	34002	27894	23907	58.1	3.90	2.41
S135	28442	25513	29098	28450	25369	62.1	3.94	2.49
S139	28811	24909	33384	28816	24885	57.9	3.97	2.50
S154	28502	25235	31982	28502	24619	68.9	4.05	2.42
S141	26614	23444	27352	26677	23144	94.8	4.05	2.19
S142	29054	25075	36780	29051	25015	57.8	4.06	2.47
S173	30051	26741	32965	30063	26648	61.0	4.15	2.60
G85.4+0.7	30017	26452	40209	30009	26270	61.7	4.29	2.66
S162	31168	27152	35539	31163	27037	67.1	4.34	2.37
S158	32765	30478	47675	32758	30458	69.1	4.87	2.21
G78.2+2.1	33540	30323	39299	33522	30352	84.5	4.88	2.22
S199	37409	32579	43175	37407	32442	76.3	5.18	2.40
G89.0+4.7	37175	33895	42922	37168	33954	86.2	5.34	2.38
S168&S169	39845	35284	46643	39849	34975	79.1	5.53	2.36
WR140	38610	35125	47571	38599	34970	85.0	5.55	2.32
S112	42519	38312	43744	42552	37927	89.4	5.86	2.40

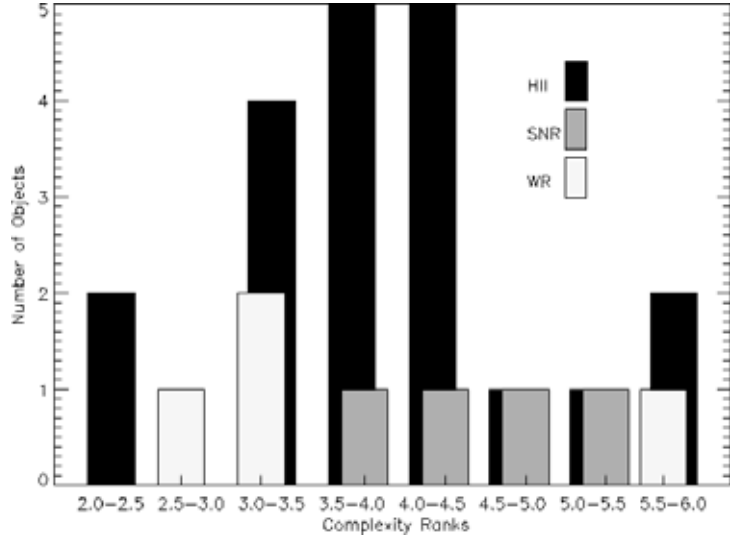


Figure 2.7: Number of H I features according to complexity ranks.

2.5.1 Complex Classification

Before making an attempt at obtaining an astrophysical description from the complexity classification shown in Table 2.3, an uncertainty analysis is warranted. Indeed, with what quantitative certainty can one say that two objects are to be considered differently with regards to complexity. An analytical description of the propagation of errors for the four original output functions (density, volume, components, and filaments) is presented in §4 of AW. The density and volume distributions are sufficiently well behaved provided that the signal-to-noise ratio in the map is sufficiently large. More precisely, the uncertainty on the distribution of density (or volume) is given by

$$\left\langle \frac{\Delta m}{m} \right\rangle = \frac{\log(\text{SNR})}{\text{SNR}}, \quad (2.18)$$

where SNR stands for signal-to-noise ratio (which is assumed to be uniform over the map). In the case under study in this thesis, the SNR is estimated to be at least $3\sqrt{N}$, where N is the number of velocity channels over which the average was performed to produce the H I image from the 21-cm data cube. On average, this yields an uncertainty of $\approx 6\%$ on the density and volume coordinates.

Furthermore, AW estimate the probability that a pixel will be erroneously larger than a given threshold level (Appendix F of AW). Their study shows that no components having less than 3 pixels should be considered, which is what was done here. Again, this yields an average uncertainty of $\approx 6\%$ on the components coordinate. The uncertainty of the filaments distribution is dominated by the uncertainty from the components distribution (Eq. (4.4) from AW), and one can thus argue that the former will be well behaved provided the latter is also well behaved. Therefore, the uncertainty on the filaments coordinate will also be considered to be 6%.

This uncertainty study should be pursued further in future, large number analyses of astrophysical maps, including the error analysis of the pixels and average spectrum coordinates and any other future output functions. But for now, the error on each of the six coordinates is estimated to be 6%. This percentage translates to a contribution of 0.03 from each coordinate on the overall ranking. Therefore, the uncertainty for each object on the overall complexity classification is $\sqrt{6(0.03)^2} \approx 0.07$. The bar chart shown in Figure 2.8 is a representation of the overall complexity ranking for each object. Small ellipses were added to show which objects have a similar overall ranking, where the overlap corresponds to the above mentioned uncertainty of 0.07. One can readily see that the conservative “choice” of 0.07 does allow a thorough discrimination between the ranking of each object. A possibly more realistic value of 0.05 for the uncertainty would certainly allow an even better precision.

Important note: Two objects having the same complexity ranking (within overlapping uncertainties) need not necessarily be considered as equally complex. The overall rank represents to contribution from all coordinates (i.e., from all output functions). Therefore, for two objects which are considered as equally complex, one should look for quantitative differences between the individual coordinates. For example, one of the two objects may be respectively more filamentary and less complex with regards to the distribution of, say, density, than the other.

Now, as can be seen from Table 2.3, H II regions, WR stars and SNRs do not seem to morph the H I in different ways. There is no indication that the H I features associated with SNRs are more or less complex than the H I associated with WRs or H II regions. The reader will note that isolating a given output function from the rest will change the

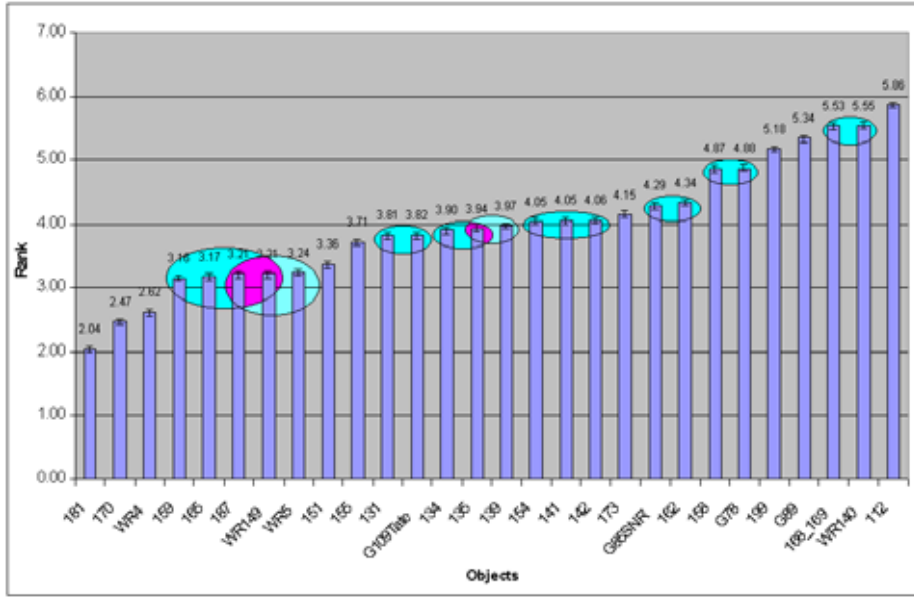


Figure 2.8: Bar chart representing the overall complexity classification with respect to the analyzed H I features.

ranking status of an object. For example, the H II region S158 would become the most complex if only a filamentary structure was taken into account. H II regions cover the whole complexity space. A careful look at Table 2.3 shows, however, that the H I features associated with SNRs have a tendency to be more complex than the H I associated with WR stars, if WR140 and G109.1-1.0 are flagged out. Of course, one relies here on small number statistics. A description of these outliers follows.

2.5.2 WR140

Arnal (1996) suggested that the interstellar bubble associated with WR140 is markedly aspherical, as the WR star is at an eccentric position with respect to the center of the H I cavity. The author mentions that a typical axial ratio for this cavity is ≥ 2 . Compared to WR4, WR5 and WR149, WR140 is classified as the most complex by far irrespective of the output function. Its filament coordinate, a signature of the ellipticity, is very high

in absolute terms, in agreement with the work of Arnal (1996). WR140 also stands out from the other three objects by being a binary system where both stars emit stellar winds (Williams et al., 1997). The variable action of both stellar winds may well be responsible for the unusual complexity of the WR140 environment.

2.5.3 G109.1-1.0

As for WR140, G109.1-1.0 also stands out from the other three SNRs but this time as less complex, but for η_a . Among the four SNRs, G109.1-1.0 is the only object associated with a molecular cloud. The latter is clearly slowing the expansion of the western half of the SNR (Tatematsu et al., 1987). The lower complexity of the associated H I could be explained by the expansion of the shock wave in a very dense medium that it cannot mold as well as the diffuse H I located on the eastern side. When the blast wave from the SN, traveling at hundreds of km s^{-1} , enters the molecular cloud, the high gas density quickly transforms the shock wave into a more benign isothermal one, traveling at tens of km s^{-1} . Since the extracted H I feature encompasses the whole area, the output functions are smoothed out.

2.5.4 The Most Complex H II Regions

Since the highest complexity ranking value is 6.0, a cut-off at 4.5 was chosen to pinpoint the most complex objects (a large complexity rank difference is present between S162 and S158). Concentrating on the H II regions only, publications from the last 30 years were searched in order to understand why S158, S199, S168, S169 and S112 standout.

S158's complexity is driven almost entirely by its filamentary structure. S158 is a very active site of star formation, its associated molecular cloud harbors at least five such sites indicated by the presence of 11 infrared point sources (Campbell & Thompson, 1984) and compact H II regions south and west of the main H II region. The analyzed H I encompasses all of them as they leave a trail of photodissociated gas, explaining the

elongated shapes (like a seashell necklace). Globally, S158 is surrounded by an H I shell resembling object B in Figure 2.9 (see Appendix in §2.9.1.)

S199 (W5) is the sample's largest H II region. The H I maps (Normandeau, Taylor & Dewdney, 1997) show many filaments and core structures. Three distinct molecular clouds are being dissociated by at least three different O stars (Heyer & Terebey, 1998). S131 and S134 are also large H II regions with many molecular clouds, but they are less complex. The difference may reside in the molecular clouds being much more numerous and smaller (Dobashi et al., 1994). The H I gas is more diffuse in these probably older star forming sites.

The last three H II regions have never been extensively studied on an individual basis, they were always observed as part of larger surveys. We can only conjecture as to the cause of such a high complexity since nothing stands out of the ordinary for these objects (Fich, Treffers, & Dahl, 1990; Fich, 1993; Caplan et al., 2000). The proximity of S168 with S169 prevented the making of separate maps. This could affect the ranking. However there is a similarity between S169 and S112 in that they are surrounded by three molecular peaks/components (Piepenbrink & Wendker, 1988; Hunter, Thronson & Wilton, 1990).

2.5.5 Correlations

Correlations have been sought between many of the physical characteristics and mathematical results. For two distributions represented by x and y , the well known Pearson (linear) correlation factor is used to evaluate the confidence level of the correlations

$$r = \frac{S_{xy}}{S_{xx}S_{yy}}, \quad (2.19)$$

where $S_{xy} = \frac{1}{n} \sum (x - \bar{x})(y - \bar{y})$ is the covariance, n is the number of elements in the distributions, S_{xx} and S_{yy} are the respective standard deviations associated to x and y (Freund, 1992). Critical values of r depend on the correlation probability percentage sought and the number of objects analyzed. For example, for 28 objects, a 95% confidence level requires that r be greater than the critical value 0.374, while for 20 objects, r must

Table 2.4: Correlation Between the Complexity of H I Features and Physical Parameters, if $\geq 80\%$ in absolute value.

Objects	Age	Area	Distance	Flux	H I Mass	$ z $	F. Dim.	Wind Vel.
All 28 Objects:								
Overall Complexity Rank	-80%
Components
Density
Filaments
Pixels
Volume
Average Spectrum	-90%	-90%	...
20 H II Regions:								
Overall Complexity Rank	95%
Components	90%
Density	90%
Filaments	...	80%	...	95%	80%
Pixels	90%
Volume	90%
Average Spectrum	80%	80%	-80%	...
SNRs:								
Overall Complexity Rank	99%	...	-80%
Components	98%	...	-80%	...	-80%
Density	99%	...	-80%	80%
Filaments	-99%
Pixels	98%	...	-80%	...	-80%
Volume	99%	...	-80%	80%
Average Spectrum	80%	-80%	-98%	80%	-80%	...
WRs:								
— No correlations $\geq 80\%$ —								

Note: A negative sign implies a linear correlation with a negative slope.

be greater than 0.444, and for 4 objects, r must be greater than 0.950 (Geller, 1975).

The correlation results are found in Table 2.4, where separate groups are considered. These groups are: all of the 28 objects, the 20 H II regions, 4 SNRs, and 4 WRs. For each of these groups, the correlation percentages between the overall complexity rank as well as the individual coordinates (each output function) and the physical parameters are shown.

2.5.5.1 Complexity vs Age

The age of the SNRs is 99% correlated with the overall complexity rank. The older an SNR is, the more complex the H I associated to the SNR is. The individual coordinates correlate differently: 99% for density and volume distributions, 98% for components and pixels distributions, 80% for the average spectrum, and no correlation ($< 80\%$) for the filaments distribution. Although the overall complexity of the H I associated to the SNRs increases with time, its filamentary structure does not change substantially. Note that there is a slight (inversely proportional 80%) correlation between the age of the objects (all 28) and the overall complexity rank.

2.5.5.2 Complexity vs Area

The only possible correlation between the area of the H II regions and complexity is with the filaments coordinate (80%). Thus, the larger the H II regions the more filamentary the associated H I structure. This weak correlation may derive from the presence of a longer, more elliptical, interface with the molecular cloud.

2.5.5.3 Complexity vs Distance

Except for the four H I features associated to SNRs, where there is an 80% inversely proportional correlation (98% for the average spectrum), there is no correlation between the overall complexity ranks and the distance to all the other objects. This is a confirmation that the revision of the components and pixels output functions was a necessary improvement to the Metric Space Technique. The slight correlation between the output functions for SNRs and distance is caused by an anti-correlation between age and distance in the sample.

2.5.5.4 Complexity vs Flux

There is a 95% correlation between the total flux of the ionizing stars for H II regions and the overall complexity rank. The presence of such a correlation implies that UV emission is responsible for the complex structure of atomic hydrogen surrounding H II regions.

2.5.5.5 Complexity vs H I Mass

The mass of the H I associated to SNRs is inversely correlated with some of the output functions (80% for the components and pixels coordinates, and 99% for the filaments coordinate). The complexity of the H I associated to SNRs seems to decrease with its size.

2.5.5.6 Complexity vs $|z|$

There is a very weak indication (80% for the density, volume and average spectrum coordinates) that the complexity of the H I associated to SNRs decreases with height (z) above the galactic plane.

2.5.5.7 Complexity vs Stellar Wind Speed

Considering only carbon type WR stars (WR4, WR5, and WR140), the complexity of the associated H I bubble increases with the terminal velocity of the stellar wind (1900 km s⁻¹, 2100 km s⁻¹, and 2870 km s⁻¹ respectively, taken from van der Hucht (2001)). Although the correlation with complexity is quite strong, $> 98\%$, it relies on only three stars (which is why this result was not presented in Table 2.4 – there is no correlation when one considers the stellar wind of all four WR stars). The fact that the WN star (WR149) decreases the correlation factor is suspicious... but explainable. In the WR

evolutionary scenario, WN stars precede WCs. The H I shell associated with the WN star may be in a transient phase.

2.5.5.8 Complexity, Physical Parameters vs Fractal Dimension: One Correlation

The fractal dimension is a tool which has often been used to help determine the complexity of structures. Most studies on interstellar clouds show that the fractal dimension is more or less universal; i.e., an average of ≈ 2.35 (actually 1.35 since most of these studies deal with the so-called perimeter-area method which yields the fractal dimension of the projection of 3-D objects in 2-D) for molecular clouds (Bazell & Désert, 1988; Scalo, 1990; Falgarone, Phillips & Walker, 1991; Elmegreen & Falgarone, 1996) as well as for H I (Vogelaar & Wakker, 1994; Stanimirovic et al., 1998; Westpfahl et al., 1999). A universal fractal dimension can inform us of the underlying physical processes which are morphing the gas. For example, some find an analogy with 4/3 Kolmogorov exponent and suggest that turbulence is a major physical process in interstellar cloud structure (Scalo, 1987; Falgarone, 1989; Falgarone & Phillips, 1990).

It is important to note that most fractal dimension results are dependent on the method used to derive the fractal dimension. In fact, whether the method used is the perimeter-area relation, one of the box-counting techniques, the wavelet transform, the Lyapunov exponent or other, three topics are important to consider: 1) the result (of the fractal dimension calculation) is dependent on the method used; 2) if we are in the presence of a multifractal process (which is, simply put, a structure which is best described by a spectrum of fractal dimensions), most methods will not detect it; and 3) if we ARE looking for a multifractal signature, we must make sure that the tool is suited to detect multifractal *functions* (which typical astrophysical images are) and not multifractal *measures*. We will talk in greater detail about these topics in Chapter 3.

But for now, curiosity prompted us to verify the fractal dimension of the H I images. Using a box-counting method for all the 28 H I features, a very similar fractal dimension is found (2.35-2.40) (see Table 2.3). There is absolutely no sign of correlation between

the fractal dimension and the complexity ranks given by the Metric Space Technique. The same is true for the fractal dimension and the physical characteristics (age, area, distance, flux, H I mass, and $|z|$). A 90% anti-correlation is found however with the average spectrum.

From the aforementioned, one may arrive at one or both of the two following conclusions: firstly, that the Metric Space Technique is a better tool to describe the differences in complexity of H I features than the fractal dimension, because it provides a solution to the degenerate nature of the fractal dimension, and/or that some (or all of the) images exhibit a multifractal structure, which the fractal dimension alone cannot quantify. A multifractal study of the present 28 H I features would be needed, but the size (in pixels) of the majority of the images is too small to undertake such a study (Arneodo, Decoster & Roux, 2000; Decoster, Roux & Arneodo, 2000; Roux, Arneodo & Decoster, 2000).

2.6 DISCUSSION

Correlations were found between the complexity ranking and a number of physical characteristics. Taking each type of object in turn, explanations are now sought. The reader must bear in mind that, statistically speaking, an 80% confidence level is not strong enough to convince (a purist would require $> 99\%$!). The physical characteristics used in this study are prone to measurement errors especially since most of them are dependent on the distance to the object. Therefore a 90% confidence level is judged sufficient to warrant further examination.

The H I features associated with H II regions come from the photodissociation of molecular hydrogen from the parent molecular cloud. The latter's structure should drive the H I complexity. Indeed no correlations were found with any of the characteristics of the ionized gas. In addition to the area (Table 2.4), the kinematics of the gas, quantified by the width of the $H\alpha$ line (Fich, Treffers, & Dahl, 1990) or the $H87\alpha$ radio recombination line (Lockman, 1989), is not correlated with the complexity ranking. However it is a well known fact that molecular clouds are clumpy. Any high resolution mm or submm map demonstrates this both visually and quantitatively with clump mass func-

tions (Johnstone et al., 2000). Therefore the correlation between the amount of ionizing photons and complexity can be explained if we assume that a large flux of UV photons will rapidly ionize all the low density, diffuse molecular/atomic gas at the interface and even deeply inside the molecular cloud. The contrast is thus increased, the interface being populated mainly, at the upper end of the flux scale, by H I fragments of various sizes and shapes. A nice illustration is the VLA observations of the M17 ionization front by Felli, Churchwell, & Massi (1984).

SNRs possess interesting correlations. However these correlations rely on only four objects. This small number does not come from a lack of candidates in the CGPS survey but rather from the difficulty to ascertain the connection between an H I feature and the SN. This article discusses the four most convincing cases. Young SNRs had to be rejected to make sure the associated H I had interacted with the blast wave. The sample's youngest SNR (G109.1-1.0) is 3000 years old. Since the cooling time can be obtained from $\approx 27000n_e^{-0.5}$, a density (n_e) of 100 cm^{-3} would satisfy the above condition. Such a high value is probable since obviously the star exploded in a massive star forming environment where the erosion of the associated molecular cloud had increased the local density.

There is a very convincing (98-99% confidence level) positive correlation of the complexity ranking with the age of SNRs. This correlation is difficult to explain since most models of the interaction of a shock wave with ISM clouds (Klein, McKee, & Colella, 1994; Xu & Stone, 1995) predict complete fragmentation on a time scale of the order of their radius (in parsec) times 10^5 years. This time scale is similar to the age of the oldest SNRs of the sample, an anti-correlation would thus have been expected. However since the clouds are accelerated outward by the blast wave, the accretion or collision with down stream material may play a role. If this correlation is confirmed, it may imply that the published models still have to be made more realistic to the peculiarities of the ISM. Referring to Table 2.1, it appears that the mass of the associated H I does not change much with age, putting a hiatus on our accretion scenario. But since the distance to SNRs are notoriously difficult to determine, our hypothesis remains plausible.

The correlation with mass is not completely independent suffice it to say that the less massive the associated H I the more filamentary (or complicated) the feature is.

Since the mass is not correlated with the age, this shows a very strong dependence with the environment into which the blast wave expands. The more diffuse the gas, the less massive the expanding shell, the more it resembles the optical filaments as when the wave expands into the pre-existing stellar wind bubble.

2.7 CONCLUSION

A mathematical formalism first derived by Adams and Wiseman, the Metric Space Technique, was improved and then used to quantify the complexity of the distribution of matter within H I features of known origin. This form description tool was applied on 28 H I features taken from the Canadian Galactic Plane Survey. The features are associated with H II regions, Wolf-Rayet stars, and supernova remnants. The 28 H I features were ordered according to their complexity and correlations between the quantitative information characterizing the complexity and the physical characteristics (age, area, distance, flux, H I mass, and $|z|$) were searched for, as well as with the fractal dimension of the H I features. In order of importance, we conclude with the following conjectures:

1. Older SNRs are associated with more complex H I emission.
2. The complexity of photo-dissociated H I emission increases with higher flux of ionizing photons.
3. The less massive H I features associated to SNRs are more filamentary.
4. The H I associated to WC stars having a high terminal velocity is more complex.
5. It may be possible to use the Metric Space Technique to distinguish the H I associated with SNRs from the H I associated with WR stars.

Clearly this study should be improved in the future using a much larger number of objects. This will be possible when the extension of the CGPS is completed and linked

with similar surveys undertaken at the VLA and the Australian Telescope to cover the Galactic plane. Simultaneously a homogeneous set of physical parameters will have to be gathered for all the objects. Some mathematical and technical improvements were discussed in §2.4. Specifically, the idea of using l^2 instead of L^2 (Appendix 2, §2.9.2) could lead to the derivation of new and possibly more useful theorems concerning the mathematical formalism. Furthermore, the use of new output functions can improve the quality of this multi-physical characteristic, morphological analysis tool. In Chapter 3, we will use the Wavelet Transform Modulus Maxima method to analyze large scale H I maps.

2.8 ACKNOWLEDGEMENTS

We gratefully acknowledge Jennifer Wiseman for providing us with some of the source codes for the output functions, and for very helpful comments throughout this project. Many thanks to Louis Nadeau who helped produce the catalog of H I features. We are also indebted to the referee for providing positive and productive remarks. The CGPS is a Canadian project with international partners, and is supported by the Natural Science and Engineering Research Council (NSERC).

2.9 APPENDICES

2.9.1 MINOR FAULT CONCERNING THE FILAMENT INDEX OF NON-CONVEX COMPONENTS

Let us begin with an informal definition of convexity. Suppose S and T are two subsets of a metric space X (in this study, these subsets are components, and X is \mathbf{R}^2). The subset S is said to be *convex* if for any two points x and y in S , the line joining x and y is also in S . More technically, S is convex if $x, y \in S$ and $0 < t < 1$ imply that

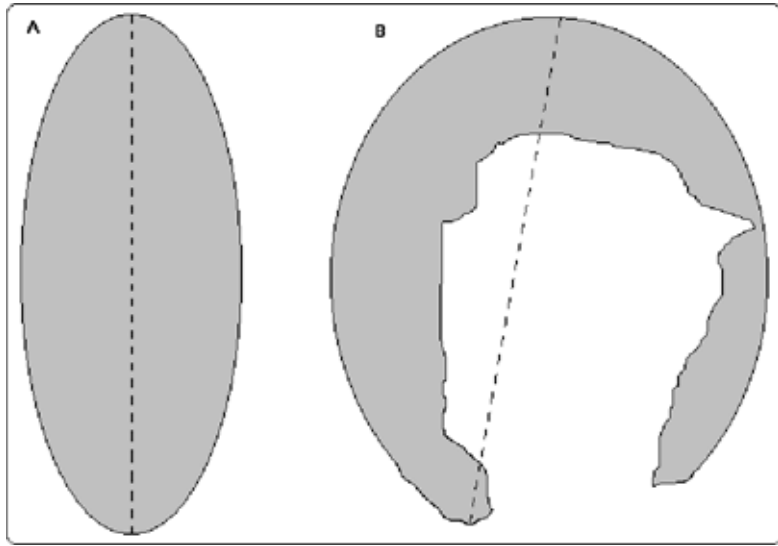


Figure 2.9: A and B have the same diameter and the same area and therefore, the same filament index, even though their structure is quite different.

$tx + (1 - t)y \in S$. A subset T which does not satisfy this condition, i.e., if we can find two points z, w in the set T and a real number $0 < t_0 < 1$ such that $t_0z + (1 - t_0)w \notin T$, then T is said to be *non-convex*.

Now, let us recall the definition of the filament index:

$$F = \frac{\pi D^2}{4A}. \quad (2.20)$$

Note first that F depends only upon two values, D and A , which are respectively the diameter and the area of the component. Now, since we use the standard definition of a diameter (i.e., for a component S , the diameter of S is $D(S) = \max_{x,y \in S} \{|x - y|\}$), there is a possibility that two components having quite different structures end up having the same filament index value (Fig 2.9).

The diameter, and therefore the filament index of non-convex components is underestimated. The cause of this problem lies in the fact that the definition of the diameter (which is quite standard in mathematical analysis and topology) is not well adapted for non-convex components. A solution to the problem would be to calculate the diameter according to the theory of length structures which would allow us to constrain the path

of the diameter to stay inside non-convex components. This topic not only extends beyond the scope of this paper but it would also present a major challenge to implement algorithmically in the filament index computer program.

2.9.2 REVISITING THE MATHEMATICAL FORMALISM: IMPROVEMENTS

The output functions (distributions of components, density, filaments, pixels, volume, and average spectrum) defined in §2.3 and §2.4 are well-defined and belong to the space (of Lebesgue measurable functions) called $L^p = L^p(\mathbf{R})$, where $1 \leq p < \infty$. A function f is said to be in L^p if

$$\int |f|^p dx < \infty. \quad (2.21)$$

In L^p we find continuous (differentiable or not) and discontinuous functions, step or constant functions, and basically, “imaginable” functions.

The (Euclidean) metric associated with L^p has been given in §2.3, i.e., for any functions $f, g \in L^p$, we have

$$d_E(f, g) = \left(\int |f(x) - g(x)|^p dx \right)^{1/p}. \quad (2.22)$$

When we calculate this integral, we have to discretize the functions f and g and in fact, the calculation is a sum.

There is another space called the space of finite sequences, denoted l_n^p , where again $1 \leq p < \infty$ and $n \in \mathbb{Z}$. An element $a \in l_n^p$ is a sequence of n real numbers of the form $(a) = \{a_1, a_2, a_3, \dots, a_n\}$, where $a_i \in \mathbf{R}$ for $i = 1, 2, 3, \dots, n$ and for which

$$\left(\sum_{i=1}^n |a_i|^p \right)^{1/p} < \infty. \quad (2.23)$$

We could take the above functions f and g by considering them as sequences of n points (where n is the number of bins used for each output function). We would then deal with f and g by considering their corresponding sequences (a_f) and $(a_g) \in l_n^p$.

By working in l_n^p rather than in L^p , the integrals would be replaced by finite sums, which is more realistic since we end up discretizing the calculation of the integrals as finite sums anyway when we implement the algorithms on a computer, and therefore avoiding the need to verify the convergence of integrals.

Chapitre 3

2D Wavelet-Transform Modulus Maxima Method

RÉSUMÉ

La méthode des Maxima du Module de la Transformée en Ondelettes (MMTO) a été utilisée pour obtenir de l'information quantitative sur la nature fractale / multifractale et sur la structure anisotrope de l'hydrogène neutre de la Galaxie à partir de données provenant du Canadian Galactic Plane Survey. Cinq mosaïques du deuxième quadrant de la Voie Lactée ont été analysées, correspondant aux bras spiraux Local, Persée et Externe, ainsi que les deux milieux “Inter-bras” situés entre ces bras spiraux. Une signature monofractale est trouvée pour les cinq mosaïques. Une signature anisotrope est détectée: la rugosité des mosaïques est plus grande dans la direction de la longitude que dans la direction de la latitude. Cette anisotropie est indépendante de l'échelle pour les inter-bras tandis qu'elle est dépendante de l'échelle pour les bras spiraux. La distribution longitudinale du H I est similaire pour les cinq mosaïques tandis que la distribution latitudinale est plus lisse dans les bras spiraux. Ces résultats tiennent pour toutes les échelles étudiées, de ~ 2 pc dans le bras Local à ~ 44 pc dans le bras Externe. Plusieurs hypothèses sont investiguées dans le but d'obtenir une explication physique: le gradient de distribution en z (scale-height gradient), l'onde de densité, l'activité de formation

d'étoiles, la photo-lévitation de nuages poussiéreux, les mouvements aléatoires de nuages H I, la corrugation et la turbulence.

3.1 INTRODUCTION

The Galactic H I has a very complex structure. At small scale, around singular objects (WR stars, SNRs, H II regions), the H I is driven by winds, dissociation, and shock fronts which induce chaotic, filamentary structures of varying complexity (Khalil, Joncas & Nekka (2004), henceforth called Paper I). At the largest scale, the H I is approximately axisymmetric in longitude with a vertical distribution (along b) often characterized by a Gaussian / exponential distribution (Lockman, 1984), give or take a few irregular structures like chimneys, etc, and the warp of the Galactic plane (Binney & Merrifield, 1998). But at the intermediate scale (e.g. portions of spiral arms), is the structure of the gas affected by singular objects and/or by the push and pull of random motions and gravity on clouds or any other kinds of oscillations, i.e. corrugation (Spicker & Feitzinger, 1986)?

3.1.1 Fractals & Multifractals

Mandelbrot coined the term *fractal* more than twenty years ago to qualify geometrically complex objects that could be characterized by a non-integer dimension (Mandelbrot, 1974a,b, 1977, 1982). A better description for these originally called “pathological mathematical monsters” (Hausdorff, 1919; Besicovitch, 1935) is that they possess details at every scale.

The Hausdorff dimension (Hausdorff, 1919), a usually non-integer value expressing the complexity of fractal sets is practically impossible to calculate by way of simple algorithms (see Li, Arneodo & Nekka (2004) for a review and the development of a new technique). The fractal dimension (D_F), which is an estimate of the Hausdorff dimension,

can be calculated with many algorithms: box-counting algorithms¹, fixed-mass and fixed-size algorithms, perimeter-area relation, divider box, triangle, slit-island, power spectral, variogram and distribution methods (for a thorough review, see Decoster (1999) and references therein). It has been documented that different methods of estimating D_F yield different results (see Lea-Cox & Wang (1993) for a discussion). Another scaling exponent, the Hurst exponent, H , also called “roughness exponent” can be alternatively used. It is related to the fractal dimension by $D_F = d - H$, where d is the Euclidean dimension of the space where the surface is embedded. Again, many algorithms are available to estimate H : height-height correlation function, variance and power spectral methods, de-trended fluctuation analysis, first return and multi-return probability distributions (see Decoster (1999) and references therein).

In the nineties, the use of the fractal dimension (D_F) in the study of the ISM was widespread. It has often been used to characterize the complexity of structures. Most studies on interstellar clouds show that the fractal dimension is more or less universal, with a value in the interval 2.2 to 2.5. Actually, results are usually between 1.2 and 1.5 since most of these studies deal with the perimeter-area method (Lovejoy, 1982; Feder, 1988) which yields the fractal dimension of the projection of 3-D objects in 2-D (see Falconer (1990) for the effects of projection on fractal objects). Such studies were done for molecular clouds (Bazell & Désert, 1988; Scalo, 1990; Falgarone, Phillips & Walker, 1991; Elmegreen & Falgarone, 1996) as well as for H I (Vogelaar & Wakker, 1994; Stanimirovic et al., 1998; Westpfahl et al., 1999). A universal fractal dimension can inform us on the underlying physical processes which are morphing the gas. For example, some find an analogy with the 4/3 Kolmogorov exponent and suggest that turbulence is a major physical process in interstellar cloud structure (Scalo, 1987; Falgarone, 1989; Falgarone & Phillips, 1990). The mathematical point of view of the fractal aspects of turbulence was discussed in Tenman (1976) and Barenblatt, Iooss & Joseph (1983).

However, if we are in the presence of a multifractal process (which is, simply put, a structure which is best described by a spectrum of fractal dimensions), most methods will not detect it since generically, they can only provide the user a single exponent. Hence, one must keep in mind that D_F and H are global quantities which do not characterize

¹Probably the first usual definition of box-counting dimension was given in Pontrjagin & Schnirelman (1932)

the local regularity of a signal or a surface.

The eighties were a very fruitful period for the development of the multifractal² formalism, (Hentschel & Procaccia, 1983; Grasseau & Proccacia, 1983a,b; Badii & Politi, 1984, 1985; Halsey et al., 1986; Collet, Lebowitz & Porzio, 1987; Paladin & Vulpiani, 1987; Grassberger, Badii & Politi, 1988; Grasseau, 1989; Mandelbrot, 1989; Rand, 1989; Argoul et al., 1990), either by way of the so-called $f(\alpha)$ spectrum or the generalized dimensions D_q . Applications on mathematical measures are presented in Falconer (1990) while the following references concern applications in physics: Feder (1988); Vicsek (1989); West (1990); Bunde & Havlin (1991); Vicsek, Schlesinger & Matsushita (1994); Wilkinson, Kanellopoulos & Megier (1995); Family et al. (1995); Frisch (1995); Arneodo et al. (1995a) and Sornette (2000).

Chappell & Scalo (2001) used a box-counting multifractal formalism to analyze several molecular cloud regions using IRAS maps. Since multifractal processes are related to multiplicative cascades, a multifractal signature can be interpreted as evidence of a hierarchical structure. Such evidence would be a confirmation of the widely accepted hypothesis that molecular clouds are “clumpy” (large clumps are divided into smaller clumps). Molecular clouds are well-defined objects with a somewhat precise boundary and are mathematically considered as “discontinuous”. They can therefore be analyzed as multifractal measures. The box-counting technique used by Chappell & Scalo (2001) is developed for the analysis of multifractal measures. However, the H I is diffuse and distributed everywhere in the Galactic disk and must be considered as “continuous” mathematical functions. The box-counting technique is not valid for the analysis of multifractal functions. However, the formalism presented here is perfectly suited for the analysis of H I.

3.1.2 The Wavelet Transform

Introduced by Morlet and Grossmann for the analysis of seismic signals (Grossmann & Morlet, 1984; Goupillaud, Grossmann, & Morlet, 1984), the wavelet transform (WT)

²The term *multifractal* was coined by Parisi & Frisch (1985)

is a mathematical tool consisting in the decomposition of a signal (or surface) on a set of functions characterized by parameters of position and scale (Grossmann & Morlet, 1985; Combes, Grossmann, & Tchamitchian, 1989; Meyer, 1990; Lemarié, 1990; Meyer, 1992; Daubechies, 1992; Ruskai et al., 1992; Chui, 1992; Meyer & Roques, 1993; Arneodo et al., 1995a; Erlebacher, Hussaini, & Jameson, 1996; Holschneider, 1996; Mallat, 1998; Torresani, 1998; Flandrin, 1998).

For the study of the ISM, the WT has been used as an analysis tool (Gill & Henriksen, 1990; Gill, 1993; Langer, Wilson & Anderson, 1993), a filtering method, (Abergel et al., 1996; Miville-Deschênes et al., 2003), and for image reconstruction (Maisinger, Hobson & Lasenby, 2003).

The term “mathematical microscope” was coined by Arneodo et al. (1995a) to describe the advantages of the multi-scale analysis of the WT coupled with the positional information, making it the perfect tool to analyze the scale-invariance properties of fractal objects (see also Arneodo (1996) and Flandrin, Abry & Goncalvès (2002)).

3.1.3 The WTMM Method

The Wavelet-Transform Modulus Maxima (WTMM) method is a wavelet-based multifractal formalism introduced by Arneodo, in collaboration with Bacry and Muzy (Muzy, Bacry & Arneodo, 1991; Bacry, Muzy & Arneodo, 1993; Muzy, Bacry & Arneodo, 1993, 1994; Arneodo, Bacry & Muzy, 1995), where the different dilations of the wavelet act as “generalized oscillating boxes” to reveal quantitative information at every scale considered. Replacing the boxes used in the standard multifractal formalism by wavelets gets rid of possible smooth behavior that either mask singularities or perturb the estimation of their strength. Moreover, it does not have the drawbacks of the structure function approach (Monin & Yaglom, 1975; Parisi & Frisch, 1985; Frisch, 1995), which were first discussed in detail in Muzy, Bacry & Arneodo (1993) or of the box-counting techniques. The structure function approach generally fails to fully characterize the multifractal properties since only the strongest singularities of the surface are a priori amenable to this analysis.

The WTMM method was generalized from 1D to 2D in Arneodo, Decoster & Roux (2000), where the formalism was first developed and tested on isotropic and anisotropic (monofractal) surfaces, and where the possible applications for edge detection and denoising were presented. The 2D formalism was then tested on simulated multifractal surfaces (Decoster, Roux & Arneodo, 2000). And in Roux, Arneodo & Decoster (2000), the authors analyzed high-resolution (LANDSAT) satellite images of (earth) cloud structure, where the intermittent nature of the clouds confirmed the relevance of the multifractal description. Furthermore, the 2D WTMM method proved very efficient to characterize the anisotropic structure induced by the convective rolls in the clouds. The detection and characterization of anisotropic structure will be discussed in great detail in the present work.

The 2D WTMM method was also successfully applied in medical imagery, where the analysis of digitized mammograms revealed two types of rough textures presenting two different monofractal scale-invariance properties, depending on the “fatty” or “dense” nature of the apparent radiology (Kestener et al., 2001). It was shown that the 2D WTMM method could be used to detect and characterize the geometrical properties of microcalcifications, first signs of the development of breast cancer (Kestener et al., 2001; Arneodo et al., 2003).

Work is now being done on the recently generalized 3D WTMM method. The latest generalization of the method has been validated by analyzing synthetic scalar fields for which the multifractal properties were known analytically (Kestener & Arneodo, 2003a). These authors have also shown that the multifractal spatial structure of 3D fields (dissipation fields and turbulent enstrophy³ flows) obtained by direct numerical simulation of the Navier-Stokes equation was best described by a multiplicative cascade process which is non-conservative, a result also found in 1D and 2D analyses. In effect, their results show that the so-called cancellation coefficient (Ott et al., 1992; Du & Ott, 1993), which they have reformulated in a simplistic way in terms of the wavelet-based multifractal formalism, is non-zero. This is a proof that this observation is not due to 3D → 2D projections effects or from the study of 2D cuts from 3D objects (Kestener & Arneodo, 2003b).

³The enstrophy is the integral of the squared vorticity.

3.1.4 Application of the 2D WTMM Method to H I

This paper presents the results of an intermediate-scale structural analysis of H I in the Galactic Plane using the 2D WTMM method. A region of about 45 by 8 degrees was covered in the analysis, with five different collapsed velocity intervals corresponding to the Local, Perseus and Outer Arms and the two “inter-arm” regions in between. Our objective is to obtain a quantitative characterization of the fractal, multifractal, and anisotropic properties of the analyzed H I, and then to draw conclusions on the turbulent nature and stratified structure of the gas. A further goal is to generate models where the fractal properties and our discovery of the anisotropic signature will be incorporated in order to “mimic” the H I as best as possible (for the range of scales studied). The work presented here aims to complement the study of Paper I, where the Metric Space Technique was used to analyze the small-scale structure of H I features associated to galactic objects of known origin. Although the two tools are very different and do not provide the same kind of output, we hope that both contributions will provide a better understanding of the evolution of the ISM in our Galaxy. However, one should keep in mind that any image analysis tool is subject to resolution limitations and finite-size effects. The work presented here is no exception.

The data are presented in §3.2. The 2D WTMM method is described in §3.3. The construction and analysis of simulated isotropic monofractal and multifractal surfaces, as well as anisotropic monofractal surfaces are dealt with in §3.4. Results are reported in §3.5, while the analysis and discussion are in §3.6. The paper ends with the conclusion in §3.7.

3.2 DATA

The data come from the Canadian Galactic Plane Survey (CGPS), where the observations were taken with the Dominion Radio Astrophysical Observatory (DRAO) synthesis telescope (Penticton, BC, Canada). A detailed description of the CGPS is given in Taylor et al. (2003).

The CGPS H I data cubes (193 synthesis pointings) were assembled in five large H I mosaics: the Local, Perseus, and Outer spiral arms, and two “Inter-arm” regions respectively located between the Local and Perseus arms, henceforth called “Inter I”, and between the Perseus and Outer arms, henceforth called “Inter II”. The five mosaics are presented in Figure 3.1. These five H I column density mosaics result from the integration of the cubes over the velocity range relevant to each structure according to galactic longitude (Table 3.1) and were constructed from the longitude-velocity plot presented in Simonson (1976), Figure 1. Unlike the Local, Inter I, and Perseus mosaics, the velocity intervals vary significantly as a function of longitude for Inter II and Outer. These latter two mosaics were difficult to construct (see Figure 1 of Simonson (1976)) so that it is possible, for example for the Inter II mosaic to be contaminated by one of its neighboring spiral arms. However, given the time and care that were invested to choose the correct velocity ranges, this contamination should be minimal. The distances shown in Table 3.1 represent average values approximated from different longitudes in the mosaics, using a flat galactic rotation curve with $R_o = 8.5$ Kpc and $v_o = 220$ km s $^{-1}$. Given the relatively high level of uncertainty of these measurements, distance effects such as streaming motions were not considered. It should be pointed out that the distances to the mosaics are not taken into account in the computational steps of the WTMM method. The distances will be used to approximate the physical size of the mosaics in the discussion. Finally, the DRAO velocity channels are separated by 0.842 km s $^{-1}$ and the rms noise varies from 2.1 to 3.2 K according to declination in an empty channel and the pixel size is 18 arc seconds.

The analysis requested the mosaics to be cut-up in subregions (white boxes in Figure 3.1). The pattern was governed to avoid extra-galactic and galactic absorption sources, by “edge-effects”, and by defects due to image construction and manipulation (the latter in Inter II and Outer only).

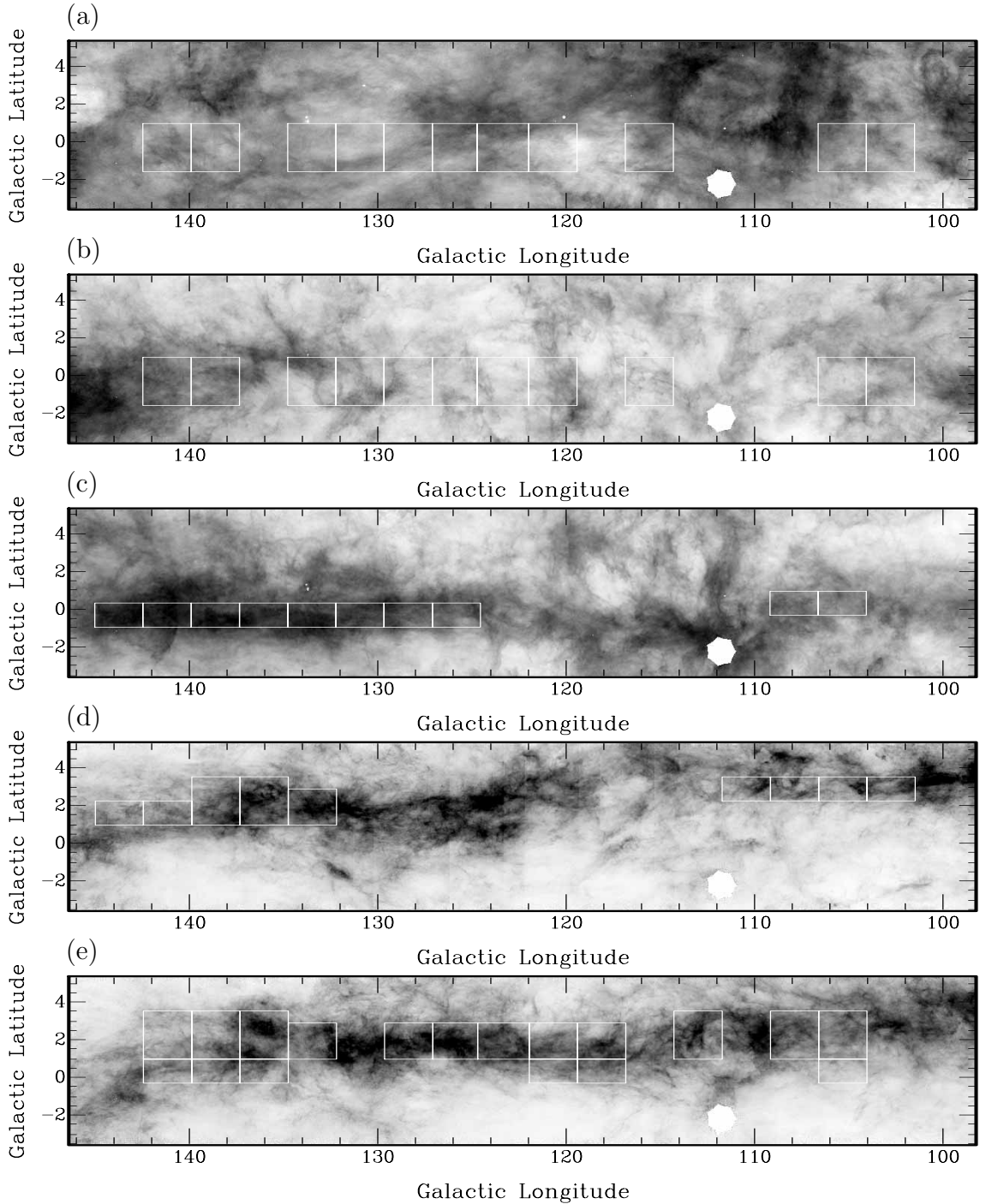


Figure 3.1: From top to bottom, the mosaics Local, Inter I, Perseus, Inter II, and Outer. The range of intensities (from white to black), which vary from one mosaic to another, are (a) [22, 85], (b) [2, 87], (c) [2, 103], (d) [0, 50], and (e) [0, 41] K km s^{-1} . White rectangles represent the sub-areas analyzed (see text for a discussion on the choice of these sub-areas).

Table 3.1: Five H I mosaics

Mosaic	Distance (pc)	Galactic Longitude (°)	Velocity Range (km/s)
Local	~ 1000	[98, 146]	[0.19, -20.43]
Inter I	~ 2500	[98, 146]	[-20.43, -34.44]
Perseus	~ 3500	[98, 146]	[-34.44, -50.11]
Inter II	~ 4700	[98, 115]	[-77.31, -88.03]
		[115, 119]	[-74.02, -83.08]
		[119, 123]	[-71.54, -81.44]
		[123, 127]	[-69.07, -78.96]
		[127, 130]	[-66.60, -76.49]
		[130, 146]	[-64.12, -74.84]
Outer	~ 6300	[98, 103]	[-88.86, -111.12]
		[103, 107]	[-88.86, -107.82]
		[107, 111]	[-88.86, -105.35]
		[111, 115]	[-88.86, -102.05]
		[115, 119]	[-83.91, -100.40]
		[119, 123]	[-82.26, -97.10]
		[123, 127]	[-79.79, -95.45]
		[127, 130]	[-77.31, -92.15]
		[130, 146]	[-74.02, -85.56]

3.3 THE 2D WAVELET-TRANSFORM MODULUS MAXIMA METHOD

The 2-D WTMM method (Arneodo, Decoster & Roux, 2000) is primordially a multifractal analysis tool which provides a way to estimate the so-called $D(h)$ spectrum of singularities, i.e. the fractal dimension of the set of points in the 2-D surface which are characterized by a specific local roughness (Hölder) exponent h , or, in the case of a monofractal signature, by a global Hurst exponent H . Moreover, an anisotropic structure can also be easily detected.

Here, the wavelet transform acts as a mathematical microscope to obtain quantitative structural information (fractal, multifractal, and anisotropic) at all scales studied. In the following description of the 2D WTMM method, comments are included regarding the drawbacks of using a box-counting multifractal formalism (Chappell & Scalo, 2001), as well as a structure function approach (Parisi & Frisch, 1985), and how the 2D WTMM method generically avoids these drawbacks.

3.3.1 Description of the 2D WTMM Method

3.3.1.1 The Wavelet Transform and the Analyzing Wavelets

Let us consider two wavelets that are, respectively, the partial derivatives with respect to x and y of a 2-D smoothing (Gaussian) function,

$$\phi_{\text{Gau}}(x, y) = e^{-(x^2+y^2)/2} = e^{-|\mathbf{x}|^2/2}, \quad (3.1)$$

namely

$$\psi_1(x, y) = \partial\phi_{\text{Gau}}(x, y)/\partial x \quad \text{and} \quad \psi_2(x, y) = \partial\phi_{\text{Gau}}(x, y)/\partial y. \quad (3.2)$$

For any function $f(x, y) \in L^2(\mathbf{R})$, (where $L^2(\mathbf{R})$ consists of all square integrable functions) the wavelet transform of f with respect to ψ_1 and ψ_2 is expressed as a vector:

$$\mathbf{T}_\psi[f](\mathbf{b}, a) = \begin{pmatrix} T_{\psi_1}[f] = a^{-2} \int d^2\mathbf{x} \psi_1(a^{-1}(\mathbf{x} - \mathbf{b})) f(\mathbf{x}) \\ T_{\psi_2}[f] = a^{-2} \int d^2\mathbf{x} \psi_2(a^{-1}(\mathbf{x} - \mathbf{b})) f(\mathbf{x}) \end{pmatrix} = \nabla\{T_{\phi_{\text{Gau}}}[f](\mathbf{b}, a)\}, \quad (3.3)$$

where a is the scale parameter and \mathbf{b} is the position vector. In Figures 3.2a and 3.2b are shown the first-order analyzing wavelets ψ_1 and ψ_2 , where the smoothing function ϕ_{Gau} is the Gaussian function defined in Eq. (3.1). In Figures 3.2c and 3.2d are shown the third-order analyzing wavelets obtained from the Mexican hat smoothing function

$$\phi_{\text{Mex}}(\mathbf{x}) = (2 - \mathbf{x}^2)e^{-|\mathbf{x}|^2/2}. \quad (3.4)$$

Using higher order wavelets, where the number of vanishing moments of ϕ is equal to the order of the wavelets, provides the WTMM method with the capability of characterizing the roughness, not only of a surface, but also of its derivatives (a capability that is absent from the box-counting and structure function approaches) (Arneodo et al., 1995a; Arneodo, Decoster & Roux, 2000). In this paper, the third-order analyzing wavelets will be used in §3.4.2 to obtain a better characterization of the simulated multifractal surfaces and to verify the authenticity of the anisotropic signature found in the five analyzed mosaics (§3.5).

The wavelet transform can be written in terms of its modulus and argument

$$\mathbf{T}_\psi[f](\mathbf{b}, a) = (\mathcal{M}_\psi[f](\mathbf{b}, a), \mathcal{A}_\psi[f](\mathbf{b}, a)), \quad (3.5)$$

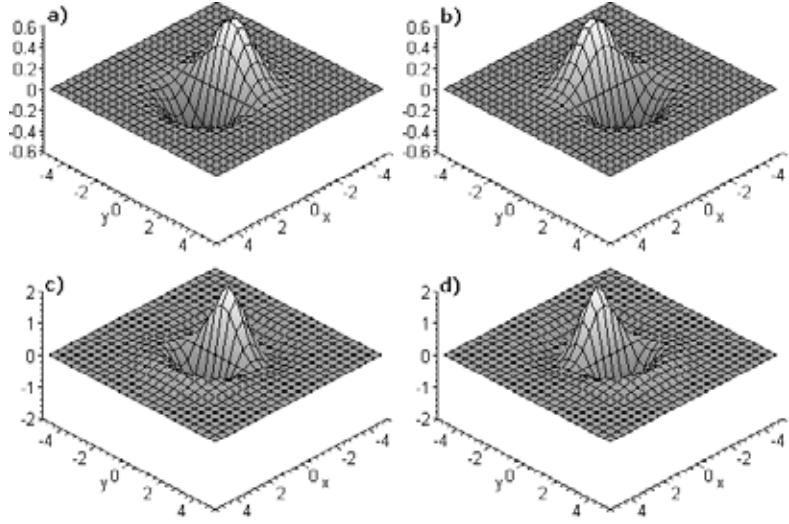


Figure 3.2: The first-order analyzing wavelets (a) ψ_1 and (b) ψ_2 defined in §3.3.1.1, obtained from a gaussian smoothing function ϕ_{Gau} (Eq. (3.1)). Third-order analyzing wavelets (c) ψ_1 and (d) ψ_2 defined in §3.3.1.1, obtained from the Mexican hat smoothing function ϕ_{Mex} (Eq. (3.4)).

where

$$\mathcal{M}_\psi[f](\mathbf{b}, a) = \sqrt{(T_{\psi 1}[f](\mathbf{b}, a))^2 + (T_{\psi 2}[f](\mathbf{b}, a))^2}, \quad (3.6)$$

and

$$\mathcal{A}_\psi[f](\mathbf{b}, a) = \text{Arg}(T_{\psi 1}[f](\mathbf{b}, a) + iT_{\psi 2}[f](\mathbf{b}, a)). \quad (3.7)$$

3.3.1.2 Global and Local Regularity Properties of Rough Surfaces: Hurst and Hölder Exponents

In this section, the term rough surface is defined, and the notions of Hurst exponent, used to characterize monofractal surfaces, and Hölder exponent, used to characterize multifractal surfaces, are also presented.

A *rough surface* refers to a surface that can be correctly described by a single-valued

self-affine⁴ function satisfying: $\forall \mathbf{x}_0 = (x_0, y_0) \in \mathbf{R}^2, \forall \mathbf{x} = (x, y) \in \mathbf{R}^2$ in the neighborhood of \mathbf{x}_0 , $\exists H \in \mathbf{R}$, such that, for any $\lambda > 0$, one has (Mandelbrot, 1977, 1982; Peitgen & Saupe, 1988; Feder, 1988; Vicsek, 1989):

$$f(x_0 + \lambda x, y_0 + \lambda^\alpha y) - f(x_0, y_0) \sim \lambda^H [f(x_0 + x, y_0 + y) - f(x_0, y_0)]. \quad (3.8)$$

If f is a stochastic process, then this identity holds for a fixed λ and \mathbf{x}_0 . Depending on the value of α , f will display either isotropic scale invariance ($\alpha = 1$) or anisotropic scale invariance ($\alpha \neq 1$) (Schertzer & Lovejoy, 1985, 1987; Schmittbuhl, Violette & Roux, 1995; Schertzer et al., 1997). The *Hurst exponent* H characterizes the global regularity of the function f (i.e. the monofractal case). Note that if $H < 1$ (which is the case in most applications), then f is nowhere differentiable and generally, a more singular surface f will be characterized by a smaller H . Also note that a totally random noise, i.e. white noise, is characterized by $H = -0.5$, while the so-called $1/f$ noise, which is actually integrated white noise is characterized by $H = -0.5 + 1 = 0.5$. The Hurst exponent is related to the usual definition of the fractal dimension $D_f = d - H$, where d represents the dimension of the space where the surface is embedded.

However, fractal functions often display *multi-affine* properties in the sense that their roughness fluctuates from point to point (i.e. the multifractal case) (Parisi & Frisch, 1985; Muzy, Bacry & Arneodo, 1991, 1994; Arneodo, Bacry & Muzy, 1995). The definition of the Hurst exponent must be changed in order to describe these multifractal functions, so that it becomes a local quantity $h(\mathbf{x}_0)$. We define the *Hölder exponent* (the strength of a singularity of a function f at the point \mathbf{x}_0) by the largest exponent $h(\mathbf{x}_0)$ such that there exists a polynomial of degree $n < h(\mathbf{x}_0)$ and a constant $C > 0$, so that for any point \mathbf{x} in the neighborhood of \mathbf{x}_0 one has (Mallat & Zhong, 1992; Mallat & Hwang, 1992):

$$|f(\mathbf{x}_0) - P_n(\mathbf{x} - \mathbf{x}_0)| \leq C|\mathbf{x} - \mathbf{x}_0|^{h(\mathbf{x}_0)}. \quad (3.9)$$

Therefore, the roughness of f at the point \mathbf{x}_0 is characterized by $h(\mathbf{x}_0)$. Like the Hurst exponent H , the higher the exponent $h(\mathbf{x}_0)$, the more regular the function f , except that the characterization is only valid for the point \mathbf{x}_0 .

In order to recover the Hölder exponent $h(\mathbf{x}_0)$ of a function f from \mathbf{R}^2 into \mathbf{R} , one needs to study the behavior of the wavelet transform modulus inside a cone $|\mathbf{x} - \mathbf{x}_0| < Ca$

⁴Objects satisfying self-similarity conditions, but with different scalings in different directions, are said to be self-affine.

in the (space-scale) half space (Jaffard, 1991; Arrault et al., 1997; Arneodo, Decoster & Roux, 2000). A very efficient way to perform point-wise regularity analysis is to use the wavelet transform modulus maxima (Mallat & Zhong, 1992; Mallat & Hwang, 1992). At a given scale $a > 0$, the *wavelet transform modulus maxima* (WTMM) are defined by the positions \mathbf{b} where the wavelet transform modulus $\mathcal{M}_\psi[f](\mathbf{b}, a)$ is locally maximum in the direction $\mathcal{A}_\psi[f](\mathbf{b}, a)$ of the gradient vector $\mathbf{T}_\psi[f]$. When analyzing rough surfaces, these WTMM lie on connected chains henceforth called *maxima chains* (Arrault et al., 1997; Arneodo, Decoster & Roux, 1999, 2000). One only needs to record the position of the local maxima of \mathcal{M}_ψ along the maxima chains together with the value of $\mathcal{M}_\psi[f]$ and $\mathcal{A}_\psi[f]$ at the corresponding locations. At each scale a , the wavelet analysis thus reduces to store those WTMM maxima (WTMMM) only. They indicate locally the direction where the signal has the sharpest variation. These WTMMM are disposed along connected curves across scales called *maxima lines* (Arneodo, Decoster & Roux, 1999, 2000). The *wavelet transform skeleton* is defined as the set of maxima lines that converge to the (x, y) -plane in the limit $a \rightarrow 0^+$. This WT skeleton contains all the information about the local Hölder regularity properties of the function f under consideration (Arneodo, Decoster & Roux, 2000).

The reader is referred to §3.9.1 in the appendix for two examples describing how the maxima lines and the wavelet transform skeleton behave when considering isolated singularities.

3.3.1.3 The 2D WTMM Method

Let f be a rough surface and S_h the set of all points \mathbf{x}_0 where the Hölder exponent (Eq.(3.9)) of f at \mathbf{x}_0 is h . The *singularity spectrum* $D(h)$ of f is the function which associates with any h , the fractal dimension of S_h :

$$D(h) = d_H\{\mathbf{x} \in \mathbf{R}^2 : h(\mathbf{x}) = h\}. \quad (3.10)$$

The maxima lines defined from the WTMMM computed at different scales can be used to detect the positions where singularities are located as well as the estimation of their strength h .

The characteristic feature of singular functions is the existence of a hierarchical distribution of singularities (Muzy, Bacry & Arneodo, 1991, 1993, 1994; Arneodo et al., 1995a; Arneodo, Bacry & Muzy, 1995; Mallat, 1998). Locally, the Hölder exponent $h(\mathbf{x}_0)$ is then governed by the singularities which accumulate at \mathbf{x}_0 . This results in unavoidable oscillations around the expected power-law behavior of the wavelet transform modulus (Muzy, Bacry & Arneodo, 1991, 1993, 1994; Arneodo, Bacry & Muzy, 1995). The estimation of the strength of a singularity located at \mathbf{x}_0 is biased by the singularities located in the neighborhood of \mathbf{x}_0 . Therefore, the exact determination of h from log-log plots is uncertain and must be avoided (Bacry et al., 1991; Vergassola et al., 1993). Hence, the determination of statistical quantities like the $D(h)$ singularity spectrum requires a method which is more feasible and more appropriate than a systematic investigation of the wavelet transform local scaling behavior.

The 2D WTMM method relies upon the space-scale partitioning given by the wavelet transform skeleton. As discussed in the two examples in §3.9.1, this skeleton (see Fig. 3.6) is defined by the set of maxima lines which point to the singularities of the considered function and therefore is likely to contain all the information concerning the fluctuations of point-wise Hölder regularity. Let us define $\mathcal{L}(a)$ as the set of all maxima lines that exist at the scale a and which contain maxima at any scale $a' \leq a$. The WTMM method consists in defining the following partition functions directly from the WTMM that belong to the wavelet transform skeleton:

$$\mathcal{Z}(q, a) = \sum_{\mathcal{L} \in \mathcal{L}(a)} \left(\sup_{(\mathbf{x}, a') \in \mathcal{L}, a' \leq a} \mathcal{M}_\psi[f](\mathbf{x}, a') \right)^q, \quad (3.11)$$

where $q \in \mathbf{R}$ and sup stands for “supremum”⁵. As compared to classical box-counting techniques discussed in §3.1 and in Chappell & Scalo (2001), the analyzing wavelet ψ plays the role of a generalized “oscillating box”, the scale a defines its size, while the WTMM skeleton indicates how to position our oscillating boxes to obtain a partition at the considered scale. Without the “sup” in equation (3.11), one would have implicitly considered a uniform covering with wavelets of the same size a . As emphasized in Muzy, Bacry & Arneodo (1991, 1993); Bacry, Muzy & Arneodo (1993); Muzy, Bacry & Arneodo (1994) and Arneodo, Bacry & Muzy (1995), the “sup” can be regarded as a way of defining

⁵The supremum is sometimes called the *least upper bound*. For a detailed discussion, see Spivak (1994), where a whole Chapter is dedicated to this topic.

a “Hausdorff like” scale-adaptive partition which will prevent divergences to show up in the calculation of $\mathcal{Z}(q, a)$ for $q < 0$.

Now, from the deep analogy that links the multifractal formalism to thermodynamics (Halsey et al., 1986; Muzy, Bacry & Arneodo, 1994; Arneodo, Bacry & Muzy, 1995), one can define the exponent $\tau(q)$ from the power-law behavior of the partition function:

$$\mathcal{Z}(q, a) \sim a^{\tau(q)}, \quad a \rightarrow 0^+, \quad (3.12)$$

where q and $\tau(q)$ play respectively the role of the inverse temperature and the free energy⁶. The main result of the wavelet-based multifractal formalism is that in place of the energy and the entropy (i.e. the variables conjugated to q and τ), one has the Hölder exponent h (Eq. (3.9)) and the singularity spectrum $D(h)$ (Eq. (3.10)). This means that the $D(h)$ singularity spectrum of f can be determined from the Legendre transform of the partition function scaling exponent $\tau(q)$:

$$D(h) = \min_q (qh - \tau(q)). \quad (3.13)$$

From the properties of the Legendre transform, it is easy to convince oneself that monofractal functions that involve singularities of unique Hölder exponent are characterized by a $\tau(q)$ spectrum which is a *linear* function of q . On the contrary, a *nonlinear* $\tau(q)$ curve is the signature of functions that display *multifractal* properties, in the sense that the Hölder exponent $h(\mathbf{x})$ is a quantity that fluctuates depending on the spatial position \mathbf{x} .

It is important to note that the exponents $\tau(q)$ are much more than simply some intermediate quantities of a rather easy experimental access. For some specific values of q , they have well known meaning (Muzy, Bacry & Arneodo, 1994):

- $q = 0$: From equations (3.11) and (3.12), one deduces that the exponent $\tau(0)$ accounts for the divergence of the number of maxima lines in the limit $a \rightarrow 0^+$. This number basically corresponds to the number of wavelets of size a required to

⁶For a short but interesting discussion about the relations between statistical mechanics and dynamical systems in general, the reader is referred to Falconer (1997), §5.6 and the references given in §5.7

cover the set \mathcal{S} of singularities of f . In full analogy with standard box-counting arguments, $-\tau(0)$ can be identified to the fractal dimension of this set:

$$-\tau(0) = d_F\{\mathbf{x}, h(\mathbf{x}) < +\infty\}. \quad (3.14)$$

- $q = 1$: As pointed out in Muzy, Bacry & Arneodo (1994), the value of the exponent $\tau(1)$ is related to the fractal dimension (capacity) of the rough surface \mathcal{S} defined by the function f . More precisely (Jaffard, 1998):

$$d_F(\mathcal{S}) = \max(2, 1 - \tau(1)). \quad (3.15)$$

- $q = 2$: It is easy to show that the exponent $\tau(2)$ is intimately related to the scaling exponent β of the spectral density :

$$S(k) = \frac{1}{2\pi} \int d\theta |\hat{f}(k, \theta)|^2 \sim k^{-\beta}, \quad (3.16)$$

where

$$\beta = 4 + \tau(2). \quad (3.17)$$

Numerical drawbacks related to the Legendre transform were presented in Cvitanovic (1987); Badii (1987); Rand (1989) and Arneodo et al. (1995a). One can avoid directly performing the Legendre transform by considering the quantities h and $D(h)$ as mean quantities defined in a canonical ensemble, i.e., with respect to their Boltzmann weights computed from the WTMM:

$$W_\psi[f](q, \mathcal{L}, a) = \frac{\left| \sup_{(\mathbf{x}, a') \in \mathcal{L}, a' \leq a} \mathcal{M}_\psi[f](\mathbf{x}, a') \right|^q}{\mathcal{Z}(q, a)}, \quad (3.18)$$

where $\mathcal{Z}(q, a)$ is the partition function defined in equation (3.11). Then one computes the expectation values:

$$h(q, a) = \sum_{\mathcal{L} \in \mathcal{L}(a)} \ln \left| \sup_{(\mathbf{x}, a') \in \mathcal{L}, a' \leq a} \mathcal{M}_\psi[f](\mathbf{x}, a') \right| W_\psi[f](q, \mathcal{L}, a), \quad (3.19)$$

and

$$D(q, a) = \sum_{\mathcal{L} \in \mathcal{L}(a)} W_\psi[f](q, \mathcal{L}, a) \ln(W_\psi[f](q, \mathcal{L}, a)), \quad (3.20)$$

from which one extracts

$$\begin{aligned} h(q) &= \lim_{a \rightarrow 0^+} h(q, a) / \ln a, \\ D(q) &= \lim_{a \rightarrow 0^+} D(q, a) / \ln a, \end{aligned} \quad (3.21)$$

and therefore the $D(h)$ singularity spectrum.

3.3.1.4 Probability Density Functions

From the definition of the partition function in equation (3.11), one can transform the discrete sum over the WTMM into a continuous integral over $\mathcal{M}_\psi[f]$:

$$\mathcal{Z}(q, a) / \mathcal{Z}(0, a) = \langle \mathcal{M}^q \rangle(a) = \int d\mathcal{M} \mathcal{M}^q P_a(\mathcal{M}), \quad (3.22)$$

where \mathcal{M} is a condensed notation for $\sup_{(\mathbf{x}, a') \in \mathcal{L}, a' \leq a} \mathcal{M}_\psi[f](\mathbf{x}, a')$. The multifractal description thus consists in characterizing how the moments of the probability density function (pdf) $P_a(\mathcal{M})$ of \mathcal{M} behave as a function of the scale parameter a . The power-law exponents $\tau(q)$ in equation (3.12) therefore quantify the evolution of the shape of the \mathcal{M} pdf across scales. At this point, let us remark that one of the main advantages of using the wavelet transform skeleton is the fact that, by definition, \mathcal{M} is different from zero and consequently that $P_a(\mathcal{M})$ generally decreases exponentially fast to zero at zero. This observation is at the heart of the WTMM method since, for this reason, one can not only compute the $\tau(q)$ spectrum for $q > 0$ but also for $q < 0$ (Muzy, Bacry & Arneodo, 1991, 1993, 1994). From the Legendre transform of $\tau(q)$ (Eq. 3.13), one is thus able to compute the whole $D(h)$ singularity spectrum, i.e. its increasing left part ($q > 0$) as well as its decreasing right part ($q < 0$).

Moreover, although isotropic analyzing wavelets are used, one can see from the two examples in §3.9.1 that from the analysis of the wavelet transform skeleton, one is able to also extract directional information via the computation of $\mathcal{A}_\psi[f](\mathbf{x}, a)$. It is thus very instructive to extend the statistical analysis to the investigation of the \mathcal{A} pdf, $P_a(\mathcal{A})$. If this angle pdf is flat, this means that the rough surface under study displays isotropic scale invariance properties. If, on the contrary, this pdf is a non-uniform distribution on $[0, 2\pi]$, this suggests that some anisotropy is present in the analyzed image. The possible existence of privileged directions can then be revealed by investigating the correlations between the values of \mathcal{A} for different maxima lines. Furthermore, $P_a(\mathcal{A})$ may evolve when varying the scale parameter a . The way its shape changes indicates whether (and how) anisotropy is enhanced (or weakened) when going from large scales to small scales.

The reader is now referred to §3.9.2 of the appendix where the numerical implementation of the 2D WTMM method is described in detail.

3.4 TEST APPLICATIONS OF THE 2D WTMM METHOD

In this section the 2D WTMM method is tested on three types of synthetic surfaces: isotropic monofractal surfaces (fractional Brownian motion), isotropic multifractal surfaces (fractionnally integrated singular cascades), and anisotropic surfaces. At the end of each corresponding following subsections, i.e. §3.4.1, §3.4.2, & §3.4.3, a description of the differences between the synthetic surfaces (and corresponding results) presented here and the work of Arneodo, Decoster & Roux (2000) and Decoster, Roux & Arneodo (2000) is outlined.

Introduced by Mandelbrot & Van Ness (1968), fractional Brownian motion (fBm) has become a very popular modeling tool used in signal and image (2D and 3D) analysis (Mandelbrot, 1982; Feder, 1988; Peitgen & Saupe, 1988; Falconer, 1990; Arneodo et al., 1995a; Arneodo, Decoster & Roux, 2000; Miville-Deschénes, Levrier & Falgarone, 2003). It has been used to calibrate the WTMM method in 1D (Muzy, Bacry & Arneodo, 1991, 1994; Arneodo, Bacry & Muzy, 1995), in 2D (Arneodo, Decoster & Roux, 1999, 2000), and in 3D (Kestener, 2003c).

Construction of fBm models for the ISM where presented in Stutzki et al. (1998). And Miville-Deschénes, Levrier & Falgarone (2003) analyzed the effects of the projection of simulated 3D fields in 2D in order to characterize the effects of projection in ISM maps. Non-fBm methods were also used to model the ISM (Hatem & Lépine, 1993).

In this section, the analysis of simulated fBm isotropic monofractal and multifractal 2D surfaces will demonstrate the accuracy and limits of the 2D WTMM method. Furthermore, we will see how the 2D WTMM method can easily characterize anisotropic structures by analyzing simulated anisotropic rough surfaces.

3.4.1 Isotropic Fractional Brownian Surfaces

In this section a review of the definition of 2D fBm is presented. Afterwards, the 2D WTMM methodology described in §3.3.1 is tested on several realizations of 2D fBm, for three different Hurst exponent values.

A 2D fBm $B_H(\mathbf{x})$ indexed by $H \in]0, 1[$, is a process with stationary zero-mean Gaussian increments whose correlation function is given by (Lévy, 1965; Mandelbrot, 1977, 1982; Peitgen & Saupe, 1988):

$$\langle B_H(\mathbf{x})B_H(\mathbf{y}) \rangle = \frac{\sigma^2}{2} (|\mathbf{x}|^{2H} + |\mathbf{y}|^{2H} - |\mathbf{x} - \mathbf{y}|^{2H}), \quad (3.23)$$

where $\langle \dots \rangle$ represents the ensemble mean value and $\mathbf{x}, \mathbf{y} \in \mathbf{R}^2$. The variance of such a process is

$$\text{var}(B_H(\mathbf{x})) = \sigma^2 |\mathbf{x}|^{2H} \quad (3.24)$$

for any $\mathbf{x} \in \mathbf{R}^2$. 2D fBm's are self-affine processes that are statistically invariant under isotropic dilations:

$$B_H(\mathbf{x}_0 + \lambda \mathbf{u}) - B_H(\mathbf{x}_0) \simeq \lambda^H [B_H(\mathbf{x}_0 + \mathbf{u}) - B_H(\mathbf{x}_0)], \quad (3.25)$$

where \mathbf{u} is a unitary vector and \simeq stands for the equality in law. The index H corresponds to the Hurst exponent. But since equation (3.25) holds for any \mathbf{x}_0 and any direction \mathbf{u} , this means that almost all realizations of the fBm process are continuous, everywhere non-differentiable, isotropically scale-invariant as characterized by a unique Hölder exponent $h(\mathbf{x}) = H$, $\forall \mathbf{x}$ (Mandelbrot, 1977, 1982; Peitgen & Saupe, 1988; Audit et al., 2002). Thus fBm surfaces are the representation of homogeneous stochastic (mono)fractal functions characterized by a singularity spectrum which reduces to a single point

$$\begin{aligned} D(h) &= 2 && \text{if } h = H, \\ &= -\infty && \text{if } h \neq H. \end{aligned} \quad (3.26)$$

By Legendre transforming $D(h)$ according to equation (3.13), one gets the following expression for the partition function exponent (Eq. (3.12)):

$$\tau(q) = qH - 2. \quad (3.27)$$

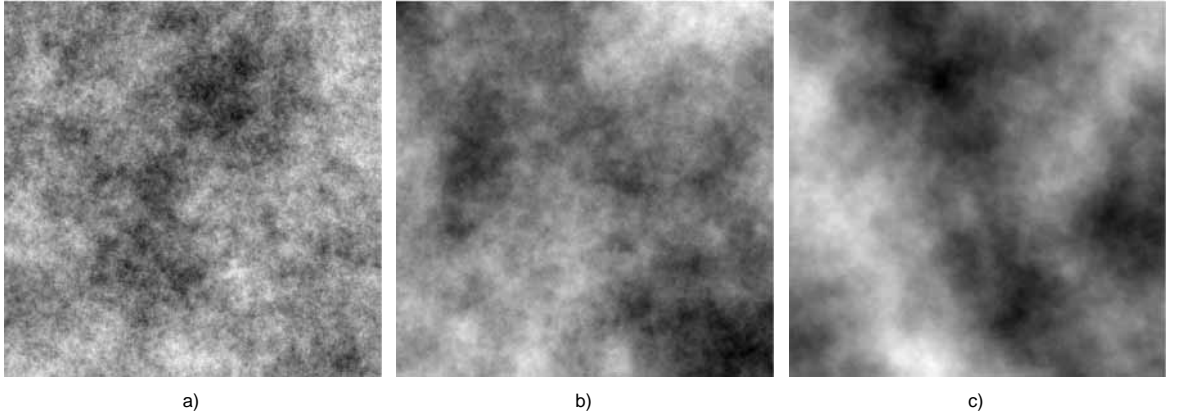


Figure 3.3: fBm surfaces generated with the Fourier transform filtering synthesis method.
a) $H = 0.2$; b) $H = 0.5$; c) $H = 0.8$.

$\tau(q)$ is a linear function of q , the signature of monofractal scaling, with a slope given by the index H of the fBm. The relationship between H and the power spectral index, β is given by

$$\beta = 2H + d, \quad (3.28)$$

where $\beta = \lim_{k \rightarrow \infty} -\frac{\log(S(|\mathbf{k}|))}{\log(|\mathbf{k}|)}$ (in Fourier space) and d represents the Euclidean dimension ($d = 2$ for a surface).

The 2D WTMM method described in §3.3.1 was tested on isotropic fBm surfaces generated by the so-called Fourier transform filtering method (Ffm) (Peitgen & Saupe, 1988). This particular synthesis method is used because of the simplicity of its implementation. Indeed it amounts to a fractional integration of a 2D “white noise” and therefore it is expected to reproduce quite faithfully the isotropic scaling invariance properties. By looking at Figures 3.3a ($H = 0.2$), 3.3b ($H = 0.5$) and 3.3c ($H = 0.8$), one can see that the fBm surfaces become less and less irregular when increasing the index H .

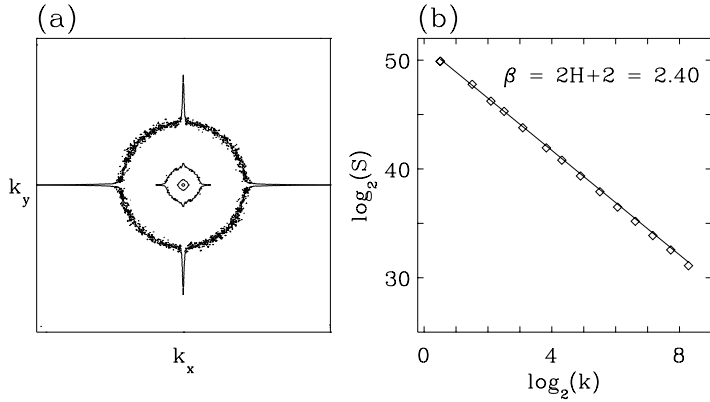


Figure 3.4: Fourier analysis of the 512×512 central part of a fBm surface $B_{H=0.2}(\mathbf{x})$. (a) A contour plot of $\ln |\hat{B}_{0.2}(\mathbf{k})|$. (b) The power spectrum $S(|\mathbf{k}|)$ vs $|\mathbf{k}|$ in a logarithmic representation. The solid line corresponds to the power-law theoretical prediction.

3.4.1.1 Fourier Analysis

The Fourier analysis of 32 (1024×1024) images of $B_{H=0.2}$ is presented in Figure 3.4. Figure 3.4a presents a contour plot of the 2D Fourier spectrum. The log-log plot of the 2D power spectrum shown in Figure 3.4b confirms the relation between the beta index and the Hurst exponent (Eq. 3.28).

3.4.1.2 Wavelet Analysis

We have wavelet transformed these 32 (1024×1024) images of $B_{H=0.2}$ with a first-order analyzing wavelet (Figures 3.2a and 3.2b). To avoid edge effects, only the 512×512 central part of the wavelet transform of each image is kept for analysis. Figure 3.5 illustrates the computation of the maxima chains and the WTMM for an individual image at three different scales. Figure 3.5b is the convolution of the original image (Fig. 3.5a) with the isotropic Gaussian smoothing filter ϕ_{Gau} (§3.3.1.1).

According to the definition of the wavelet transform modulus maxima, the maxima chains correspond to well defined edge curves of the smoothed image. The local maxima

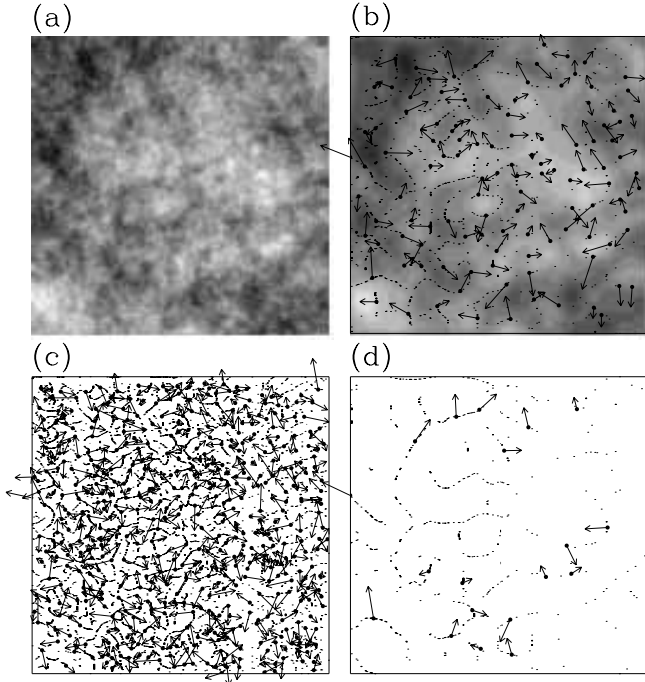


Figure 3.5: 2D wavelet transform analysis of $B_{H=0.2}(\mathbf{x})$. ψ is a first-order radially symmetric analyzing function (see Fig. 3.2). (a) 32 grey-scale coding of the original image. In (b) $a = 2^{2.9}\sigma_W$, (c) $a = 2^{1.9}\sigma_W$ and (d) $a = 2^{3.9}\sigma_W$ (where $\sigma_W = 13$ pixels), are shown the maxima chains; the local maxima of \mathcal{M}_ψ along these chains are indicated by (•) from which originate an arrow whose length is proportional to \mathcal{M}_ψ and its direction (with respect to the x -axis) is given by \mathcal{A}_ψ . In (b), the smoothed image $\phi_{\mathbf{b},a} * B_{H=0.2}$ is shown as a grey-scale coded background from white (min) to black (max).

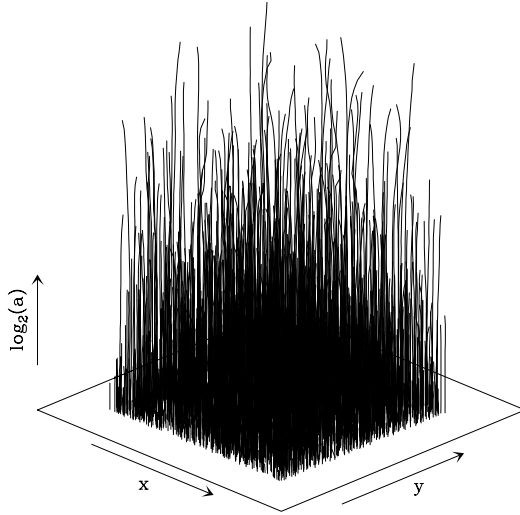


Figure 3.6: Wavelet transform skeleton of an isotropic 2D fBm surface. (Figure taken from Arneodo, Decoster & Roux (2000).)

of \mathcal{M}_ψ along these curves are located at the points where the sharpest intensity variation is observed. The corresponding arrows clearly indicate that locally, the gradient vector points in the direction (as given by \mathcal{A}_ψ) of maximum change of the intensity surface. When going from large scale (Fig. 3.5d) to small scale (Fig.3.5c), the characteristic average distance between two nearest neighbour WTMM decreases like a . This means that the number of WTMM and in turn, the number of maxima lines, proliferates across scales like a^{-2} . An example of a wavelet transform skeleton is shown in Figure 3.6.

3.4.1.3 Numerical Computation of the $\tau(q)$ and $D(h)$ spectra

The results obtained from the computation of the $\tau(q)$ and $D(h)$ spectra using the 2D WTMM method described in §3.3.1 are presented in Figure 3.7. In Figure 3.7a, the partition function $\mathcal{Z}(q, a)$ (over 32 images of $B_{H=0.5}(\mathbf{x})$) displays a remarkable scaling behavior over more than 3 octaves when plotted versus a in a logarithmic representation, where a is expressed in σ_W units (throughout this paper, $\sigma_W = 13$ pixels). Moreover, for

a wide range of values of $q \in [-4, 4]$, the data are in good agreement with the theoretical $\tau(q)$ spectrum (Eq. (3.27)). When proceeding to a linear regression fit of the data over the first two octaves, one gets the $\tau(q)$ spectra shown in Figure 3.7c for three values of the fBm index $H = 0.2, 0.5$ and 0.8 . Whatever H , the data systematically fall on a straight line, the signature of monofractal scaling properties. However, the slope of this straight line provides a slight underestimate of the corresponding Hurst exponent H . This behavior is also seen in Figures 3.7a and 3.7b for the $\mathcal{Z}(q, a)$ and $h(q, a)$ functions for individual q values. Let us point out that a few percent underestimate has been also reported when performing similar analysis of 1D fBm (Muzy, Bacry & Arneodo, 1991, 1994; Arneodo, Bacry & Muzy, 1995; Audit et al., 2002). Theoretical investigation of finite-size effects and statistical convergence has been recently performed to explain this experimental observation (Audit et al., 2002).

3.4.1.4 Probability Density Functions

In Figure 3.8 are shown the probability density functions (pdfs)

$$P_a(\mathcal{M}) = \int d\mathcal{A} P_a(\mathcal{M}, \mathcal{A}) \quad (3.29)$$

and

$$P_a(\mathcal{A}) = \int d\mathcal{M} P_a(\mathcal{M}, \mathcal{A}), \quad (3.30)$$

computed for four different values of the scale parameter with $B_{H=0.2}(\mathbf{x})$. As seen in Figure 3.8a, $P_a(\mathcal{M})$ is not a Gaussian, but decreases fast to zero at zero. This explains that when concentrating on the wavelet transform skeleton, the discrete sum in the r.h.s. of equation (3.11) no longer diverges when considering negative q values⁷. This critical remark is at the heart of the 2D WTMM method: By allowing us to compute the $\tau(q)$ spectrum for negative as well as positive q values, the 2D WTMM method is a definite step beyond the 2D structure function method which is simply undefined for negative q values and is therefore intrinsically restricted to positive q values, which correspond only

⁷Note that since perfect statistical conditions do not exist, i.e., an infinite number of infinite images, one can see that the r.h.s. of equation (3.11) will diverge for large values of $|q|$ for a small number of statistics, especially for $q < 0$. One must thus be wary of multifractal studies using values as large as $q = |20|$ (Chappell & Scalo, 2001).

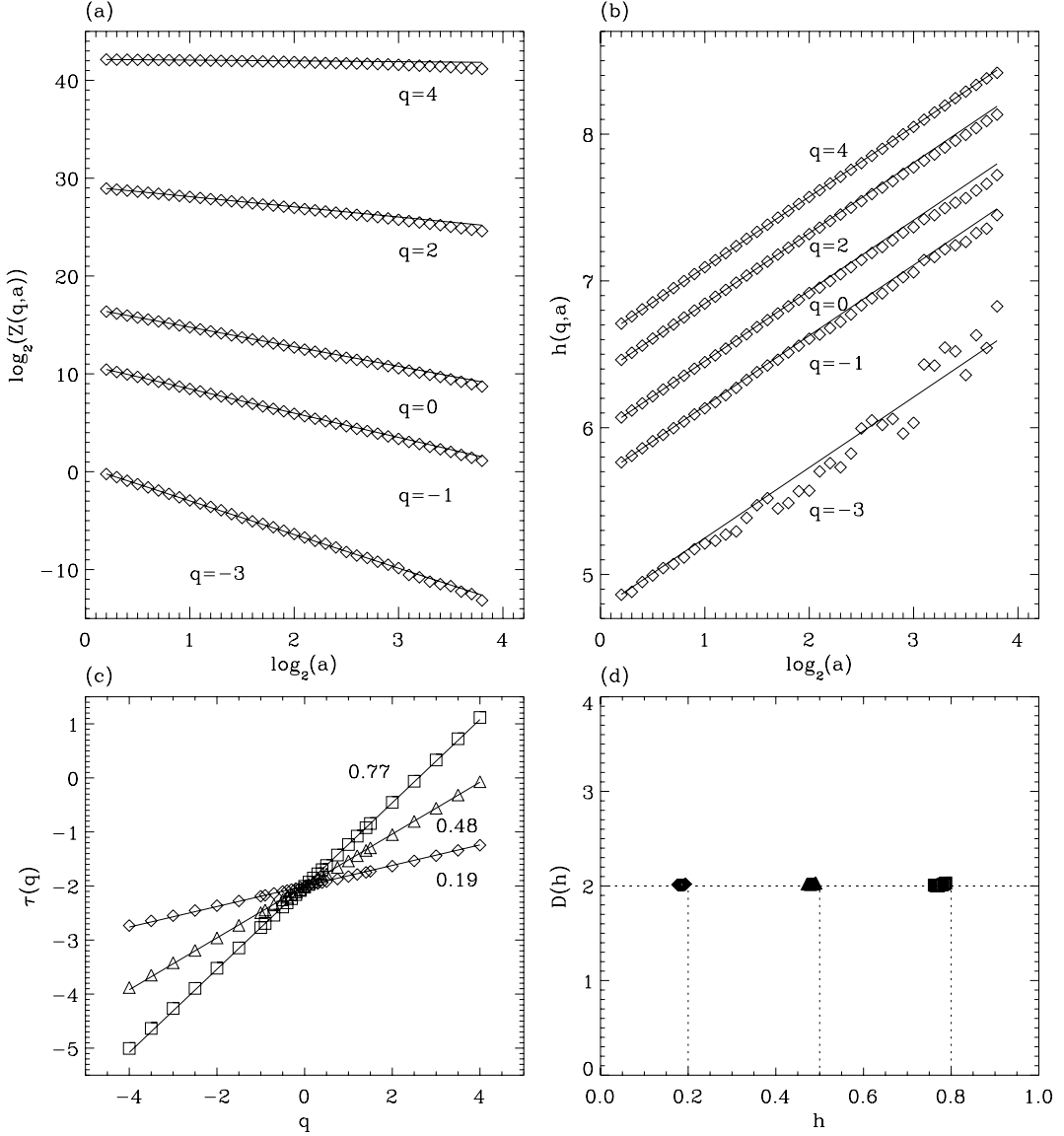


Figure 3.7: Determination of the $\tau(q)$ and $D(h)$ spectra of 2D fBm with the 2D WTMM method. (a) $\log_2 \mathcal{Z}(q,a)$ vs $\log_2 a$; the solid lines correspond to the theoretical predictions $\tau(q) = qH - 2$ (Eq. (3.27)) with $H = 0.5$. (b) $h(q,a)$ vs $\log_2 a$; the solid lines correspond to the theoretical slope $H = 0.5$. (c) $\tau(q)$ vs q for $H = 0.2$ (\diamond), 0.5 (\triangle) and 0.8 (\square); the solid lines correspond to linear regression fit estimates of H . (d) $D(h)$ vs h as obtained from the scaling behavior of $D(q,a)$ vs $\log_2 a$ (Eq. (3.21)); the symbols have the same meaning as in (c). First-order analyzing wavelets. These results correspond to an averaging over 32 (1024×1024) fBm images. a is expressed in $\sigma_W = 13$ units.

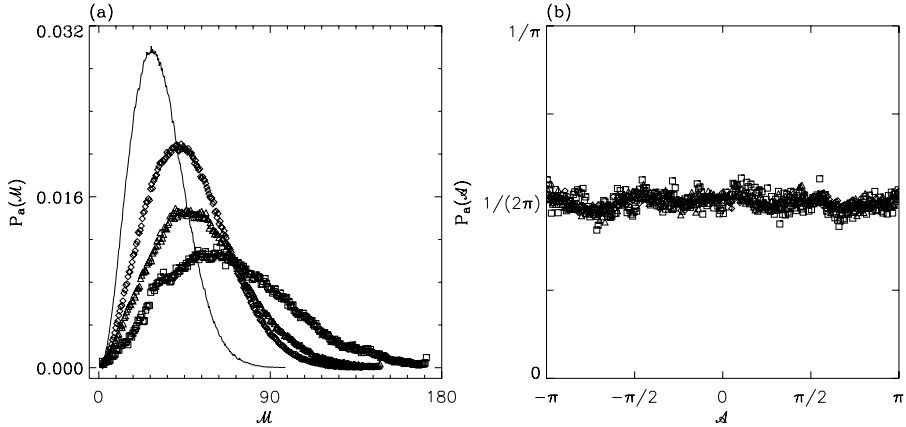


Figure 3.8: Pdfs of the WT MMMM coefficients of $B_{H=0.2}(\mathbf{x})$ as computed at different scales $a = 1$ (full line), 2 (\diamond), 4 (\triangle), 8 (\square) (in $\sigma_W = 13$ units). (a) $P_a(\mathcal{M})$ vs \mathcal{M} . (b) $P_a(\mathcal{A})$ vs \mathcal{A} . ψ is the first-order analyzing wavelet shown in Figure 3.2. These results correspond to averaging over 32 (1024×1024) fBm images.

to the strongest singularities of the analyzed surfaces. For a detailed discussion on the structure function approach versus the WTMM method, see Muzy, Bacry & Arneodo (1993).

The corresponding pdfs $P_a(\mathcal{A})$ are represented in Figure 3.8b. $P_a(\mathcal{A})$ clearly does not evolve across scales. Moreover, except for some small amplitude fluctuations observed at the largest scale, $P_a(\mathcal{A}) = 1/2\pi$ is a flat distribution as expected for statistically isotropic scale-invariant rough surfaces.

Let us now consider the problem of statistical convergence of the $\tau(q)$ and $D(h)$ spectra, i.e. the statistical convergence of the partition function $\mathcal{Z}(q, a)$. According to equation (3.22), $\mathcal{Z}(q, a)$ is the integral of $\mathcal{M}^q P_a(\mathcal{M})$. One can show that the monofractal self-similarity relationships yield the following rescaling properties (Arneodo, Decoster & Roux, 2000):

$$a^{-qH} \mathcal{M}^q P_a(\mathcal{M}) = \mathcal{F}_q(\mathcal{M}/a^H), \quad (3.31)$$

where \mathcal{F}_q are q -dependent functions that do not depend upon the scale parameter a . The validity of the above equation is addressed in Figure 3.9 for $q \in [-3, 4]$. The data collected at different scales actually collapse on a single distribution whose shape clearly

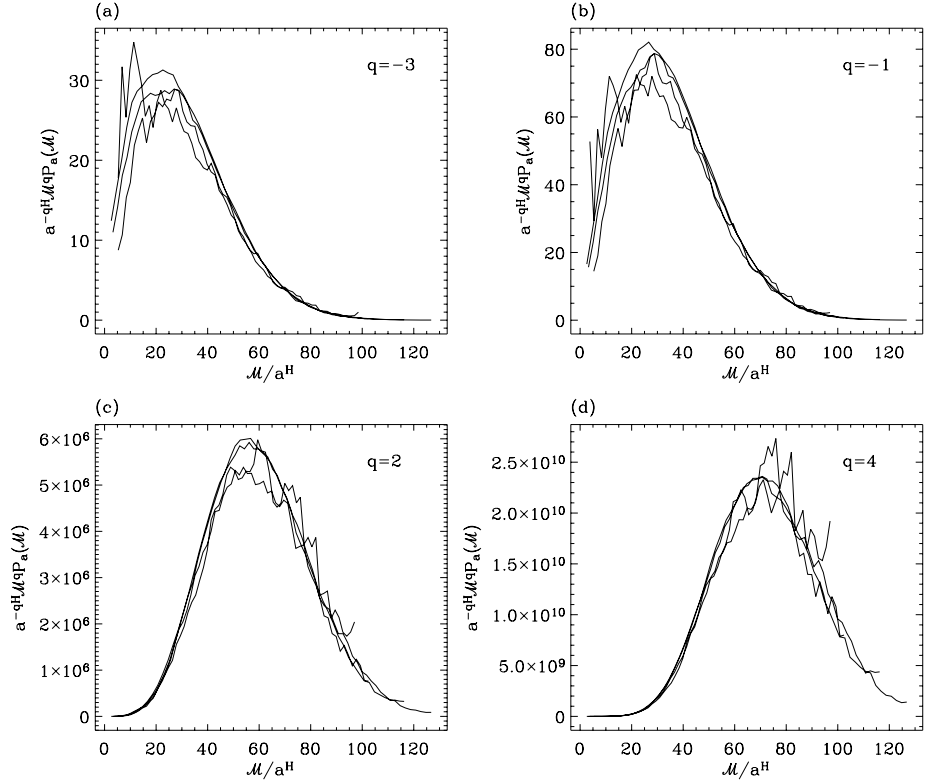


Figure 3.9: Pdfs of the WT MMMM coefficients of $B_{H=0.2}(\mathbf{x})$ as computed at different scales $a = 1, 2, 4, 8$ (in $\sigma_W = 13$ units). $a^{-qH} \mathcal{M}^q P_a(M)$ vs M/a^H for $q = -3$ (a), $q = -1$ (b), $q = 2$ (c), and $q = 4$ (d). Same 2D WTMM computations for $B_{H=0.2}(\mathbf{x})$ as in Figure 3.8.

depends upon q , in good agreement with equation (3.31). Because of the progressive lack of statistics when one increases a , the distributions obtained at the largest scales become more and more noisy (especially for large values of $|q|$). This means that the integral of these distributions, i.e. $\mathcal{Z}(q, a)$, is less and less accurately estimated at large scales. This explains the requirement of estimating the Hurst exponent of 2D fBm over a rather narrow range of scales at small scales (Audit et al., 2002).

The main difference between the characteristics of the synthetic surfaces presented in this section and those presented in Arneodo, Decoster & Roux (2000) is the choice of the Hurst exponent values. Indeed, our choice of $H = 0.2, 0.5$, and 0.8 is broader than the values chosen by Arneodo, Decoster & Roux (2000), i.e. $H = 1/3, 1/2$, and $2/3$. Other than the obvious requisite of taking different values than those previously published, the goal here was also to test the robustness of the 2D WTMM methodology

on “extreme” values. Indeed, the Hurst exponents $H = 0.2$ and $H = 0.8$ characterize surfaces that are respectively extremely anti-correlated and correlated. In the former case, finite-resolution effects could have prevented the method from characterizing adequately the Hurst exponent $H = 0.2$. Fluctuations corresponding to the smallest scales could be so great that the smallest scale available to the wavelet transform (i.e. σ_W) could not characterize them with adequate accuracy. For the case $H = 0.8$, finite-size effects could be to blame. Indeed, with such a large value of H , the structures in the synthetic surfaces could be so extremely correlated that the size of the images (1024×1024) could be insufficient to allow an adequate characterization.

Fortunately, it was shown above that the 2D WTMM method could easily deal with fBm surfaces with Hurst exponents at least as low as $H = 0.2$ and at least as high as $H = 0.8$. This is novel. The work presented in this thesis can thus be seen as an extension of the results presented in Arneodo, Decoster & Roux (2000).

3.4.2 Multifractal Rough Surfaces

In this section the 2D WTMM method is tested on synthetic multifractal rough surfaces generated with fractionally integrated singular cascades (FISC). For a thorough review, see Decoster, Roux & Arneodo (2000), where the so-called W-cascades are also the topic of a vast study. The FISC algorithm is used for its simplicity and is perfectly adequate to calibrate the 2D WTMM method. Surfaces generated with FISC are constructed in two steps. First, a specific singular multiplicative cascade model is generated, in our case, the so-called p -model ($0 \leq p \leq 0.5$) (or “binomial” model) (Meneveau & Sreenivasan, 1987). By choosing a value of p which is strictly less than $1/2$, an unequal quantity of mass is given to the successive generations of the multiplicative cascade, yielding the multifractal process. Second, the cascade is filtered in Fourier space (fractional integration) in order to transform the p -model multifractal measure into a multifractal function, which in our case is a rough surface.

Analytical results from Decoster, Roux & Arneodo (2000) yield the following theo-

retical multifractal properties. The $\tau(q)$ spectrum defined in Eq. 3.12 is given by

$$\tau(q) = -1 - q(1 - H^*) - \log_2(p^q + (1 - p)^q), \quad (3.32)$$

where H^* is the order of fractional integration. The power spectrum scaling exponent β is

$$\beta = \tau(2) + 4 = 1 + 2H^* - \log_2(2p^2 - 2p + 1). \quad (3.33)$$

And the lower and upper limits of the domain of the $D(h)$ singularity spectrum are

$$h_{\min} = H^* - 1 - \log_2(1 - p), \quad (3.34)$$

and

$$h_{\max} = H^* - 1 - \log_2(p). \quad (3.35)$$

Note that if $p = 1/2$, the process is monofractal and $h = H^*$. However, for any other value of $p \in [0, 1/2[$, a multifractal scaling is generated, where the Hölder exponent h fluctuates from point to point in the interval $h \in [h_{\min}, h_{\max}]$.

3.4.2.1 Fourier Analysis

The Fourier analysis of the central 512×512 part of $32 1024 \times 1024$ images with multifractal parameters $p = 0.38$ and $H^* = 0.42$ is presented in Figure 3.10. Figure 3.10a presents a contour plot of the 2D Fourier spectrum. The log-log plot of the 2D power spectrum shown in Figure 3.10b confirms the relation between the beta index and the Hurst exponent ($\beta = \tau(2) + 4$). It is important to note that the Fourier analysis alone cannot distinguish between monofractal and multifractal rough surfaces. In particular, a fractional Brownian surface $B_H(\mathbf{x})$ with the index $H = (\tau(2) + 2)/2$ displays the same power-law decay seen in Figure 3.10b.

3.4.2.2 Wavelet Analysis

We have wavelet transformed these $32 (1024 \times 1024)$ images generated with the FISC model with the above parameter values with a first-order analyzing wavelet (Figures 3.2a

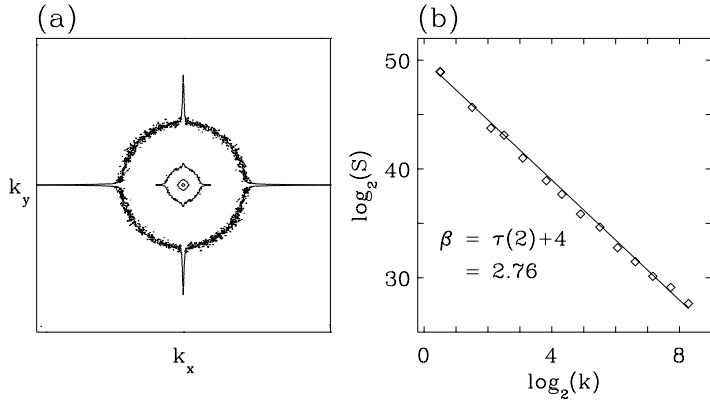


Figure 3.10: Fourier analysis of the 512×512 central part of a multifractal surface generated with the FISC model with parameters $p = 0.38$ and $H^* = 0.42$. (a) A contour plot of the 2D Fourier spectrum. (b) The power spectrum $S(|\mathbf{k}|)$ vs $|\mathbf{k}|$ in a logarithmic representation. The solid line corresponds to the power-law theoretical prediction.

and 3.2b), as well as with a third-order analyzing wavelet (Figures 3.2c and 3.2d). To avoid edge effects, only the 512×512 central part of the wavelet transform of each image is kept for analysis. Figure 3.11 illustrates the computation of the maxima chains and the WTMMM for an individual image at three different scales. In Figure 3.11b is shown the convolution of the original image (Fig. 3.11a) with the isotropic Gaussian smoothing filter ϕ_{Gau} (§3.3.1.1).

3.4.2.3 Numerical Computation of the $\tau(q)$ and $D(h)$ spectra

From the WTMMM defined on these maxima chains, one constructs the WT skeleton according to the procedure described in §3.3.1. From the WT skeletons of 32 (1024×1024) images like the one in Figure 3.11a, one computes the partition functions $\mathcal{Z}(q, a)$. Both the first-order (\diamond) and third-order (\square) wavelets were used. As shown in Figure 3.12a, when plotted versus the scale parameter a in a logarithmic representation, these partition functions display a rather impressive scaling behavior over a range of scales of about 4 octaves (i.e., $\sigma_W \lesssim a \lesssim 16\sigma_W$) when using the third-order wavelet. When processing to a linear regression fit of the data over the first four octaves, one gets the

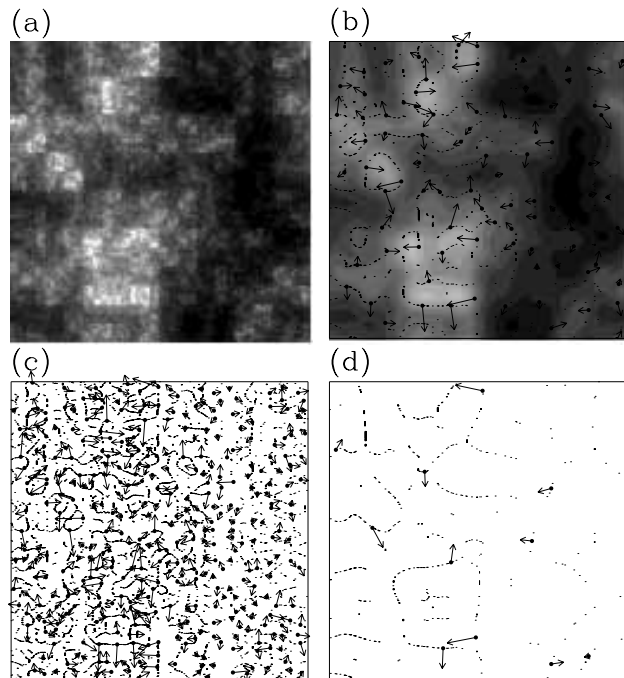


Figure 3.11: 2D wavelet transform analysis of a multifractal rough surface generated with the FISC model with parameter values $p = 0.38$ and $H^* = 0.42$. ψ is the first-order radially symmetric analyzing wavelet shown in Figure 3.2. (a) 32 grey-scale coding of the original (1024×1024) image. In (b) $a = 2^{2.9}\sigma_W$, (c) $a = 2^{1.9}\sigma_W$ and (d) $a = 2^{3.9}\sigma_W$ (in $\sigma_W = 13$ units), are shown the maxima chains and the WTMMM. In (b), the smoothed image $\phi_{\mathbf{b},a} * f$ is shown as a grey-scale coded background from white (min) to black (max).

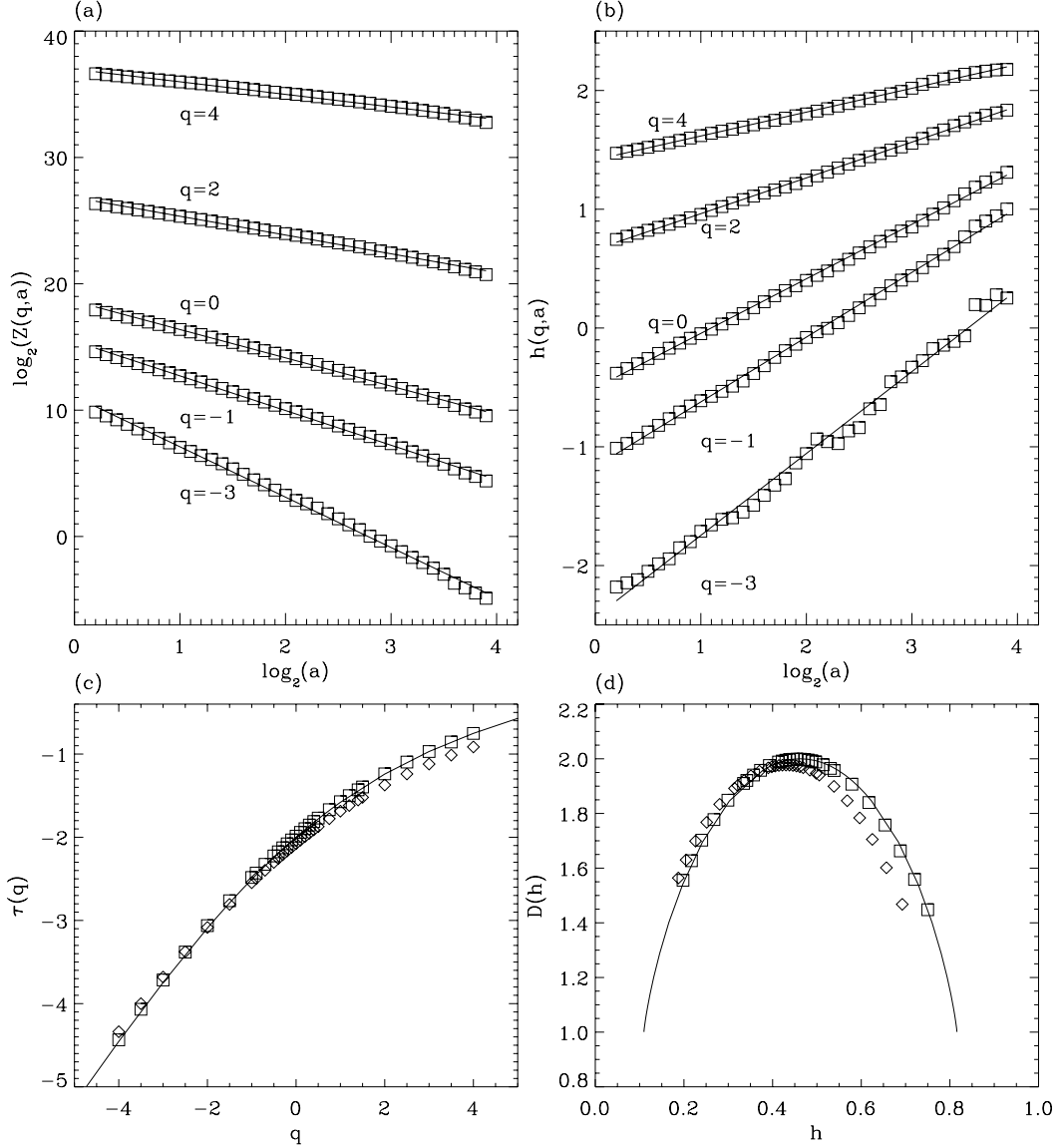


Figure 3.12: Determination of the $\tau(q)$ and $D(h)$ spectra of multifractal rough surfaces generated with the FISC model, using the 2D WTMM method. Results obtained using both the first-order (\diamond) and third-order (\square) radially symmetric analyzing wavelets shown in Figure 3.2. (a) $\log_2 \mathcal{Z}(q, a)$ vs $\log_2 a$; the solid lines correspond to linear regression fit of the data over the first four octaves. (b) $h(q, a)$ vs $\log_2 a$; the solid lines correspond to linear regression fit estimates of $h(q)$. (c) $\tau(q)$ vs q as obtained from linear regression fit of the data in (a) over the first four octaves. (d) $D(h)$ vs h as obtained from the scaling behavior of $D(q, a)$ vs $\log_2 a$ (Eq. (3.21)); the symbols have the same meaning as in (c). In (c) and (d), the solid lines represent the theoretical spectra. These results correspond to an averaging over 32 (1024×1024) images. a is expressed in σ_W units, where $\sigma_W = 13$ pixels.

$\tau(q)$ spectrum (\diamond and \square) shown in Figure 3.12c. For the range of q values where scaling is operating, the numerical data are in remarkable agreement with the theoretical nonlinear $\tau(q)$ spectrum given by equation (3.32) when using the third-order wavelet. Similar quantitative agreement is observed on the $D(h)$ singularity spectrum in Figure 3.12d. The limitations of the first-order wavelet are discussed in Decoster, Roux & Arneodo (2000) and Roux, Arneodo & Decoster (2000). In Figure 3.12b are reported the results for the expectation values $h(q, a)$ (Eq. (3.19)) vs $\log_2 a$; it is clear on this figure that the slope $h(q)$ depends upon q , the hallmark of multifractal scaling. From equations (3.34) and (3.35), the multifractal rough surfaces under study display intermittent fluctuations corresponding to Hölder exponent values ranging from $h_{\min} = 0.110$ to $h_{\max} = 0.816$. Unfortunately, to capture the strongest and weakest singularities, one needs to compute the $\tau(q)$ spectrum for very large values of $|q|$. This requires the processing of many more images of much larger size. However, one can readily see that the structure function approach, for which negative q values are not defined, could only characterize the left half of the parabola in Figure 3.12d.

3.4.2.4 Probability Density Functions

In Figure 3.13 are shown the pdfs $P_a(\mathcal{M})$ and $P_a(\mathcal{A})$, computed for four different values of the scale parameter a . Figure 3.13a shows that $P_a(\mathcal{M})$ is not a Gaussian, but decreases fast to zero at zero, as seen for the monofractal fBm surfaces in §3.4.1. The corresponding pdfs $P_a(\mathcal{A})$ are represented in Figure 3.13b. $P_a(\mathcal{A})$ clearly does not evolve across scales. However, the curves are clearly peaked at 0 , $\pm\pi/2$, and $\pm\pi$. This behavior is explained by the square lattice anisotropy underlying the 2D wavelet tree decomposition. Again, larger images, in larger numbers, would be needed to minimize this behavior. With large statistical quantities, the curves shown in Figure 3.13b become flat like those shown in Figure 3.8b.

The difference between the results presented in this section and those presented in the first part of Decoster, Roux & Arneodo (2000) lies in our choice of the parameters $p = 0.38$ and $H^* = 0.42$, where these authors had used $p = 0.32$ and $H^* = 0.638$. Again, as seen in §3.4.1, the choice of different parameters was not only warranted by a need to

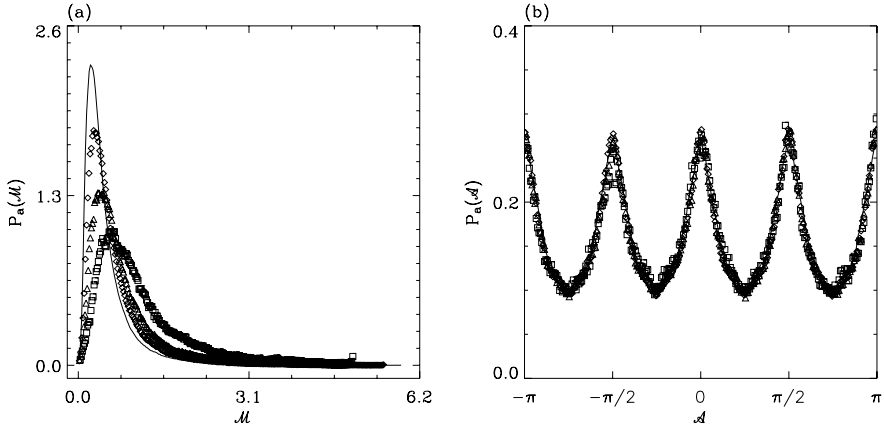


Figure 3.13: Pdfs of the WT MMMM coefficients of synthetic multifractal rough surfaces generated with the FISC model ($p = 0.38$ and $H^* = 0.42$). (a) $P_a(\mathcal{M})$ vs \mathcal{M} . (b) $P_a(\mathcal{A})$ vs \mathcal{A} . ψ is a first-order radially symmetric analyzing wavelet. Four different scales $a = 1$ (full line), 2 (\diamond), 4 (\triangle), 8 (\square) (in $\sigma_W = 13$ units) are shown. These results correspond to averaging over 32 (1024 \times 1024) images.

choose arbitrarily different values. The goal here was to choose values that correspond to h_{\min} and h_{\max} which are both in the interval $[0, 1]$. Indeed, one can easily see that with $p = 0.32$ and $H^* = 0.638$, the corresponding values for h_{\min} and h_{\max} are respectively 0.194 ($\in [0, 1]$) and 1.282 (> 1) (Decoster, Roux & Arneodo, 2000) and with $p = 0.38$ and $H^* = 0.42$, the corresponding values for h_{\min} and h_{\max} are respectively 0.110 and 0.816 (both of which are $\in [0, 1]$; this section).

Now, why is it important to choose parameters p and H^* that yield corresponding values of h_{\min} and h_{\max} below or above 1? The answer lies in the choice of the analyzing wavelets. Indeed, only the third-order wavelet is a priori capable of characterizing singularities with a Hölder exponent greater than 1 (but less than 3). Decoster, Roux & Arneodo (2000) used this argumentation to justify the need to use the third-order wavelet to obtain a better characterization of their multifractal synthetic surfaces (which were also generated with the FISC algorithm, obviously). However, for the case presented in this paper, one can clearly see that even though both h_{\min} and h_{\max} are within the interval $[0, 1]$, the use of only the first-order wavelet was not sufficient. Too many oscillatory behaviors, most probably caused by the square lattice anisotropy of the underlying multiplicative cascade, prevented the first-order wavelet to provide an adequate

characterization of these surfaces. It was thus shown that the more stable third-order analyzing wavelet yielded more accurate results. Again, this contribution has been put forward from the work of this thesis.

3.4.3 Anisotropic Surfaces

Standard 2D fBm models are not always sufficient in fully characterizing real world surfaces (Mandelbrot, 1977, 1982; Feder, 1988; West, 1990; Arneodo, Decoster & Roux, 2000). As seen in the previous section, allowing spatial fluctuations in the local Hölder regularity, i.e., multifractality, gives more flexibility to these models. However, another limitation is the isotropy, which is rather idealistic in the case of real textures. In this section we address the issue of anisotropic rough surfaces (Schertzer & Lovejoy, 1985, 1987; Peitgen & Saupe, 1988; Schmittbuhl, Violette & Roux, 1995; Schertzer et al., 1997).

A natural way of introducing some anisotropy in the fast Fourier transform filtering surface synthesis method is to use different fractional integration orders in two orthogonal directions of space. However, although the concept of 2D anisotropic fBm is well-defined mathematically, it has never been validated numerically (to the best of our knowledge). For example, Makse et al. (1996) use a Fourier filtering method, where the correlation function was slightly changed in order to account for long-range correlations ($0.5 < H < 1$). This method not only fails numerically, but one can show that it also fails mathematically (for theoretical images of infinite size). All other fBm-based methods tested produced negative or inconclusive results, at least numerically.

In an attempt to palliate the drawbacks of the 2D anisotropic fBm, recent progress has been accomplished in the study of fractional Brownian “sheets” (fBs), where the main difference between the two lies in the homogeneity of the initial conditions of the random process. For a technical description, see Pesquet-Popescu & Lévy Véhel (2002) and Montseny (2004).

We introduce the exponents H_x and H_y to describe the global Hurst regularity in the

x and y directions respectively⁸. An anisotropic surface is thus described as a self-affine two-dimensional function where $H_x \neq H_y$.

Two methods are used here to estimate the individual Hurst exponents H_x and H_y . The first method consists in a simple 1D Fourier analysis of x -directional and y -directional cuts (estimation of the directional power spectral indices, $\beta_x = 2H_x + 1$ and $\beta_y = 2H_y + 1$), and the second, explained below in §3.4.3.4, consists in the analysis of the horizontal and vertical wavelet transform components, T_{ψ_1} and T_{ψ_2} (see §3.3.1.1).

3.4.3.1 Fourier Analysis

We have generated 32 (1024×1024) images (fBs) of $B_{H_x=0.10, H_y=0.50}(\mathbf{x})$ where the regularity of the x -direction, $H_x = 0.10$, differs from the regularity of the y -direction, $H_y = 0.50$. The reader is invited to look ahead to Figure 3.15a where such an image is presented. The Fourier analysis is presented in Figure 3.14. Figure 3.14a presents a contour plot of the 2D Fourier spectrum, where the anisotropic signature is translated as a preference in the x direction in the $k_x - k_y$ plane. The log-log plot of the 2D power spectrum shown in Figure 3.14b confirms the relation between the beta index and the minimal Hurst exponent $H = \min(H_x, H_y) = H_x$, i.e. $\beta = 2H_x + 2$. The actual value of the fitted slope is given by $\beta = 2.261 \pm 0.054^9$, a slight over-estimation. The individual spectral indices calculated from the 1D cuts (Fig. 3.14c and 3.14d) are $\beta_x = 1.224 \pm 0.012$ and $\beta_y = 1.965 \pm 0.006$. These values are also slightly over (resp. under) estimated, which is expected for such a large difference between the theoretical values $\beta_x = 1.20$ and $\beta_y = 2.00$ (Montseny, 2004). The departure of the calculated values from the theoretical $\beta_x = 1.20$ and $\beta_y = 2.00$ (i.e. the values that were entered in the algorithm) can be seen in Figures 3.14c and 3.14d.

⁸Only the horizontal (x) and vertical (y) directions are considered here to avoid over-crowding this text. More generally, anisotropic structure can be defined in any direction, where the individual Hurst exponents would be defined as H_θ and $H_{\theta+\pi/2}$

⁹The presented uncertainties for β , β_x , and β_y correspond to the χ^2 errors from the fitted slopes.

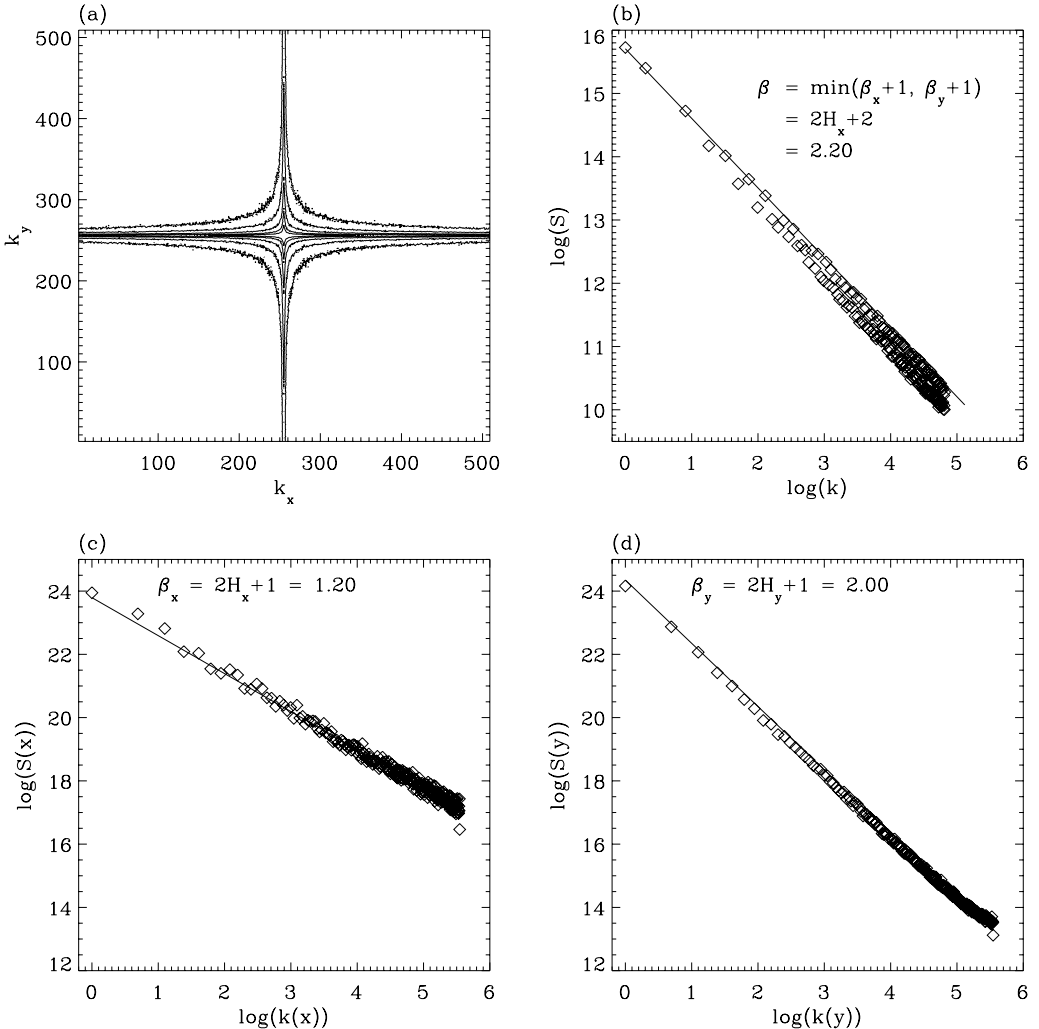


Figure 3.14: Fourier analysis of the 512×512 central part of the simulated anisotropic surfaces $B_{H_x=0.10, H_y=0.50}(\mathbf{x})$. (a) A contour plot of $\ln |\hat{B}_{H_x=0.10, H_y=0.50}(\mathbf{k})|$. (b) The power spectrum $S(|\mathbf{k}|)$ vs $|\mathbf{k}|$ in a logarithmic representation. (c) The averaged power spectra of the one-dimensional x -cuts. (d) The averaged power spectra of the one-dimensional y -cuts. The solid lines correspond to the power-law theoretical predictions in each case.

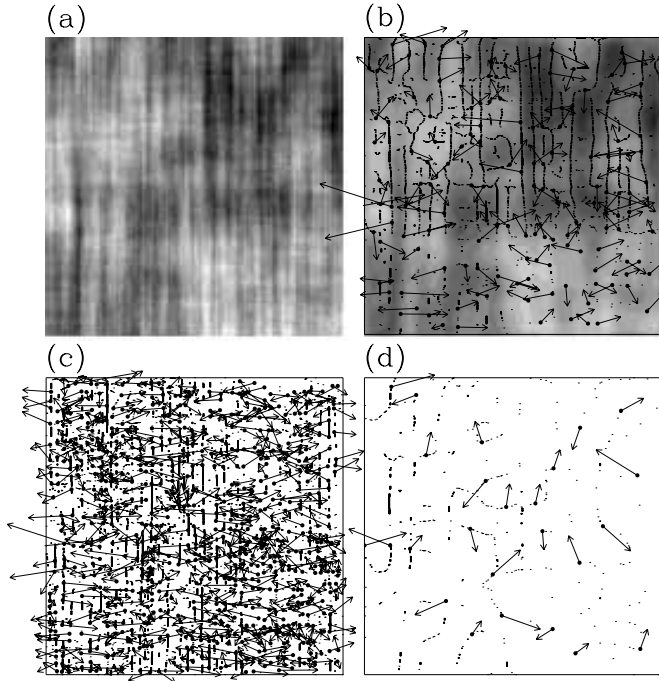


Figure 3.15: 2D wavelet transform analysis of $B_{H_x=0.10, H_y=0.50}(\mathbf{x})$. ψ is a first-order radially symmetric analyzing function (see Fig. 3.2). (a) 32 grey-scale coding of the original image. In (b) $a = 2^{2.9}\sigma_W$, (c) $a = 2^{1.9}\sigma_W$ and (d) $a = 2^{3.9}\sigma_W$, are shown the maxima chains; the local maxima of \mathcal{M}_ψ along these chains are indicated by (\bullet) from which originate an arrow whose length is proportional to \mathcal{M}_ψ and its direction (with respect to the x -axis) is given by \mathcal{A}_ψ . In (b), the smoothed image $\phi_{\mathbf{b},a} * B_{H_x=0.10, H_y=0.50}$ is shown as a grey-scale coded background from white (min) to black (max).

3.4.3.2 Wavelet Analysis

We have wavelet transformed these 32 (1024×1024) images of $B_{H_x=0.10, H_y=0.50}(\mathbf{x})$ with a first-order analyzing wavelet (Figures 3.2a and 3.2b). From a visual inspection of Figure 3.15, one can see that the maxima chains show a vertical tendency, which becomes more and more pronounced when going to small values of a . In the meantime, the WTMM proliferate like a^{-2} , with a characteristic evolution of the corresponding arrows towards a general alignment to the x -direction, i.e., \mathcal{A}_ψ converges to 0 and $\pm\pi$. There are a few horizontal maxima chains, especially at large scales which follow the square lattice anisotropy similar to the multifractal surfaces (§3.4.2), a phenomenon caused by the construction algorithm. The analysis of larger images, in larger numbers would eliminate this behavior.

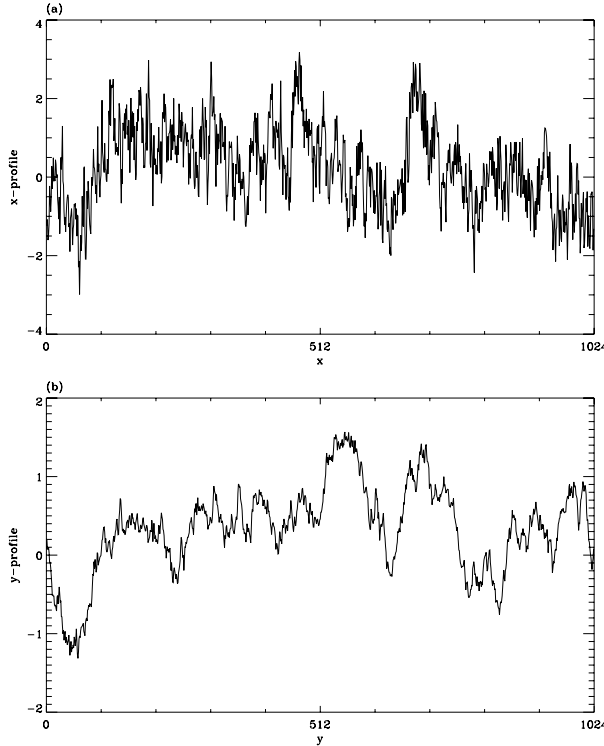


Figure 3.16: One-dimensional cuts taken from one realization of $B_{H_x=0.10, H_y=0.50}(\mathbf{x})$ (Fig. 3.15a). (a) x -profile. (b) y -profile.

A visual inspection of the x and y -profiles presented in Figure 3.16 (obtained from Figure 3.15a confirms that the “roughness” is greater in the x direction (where $H_x = 0.10$) than in the y direction (where $H_y = 0.50$).

3.4.3.3 Numerical Computation of the $\tau(q)$ and $D(h)$ spectra

In Figure 3.17 are reported the results of the computation of the $\tau(q)$ and $D(h)$ spectra using the 2D WTMM method described in §3.3.1. As shown in Figure 3.17a, the partition function $\mathcal{Z}(q, a)$ over 32 (1024 x 1024) images, displays a well defined scaling behavior over the range of scales $1 \leq a \leq 6$ (in σ_W units) when using the first-order wavelet. A linear regression fit of the data for $-4 \leq q \leq 4$ yields the numerical $\tau(q)$ spectrum shown in Figure 3.17c. All the data points fall on a straight line of slope $H_x = 0.12$, which is in agreement with the estimated β_x above (§3.4.3.1) and gives a confirmation that the departure from the theoretical values was indeed caused by the

construction process. Note that there is an indication that the slope of the expectation values, $h(q, a)$ correspond to the global Hurst exponent, $H = H_y$ at the largest scales (as can be seen from Figure 3.17b). This is especially true for negative values of q .

When completing this analysis by computing $D(q)$ form the scaling behavior of $D(q, a)$ (Eq. (3.21)), one gets to the conclusion that the $D(h)$ singularity spectrum reduces to a single point $D(h = 0.12) = 1.96 \pm 0.04$ ($D(h) = -\infty$ elsewhere). These results demonstrate that, up to finite-size effects, the 2D WTMM method is powerful enough to account quantitatively for the homogeneous (monofractal) anisotropic scaling properties of rough surfaces, where the minimal directional Hurst exponent is detected.

3.4.3.4 Probability Density Functions

In Figure 3.18 are reported the results of the computation of the pdfs $\mathcal{P}_a(\mathcal{M})$ and $\mathcal{P}_a(\mathcal{A})$, from the same set of 32 (1024 x 1024) images of anisotropic rough surfaces ($B_{H_x=0.10, H_y=0.50}(\mathbf{x})$). $\mathcal{P}_a(\mathcal{A})$ becomes more and more sharply peaked (Fig. 3.18b) at two values $\mathcal{A} = 0$ and $\pm\pi$, which correspond to the x -direction associated with the smallest scaling exponent $H = \min(H_x, H_y) = H_x = 0.10$. There are small peaks at $\pm\pi/2$ which is caused by the square lattice anisotropy of the simulated surfaces.

When one keeps zooming with our mathematical microscope, it turns out that what is happening in the x -direction of the rough surfaces under study, ultimately governs their scale invariance properties, which explains why both global analysis tools above (the global β and H) yielded the minimal value of the directional roughness exponents (resp. β_x and H_x).

In fact, the two components of the 2D continuous wavelet transform behave as:

$$T_{\psi_1}[f](\mathbf{b}, a) \sim a^{H_x}, \quad (3.36)$$

and

$$T_{\psi_2}[f](\mathbf{b}, a) \sim a^{H_y}, \quad (3.37)$$

and this, independently of the specific spatial location \mathbf{b} . As shown in Figure 3.19, one recovers this anisotropic scaling behavior on the WTMMM. Indeed, when restricting the

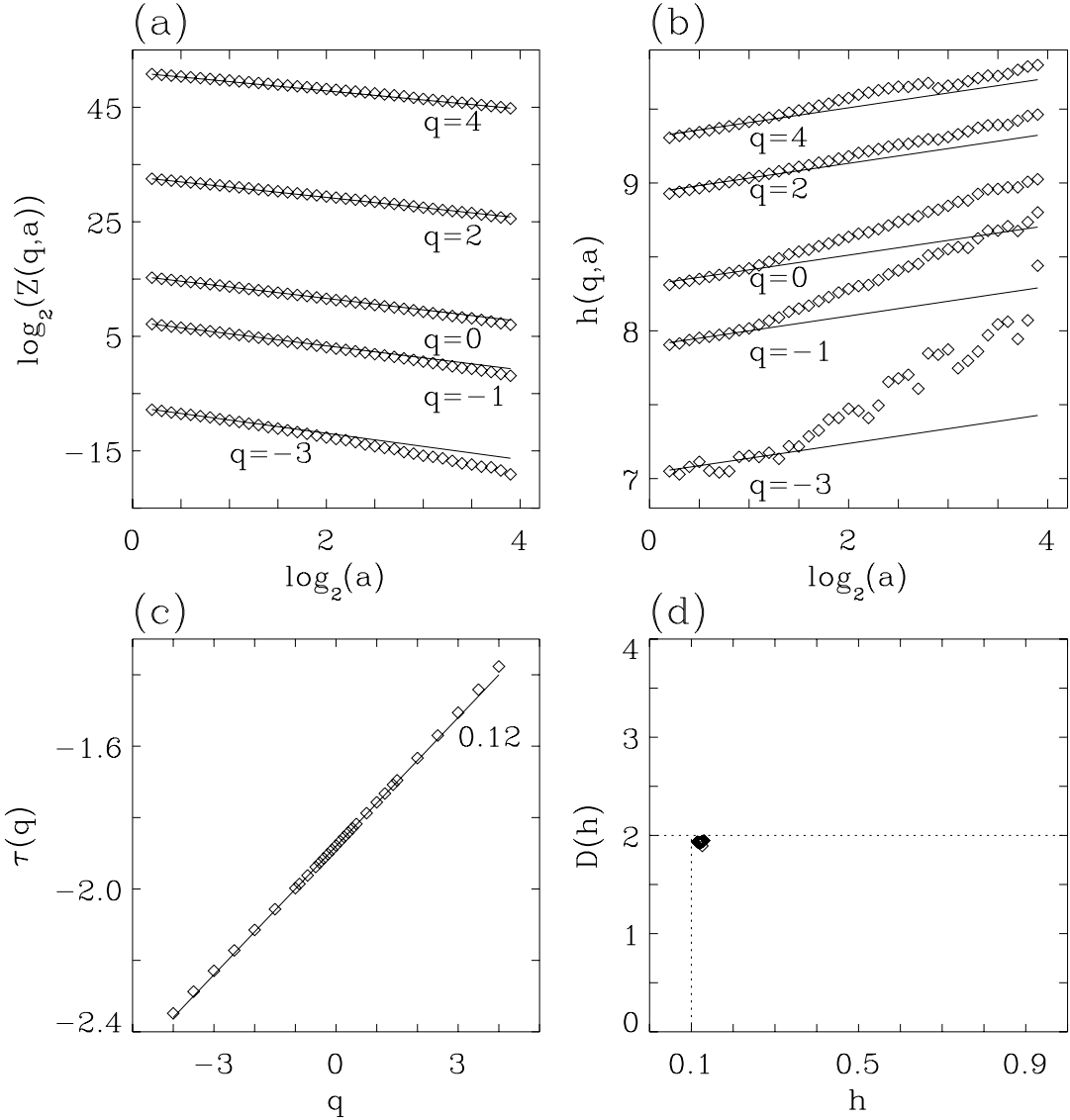


Figure 3.17: Determination of the $\tau(q)$ and $D(h)$ spectra of the fBm $B_{H_x=0.10, H_y=0.50}(\mathbf{x})$ with the 2D WTMM method. (a) $\log_2 Z(q, a)$ vs $\log_2 a$; the solid lines correspond to the theoretical predictions $\tau(q) = qH - 2$ (Eq. (3.27)) with $H = \min(H_x, H_y) = 0.10$. (b) $h(q, a)$ vs $\log_2 a$; the solid lines correspond to the theoretical slope $H = \min(H_x, H_y) = 0.10$. (c) $\tau(q)$ vs q ; the solid line corresponds to a linear regression fit estimate of H . (d) $D(h)$ vs h as obtained from the scaling behavior of $D(q, a)$ vs $\log_2 a$ (Eq. (3.21)). First-order analyzing wavelets. These results correspond to an averaging over 32 (1024×1024) simulated surfaces. a is expressed in $\sigma_W = 13$ units.

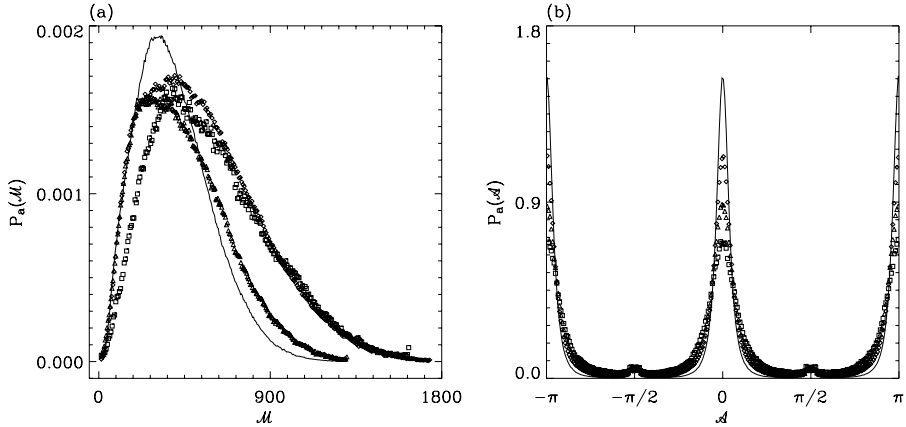


Figure 3.18: Pdfs of the WTMM coefficients of $B_{H_x=0.10, H_y=0.50}(\mathbf{x})$ as computed at different scales $a = 1$ (full line), 2 (\diamond), 4 (\triangle), 8 (\square) (in $\sigma_W = 13$ units). (a) $P_a(\mathcal{M})$ vs \mathcal{M} . (b) $P_a(\mathcal{A})$ vs \mathcal{A} . ψ is the first-order analyzing wavelet shown in Figure 3.2. These results correspond to averaging over 32 (1024×1024) simulated surfaces.

computation of the pdfs of T_{ψ_1} and T_{ψ_2} to the wavelet transform skeleton, one obtains the following remarkable self-similarity properties:

$$P\left(T_{\psi_1}[f](\mathcal{L}(a))\right) = \mathcal{P}_1\left(T_{\psi_1}[f](\mathcal{L}(a))/a^{H_x}\right), \quad (3.38)$$

and

$$P\left(T_{\psi_2}[f](\mathcal{L}(a))\right) = \mathcal{P}_2\left(T_{\psi_2}[f](\mathcal{L}(a))/a^{H_y}\right), \quad (3.39)$$

where \mathcal{P}_1 and \mathcal{P}_2 are two universal functions that do not depend upon the scale parameter a . One thus finds that the local Hölder regularity is governed by $H_x = 0.10 = \min(0.10, 0.50) = \min(H_x, H_y)$. These results corroborate the conclusions derived from the computation of the $\tau(q)$ and $D(h)$ spectra in Figure 3.17. The anisotropic random surface generated in Figure 3.15a, is a homogeneous (monofractal) rough surface which is invariant with respect to anisotropic dilations. Its local Hölder regularity is the same at each spatial point and is governed by the scaling behavior properties in the direction of minimal regularity. To conclude, let us emphasize that, beyond its ability to characterize statistically the Hölder regularity properties, the 2D WTMM method also accounts for possible departure from isotropic scaling. This characterization of directional regularity for $H_x, H_y \in [0, 1]$ is novel. In the case under study in this section, both scaling exponents $H_x = 0.11$ and $H_y = 0.49$ have been numerically estimated with high accuracy, as compared to the results obtained from the Fourier analysis. One can thus conclude that

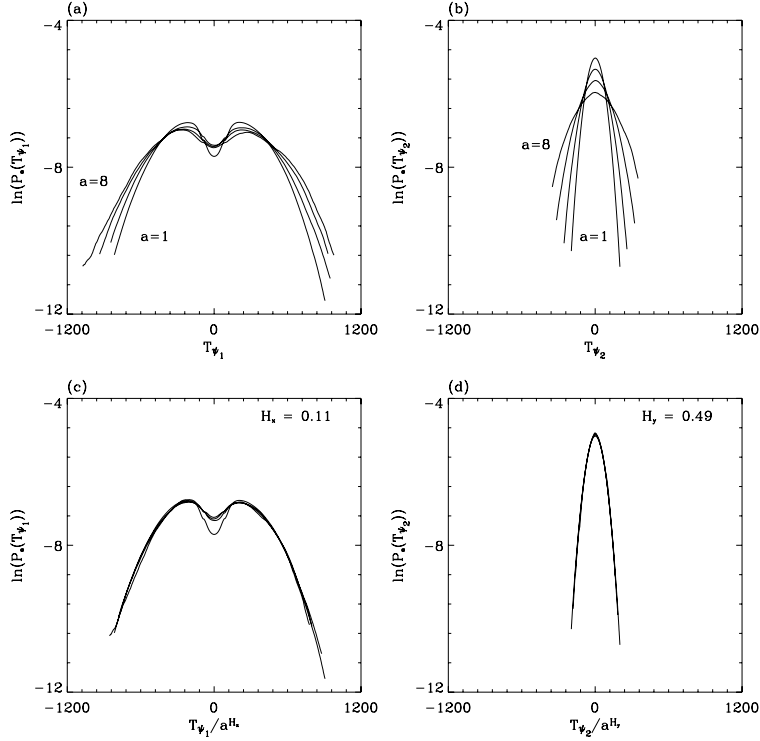


Figure 3.19: Pdfs of the x and y components of the WTMM coefficients of the surfaces $B_{H_x=0.10, H_y=0.50}(\mathbf{x})$ as computed with the first-order wavelet at the scales $a = 1, 2, 4$, and 8 (in $\sigma_W = 13$ units). (a) $\ln(P_a(T_{\psi_1}))$ vs T_{ψ_1} ; (b) $\ln(P_a(T_{\psi_2}))$ vs T_{ψ_2} . In (c) and (d), the pdfs are rescaled by a^{H_x} and a^{H_y} respectively.

the fBs algorithm reaches an acceptable sensitivity limit when generating anisotropic surfaces of at most $|H_y - H_x| = 0.40$.

3.4.3.5 Sensitivity test

The sensitivity of our two techniques (directional analyses of the x and y components for the Fourier analysis and wavelet transform) must now be tested for smaller values of $|H_y - H_x|$. In what follows, a quick overview of a supplemental study will demonstrate more precisely the limitations of both techniques.

Two sets of 32 (1024×1024) anisotropic surfaces (fBs) were generated, with $(H_x, H_y) =$

$(0.41, 0.44)$ and $(H_x, H_y) = (0.45, 0.52)$ respectively. The Fourier analysis of both types of surfaces ($B_{H_x=0.41, H_y=0.44}(\mathbf{x})$ and $B_{H_x=0.45, H_y=0.52}(\mathbf{x})$) are presented in Figures 3.20 and 3.21. The individual power spectral exponents are respectively $\beta_x = 1.821 \pm 0.012$, $\beta_y = 1.885 \pm 0.011$ and $\beta_x = 1.899 \pm 0.019$, $\beta_y = 2.007 \pm 0.020$, while the global (2D) spectral exponents are $\beta = 2.835 \pm 0.029$ and $\beta = 2.902 \pm 0.031$. Note that the anisotropic signature of these surfaces does not show in Figures 3.20a and 3.21a.

The wavelet analysis shown in Figures 3.22 and 3.23 does not allow one to discriminate the preference of the direction of maxima chains (the square lattice anisotropy dominates), except, perhaps at the smallest scales shown for $B_{H_x=0.45, H_y=0.52}(\mathbf{x})$ (Fig. 3.23c).

As shown in Figures 3.24 and 3.25, the partition functions $\mathcal{Z}(q, a)$ and expectation values $h(q, a)$ yield the $\tau(q)$ and $D(h)$ spectra which are in good agreement with the theoretical values. From the $\tau(q)$ spectra, one obtains $H = 0.40 \pm 0.01$ and $H = 0.45 \pm 0.01$ respectively, where both values correspond to the minimal Hurst exponent ($H = \min(H_x, H_y)$). The $D(h)$ singularity spectra reduce to single points: $D(h = 0.40) = 2.04 \pm 0.04$ and $D(h = 0.45) = 1.98 \pm 0.04$.

The probability density functions shown in Figures 3.26 and 3.27 behave as expected, i.e., $P_a(\mathcal{M})$ is not a Gaussian, but decreases fast to zero at zero, and $P_a(\mathcal{A})$ is peaked at 0 and $\pm\pi$. The peaks at $\pm\pi/2$ are caused by the square lattice anisotropy discussed above (§3.4.3.4).

The original and rescaled pdfs of the individual components of the wavelet transform are shown in Figures 3.28 and 3.29. The individual Hurst exponents are recovered with very high accuracy. Indeed, one finds $H_x = 0.41 \pm 0.01$ and $H_y = 0.44 \pm 0.01$ for $B_{H_x=0.41, H_y=0.44}(\mathbf{x})$, and $H_x = 0.45 \pm 0.01$ and $H_y = 0.52 \pm 0.01$ for $B_{H_x=0.45, H_y=0.52}(\mathbf{x})$. This quick study shows that our techniques are capable of analyzing anisotropic surfaces with $|H_y - H_x|$ down to at least 0.03.

Figure 3.30, which corresponds to the rescaled pdfs of T_{ψ_1} by different neighboring values of H_x , confirms the choice of the uncertainty, $\sigma = 0.01$.

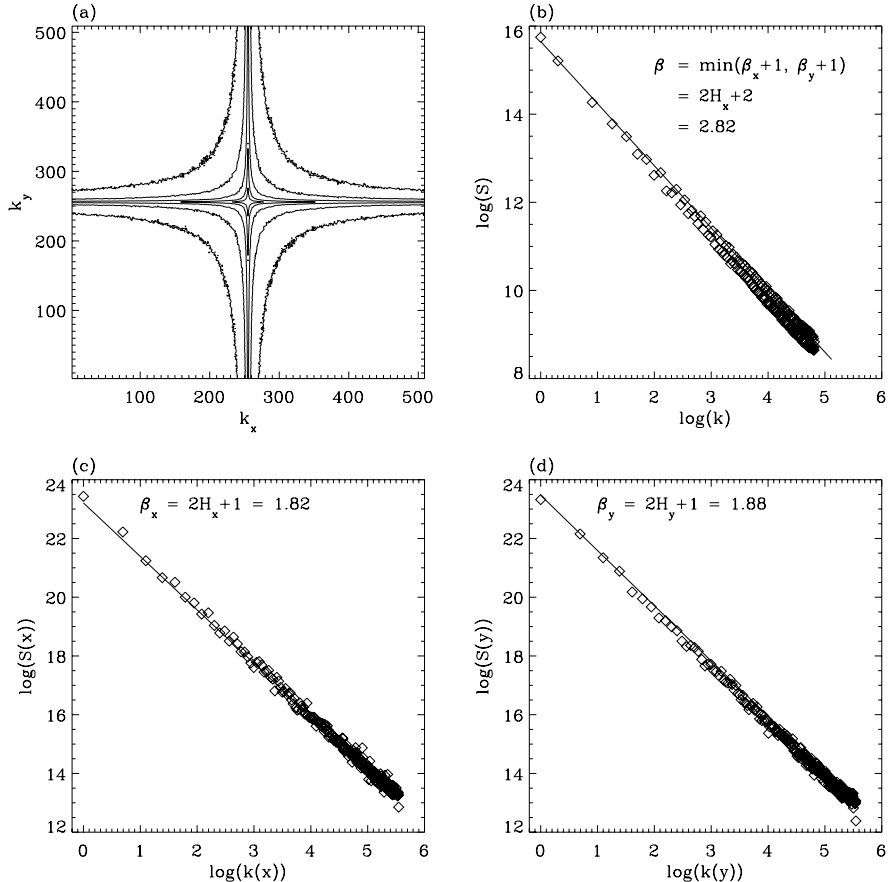


Figure 3.20: Fourier analysis of the 512×512 central part of the simulated anisotropic surfaces $B_{H_x=0.41, H_y=0.44}(\mathbf{x})$. (a) A contour plot of $\ln |\hat{B}_{H_x=0.41, H_y=0.44}(\mathbf{k})|$. (b) The power spectrum $S(|\mathbf{k}|)$ vs $|\mathbf{k}|$ in a logarithmic representation. (c) The averaged power spectra of the one-dimensional x -cuts. (d) The averaged power spectra of the one-dimensional y -cuts. The solid lines correspond to the power-law theoretical predictions in each case.

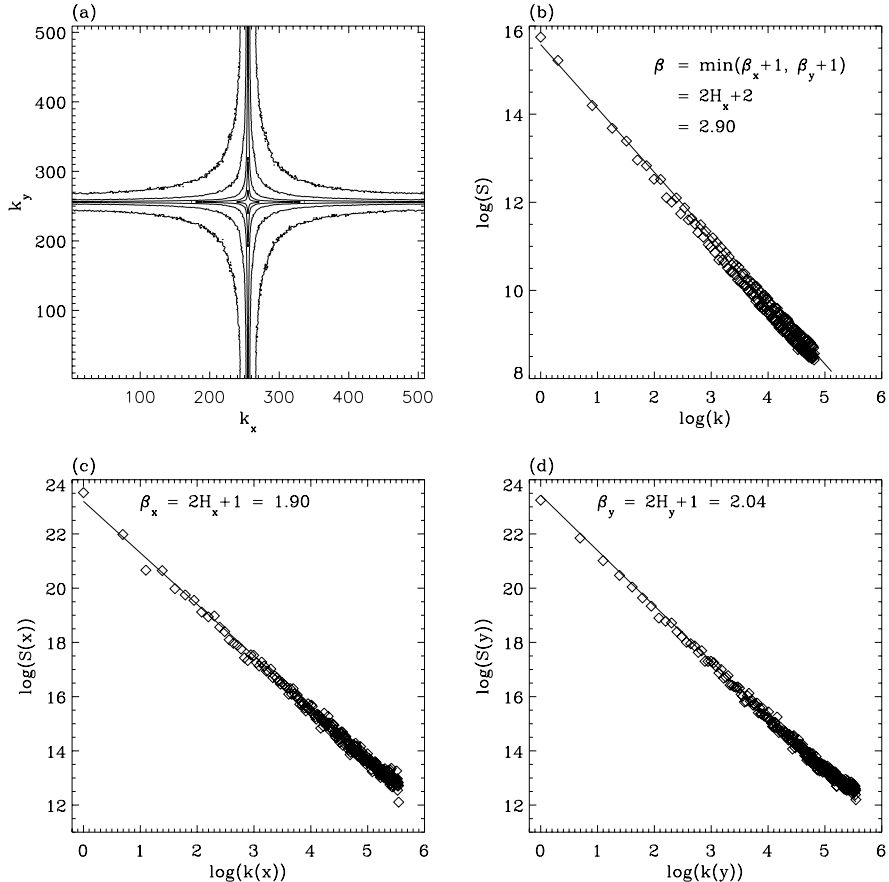


Figure 3.21: Fourier analysis of the 512×512 central part of the simulated anisotropic surfaces $B_{H_x=0.45, H_y=0.52}(\mathbf{x})$. (a) A contour plot of $\ln |\hat{B}_{H_x=0.45, H_y=0.52}(\mathbf{k})|$. (b) The power spectrum $S(|\mathbf{k}|)$ vs $|\mathbf{k}|$ in a logarithmic representation. (c) The averaged power spectra of the one-dimensional x -cuts. (d) The averaged power spectra of the one-dimensional y -cuts. The solid lines correspond to the power-law theoretical predictions in each case.

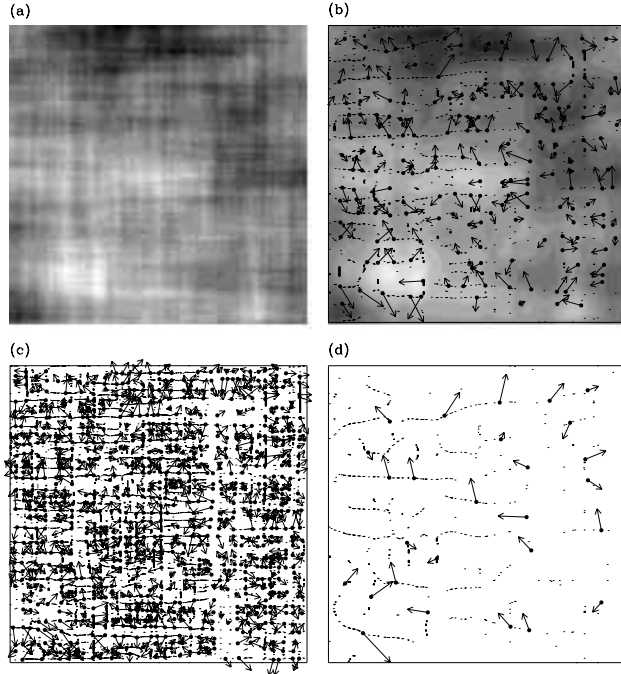


Figure 3.22: 2D wavelet transform analysis of $B_{H_x=0.41, H_y=0.44}(\mathbf{x})$. ψ is a first-order radially symmetric analyzing function (see Fig. 3.2). (a) 32 grey-scale coding of the original image. In (b) $a = 2^{2.9}\sigma_W$, (c) $a = 2^{1.9}\sigma_W$ and (d) $a = 2^{3.9}\sigma_W$, are shown the maxima chains; the local maxima of \mathcal{M}_ψ along these chains are indicated by (•) from which originate an arrow whose length is proportional to \mathcal{M}_ψ and its direction (with respect to the x -axis) is given by \mathcal{A}_ψ . In (b), the smoothed image $\phi_{\mathbf{b},a} * B_{H_x=0.41, H_y=0.44}$ is shown as a grey-scale coded background from white (min) to black (max).

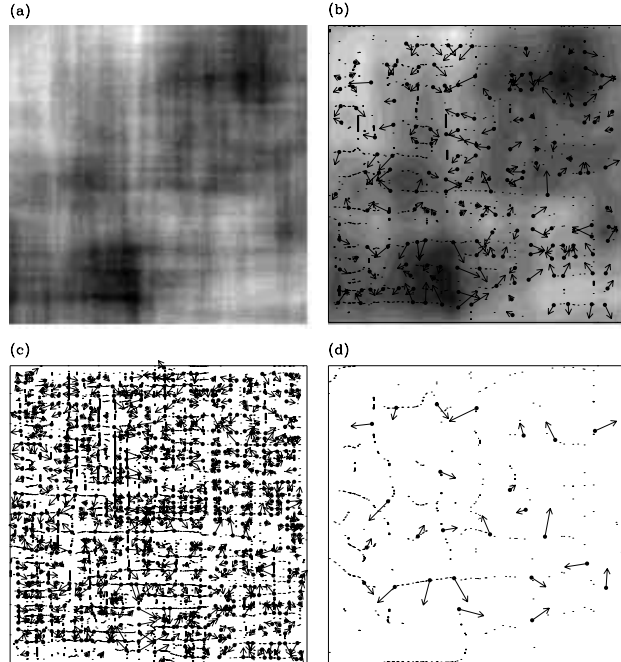


Figure 3.23: 2D wavelet transform analysis of $B_{H_x=0.45, H_y=0.52}(\mathbf{x})$. ψ is a first-order radially symmetric analyzing function (see Fig. 3.2). (a) 32 grey-scale coding of the original image. In (b) $a = 2^{2.9}\sigma_W$, (c) $a = 2^{1.9}\sigma_W$ and (d) $a = 2^{3.9}\sigma_W$, are shown the maxima chains; the local maxima of \mathcal{M}_ψ along these chains are indicated by (\bullet) from which originate an arrow whose length is proportional to \mathcal{M}_ψ and its direction (with respect to the x -axis) is given by \mathcal{A}_ψ . In (b), the smoothed image $\phi_{\mathbf{b},a} * B_{H_x=0.45, H_y=0.52}$ is shown as a grey-scale coded background from white (min) to black (max).

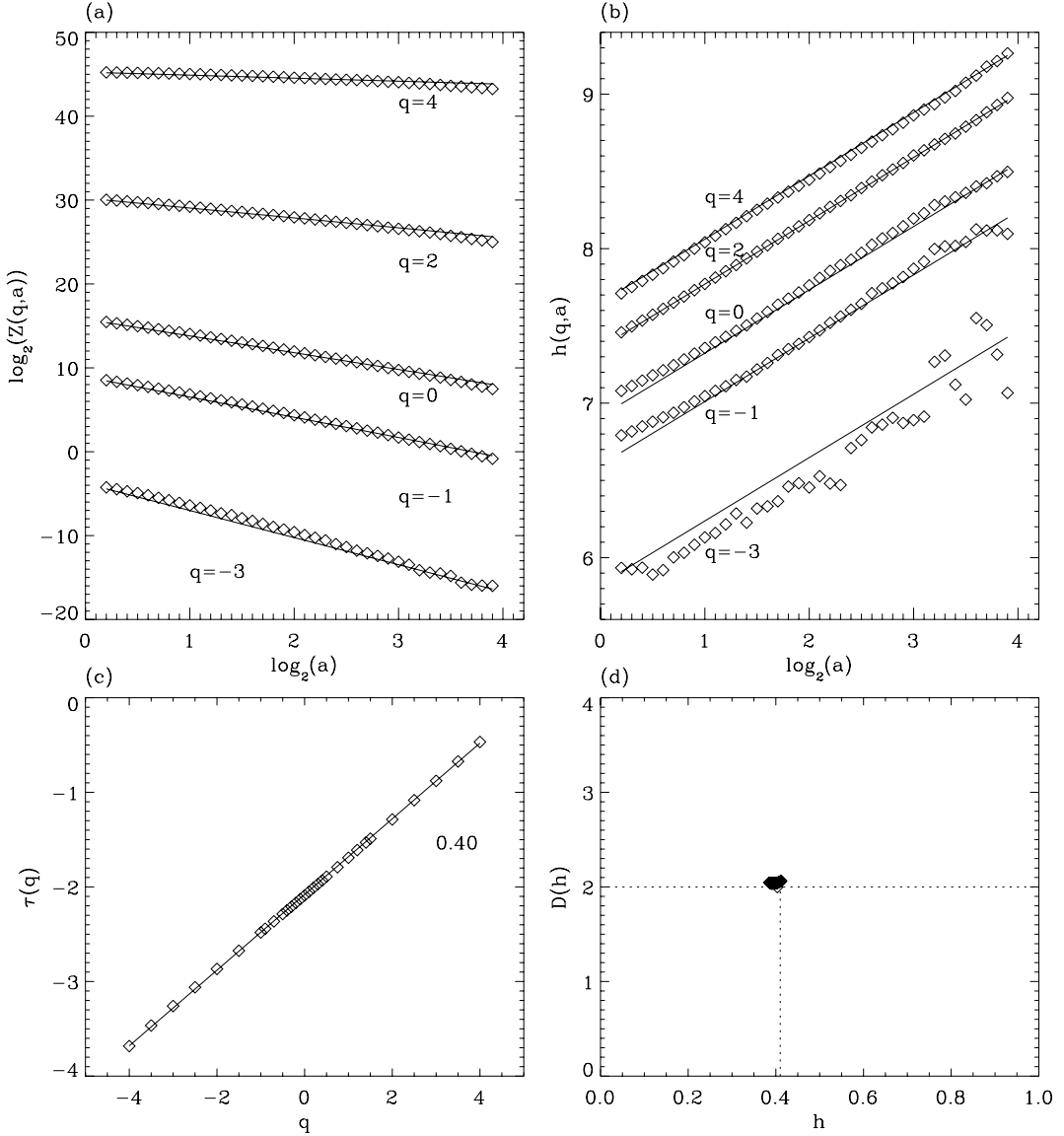


Figure 3.24: Determination of the $\tau(q)$ and $D(h)$ spectra of the fBs $B_{H_x=0.41, H_y=0.44}(x)$ with the 2D WTMM method. (a) $\log_2 \mathcal{Z}(q, a)$ vs $\log_2 a$; the solid lines correspond to the theoretical predictions $\tau(q) = qH - 2$ (Eq. (3.27)) with $H = \min(H_x, H_y) = 0.41$. (b) $h(q, a)$ vs $\log_2 a$; the solid lines correspond to the theoretical slope $H = \min(H_x, H_y) = 0.41$. (c) $\tau(q)$ vs q ; the solid line corresponds to a linear regression fit estimate of H . (d) $D(h)$ vs h as obtained from the scaling behavior of $D(q, a)$ vs $\log_2 a$ (Eq. (3.21)). First-order analyzing wavelets. These results correspond to an averaging over 32 (1024×1024) simulated surfaces. a is expressed in $\sigma_W = 13$ units.

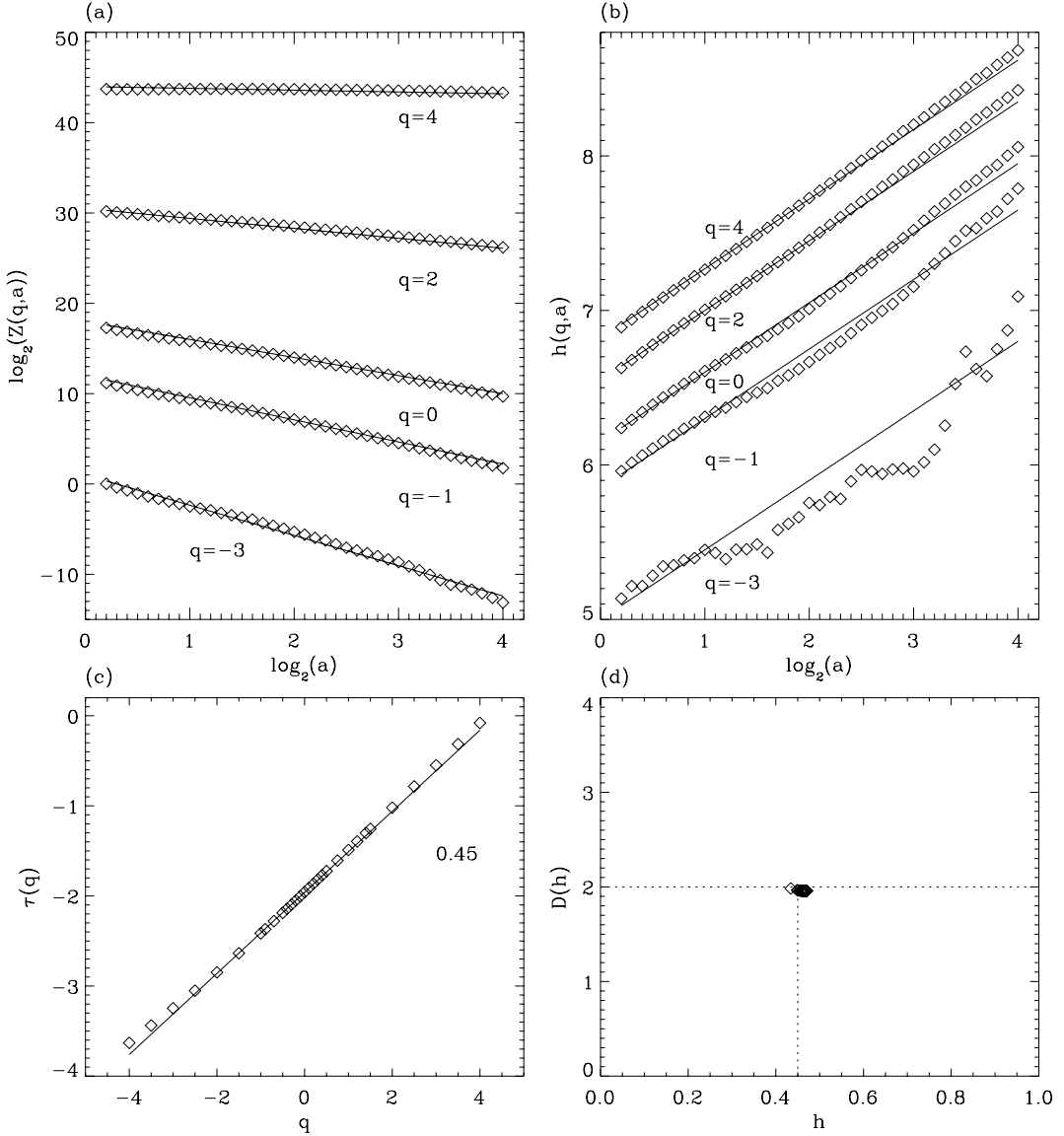


Figure 3.25: Determination of the $\tau(q)$ and $D(h)$ spectra of the fBs $B_{H_x=0.45, H_y=0.52}(x)$ with the 2D WTMM method. (a) $\log_2 Z(q,a)$ vs $\log_2 a$; the solid lines correspond to the theoretical predictions $\tau(q) = qH - 2$ (Eq. (3.27)) with $H = \min(H_x, H_y) = 0.45$. (b) $h(q,a)$ vs $\log_2 a$; the solid lines correspond to the theoretical slope $H = \min(H_x, H_y) = 0.45$. (c) $\tau(q)$ vs q ; the solid line corresponds to a linear regression fit estimate of H . (d) $D(h)$ vs h as obtained from the scaling behavior of $D(q,a)$ vs $\log_2 a$ (Eq. (3.21)). First-order analyzing wavelets. These results correspond to an averaging over 32 (1024×1024) simulated surfaces. a is expressed in $\sigma_W = 13$ units.

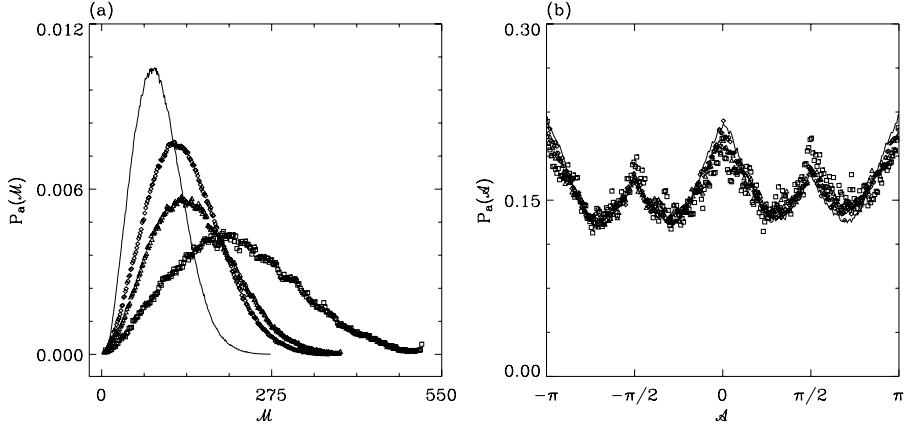


Figure 3.26: Pdfs of the WT MMMM coefficients of $B_{H_x=0.41, H_y=0.44}(\mathbf{x})$ as computed at different scales $a = 1$ (full line), 2 (\diamond), 4 (\triangle), 8 (\square) (in $\sigma_W = 13$ units). (a) $P_a(\mathcal{M})$ vs \mathcal{M} . (b) $P_a(\mathcal{A})$ vs \mathcal{A} . ψ is the first-order analyzing wavelet shown in Figure 3.2. These results correspond to averaging over 32 (1024×1024) simulated surfaces.

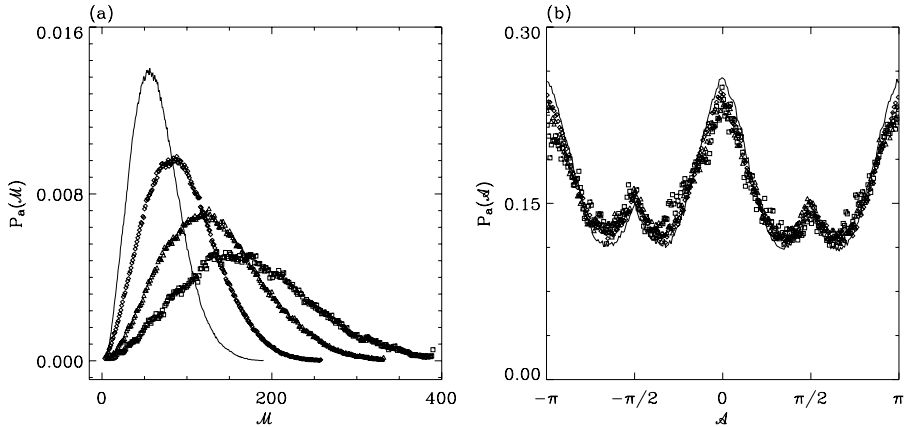


Figure 3.27: Pdfs of the WT MMMM coefficients of $B_{H_x=0.45, H_y=0.52}(\mathbf{x})$ as computed at different scales $a = 1$ (full line), 2 (\diamond), 4 (\triangle), 8 (\square) (in $\sigma_W = 13$ units). (a) $P_a(\mathcal{M})$ vs \mathcal{M} . (b) $P_a(\mathcal{A})$ vs \mathcal{A} . ψ is the first-order analyzing wavelet shown in Figure 3.2. These results correspond to averaging over 32 (1024×1024) simulated surfaces.

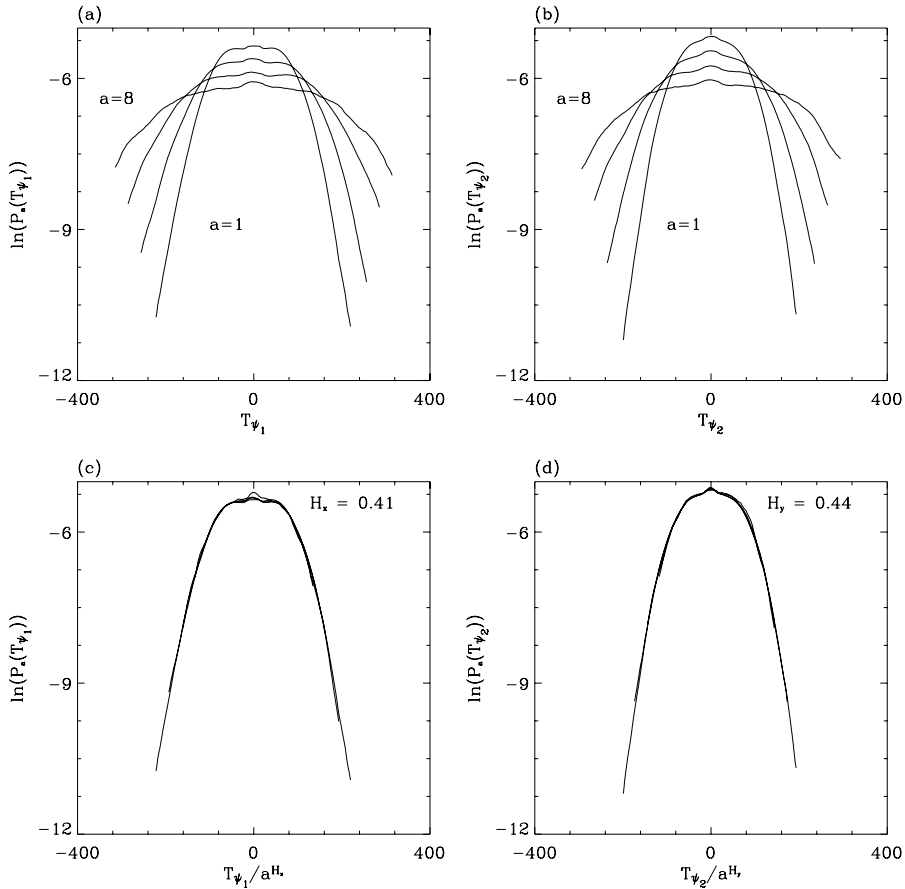


Figure 3.28: Pdfs of the x and y components of the WT MMMM coefficients of the surfaces $B_{H_x=0.41, H_y=0.44}(\mathbf{x})$ as computed at the scales $a = 1, 2, 4,$ and 8 (in $\sigma_W = 13$ units). (a) $\ln(P_a(T_{\psi_1}))$ vs T_{ψ_1} ; (b) $\ln(P_a(T_{\psi_2}))$ vs T_{ψ_2} . In (c) and (d), the pdfs are rescaled by a^{H_x} and a^{H_y} respectively.

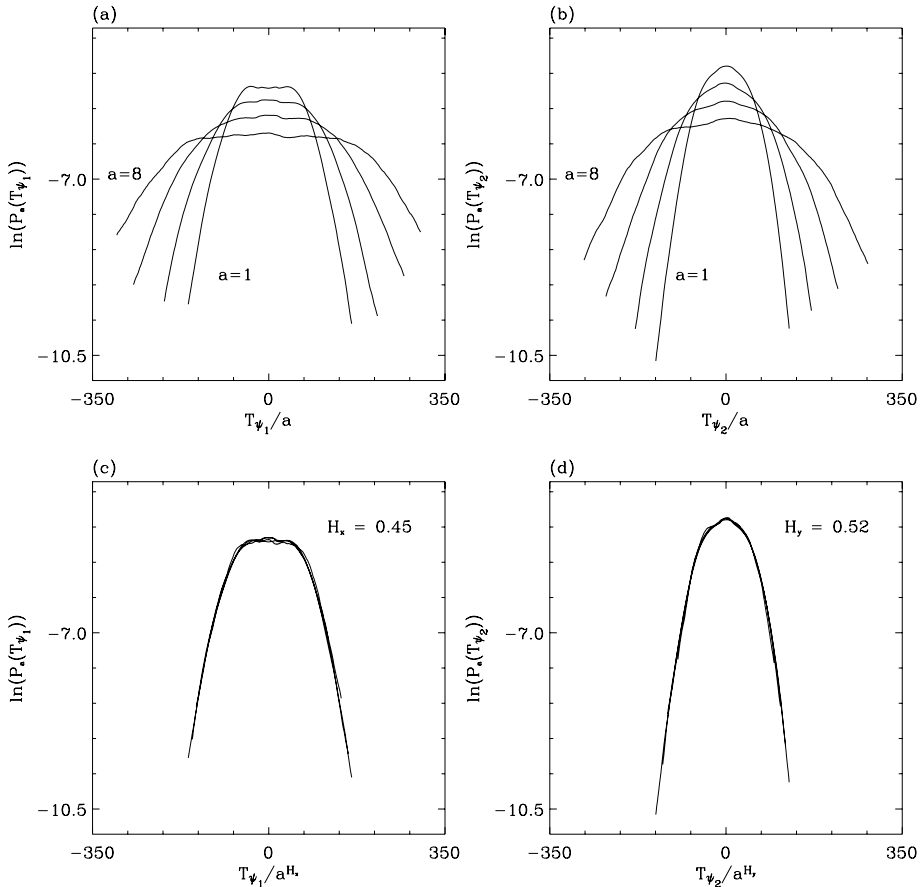


Figure 3.29: Pdfs of the x and y components of the WT MMMM coefficients of the surfaces $B_{H_x=0.45, H_y=0.52}(\mathbf{x})$ as computed at the scales $a = 1, 2, 4$, and 8 (in $\sigma_W = 13$ units). (a) $\ln(P_a(T_{\psi_1}))$ vs T_{ψ_1}/a ; (b) $\ln(P_a(T_{\psi_2}))$ vs T_{ψ_2}/a . In (c) and (d), the pdfs are rescaled by a^{H_x} and a^{H_y} respectively.

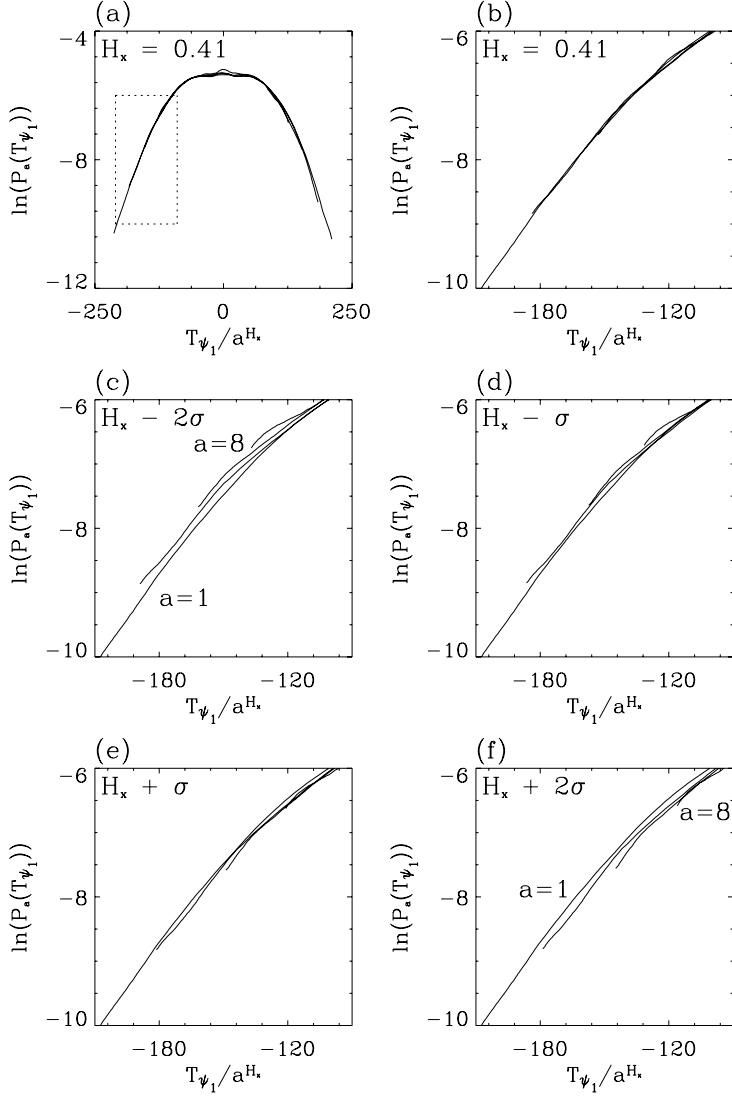


Figure 3.30: Rescaled pdfs of the x components of the WT MMMM coefficients of the surfaces $B_{H_x=0.41, H_y=0.44}(\mathbf{x})$ as computed at the scales $a = 1, 2, 4,$ and 8 (in $\sigma_W = 13$ units). Figure 3.28c is reported in (a). (b) is a zoom-in corresponding to the dashed rectangle in (a). In (c)-(f), the pdfs were rescaled with neighboring values of H_x . $\sigma = 0.01$.

Once again, there are major differences between the anisotropic surfaces presented here and the ones presented in Arneodo, Decoster & Roux (2000). These authors have used a very simple construction rule where 1D fBm signals of a fixed Hurst exponent $H = 1/3$ were stacked together horizontally. By doing so, the horizontal Hurst exponent of the surface is that of the 1D fBm signals, i.e. $H_x = 1/3$ and since for a fixed x value, the corresponding vertical cut of the surface consists of totally random points, the vertical Hurst exponent is $H_y = -0.5$. It is important to emphasize this major distinction between their anisotropic analysis and the fractional Brownian sheets presented here. By definition, the construction rule presented in Arneodo, Decoster & Roux (2000) cannot allow for the choice of the two directional Hurst exponents, H_x and H_y ; one of the two *must* be equal to -0.5 . The characterization of anisotropic surfaces with both directional Hurst exponents in the interval $[0, 1]$ is novel. To the best of our knowledge, no previous work deals with such values. Moreover, the self-similarity properties reported in Eqs. (3.38) and (3.39) are also novel. These properties are different if one of the directional Hurst exponents is less than 0 (e.g. $H_y = -0.5$).

The work presented in this section of the thesis is a major contribution to the science of image analysis. To the best of our knowledge, it is a definite step beyond any published result on the analysis of anisotropic structures, including any previous work from Arneodo and his collaborators.

3.5 RESULTS

3.5.1 Noise Analysis and Filtering

The 2D WTMM method was used to analyze the five mosaics presented in §3.2 (see also Figure 3.1 and Table 3.1). However, the question of the noise in the CGPS data must be addressed before continuing. Originally discussed in Miville-Deschénes et al. (2003), the images obtained from DRAO exhibit a granular structure which is attributed to instrumental noise. A thorough analysis of the noise itself, of its effects on the mosaics, and a filtering method are presented in this section.

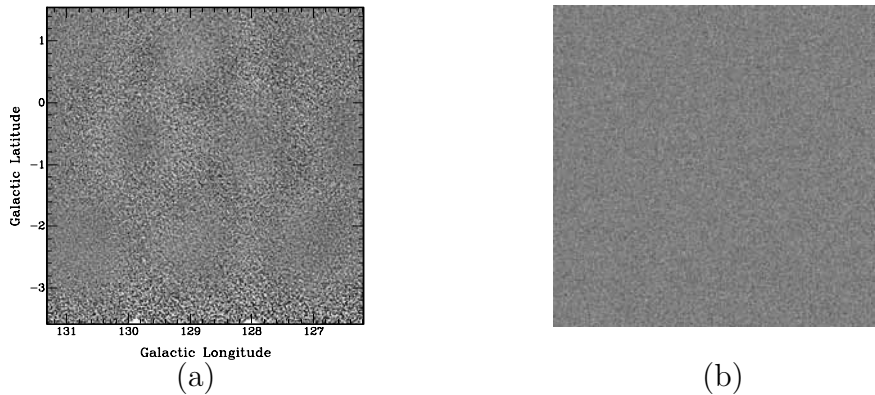


Figure 3.31: 512×512 sample noise images. (a) DRAO noise; (b) Synthetic noise.

3.5.1.1 Noise Analysis from the DRAO Empty Channels

The 2D WTMM analysis presented in this subsection will demonstrate the differences between noise mosaics constructed from some empty channels of the 21-cm data cubes (henceforth called the “DRAO noise”) and synthetic pure white noise (henceforth called “synthetic noise”). For the latter, an isotropic monofractal behavior is expected, with $D(h = -1) = 2.0$.

Figure 3.31 shows a sample of each of the two noise mosaics, with the DRAO noise in 3.31a and the synthetic noise in 3.31b. In order to make an adequate comparison, the number of (empty) velocity channels used to construct the DRAO noise mosaics was chosen to be similar to the average number of velocity channels used to construct five mosaics, corresponding to the three spiral arms and the two inter-arm regions. From a simple visual inspection of Figure 3.31, one can clearly see differences between the DRAO and synthetic noise images. By definition, the synthetic noise is a totally uncorrelated surface, where at the smallest scale, each pixel is randomly different from its neighbor, and at larger scales, no correlated structure exists. However, from the DRAO noise surface, one can clearly see that at the smallest scales, two neighboring pixels are not necessarily uncorrelated. Indeed, the “granularity” seen at the smallest scales of the DRAO noise (black components on a white background) are composed of many pixels. Therefore, any two neighboring pixels on one of these components (or grains) are extremely correlated. At the largest scales, a careful inspection of the DRAO noise surface shows a correlation

caused by the so-called “honeycomb structure”, a signature of the effects of the choice of the synthesis telescope pointings. A detailed, quantitative description of these differences between the DRAO and synthetic surfaces follows.

A Fourier analysis similar to what was done in §3.4 is presented in Figure 3.32, except that the results presented here correspond to an averaging over the central 512×512 parts of 16 (instead of 32) 1024×1024 DRAO (\diamond) and synthetic (\bullet) noise surfaces. The contour plot shown in Figure 3.32a, corresponding to the synthetic noise, seems perfectly random. Indeed, this is to be expected since all pixels are totally uncorrelated at all scales: no preferred scale exists where more power would be represented. This evenly distributed power translates as a flat 2D power spectrum (Fig. 3.32b, \bullet). The same is true for the analysis of the 1D x and y -cuts (Figs. 3.32c and 3.32d respectively, \bullet). On the other hand, although the power spectra obtained from the 2D surfaces (Fig. 3.32b) and 1D x and y cuts (Figs. 3.32c and 3.32d respectively) from the DRAO noise (\diamond) show a relatively flat slope for the intermediate scales, one can clearly see a tangible steepening of the slope at large scales (low values of the wave vector k) and a spectacular steepening of the slope at small scales (large k). This is in agreement with the above discussion, i.e., the large scale honeycomb structure, and the extremely correlated small scale granularity. Finally, note that there is no indication of a directional preference (anisotropy) from the power spectral analysis of the 1D cuts.

The computation of the $\tau(q)$ and $D(h)$ spectra for both the DRAO (\diamond) and synthetic (\bullet) noise surfaces are shown in Figure 3.33. Even though only 16 images were used, Figure 3.33 yields a precise estimation of the Hurst exponents for the synthetic noise surfaces (\bullet), i.e., $D(h = -1.00) = 2.01 \pm 0.02$, as well as the DRAO noise surfaces (\diamond), i.e., $D(h = -1.06) = 2.02 \pm 0.04$. Indeed, one can compare the (negative) slopes of the expectation values ($h(q, a)$) shown in Figure 3.33b to those of §3.4, which are positive (corresponding to positive Hurst exponents). Moreover, the behavior of the expectation values for the DRAO noise surfaces (\diamond) shown in Figure 3.33b is in agreement with the above discussion, namely that the surfaces tend to be more correlated respectively at small and large scales, which translates as a higher value for the Hurst exponent, H , and thus a more positive (or rather, less negative) slope for $h(q, a)$.

The probability density functions $P_a(\mathcal{M})$ and $P_a(\mathcal{A})$ are shown in Figure 3.34. Unlike

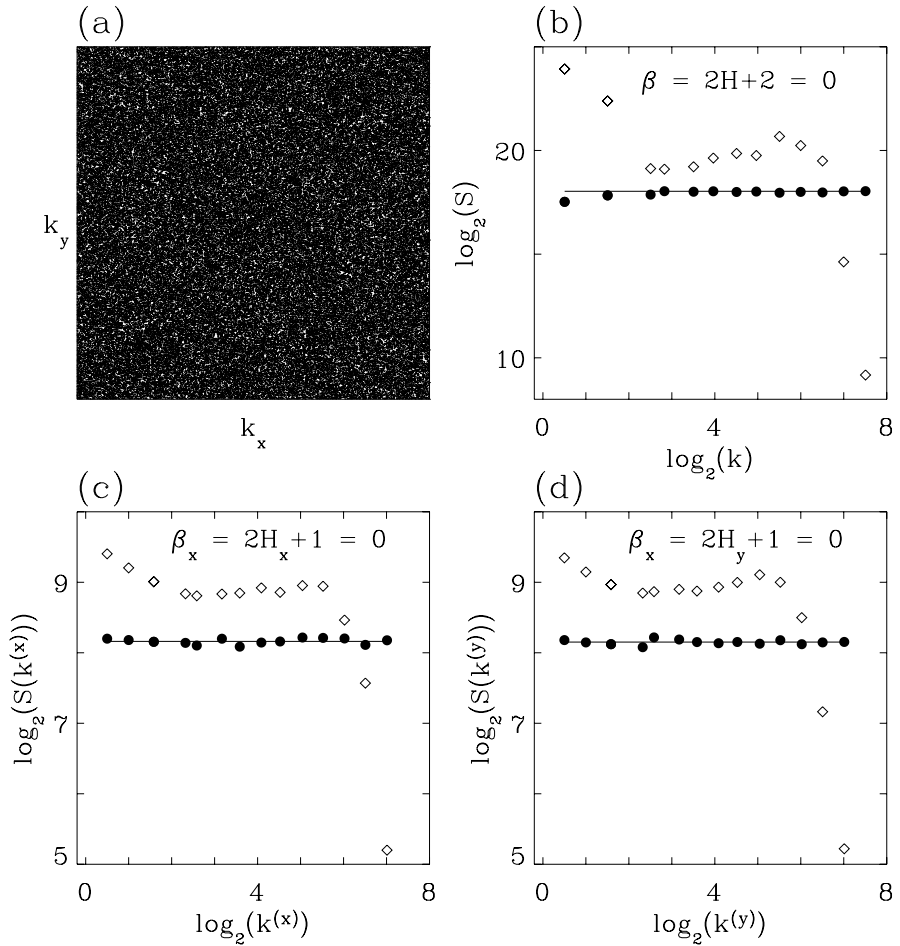


Figure 3.32: Fourier analysis of the 512×512 central part of the DRAO (\diamond) and synthetic (\bullet) noise surfaces. (a) A contour plot of the Fourier transform of a synthetic noise surface. (b) The power spectra $S(|\mathbf{k}|)$ vs $|\mathbf{k}|$ in a logarithmic representation. (c) The averaged power spectra of the one-dimensional x -cuts. (d) The averaged power spectra of the one-dimensional y -cuts. The solid lines correspond to the power-law theoretical predictions for the synthetic noise. Note: These results correspond to an averaging over 16 surfaces (instead of the usual 32).

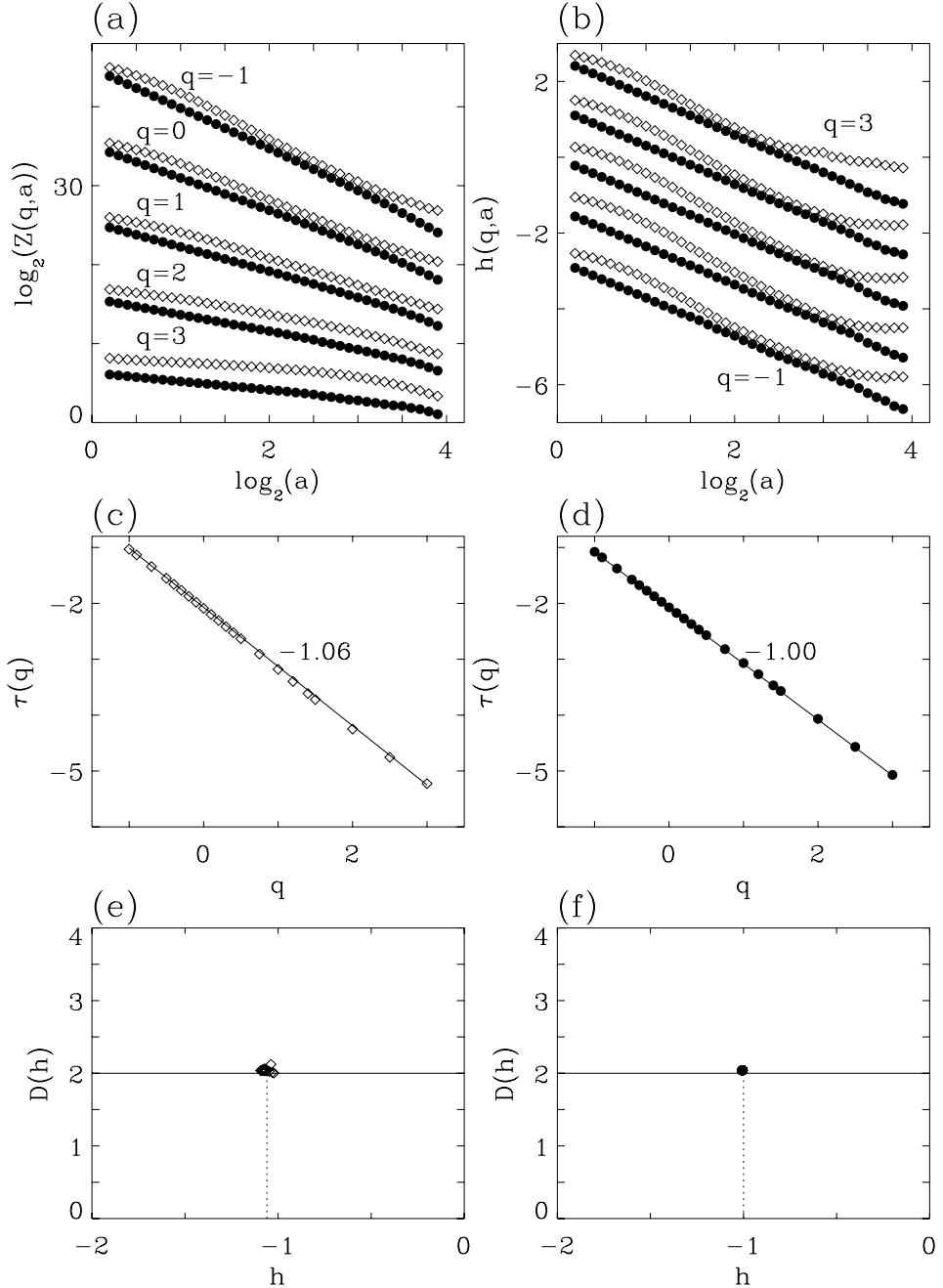


Figure 3.33: Determination of the $\tau(q)$ and $D(h)$ spectra of the DRAO (\diamond) and synthetic (\bullet) noise mosaics with the 2D WTMM method. (a) $\log_2 \mathcal{Z}(q, a)$ vs $\log_2 a$. (b) $h(q, a)$ vs $\log_2 a$. $\tau(q)$ vs q for the DRAO (c) and synthetic (d) noise surfaces; the solid lines corresponds to a linear regression fit estimate of H . $D(h)$ vs h as obtained from the scaling behavior of $D(q, a)$ vs $\log_2 a$ (Eq. (3.21)) for the DRAO (e) and synthetic (f) noise surfaces. First-order analyzing wavelets. These results correspond to an averaging over 16 (1024×1024) surfaces. a is expressed in σ_W units, where $\sigma_W = 13$ pixels.

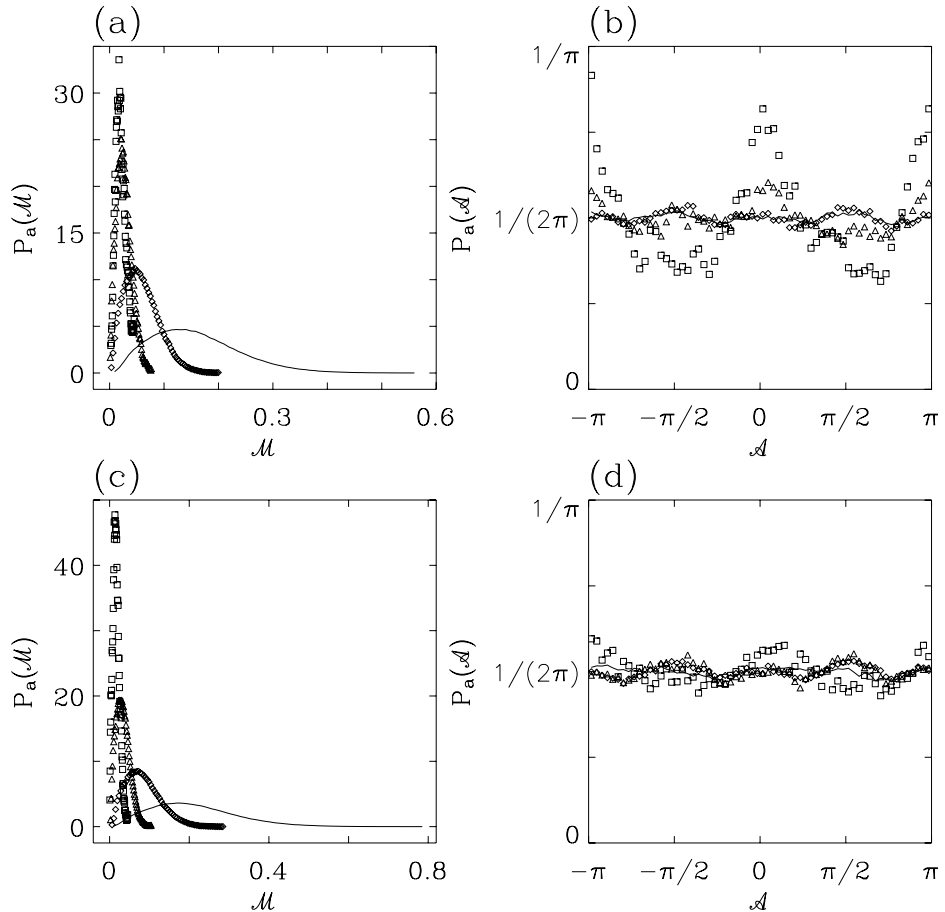


Figure 3.34: Pdfs of the WT MMMM coefficients of the DRAO noise surfaces as computed at different scales $a = 1$ (full line), 2 (\diamond), 4 (\triangle), 8 (\square) (in $\sigma_W = 13$ units). (a) $P_a(\mathcal{M})$ vs \mathcal{M} . (b) $P_a(\mathcal{A})$ vs \mathcal{A} ; ψ is the first-order analyzing wavelet. (c) $P_a(\mathcal{M})$ vs \mathcal{M} . (d) $P_a(\mathcal{A})$ vs \mathcal{A} ; ψ is the third-order analyzing wavelet. These results correspond to an averaging over 16 (1024×1024) surfaces.

the modulus pdfs analyzed in §3.4, the $P_a(\mathcal{M})$ pdfs shown in Figure 3.34a, where a first-order analyzing wavelet was used, show a widening of the curves with decreasing scale. This is caused by the fact that the underlying Hurst exponent here is negative ($H = -1$).

In Figure 3.34b, there are small oscillations in the pdfs of the arguments, $P_a(\mathcal{A})$, with peaks at 0 , $\pm\pi/2$, and $\pm\pi$ for the smallest scales (full line and \diamond). This finite-size effect is to be expected and is comparable to what was observed for the isotropic fBm surfaces in §3.4.1. However, for the largest scales (\triangle and \square), there are two clear peaks at 0 and $\pm\pi$. This is caused by the large scale correlation discussed above: a signature of the honeycomb effect. Since these DRAO noise surfaces were cut-up in a systematic and similar way for all 16 analyzed surfaces, the position of the honeycomb lattice is similar, and in fact, accentuated when averaging over the 16 surfaces. One way to get rid of the anisotropic signature would be to construct a large DRAO noise mosaic similar to the spiral and inter-arm mosaics presented in Figure 3.1, which would imply a relatively important work investment. Instead, one can use the third-order analyzing wavelet, which is blind to linear and quadratic behaviors¹⁰. The third-order analyzing wavelet was thus used in Figure 3.34d, where one can clearly see the dampening of the large scale peaks from Figure 3.34b. This is a spectacular demonstration of the strength of the 2D WTMM method. Indeed, the large scale anisotropy is easily dealt with and one can be certain that the honeycomb structure will not affect the results presented in this paper.

As will be shown in what follows, another, perhaps equally important topic that should be emphasized, is that the values of the modulus of the wavelet transform (range of x values in Figures 3.34a and 3.34c) is quite small compared to the values of the modulus of the five analyzed mosaics. This means that even if there were an anisotropic structure in the DRAO noise surfaces, corresponding to an artificial (instrumental) anisotropic signature, its contribution to the mosaics would be so small as to have absolutely no effect on the results.

¹⁰In fact, an n -order analyzing wavelet is blind to polynomial behaviors of degree $n - 1$ (Arneodo, Decoster & Roux, 2000).

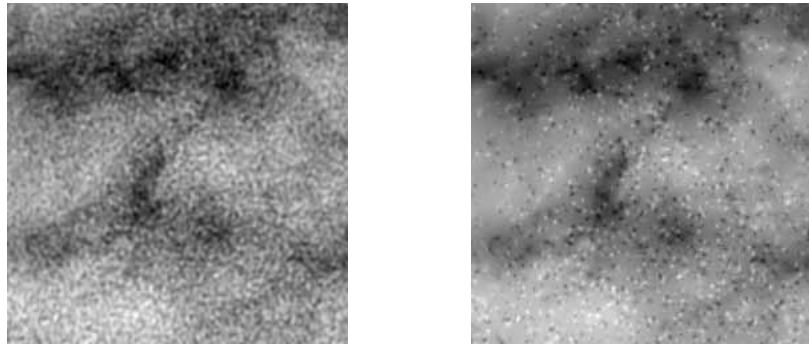


Figure 3.35: Effects of the filtering algorithm: The original (left) and filtered (right) 256×256 sub-regions were chosen randomly from the Inter I mosaic.

3.5.1.2 Filtering

In order to deal as best as possible with the granularity of the DRAO data, the filtering method presented in Miville-Deschénes et al. (2003), based on the wavelet-based “à trous” algorithm, was used here to filter the five mosaics. The method consists in the decomposition of the images on a wavelet basis. In order to improve the signal to noise ratio, only the wavelet coefficients satisfying a threshold condition relative to the amplitude of the noise are kept in the reconstruction algorithm. A before-and-after visualization is presented in Figure 3.35.

The effects of the filtering on the Local arm mosaic are shown in Figure 3.36. In Figure 3.36a are shown the expectation values, $h(q, a)$, plotted vs $\log_2 a$. The 2D power spectrum is shown in Figure 3.36b, and the 1D power spectra for the x and y -cuts are shown in Figures 3.36c and 3.36d. Close analysis of the power spectra presented in Miville-Deschénes et al. (2003) indicates that the DRAO observations are too noisy to be used to study H I structure on scales less than 5 arc minutes in diameter. With the unfiltered data, the wavelet analysis (using a first-order wavelet, where $\sigma_W = 13$ pixels) reaches areas of only $\sim 2^{1.4}\sigma_W = 34$ pixels in diameter. Filtering improves the scale span down to areas of $2^{0.9}\sigma_W = 24$ pixels in diameter only (≈ 7 arc minutes). Sensitivities 5 times larger than the current DRAO values are necessary to reach the resolution limit of the telescope.

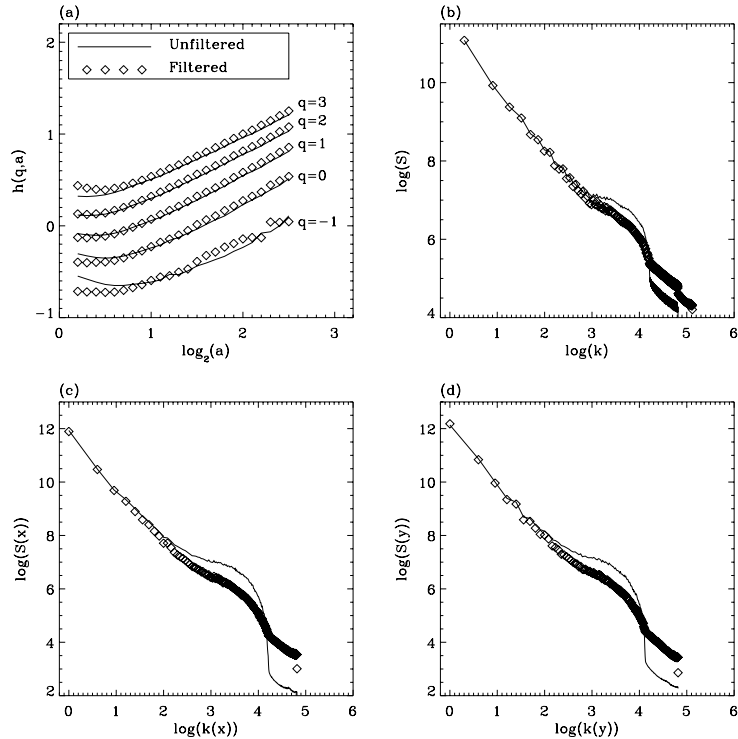


Figure 3.36: Comparisons between the filtered (\diamond) and unfiltered (full line) mosaics on the expectation values $h(q, a)$ and Fourier analysis for the Local arm subregions. (a) $h(q, a)$ vs a . (b) The power spectrum $S(|\mathbf{k}|)$ vs $|\mathbf{k}|$ in a logarithmic representation. (c) The averaged power spectra of the one-dimensional x -cuts. (d) The averaged power spectra of the one-dimensional y -cuts.

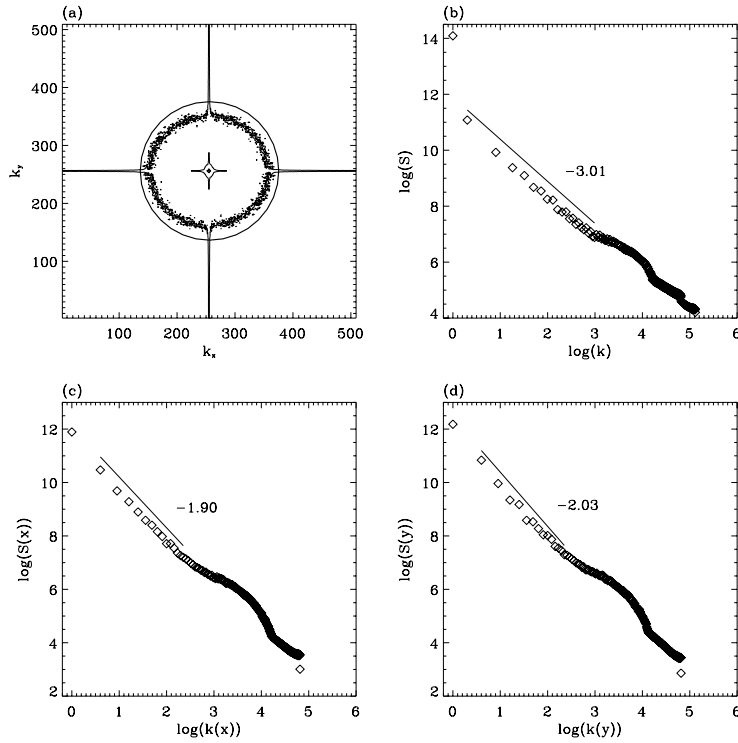


Figure 3.37: Fourier analysis of the Local arm subregions. (a) A contour plot similar to Figure 3.4a, where a black circle was added to help the reader see the slight ellipticity of the contour. (b) The power spectrum $S(|\mathbf{k}|)$ vs $|\mathbf{k}|$ in a logarithmic representation. The solid line corresponds to a power-law fit. (c) The averaged power spectra of the one-dimensional x -cuts. (d) The averaged power spectra of the one-dimensional y -cuts.

The following two sub-sections correspond to the spiral arms and the inter arms taken separately.

3.5.2 The Three Spiral Arms

3.5.2.1 Fourier Analysis

The Fourier analysis of the subregions outlined in white in Figures 3.1a, c, and e are presented in Figures 3.37, 3.38, and 3.39.

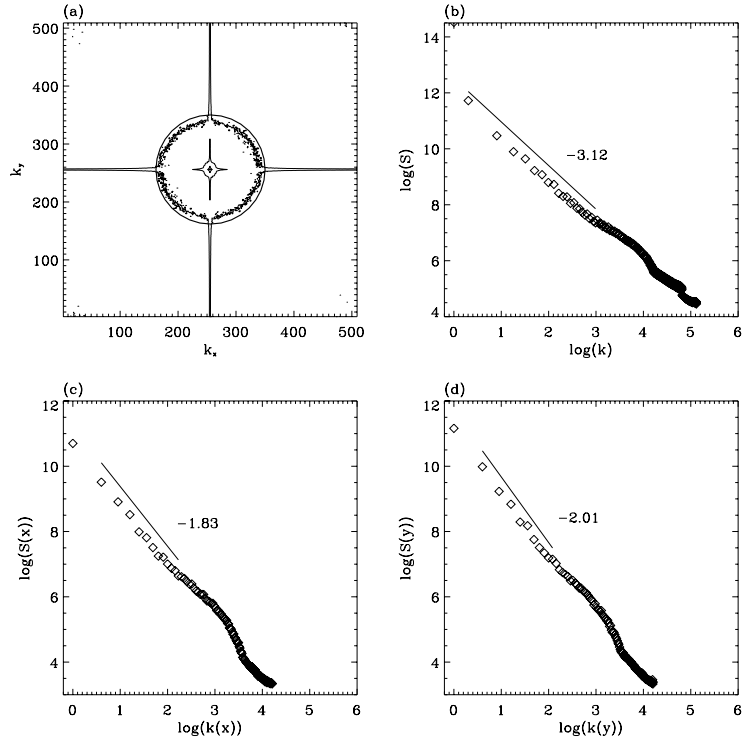


Figure 3.38: Fourier analysis of the Perseus arm subregions. (a) A contour plot similar to Figure 3.4a, where a black circle was added to help the reader see the slight ellipticity of the contour. (b) The power spectrum $S(|\mathbf{k}|)$ vs $|\mathbf{k}|$ in a logarithmic representation. The solid line corresponds to a power-law fit. (c) The averaged power spectra of the one-dimensional x -cuts. (d) The averaged power spectra of the one-dimensional y -cuts.

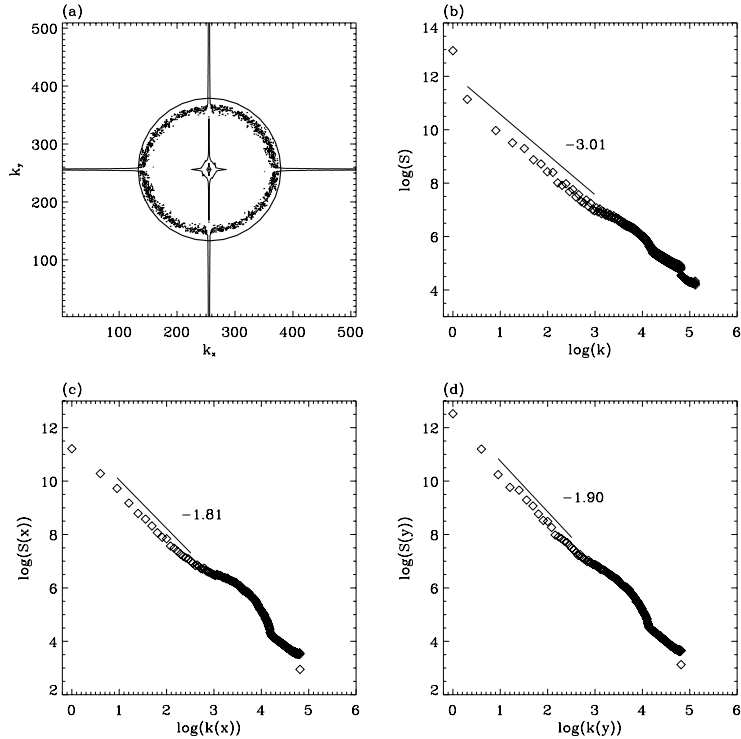


Figure 3.39: Fourier analysis of the Outer arm subregions. (a) A contour plot similar to Figure 3.4a, where a black circle was added to help the reader see the slight ellipticity of the contour. (b) The power spectrum $S(|\mathbf{k}|)$ vs $|\mathbf{k}|$ in a logarithmic representation. The solid line corresponds to a power-law fit. (c) The averaged power spectra of the one-dimensional x -cuts. (d) The averaged power spectra of the one-dimensional y -cuts.

Figures 3.37a, 3.38a, and 3.39a present the contour plot of the 2D Fourier spectrum, where a circle was added to help the reader see the slight ellipticity of the contour. As was done for the simulated surfaces (§3.4.1, 3.4.2, and 3.4.3), where the analysis was performed by averaging over the 32 central 512×512 parts of the original 1024×1024 images, all results presented here correspond to an averaging over all white subregions presented in Figures 3.1a-e. From the log-log plots of the 2D power spectrum shown in Figures 3.37b, 3.38b, and 3.39b the beta indices were estimated to be $\beta = 3.01 \pm 0.05$, 3.12 ± 0.05 , and 3.01 ± 0.06 for the Local, Perseus, and Outer arms respectively¹¹. The range of the fits correspond to the length of the straight lines located above the log-log plots. A further Fourier analysis was performed by calculating the power spectrum on the x and y one-dimensional cuts of each mosaic. The fact that the $\beta_x = 1.90 \pm 0.04$, 1.83 ± 0.05 , and 1.81 ± 0.06 are strictly less than the $\beta_y = 2.03 \pm 0.10$, 2.01 ± 0.05 , and 1.90 ± 0.05 is in agreement with the slightly elliptical shape of the contour found in Figures 3.37a, 3.38a, and 3.39a. This could be interpreted as a first indication that an anisotropic structure is present in these three mosaics. However, one cannot solidly quantify this affirmation with the Fourier analysis only.

3.5.2.2 Wavelet Analysis

We have wavelet transformed the subregions of the Local, Perseus, and Outer arms with a first-order analyzing wavelet (Figures 3.2a and 3.2b). Again, to avoid edge effects, only the central parts of the wavelet transform of each 1024×1024 image, which are represented by the white subregions in Figures 3.1a, c, and e, are kept for analysis. All of these subregions are $\leq 512 \times 512$. In Figures 3.40, 3.41, and 3.42 are illustrated the computation of the maxima chains and the WTMM for an individual image at three different scales. In Figures 3.40b, 3.41b, and 3.42b are shown the convolution of the original images (Fig. 3.40a, 3.41a, and 3.42a) with the isotropic Gaussian smoothing filter ϕ_{Gau} (§3.3.1.1).

As seen for the study of simulated surfaces in Sections 3.4.1, 3.4.2, and 3.4.3, the maxima chains correspond to well defined edge curves of the smoothed image. The

¹¹The presented uncertainties for β , β_x , and β_y correspond to the χ^2 errors from the fitted slopes.

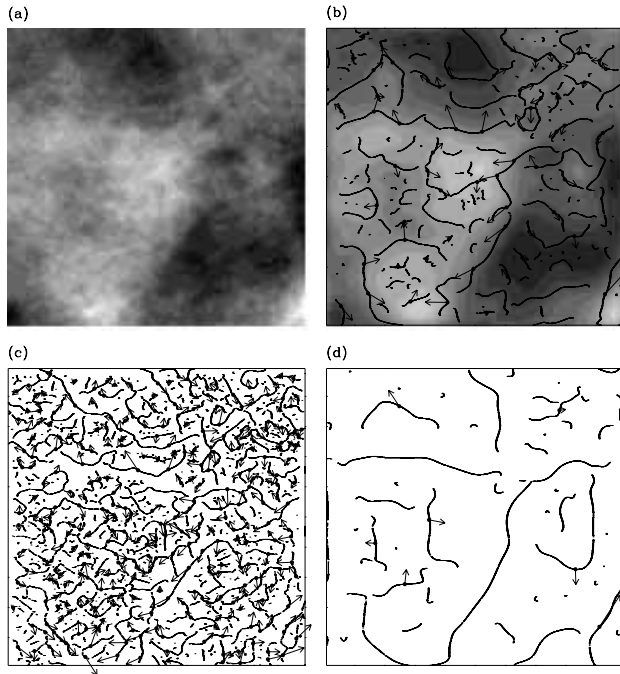


Figure 3.40: 2D wavelet transform analysis of one Local arm subregion. ψ is a first-order radially symmetric analyzing function (see Fig. 3.2). (a) 32 grey-scale coding of the original image, where the intensities range from 16 to 77 K km s^{-1} . In (b) $a = 2^{2.9}\sigma_W$, (c) $a = 2^{1.9}\sigma_W$ and (d) $a = 2^{3.9}\sigma_W$, are shown the maxima chains; the local maxima of \mathcal{M}_ψ along these chains are indicated by (\bullet) from which originate an arrow whose length is proportional to \mathcal{M}_ψ and its direction (with respect to the x -axis) is given by \mathcal{A}_ψ . In (b), the smoothed image is shown as a grey-scale coded background from white (min) to black (max).

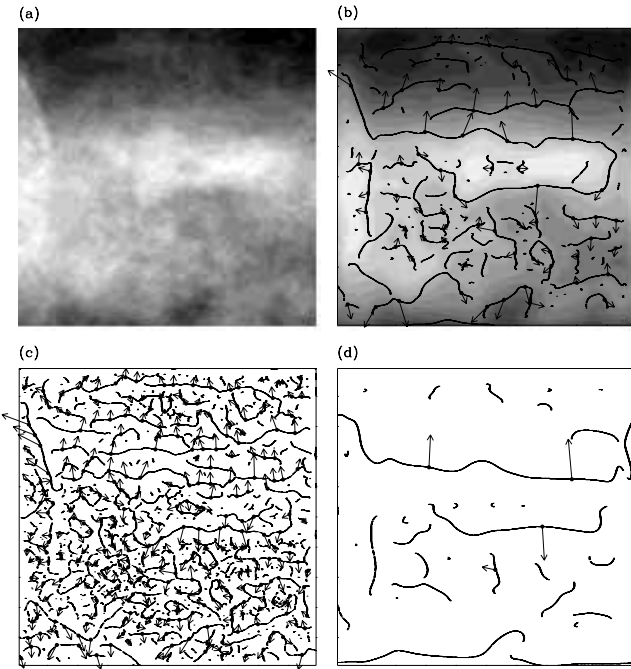


Figure 3.41: 2D wavelet transform analysis of one Perseus arm subregion. ψ is a first-order radially symmetric analyzing function (see Fig. 3.2). (a) 32 grey-scale coding of the original image, where the intensities range from 20 to 114 K km s^{-1} . In (b) $a = 2^{2.9}\sigma_W$, (c) $a = 2^{1.9}\sigma_W$ and (d) $a = 2^{3.9}\sigma_W$, are shown the maxima chains; the local maxima of \mathcal{M}_ψ along these chains are indicated by (\bullet) from which originate an arrow whose length is proportional to \mathcal{M}_ψ and its direction (with respect to the x -axis) is given by \mathcal{A}_ψ . In (b), the smoothed image is shown as a grey-scale coded background from white (min) to black (max).

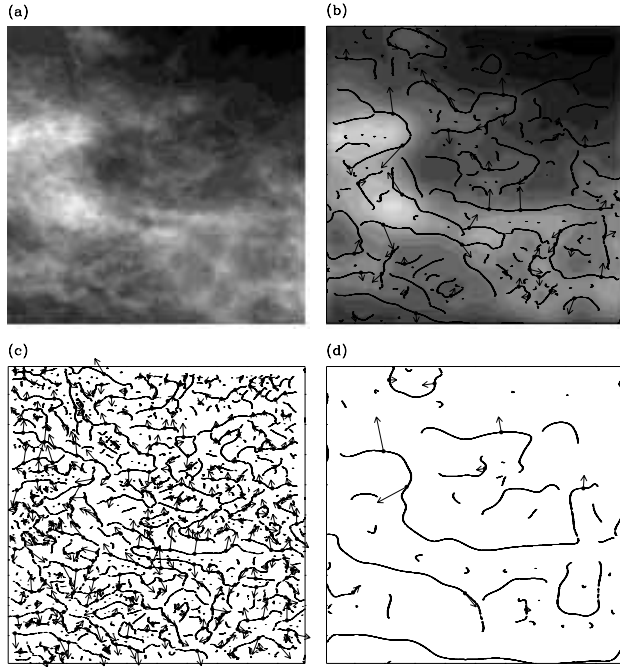


Figure 3.42: 2D wavelet transform analysis of one Outer arm subregion. ψ is a first-order radially symmetric analyzing function (see Fig. 3.2). (a) 32 grey-scale coding of the original image, where the intensities range from 0 to 40 K km s^{-1} . In (b) $a = 2^{2.9}\sigma_W$, (c) $a = 2^{1.9}\sigma_W$ and (d) $a = 2^{3.9}\sigma_W$, are shown the maxima chains; the local maxima of \mathcal{M}_ψ along these chains are indicated by (\bullet) from which originate an arrow whose length is proportional to \mathcal{M}_ψ and its direction (with respect to the x -axis) is given by \mathcal{A}_ψ . In (b), the smoothed image is shown as a grey-scale coded background from white (min) to black (max).

local maxima of \mathcal{M}_ψ along these curves are located at the points where the sharpest intensity variation is observed. The corresponding arrows clearly indicate that locally, the gradient vector points in the direction (as given by \mathcal{A}_ψ) of maximum change of the intensity surface. When going from large scale (Fig. 3.40d, 3.41d, and 3.42d) to small scale (Fig. 3.40c, 3.41c, and 3.42c), the characteristic average distance between two nearest neighbour WTMMM decreases like a . This means that the number of WTMMM and in turn, the number of maxima lines, proliferates across scales like a^{-2} , like isotropic fBm and anisotropic fBs monofractal surfaces.

3.5.2.3 Numerical Computation of the $\tau(q)$ and $D(h)$ spectra

The results obtained from the computation of the $\tau(q)$ and $D(h)$ spectra using the 2D WTMM method described in §3.3.1 are presented in Figures 3.43, 3.44, and 3.45. In Figures 3.43a, 3.44a, and 3.45a, and 3.43b, 3.44b, and 3.45b the partition function $\mathcal{Z}(q, a)$ and the expectation values $h(q, a)$ display excellent scaling behaviors over the range $a \in [2^{0.9}\sigma_W, 2^{3.0}\sigma_W]$ when plotted versus a , where the range of values of q is $q \in [-1, 3]$. One can clearly see that although the mosaics were filtered to minimize the noise, the wavelet analysis is restricted to the scales larger than $a = 2^{0.9}\sigma_W$ (where $\sigma_W = 13$ pixels).

When proceeding to a linear regression fit of the data over the ranges $a \in [2^{1.1}, 2^{2.6}]$, $a \in [2^{1.0}, 2^{2.6}]$, and $a \in [2^{0.9}, 2^{2.6}]$ respectively (in $\sigma_W = 13$ units) for each spiral arm, one gets the $\tau(q)$ spectra shown in Figures 3.43c, 3.44c, and 3.45c. The data fall on straight lines, the signature of monofractal scaling properties. The slopes of these straight lines correspond to the Hurst exponents $H = 0.52 \pm 0.03$, $H = 0.53 \pm 0.03$, and $H = 0.51 \pm 0.03$ respectively for the Local, Perseus, and Outer arms, when averaged over all subregions. Accordingly, the $D(h)$ singularity spectra shown in Figures 3.43d, 3.44d, and 3.45d collapse to single points $D(h = 0.52) = 2.02 \pm 0.03$, $D(h = 0.53) = 2.01 \pm 0.03$, and $D(h = 0.51) = 2.03 \pm 0.03$, a remarkably precise result considering the relatively small amount of available data.

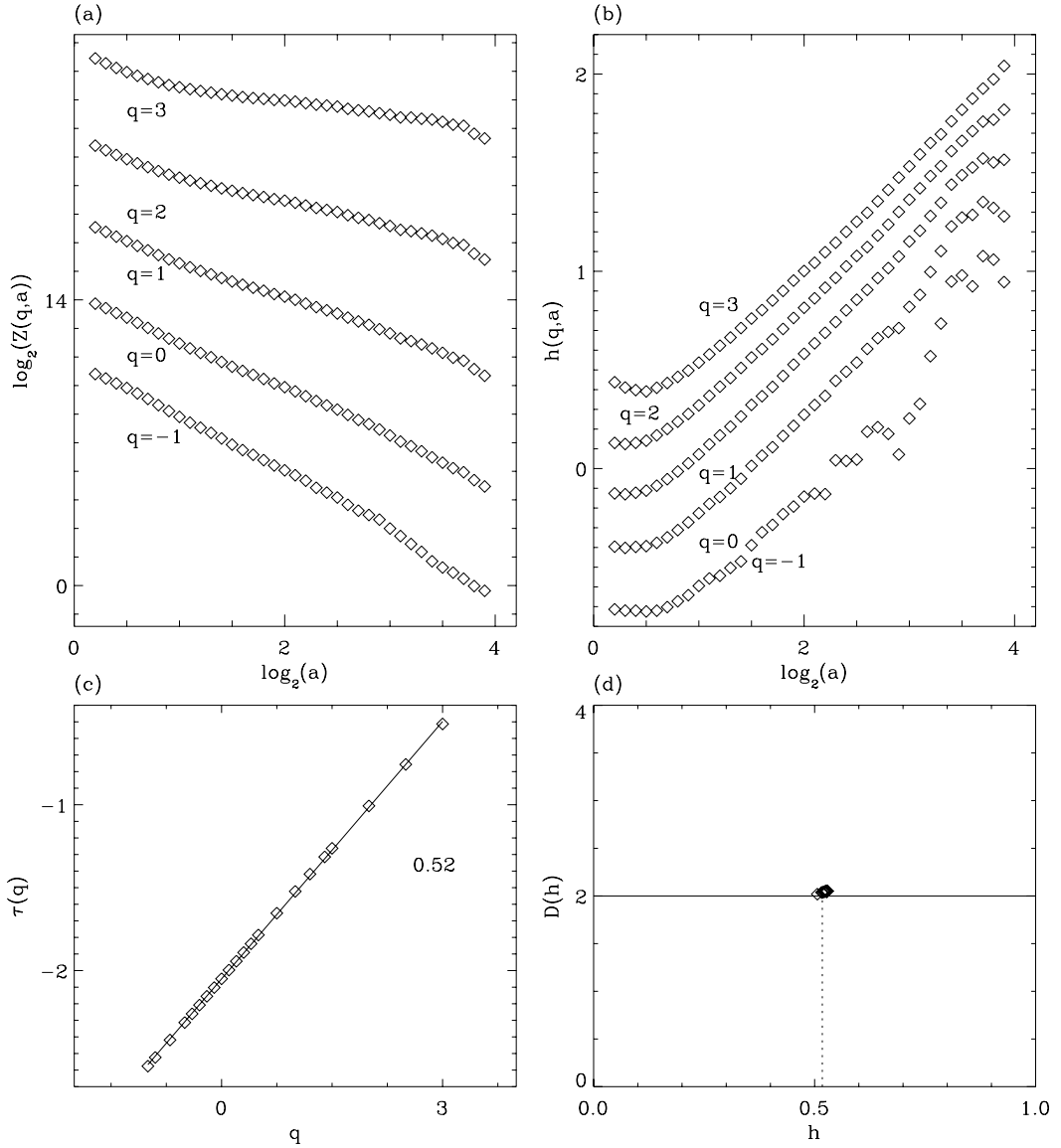


Figure 3.43: Determination of the $\tau(q)$ and $D(h)$ spectra of the Local arm subregions with the 2D WTMM method. (a) $\log_2 \mathcal{Z}(q,a)$ vs $\log_2 a$. (b) $h(q,a)$ vs $\log_2 a$. (c) $\tau(q)$ vs q ; the solid line corresponds to the curve $\tau(q) = qH - 2$, where $H = 0.52$. (d) $D(h)$ vs h as obtained from the scaling behavior of $D(q,a)$ vs $\log_2 a$ (Eq. (3.21)); the symbols have the same meaning as in (c) and the vertical dashed line corresponds to the value of H found in (c). First-order analyzing wavelets. These results correspond to an averaging over all subregions outlined in white in Figure 3.1a. a is expressed in $\sigma_W = 13$ units.

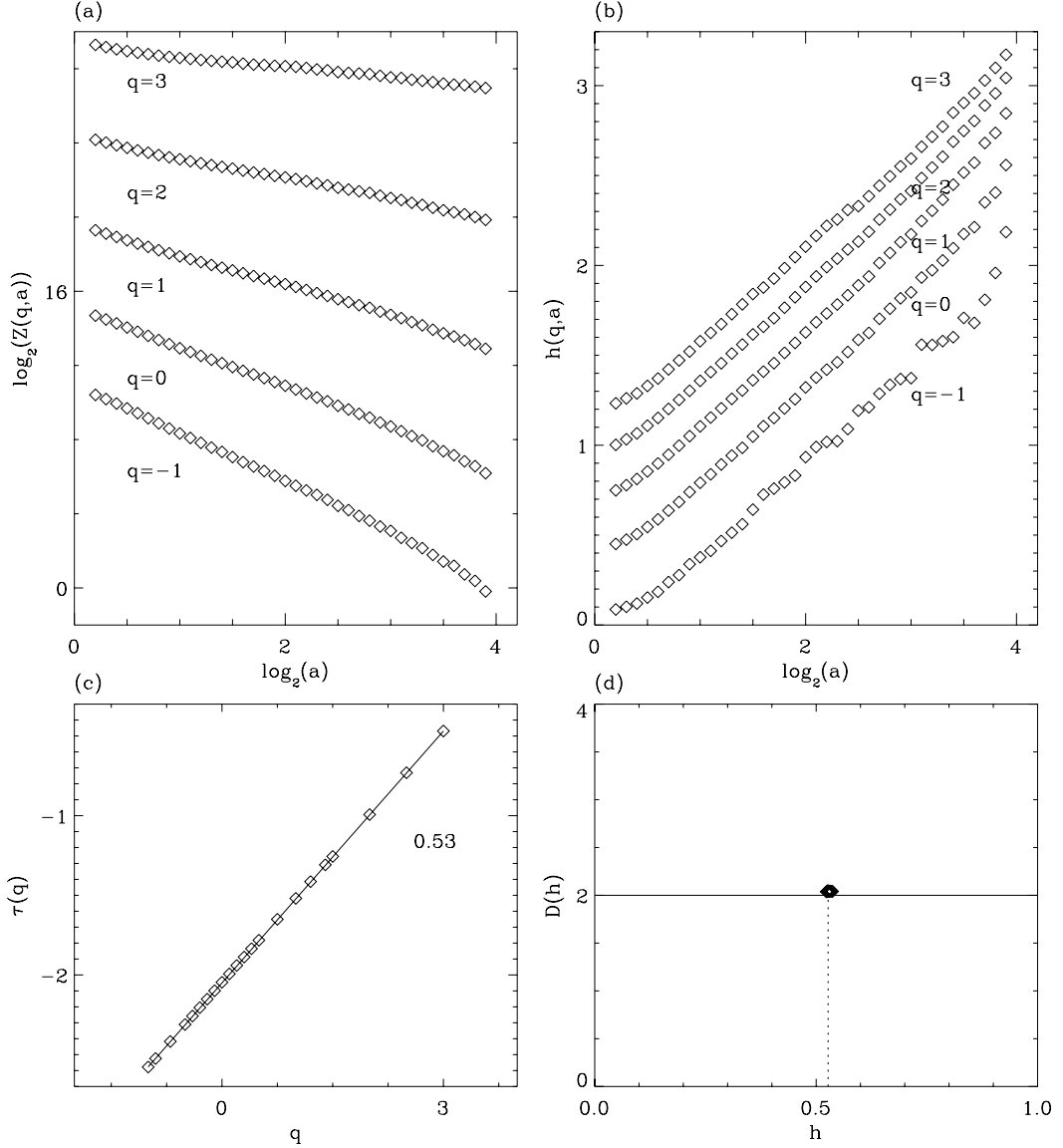


Figure 3.44: Determination of the $\tau(q)$ and $D(h)$ spectra of the Perseus arm subregions with the 2D WTMM method. (a) $\log_2 \mathcal{Z}(q, a)$ vs $\log_2 a$. (b) $h(q, a)$ vs $\log_2 a$. (c) $\tau(q)$ vs q ; the solid line corresponds to the curve $\tau(q) = qH - 2$, where $H = 0.53$. (d) $D(h)$ vs h as obtained from the scaling behavior of $D(q, a)$ vs $\log_2 a$ (Eq. (3.21)); the symbols have the same meaning as in (c) and the vertical dashed line corresponds to the value of H found in (c). First-order analyzing wavelets. These results correspond to an averaging over all subregions outlined in white in Figure 3.1c. a is expressed in $\sigma_W = 13$ units.

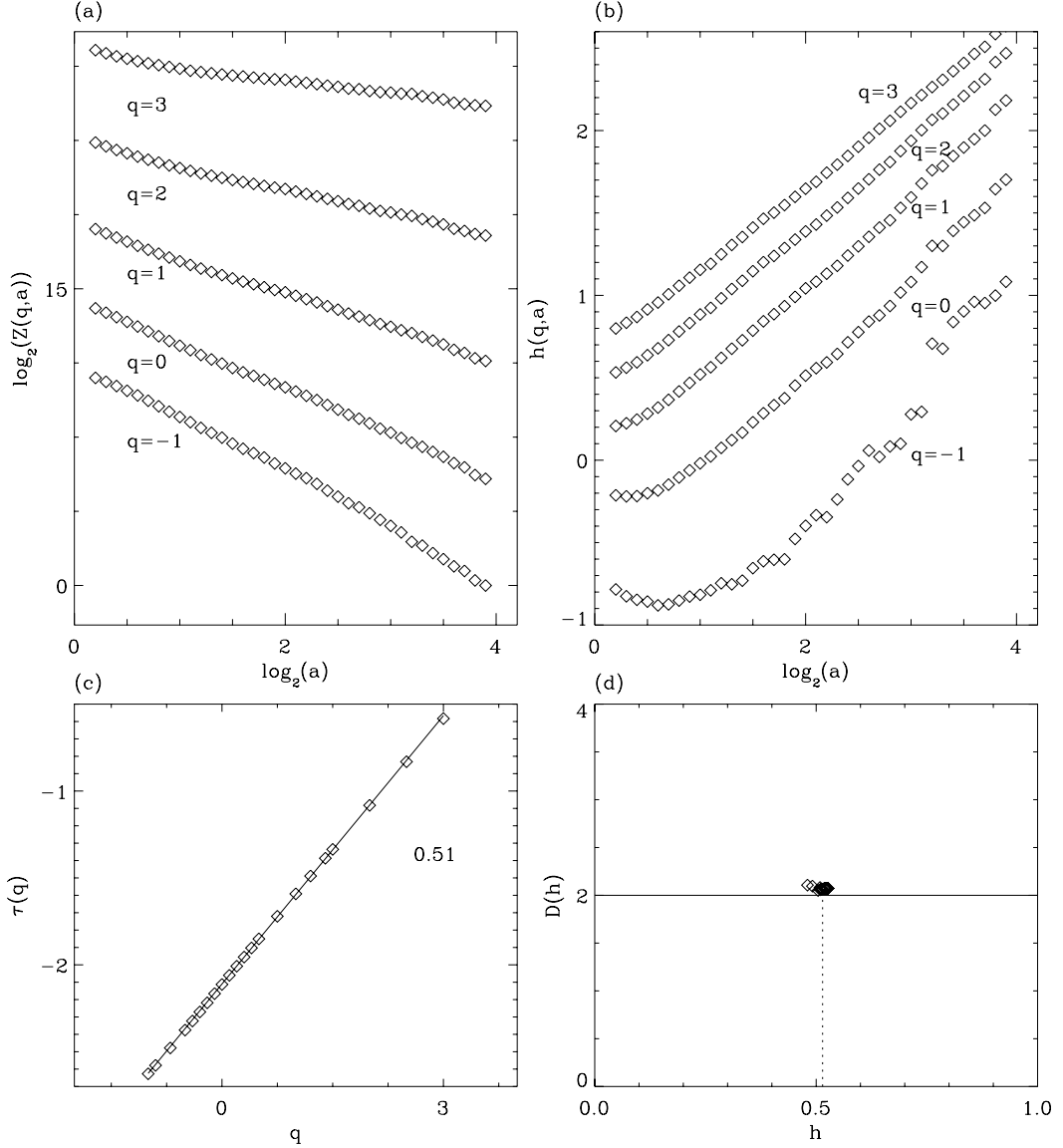


Figure 3.45: Determination of the $\tau(q)$ and $D(h)$ spectra of the Outer subregions with the 2D WTMM method. (a) $\log_2 \mathcal{Z}(q, a)$ vs $\log_2 a$. (b) $h(q, a)$ vs $\log_2 a$. (c) $\tau(q)$ vs q ; the solid line corresponds to the curve $\tau(q) = qH - 2$, where $H = 0.51$. (d) $D(h)$ vs h as obtained from the scaling behavior of $D(q, a)$ vs $\log_2 a$ (Eq. (3.21)); the symbols have the same meaning as in (c) and the vertical dashed line corresponds to the value of H found in (c). First-order analyzing wavelets. These results correspond to an averaging over all subregions outlined in white in Figure 3.1e. a is expressed in $\sigma_W = 13$ units.

3.5.2.4 Probability Density Functions

In Figures 3.46, 3.47, and 3.48 are shown the pdfs $P_a(\mathcal{M})$ and $P_a(\mathcal{A})$, computed for four different values of the scale parameters $a = 2^{1.0}$, $2^{1.5}$, $2^{2.0}$, and $2^{2.5}$ (in $\sigma_W = 13$ units). As seen in Figures 3.46a, 3.47a, and 3.48a, where a first-order wavelet was used, $P_a(\mathcal{M})$ is not a Gaussian, but decreases fast to zero at zero, an expected property which was discussed in §3.4.1. Note that the $P_a(\mathcal{M})$ curves are wider for the Perseus mosaics (Fig. 3.47a) than for the two other spiral arms (Fig. 3.46a and 3.48a). This is simply the signature of the intensity levels being much more variable in the Perseus mosaic than in the other two (see Figure caption 3.1). The corresponding pdfs $P_a(\mathcal{A})$ are represented in Figures 3.46b, 3.47b, and 3.48b. $P_a(\mathcal{A})$ is clearly peaked at $\pm\pi/2$. This is a solid confirmation that the mosaics exhibit an anisotropic signature. In Figures 3.46c, 3.47c, 3.48c and 3.46d, 3.47d, 3.48d are shown the pdfs $P_a(\mathcal{M})$ and $P_a(\mathcal{A})$ using a third-order wavelet. The fact that the peaks do not fade when going from the first-order to the third-order wavelet is a confirmation that the anisotropy is not caused by a large-scale structure in the mosaic, as seen in the study of Earth clouds presented in Roux, Arneodo & Decoster (2000), where large convective rolls created the anisotropic signature. This is proof that the anisotropic signature detected in the mosaics is not caused by the large-scale shape of the galactic disk and the anisotropy is therefore inherent to the analyzed H I structure. As seen in §3.4.3 with the simulated anisotropic surfaces, having many more WTMM pointing towards $\pm\pi/2$ tells us that the direction of greatest intensity variation is vertical. This should be interpreted as a situation where vertical structures are more “complex” than horizontal structures, characterized by Hurst exponents $H_x > H_y$. However, this is surprisingly and interestingly not the case here. An explanation is given in the next paragraphs.

In Figures 3.49a, 3.50a, 3.51a and 3.49b, 3.50b, 3.51b are shown the pdfs of the x and y components of the wavelet transform in logarithmic form: $\ln(P_a(T_{\psi_1}))$ vs T_{ψ_1} and $\ln(P_a(T_{\psi_2}))$ vs T_{ψ_2} . Unlike the results obtained from Figures 3.19, 3.28, and 3.29, for the simulated anisotropic surfaces (§3.4.3), the T_{ψ_2} curves of Figures 3.49b, 3.50b, and 3.51b are wider than those of Figures 3.49a, 3.50a, and 3.51a, even though we expect to have $H_x > H_y$. And in fact, when calculating the individual Hurst exponents by rescaling these curves by H_x and H_y respectively, we find $(H_x, H_y) = (0.42, 0.52)$,

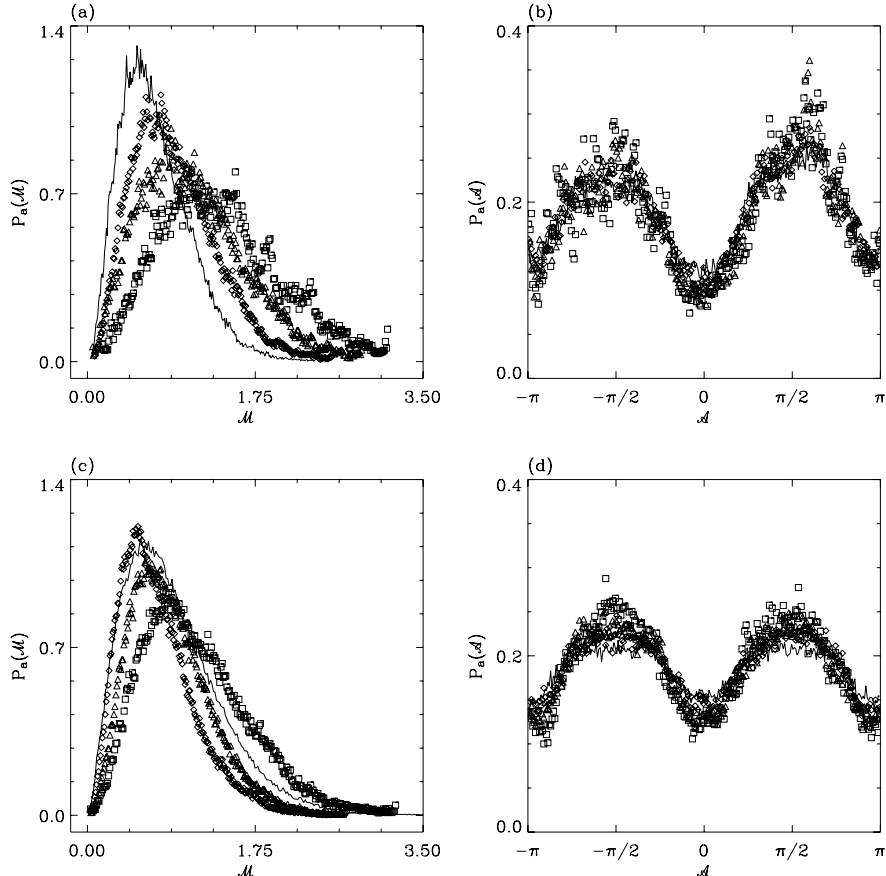


Figure 3.46: Pdfs of the WTMMM coefficients of the Local arm subregions as computed at different scales $a = 2^{1.0}$ (full line), $2^{1.5}$ (\diamond), $2^{2.0}$ (\triangle), $2^{2.5}$ (\square) (in σ_W units, where $\sigma_W = 13$ pixels). (a) $P_a(\mathcal{M})$ vs \mathcal{M} , (b) $P_a(\mathcal{A})$ vs \mathcal{A} , where ψ is the first-order analyzing wavelet. (c) $P_a(\mathcal{M})$ vs \mathcal{M} , (d) $P_a(\mathcal{A})$ vs \mathcal{A} , where ψ is the third-order analyzing wavelet. These results correspond to an averaging over all subregions outlined in white in Figure 3.1a.

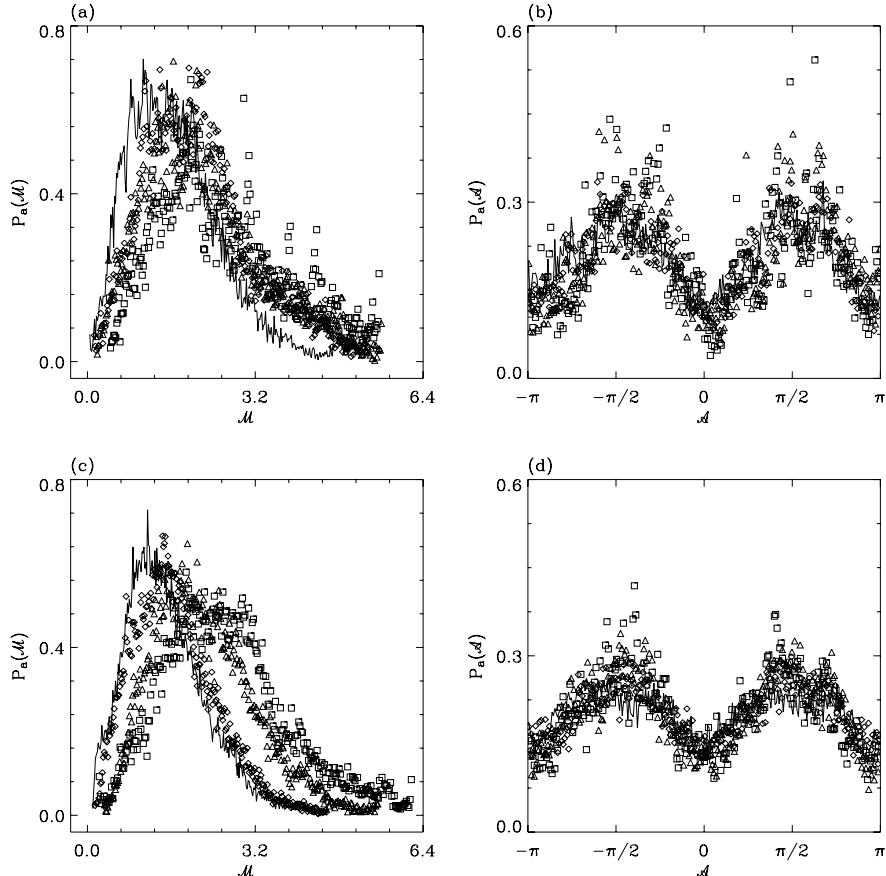


Figure 3.47: Pdfs of the WTMM coefficients of the Perseus arm subregions as computed at different scales $a = 2^{1.0}$ (full line), $2^{1.5}$ (\diamond), $2^{2.0}$ (\triangle), $2^{2.5}$ (\square) (in σ_W units, where $\sigma_W = 13$ pixels). (a) $P_a(\mathcal{M})$ vs \mathcal{M} , (b) $P_a(\mathcal{A})$ vs \mathcal{A} , where ψ is the first-order analyzing wavelet. (c) $P_a(\mathcal{M})$ vs \mathcal{M} , (d) $P_a(\mathcal{A})$ vs \mathcal{A} , where ψ is the third-order analyzing wavelet. These results correspond to an averaging over all subregions outlined in white in Figure 3.1c.

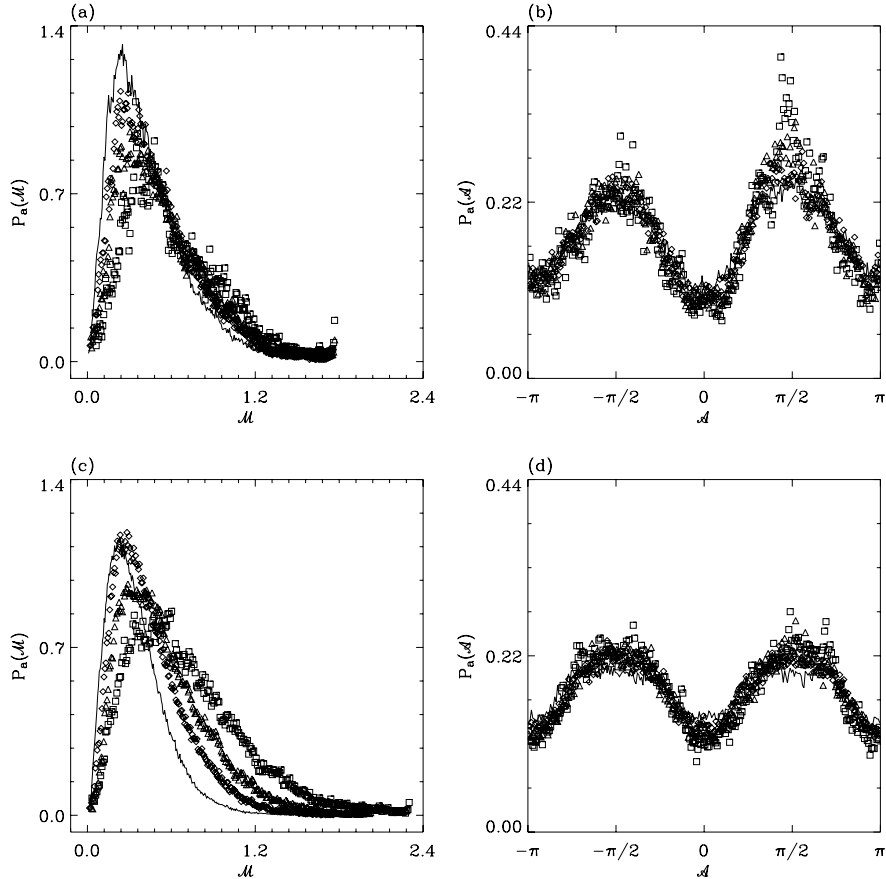


Figure 3.48: Pdfs of the WT MMMM coefficients of the Outer arm subregions as computed at different scales $a = 2^{1.0}$ (full line), $2^{1.5}$ (\diamond), $2^{2.0}$ (\triangle), $2^{2.5}$ (\square) (in σ_W units, where $\sigma_W = 13$ pixels). (a) $P_a(\mathcal{M})$ vs \mathcal{M} , (b) $P_a(\mathcal{A})$ vs \mathcal{A} , where ψ is the first-order analyzing wavelet. (c) $P_a(\mathcal{M})$ vs \mathcal{M} , (d) $P_a(\mathcal{A})$ vs \mathcal{A} , where ψ is the third-order analyzing wavelet. These results correspond to an averaging over all subregions outlined in white in Figure 3.1e.

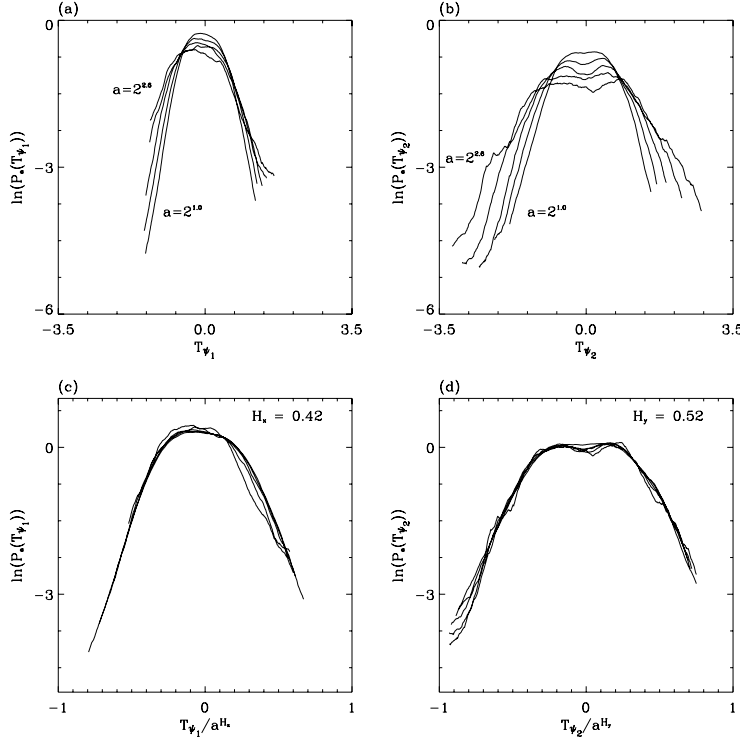


Figure 3.49: Pdfs of the x and y components of the WTMM coefficients of the Local arm subregions as computed with a first-order wavelet at the scales $a = 2^{1.0}, 2^{1.4}, 2^{1.8}, 2^{2.2}$, and $2^{2.6}$ (in $\sigma_W = 13$ units). (a) $\ln(P_a(T_{\psi_1}))$ vs T_{ψ_1} ; (b) $\ln(P_a(T_{\psi_2}))$ vs T_{ψ_2} . In (c) and (d), the pdfs are rescaled by a^{H_x} and a^{H_y} respectively.

$(H_x, H_y) = (0.42, 0.52)$, and $(H_x, H_y) = (0.43, 0.52)$ ($\pm\sigma = 0.03$) respectively for the Local, Perseus, and Outer arms. Therefore, the global Hurst exponents found in §3.5.2.3 above ($H = 0.52$, $H = 0.53$, and $H = 0.51$) are not equal to $\min(H_x, H_y)$ but are rather equal to $\max(H_x, H_y)$. The analysis of the rescaled pdfs using the third-order wavelet confirms these results. Indeed, the third-order wavelet yields $(H_x, H_y) = (0.40, 0.50)$, $(H_x, H_y) = (0.40, 0.50)$, and $(H_x, H_y) = (0.41, 0.48)$ ($\pm\sigma = 0.03$) respectively for the Local, Perseus, and Outer arms. Only the results for the Local arm using the third-order wavelet are shown in Figure 3.52.

Figure 3.53, which corresponds to the rescaled pdfs of T_{ψ_1} by different neighboring values of H_x (Local arm, third-order wavelet), confirms the choice of the uncertainty, $\sigma = 0.03$.

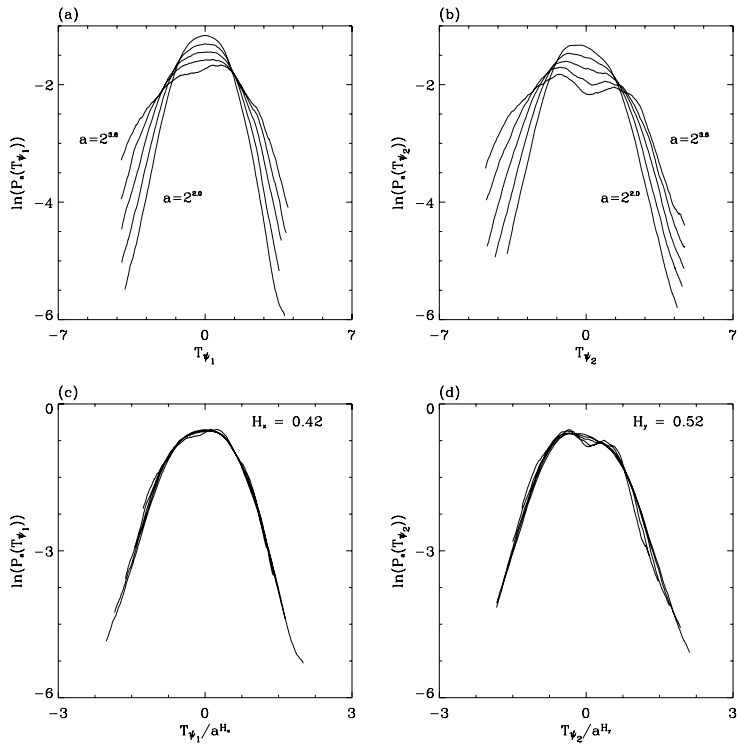


Figure 3.50: Pdfs of the x and y components of the WTMM coefficients of the Perseus arm subregions as computed at the scales $a = 2^{1.0}, 2^{1.4}, 2^{1.8}, 2^{2.2}$, and $2^{2.6}$ (in σ_W units). (a) $\ln(P_a(T_{\psi_1}))$ vs T_{ψ_1} ; (b) $\ln(P_a(T_{\psi_2}))$ vs T_{ψ_2} . In (c) and (d), the pdfs are rescaled by a^{H_x} and a^{H_y} respectively.

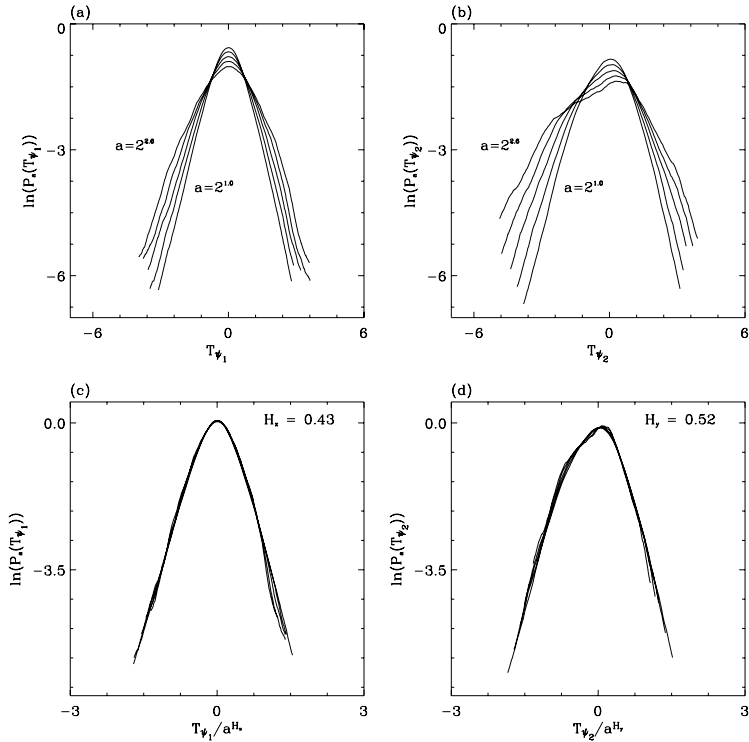


Figure 3.51: Pdfs of the x and y components of the WT MMMM coefficients of the Outer arm subregions as computed at the scales $a = 2^{1.0}, 2^{1.4}, 2^{1.8}, 2^{2.2}, \text{ and } 2^{2.6}$ (in σ_W units). (a) $\ln(P_a(T_{\psi_1}))$ vs T_{ψ_1} ; (b) $\ln(P_a(T_{\psi_2}))$ vs T_{ψ_2} . In (c) and (d), the pdfs are rescaled by a^{H_x} and a^{H_y} respectively.

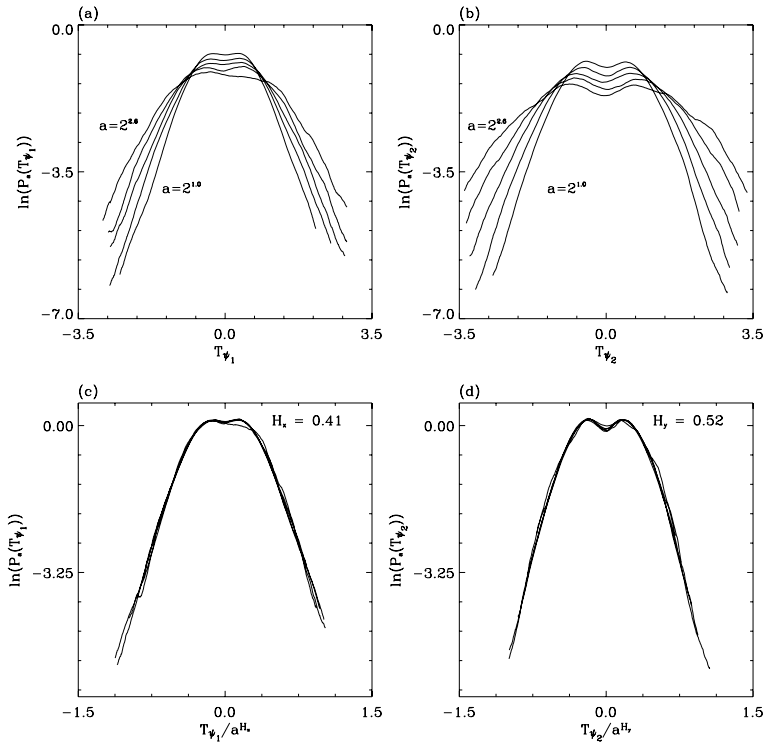


Figure 3.52: Pdfs of the x and y components of the WT MMMM coefficients of the Local arm subregions as computed with a third-order wavelet at the scales $a = 2^{1.0}, 2^{1.4}, 2^{1.8}, 2^{2.2}$, and $2^{2.6}$ (in σ_W units). (a) $\ln(P_a(T_{\psi_1}))$ vs T_{ψ_1} ; (b) $\ln(P_a(T_{\psi_2}))$ vs T_{ψ_2} . In (c) and (d), the pdfs are rescaled by a^{H_x} and a^{H_y} respectively.

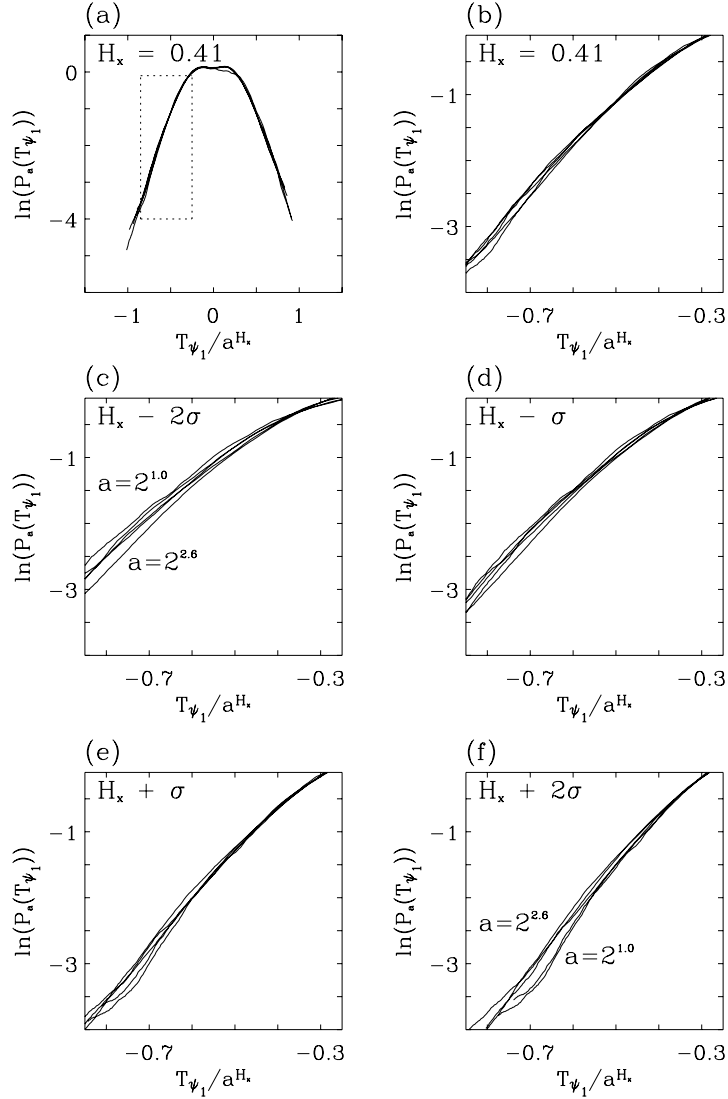


Figure 3.53: Rescaled pdfs of the x components of the WT MMMM coefficients of the Local arm subregions as computed with a third-order wavelet at the scales $a = 2^{1.0}, 2^{1.4}, 2^{1.8}, 2^{2.2}$, and $2^{2.6}$ (in σ_W units). Figure 3.52c is reported in (a). (b) is a zoom-in corresponding to the dashed rectangle in (a). In (c)-(f), the pdfs were rescaled with neighboring values of H_x . $\sigma = 0.03$.

From Figures 3.49a, 3.50a, 3.51a and 3.49b, 3.50b, 3.51b the difference between the width of the curves of $\ln(P_a(T_{\psi_2}))$ vs T_{ψ_2} and $\ln(P_a(T_{\psi_1}))$ vs T_{ψ_1} is quite important. The behavior of the wavelet transform is much more variable in T_{ψ_2} than in T_{ψ_1} , explaining the larger width of the former compared to the latter. This phenomenon affects the global value of the Hurst exponent when calculated with the 2D WTMM methodology (§3.3.1). In effect, since the global H is obtained from the scaling behavior of $\mathcal{M} = (T_{\psi_1}^2 + T_{\psi_2}^2)^{1/2} \sim a^H$, the contribution to \mathcal{M} from T_{ψ_2} is so strong that it dominates the scaling law behavior. And since $T_{\psi_2} \sim a^{H_y}$ (Eq. (3.37)), the global Hurst exponent is equal to the y component of the wavelet transform, i.e., $H = H_y = \max(H_x, H_y)$ (± 0.03).

Furthermore, since the noise restrains us from having access to the smallest scales, where the notions of Hölder and Hurst exponents are valid (i.e., when $a \rightarrow 0^+$, see §3.3.1), it is not unequivocal that the measured global Hurst exponent should be the minimal value of H_x and H_y . If one could have access to the smallest range of scales ($a \rightarrow 0^+$), the global Hurst exponent would be equal to the minimum of the x and y components, i.e., $H = \min(H_x, H_y)$, as seen for the simulated anisotropic surfaces.

Note that any other fractal or multifractal analysis tool would have only detected the global Hurst exponent of these mosaics ($\max(H_x, H_y)$), a clear evidence demonstrating how the wavelet transform is the perfect analysis tool for anisotropic fractal analyses.

Now, physical and/or instrumental processes must exist to explain these two phenomena (the mere presence of an anisotropic signature and the fact that \mathcal{M} scales with $\sim a^{\max(H_x, H_y)}$ instead of $\sim a^{\min(H_x, H_y)}$). Such a discussion is postponed to §3.6.2.

This section concludes with the analysis of the statistical convergence of the partition function for the mosaics (see §3.4.1.4). As an example, Figure 3.54, corresponding to the Local arm, validates the choice for the range of acceptable values for $q \in [-1, 3]$ for all mosaics. The data collected at different scales collapse on a single distribution whose shape depends on q . This is a confirmation that the WTMM analysis is greatly affected by the fact that the number of sub-regions in the mosaics do not total $32 \times 1024 \times 1024$ images and, perhaps more importantly, the fact that the smallest scales (where the WTMM are found in greatest numbers: $N_{WTMM} \sim a^{-2}$) are unavailable due to the noise.

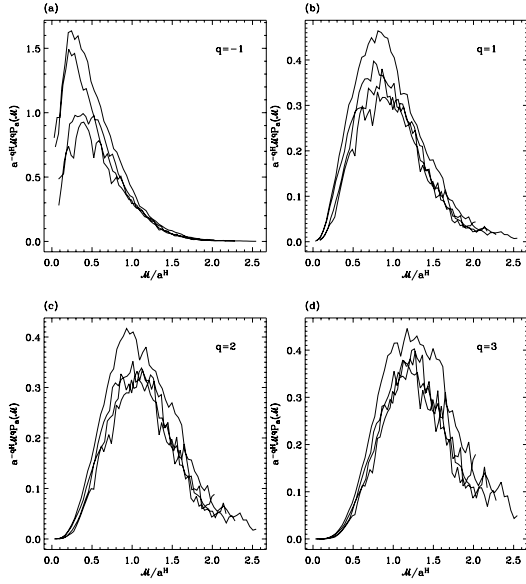


Figure 3.54: Pdfs of the WTMM coefficients for the Local arm mosaic as computed at different scales $a = 2^{1.0}, 2^{1.5}, 2^{2.0}, 2^{2.5}$ (in $\sigma_W = 13$ units). $a^{-qH} \mathcal{M}^q P_a(\mathcal{M})$ vs \mathcal{M}/a^H for $q = -1$ (a), $q = 1$ (b), $q = 2$ (c), and $q = 3$ (d). Same 2D WTMM computations as in Figure 3.46.

3.5.3 The Two Inter-Arms

3.5.3.1 Fourier Analysis

The Fourier analysis of the subregions outlined in white in Figures 3.1b and d are presented in Figures 3.55 and 3.56. The beta indices obtained from the log-log plots of the 2D power spectrum shown in Figures 3.55b and 3.56b are 3.01 ± 0.02 and 3.09 ± 0.04 for the Inter I and Inter II mosaics respectively. The individual beta indices are $\beta_x = 1.90 \pm 0.04$ and 1.88 ± 0.06 and $\beta_y = 1.90 \pm 0.03$ and 1.87 ± 0.04 . Large uncertainties prevent us from comparing these results with the slightly elliptical shape of the contour found in Figures 3.55a and 3.56a. Therefore, from the Fourier analysis alone, one cannot say whether or not an anisotropic structure is present in these two mosaics since these spectral indices do not yield enough quantitative information to compare the roughness nor the strength of this anisotropic signature with those of the three spiral arms.

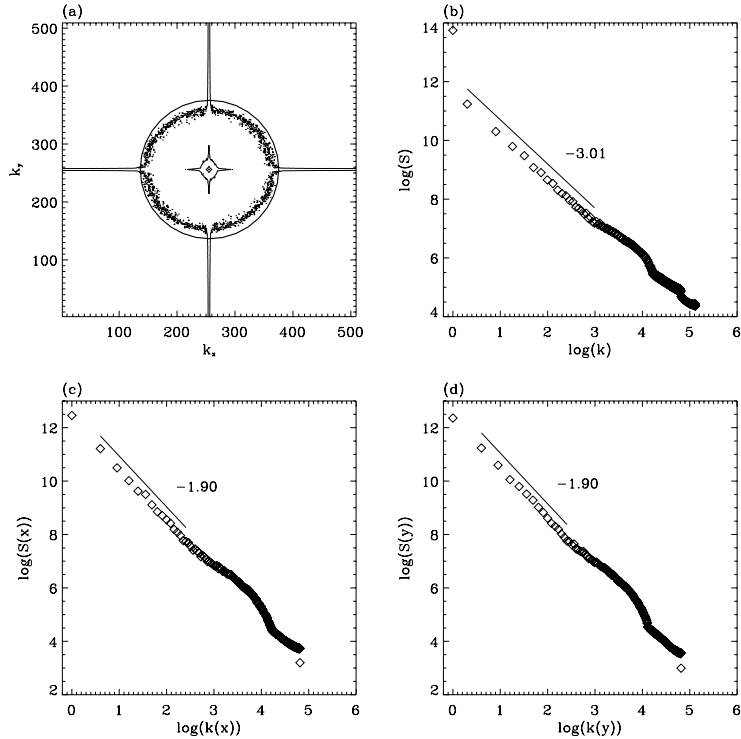


Figure 3.55: Fourier analysis of the Inter I subregions. (a) A contour plot similar to Figure 3.4a, where a black circle was added to help the reader see the slight ellipticity of the contour. (b) The power spectrum $S(|\mathbf{k}|)$ vs $|\mathbf{k}|$ in a logarithmic representation. The solid line corresponds to a power-law fit. (c) The averaged power spectrum of the one-dimensional x -cuts. (d) The averaged power spectrum of the one-dimensional y -cuts.

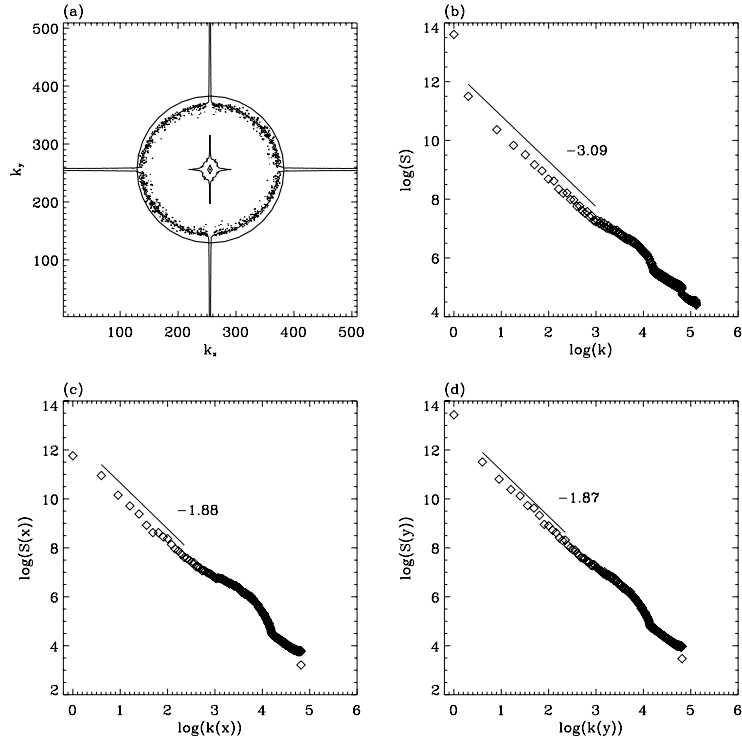


Figure 3.56: Fourier analysis of the Inter II subregions. (a) A contour plot similar to Figure 3.4a, where a black circle was added to help the reader see the slight ellipticity of the contour. (b) The power spectrum $S(|\mathbf{k}|)$ vs $|\mathbf{k}|$ in a logarithmic representation. The solid line corresponds to a power-law fit. (c) The averaged power spectrum of the one-dimensional x -cuts. (d) The averaged power spectrum of the one-dimensional y -cuts.

3.5.3.2 Wavelet Analysis

The wavelet analysis for the subregions of the Inter I and Inter II mosaics with a first-order analyzing wavelet is presented in Figures 3.57 and 3.58. As seen for the study of simulated surfaces in §3.4.1, 3.4.2, and 3.4.3, as well as the study of the three spiral arms in §3.5.2, the maxima chains correspond to well defined edge curves of the smoothed image. Again, when going from large scale (3.57d and 3.58d) to small scale (Figures 3.57c and 3.58c), the characteristic average distance between two nearest neighbour WTMMs decreases like a . This means that the number of WTMMs and in turn, the number of maxima lines, proliferates across scales like a^{-2} .

3.5.3.3 Numerical Computation of the $\tau(q)$ and $D(h)$ spectra

The results obtained from the computation of the $\tau(q)$ and $D(h)$ spectra are presented in Figures 3.59 and 3.60. In Figures 3.59a and 3.60a, and Figures 3.59b and 3.60b the partition function $\mathcal{Z}(q, a)$ and the expectation values $h(q, a)$ display excellent scaling behaviors over the range $a \in [2^{0.9}\sigma_W, 2^{3.0}\sigma_W]$ when plotted versus a , where the range of values of q is $q \in [-1, 3]$. However, as seen for the three spiral arms (§3.5.2), one can clearly see that although the mosaics were filtered to minimize the effect of the noise, the wavelet analysis is restricted to the scales larger than $a = 2^{0.9}\sigma_W$ (where $\sigma_W = 13$ pixels).

When proceeding to a linear regression fit of the data over the ranges $a \in [2^{1.0}, 2^{2.5}]$ and $a \in [2^{1.0}, 2^{3.0}]$ respectively (in $\sigma_W = 13$ units), one gets the $\tau(q)$ spectra shown in Figures 3.59c and 3.60c. The first quantitative difference between the spiral arms and the inter-arm mosaics is that the data do not fall exactly on straight lines. However, the departure from linearity is very slight. Many more data, and less noisy mosaics would be needed to have access to values of q outside of the range $[-1, 3]$. Therefore, one can only say that there is a slight possibility that the two inter-arm mosaics display multifractal scaling, and they will thus be considered as monofractal.

The slopes of the $\tau(q)$ spectra correspond to the Hurst exponents $H = 0.44 \pm 0.03$,

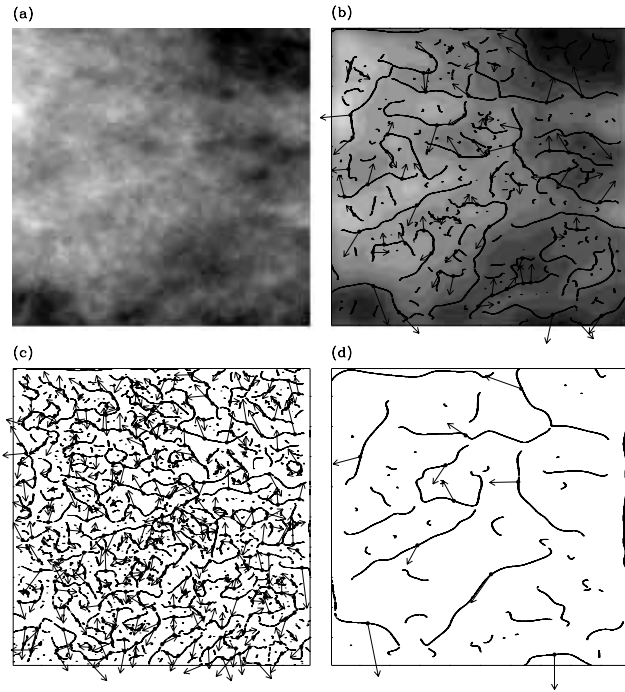


Figure 3.57: 2D wavelet transform analysis of one Inter I subregion. ψ is a first-order radially symmetric analyzing function (see Fig. 3.2). (a) 32 grey-scale coding of the original image, where the intensities range from 18 to 91 K km s^{-1} . In (b) $a = 2^{2.9}\sigma_W$, (c) $a = 2^{1.9}\sigma_W$ and (d) $a = 2^{3.9}\sigma_W$, are shown the maxima chains; the local maxima of \mathcal{M}_ψ along these chains are indicated by (\bullet) from which originate an arrow whose length is proportional to \mathcal{M}_ψ and its direction (with respect to the x -axis) is given by \mathcal{A}_ψ . In (b), the smoothed image is shown as a grey-scale coded background from white (min) to black (max).

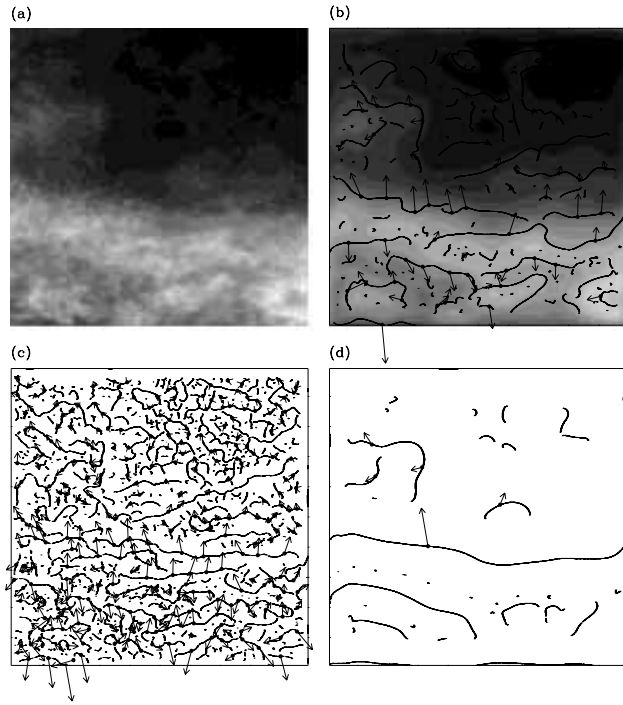


Figure 3.58: 2D wavelet transform analysis of one Inter II subregion. ψ is a first-order radially symmetric analyzing function (see Fig. 3.2). (a) 32 grey-scale coding of the original image, where the intensities range from 0 to 45 K km s^{-1} . In (b) $a = 2^{2.9}\sigma_W$, (c) $a = 2^{1.9}\sigma_W$ and (d) $a = 2^{3.9}\sigma_W$, are shown the maxima chains; the local maxima of \mathcal{M}_ψ along these chains are indicated by (•) from which originate an arrow whose length is proportional to \mathcal{M}_ψ and its direction (with respect to the x -axis) is given by \mathcal{A}_ψ . In (b), the smoothed image is shown as a grey-scale coded background from white (min) to black (max).

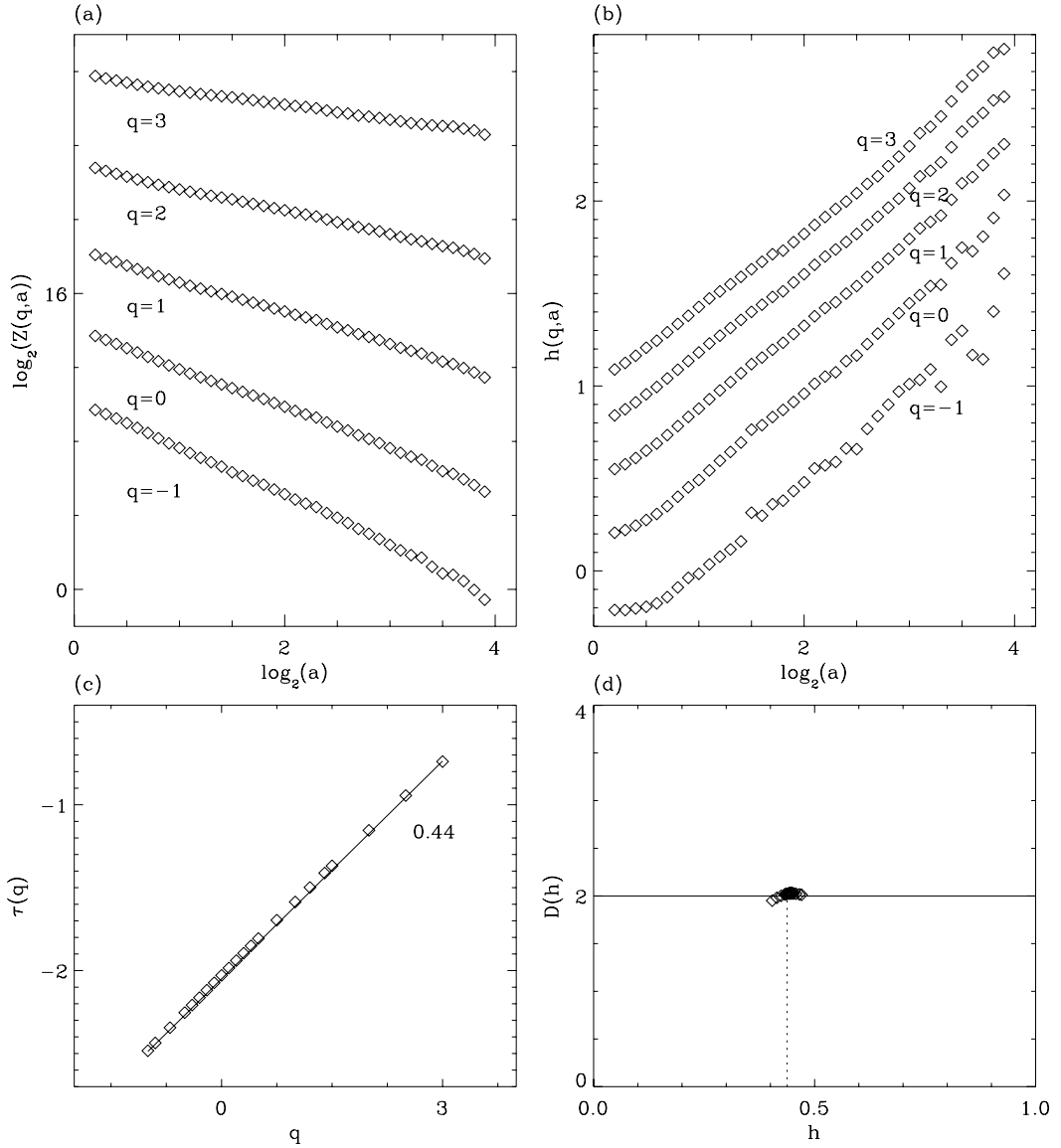


Figure 3.59: Determination of the $\tau(q)$ and $D(h)$ spectra of the Inter I subregions with the 2D WTMM method. (a) $\log_2 \mathcal{Z}(q,a)$ vs $\log_2 a$. (b) $h(q,a)$ vs $\log_2 a$. (c) $\tau(q)$ vs q ; the solid line corresponds to the curve $\tau(q) = qH - 2$, where $H = 0.44$. (d) $D(h)$ vs h as obtained from the scaling behavior of $D(q,a)$ vs $\log_2 a$ (Eq. (3.21)); the symbols have the same meaning as in (c) and the vertical dashed line corresponds to the value of H found in (c). First-order analyzing wavelets. These results correspond to an averaging over all subregions outlined in white in Figure 3.1b. a is expressed in $\sigma_W = 13$ units.

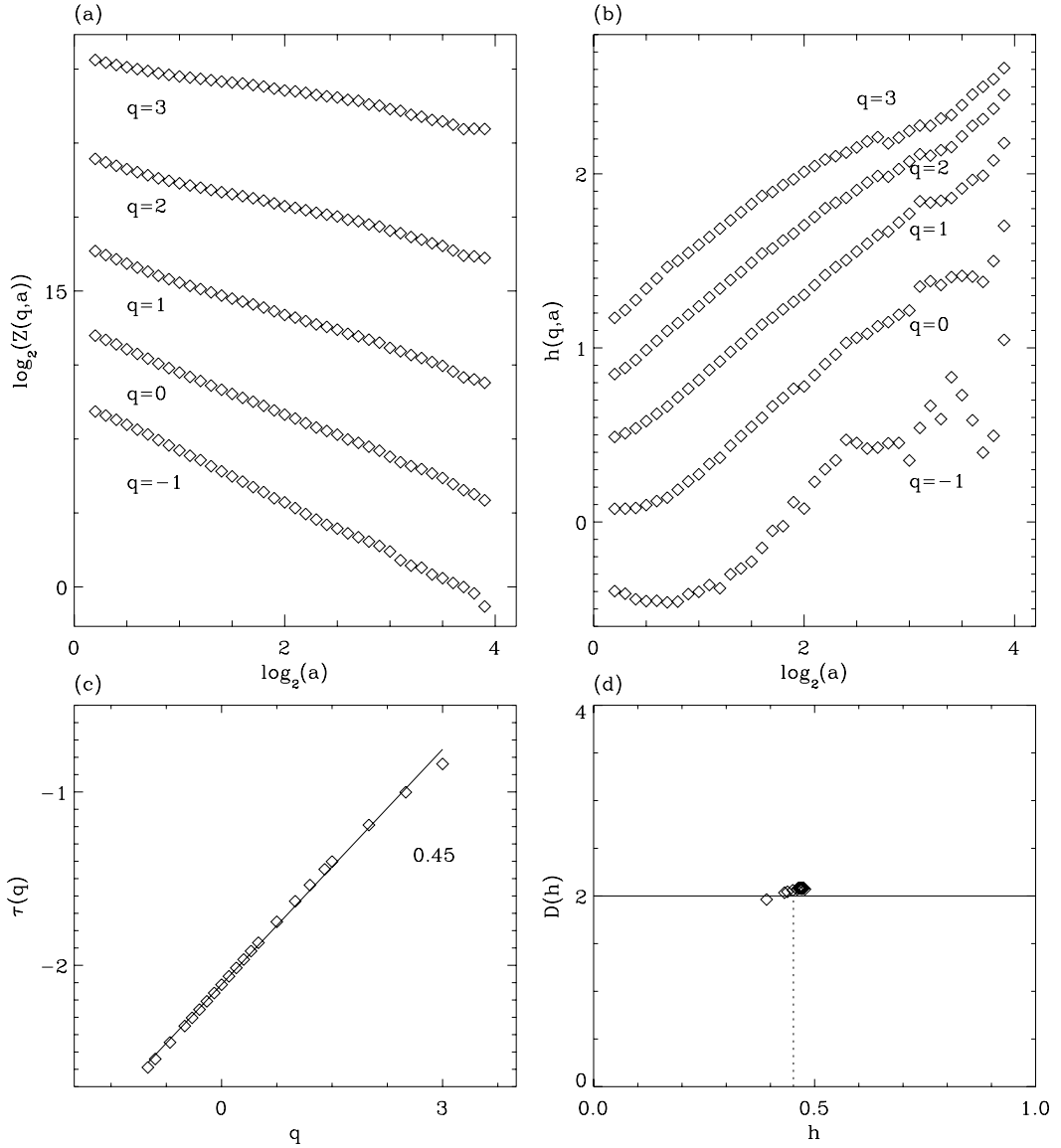


Figure 3.60: Determination of the $\tau(q)$ and $D(h)$ spectra of the Inter II subregions with the 2D WTMM method. (a) $\log_2 Z(q,a)$ vs $\log_2 a$. (b) $h(q,a)$ vs $\log_2 a$. (c) $\tau(q)$ vs q ; the solid line corresponds to the curve $\tau(q) = qH - 2$, where $H = 0.45$. (d) $D(h)$ vs h as obtained from the scaling behavior of $D(q,a)$ vs $\log_2 a$ (Eq. (3.21)); the symbols have the same meaning as in (c) and the vertical dashed line corresponds to the value of H found in (c). First-order analyzing wavelets. These results correspond to an averaging over all subregions outlined in white in Figure 3.1d. a is expressed in $\sigma_W = 13$ units.

and $H = 0.45 \pm 0.03$ respectively for the Inter I and Inter II mosaics. Accordingly, the $D(h)$ singularity spectra shown in Figures 3.59d and 3.60d correspond to $D(h = 0.44) = 2.00 \pm 0.03$ and $D(h = 0.45) = 2.03 \pm 0.03$.

3.5.3.4 Probability Density Functions

In Figures 3.61 and 3.62 are shown the pdfs $P_a(\mathcal{M})$ and $P_a(\mathcal{A})$, computed for four different values of the scale parameters $a = 2^{1.0}$, $2^{1.5}$, $2^{2.0}$, and $2^{2.5}$ (in $\sigma_W = 13$ units). The corresponding pdfs $P_a(\mathcal{A})$ are represented in Figures 3.61b and 3.62b. Again, $P_a(\mathcal{A})$ is clearly peaked at $\pm\pi/2$, a behavior very similar to the three spiral arms. This is a solid confirmation that, even though the study of the individual beta indices (β_x and β_y) did not exhibit quantitative anisotropic information, the mosaics do have an anisotropic structure. In Figures 3.61c, 3.62c and 3.61d, 3.62d are shown the pdfs $P_a(\mathcal{M})$ and $P_a(\mathcal{A})$ using a third-order wavelet. The fact that the peaks do not fade when going from the first-order to the third-order wavelet is a confirmation that the anisotropy is not caused by a large-scale structure in the mosaic, a confirmation that the anisotropy signature, like the one found in the spiral arms, is inherent to the analyzed H I structure. And like the spiral arms, many more WTMM pointing towards $\pm\pi/2$ tells us that the direction of greatest intensity variation is vertical, which is interpreted as a situation where vertical structures are more “complex” than horizontal structures, characterized by Hurst exponents $H_x > H_y$. However, as seen for the spiral arms, this is not the case here.

In Figures 3.63a, 3.64a and 3.63b, 3.64b are shown the pdfs of the x and y components of the wavelet transform in logarithmic form: $\ln(P_a(T_{\psi_1}))$ vs T_{ψ_1} and $\ln(P_a(T_{\psi_2}))$ vs T_{ψ_2} . Like the pdfs of the x and y components for the spiral arms, the T_{ψ_2} curves of Figures 3.63b and 3.64b are wider than those of Figures 3.63a and 3.64a. When calculating the individual Hurst exponents by rescaling these curves by H_x and H_y respectively, we find $(H_x, H_y) = (0.45, 0.44)$ and $(H_x, H_y) = (0.42, 0.45)$ ($\pm\sigma = 0.03$) respectively for the Inter I, and Inter II mosaics. The analysis of the rescaled pdfs using the third-order wavelet yields $(H_x, H_y) = (0.41, 0.43)$ and $(H_x, H_y) = (0.42, 0.45)$ ($\pm\sigma = 0.03$) respectively for the Inter I and Inter II mosaics. Therefore from the first and third-order wavelet analysis

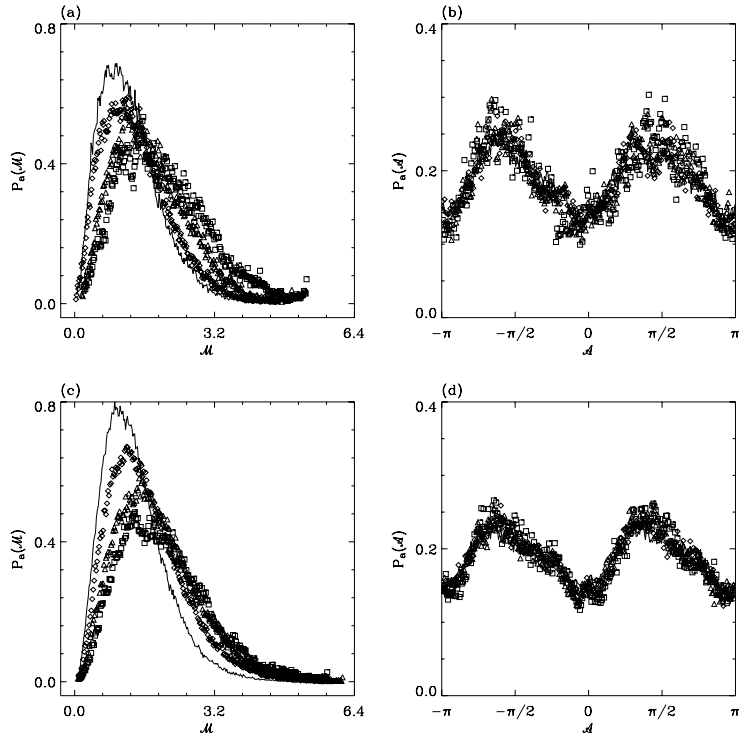


Figure 3.61: Pdfs of the WT MMMM coefficients of the Inter I subregions as computed at different scales $a = 2^{1.0}$ (full line), $2^{1.5}$ (\diamond), $2^{2.0}$ (\triangle), $2^{2.5}$ (\square) (in σ_W units, where $\sigma_W = 13$ pixels). (a) $P_a(\mathcal{M})$ vs \mathcal{M} , (b) $P_a(\mathcal{A})$ vs \mathcal{A} , where ψ is the first-order analyzing wavelet. (c) $P_a(\mathcal{M})$ vs \mathcal{M} , (d) $P_a(\mathcal{A})$ vs \mathcal{A} , where ψ is the third-order analyzing wavelet. These results correspond to an averaging over all subregions outlined in white in Figure 3.1b.

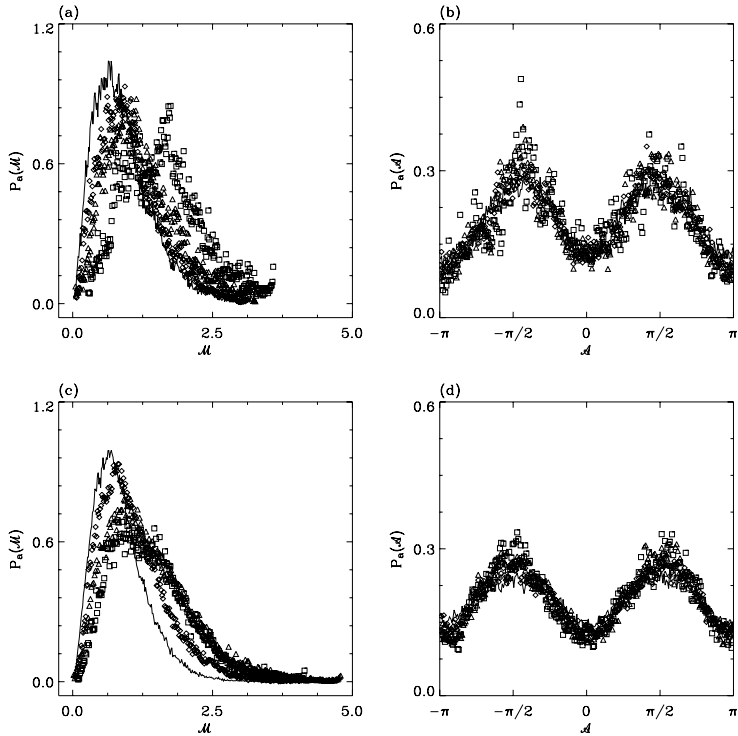


Figure 3.62: Pdfs of the WT MMMM coefficients of the Inter II subregions as computed at different scales $a = 2^{1.0}$ (full line), $2^{1.5}$ (\diamond), $2^{2.0}$ (\triangle), $2^{2.5}$ (\square) (in σ_W units, where $\sigma_W = 13$ pixels). (a) $P_a(\mathcal{M})$ vs \mathcal{M} , (b) $P_a(\mathcal{A})$ vs \mathcal{A} , where ψ is the first-order analyzing wavelet. (c) $P_a(\mathcal{M})$ vs \mathcal{M} , (d) $P_a(\mathcal{A})$ vs \mathcal{A} , where ψ is the third-order analyzing wavelet. These results correspond to an averaging over all subregions outlined in white in Figure 3.1d.

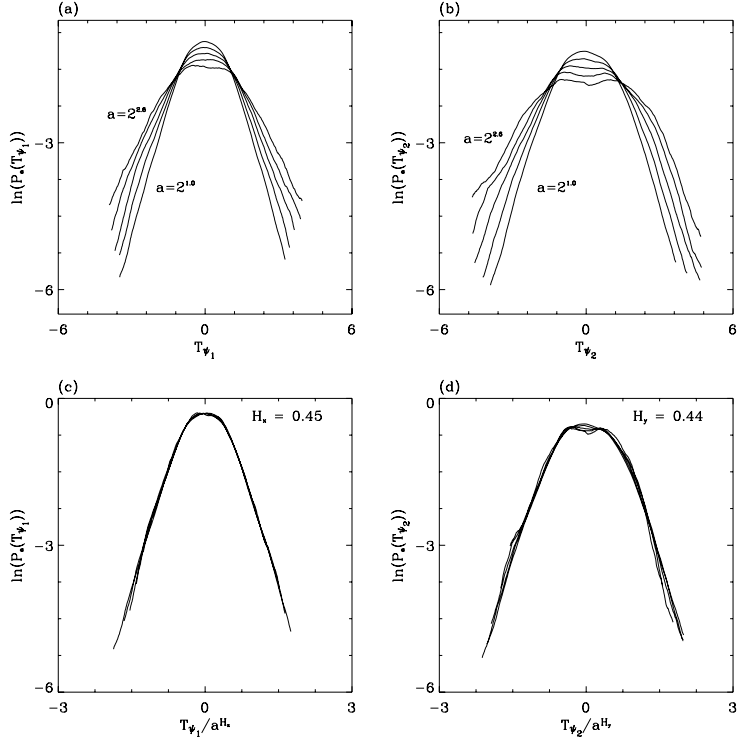


Figure 3.63: Pdfs of the x and y components of the WT MMMM coefficients of the Inter I subregions as computed at the scales $a = 2^{1.0}, 2^{1.4}, 2^{1.8}, 2^{2.2}$, and $2^{2.6}$ (in σ_W units). (a) $\ln(P_a(T_{\psi_1}))$ vs T_{ψ_1} ; (b) $\ln(P_a(T_{\psi_2}))$ vs T_{ψ_2} . In (c) and (d), the pdfs are rescaled by a^{H_x} and a^{H_y} respectively.

of the rescaled pdfs, one cannot determine whether $H_x < H_y$ or $H_x > H_y$ (within 1σ). This means that for both Inter-arm regions, the global Hurst exponents found above are actually the same as the directional Hurst exponent, i.e., $H \sim H_x \sim H_y \sim 0.43 \pm 0.03$.

However, the Inter-arm mosaics do not display isotropic scaling, in which case the pdfs of the arguments ($P_a(\mathcal{A})$) should be flat like the ones for the isotropic monofractal fBm surfaces (Fig. 3.8b). Indeed, there is no doubt that the $P_a(\mathcal{A})$ curves for the Inter-arm mosaics are peaked at $\pm\pi/2$ (Fig. 3.61b,d and 3.62b,d). How then, can one have $H_x = H_y$? The answer comes from the very important fact that the T_{ψ_2} curves of Figures 3.63b and 3.64b are wider than those of Figures 3.63a and 3.64a. The strong contribution from T_{ψ_2} to $\mathcal{M} = (T_{\psi_1}^2 + T_{\psi_2}^2)^{1/2}$ causes the presence of these peaks. This means that the strength of the preferred direction of the WT MMMM (the arrows shown in Figures 3.57b-d and 3.58b-d), i.e. $\pm\pi/2$, does not change with scale.

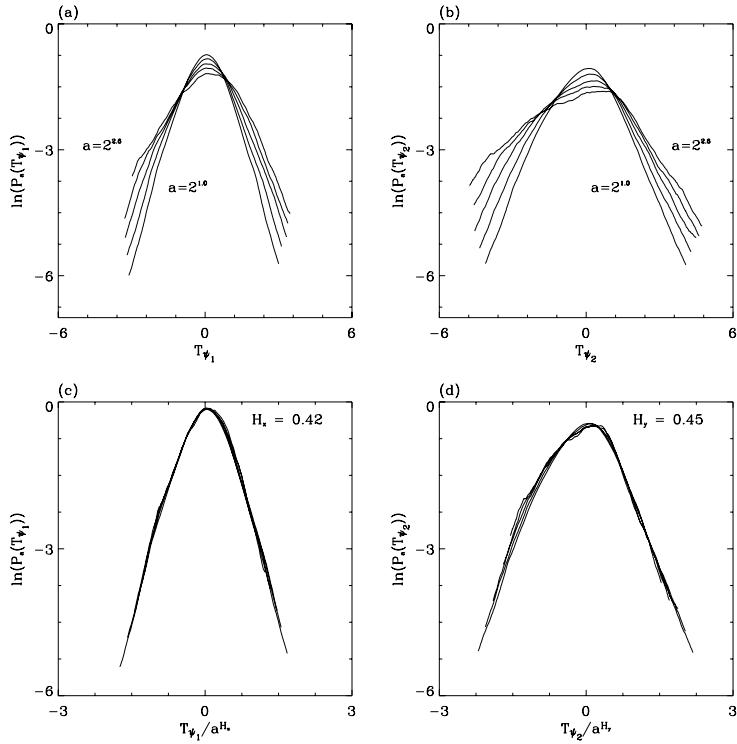


Figure 3.64: Pdfs of the x and y components of the WT MMMM coefficients of the Inter II subregions as computed at the scales $a = 2^{1.0}, 2^{1.4}, 2^{1.8}, 2^{2.2}, \text{ and } 2^{2.6}$ (in σ_W units). (a) $\ln(P_a(T_{\psi_1}))$ vs T_{ψ_1} ; (b) $\ln(P_a(T_{\psi_2}))$ vs T_{ψ_2} . In (c) and (d), the pdfs are rescaled by a^{H_x} and a^{H_y} respectively.

Table 3.2: Hurst Exponents for the Five H I mosaics

Mosaic	Distance (pc)	Physical Scale ^a (pc)	Global H (Gau) (± 0.03)	(H_x, H_y) (Gau) (± 0.03)	(H_x, H_y) (Mex) (± 0.03)
Local	~ 1000	$\sim 2 - 4$	0.52	(0.42, 0.52)	(0.41, 0.52)
Inter I	~ 2500	$\sim 6 - 16$	0.44	(0.45, 0.44)	(0.41, 0.43)
Perseus	~ 3500	$\sim 8 - 24$	0.53	(0.42, 0.52)	(0.40, 0.50)
Inter II	~ 4700	$\sim 11 - 43$	0.45	(0.42, 0.45)	(0.42, 0.45)
Outer	~ 6300	$\sim 14 - 44$	0.51	(0.43, 0.52)	(0.41, 0.48)

a. Range of physical scales used to estimate the scaling exponents with the 2D WTMM method.

Therefore, there are two types of anisotropic signatures. First, there is the anisotropic signature caused only by the greater variability of the y component of the wavelet transform (T_{ψ_2}). The second is the more intuitive anisotropic scaling caused by different directional scaling exponents, i.e., $H_x \neq H_y$. In other words, the ratio of the number of horizontal versus vertical arrows (shown in Figures 3.57b-d and 3.58b-d) does not change with scale for the inter-arms mosaics, while this ratio does change with scale for the spiral arms (Fig.3.40b-d, 3.41b-d, and 3.42b-d).

3.6 ANALYSIS AND DISCUSSION

A summary of the results obtained from the 2D WTMM analysis is presented in Table 3.2. Before starting the analysis, the reader must be reminded that the regions examined here were chosen very carefully. It has been known for some time (see Burton (1976)) that the calculation of the column density is affected by regions where the opacity is ≥ 1 . Therefore, areas with strong absorption features were avoided. Since the galactic plane is sampled, optical thinness is not claimed for every pixel! The sampled area ($101^\circ \leq l \leq 145^\circ, |b| \lesssim 2^\circ$) is especially simple and favorable. The spiral arms are arranged in such a way that lines of constant spiral phase are approximatively lines of constant radial velocity as well. Hence the column density maps combine both velocity field fluctuations and density fluctuations as sources of T_B variations (Rohlfs, 1974).

The following general analysis is presented in two parts. A recap of the results presented in §3.5 together with the differences and similarities between the results obtained from the spiral and inter arm mosaics are presented in §3.6.1, and the astrophysical discussion is presented in §3.6.2.

3.6.1 Spiral vs Inter Arms

The global Hurst exponents for the inter-arm mosaics ($H = 0.44$ and $H = 0.45 \pm 0.03$) are strictly less (within uncertainty) than those of the spiral arms ($H = 0.52$, $H = 0.53$, and $H = 0.51 \pm 0.03$) for the physical scales shown in Table 3.2. Therefore, the H I from the spiral arms is smoother than the H I from the inter-arm regions. Note that the Fourier analysis alone cannot give such precise quantitative information. Indeed, the power spectra analysis gives essentially the same slope whether considering the arms (§3.5.2.1) or inter-arms (§3.5.3.1), i.e. ~ -3.0 . Only the Perseus arm has a significantly larger slope (-3.12). However, within each arm of inter-arm, the slopes vary significantly from one region to the next (Table 3.3). The standard deviations of the mean slopes for all regions are larger than the uncertainties. Again, the Perseus arm has the larger variations. No trends were found between individual slopes and longitude. The overall slope of -3.0 confirms the results of Crovisier & Diskey (1983) and Dickey et al. (2001) but for a much larger section of the Milky Way. These authors observed one 3.2 and two 1.5 square degree areas of the inner Galaxy respectively. Green (1993) analyzed a section of the second quadrant ($l = 140^\circ, b = 0^\circ$) located in our survey, using a different technique. Green worked directly with the *uv*-plane visibilities. His power-law indices are smaller: $-2.4, -2.4, -2.8$ for the arms and $-2.5, -3.0$ for the inter-arms, and with larger uncertainties (± 0.1 to ± 0.3). Hence Green (1993) found a steepening of the slope for the further H I (Inter II and the Outer arm). The results presented here do not follow a similar trend, either in our complete sample or for the regions corresponding to Green's fields. This could be explained by the higher sensitivity of the CGPS data and the different scales that were used to derive the slopes (we were very careful not to include the noise affected small scales, see the first paragraph of §3.5 and Miville-Deschénes et al. (2003)).

Table 3.3: Power Spectral Indices for the Five H I mosaics

Mosaic	Avg β from ind. slopes	σ	Smallest β	Largest β	β from avg slopes
Local	3.01	0.08	2.84 ± 0.05	3.11 ± 0.09	3.01 ± 0.05
Inter I	3.01	0.08	2.91 ± 0.05	3.18 ± 0.06	3.01 ± 0.02
Perseus	3.12	0.13	2.90 ± 0.04	3.37 ± 0.05	3.12 ± 0.05
Inter II	3.09	0.07	2.96 ± 0.04	3.18 ± 0.05	3.09 ± 0.04
Outer	3.01	0.06	2.91 ± 0.09	3.09 ± 0.09	3.01 ± 0.06

Two types of anisotropic structures are detected at all scales studied. For all mosaics (spiral arm and inter-arm), the contribution from the y component of the wavelet transform (T_{ψ_2}) is so great that it dominates the value of the modulus \mathcal{M} . This greater variability of T_{ψ_2} , compared to the variability of T_{ψ_1} , causes the first type of anisotropic signature. The study of the directional Hurst exponents for the inter-arms mosaics, where one finds $H_x \sim H_y \sim 0.43$, implies that these mosaics only exhibit this type of anisotropic signature. The spiral arms show a further anisotropic signature (anisotropic scaling) since the directional Hurst exponents are strictly unequal ($H_x \sim 0.40$ and $H_y \sim 0.50$). Indeed, unlike the study of the anisotropic surfaces in §3.4.3 which showed that $\mathcal{M} \sim a^{\min(H_x, H_y)}$, the results for the spiral arms show that $\mathcal{M} \sim a^{\max(H_x, H_y)}$. The physical phenomena possibly responsible for the greater variability are discussed in §3.6.2.1.

When compared to the H I from the inter-arm regions, the H I from the spiral arms has been “elongated” in the vertical (galactic latitude) direction. Again, the Fourier analysis cannot yield such results from the calculated β_x and β_y .

There is a possibility, albeit small, that the inter-arm regions exhibit multifractal scaling (Figures 3.59d and 3.60d). Some comparisons could be made with the aggregates found in dense human breast tissue (Kestener et al., 2001; Kestener, 2003c). In effect, these latter exhibit a slight departure from monofractality. The 2D WTMM method was used to show that these surfaces consisted of aggregates superposed on a dense background. Such a geometry could be present in the two inter-arm regions. A further study on H I aggregates from the two inter-arm regions is required and shall be pursued in the very near future.

3.6.2 Astrophysical Discussion

3.6.2.1 Scale-Height Relation

One is tempted to look for a correlation between the results presented here and the scale-height gradient of the Galaxy. In fact, a logical approach would consist in the construction and analysis of simulated surfaces where such a gradient would be present. For example, the H I vertical distribution from Lockman (1984) could be combined to a monofractal isotropic surface (§3.4.1). However, the function given in Lockman (1984) consists in the sum of two gaussians and an exponential. Therefore, the “Lockman” function is infinitely differentiable and its roughness (or rather, its smoothness) is thus represented by a Hurst exponent of $H = \infty$. The combination of such a function to a 2D fBm surface (where H is usually $\in [0, 1]$) will not affect calculations of the WTMMM and therefore, will not cause an anisotropic signature.

This does not necessarily mean that the anisotropic signature is not caused by the scale-height (vertical) gradient of the galactic H I. It could very well be. However, it would mean that its distribution could not be given by such a smooth function as the “Lockman” function, but rather by a much more complex function characterized by a Hurst exponent, H , in the interval $[0, 1]$ instead of $H = \infty$.

Furthermore, the scale-height gradient could be responsible for the greater variability of the y (vertical) component of the wavelet transform, which causes the widening of the pdfs of T_{ψ_2} for all mosaics, and as seen in §3.5.2.4 and 3.5.3.4, causes the modulus of the wavelet transform (\mathcal{M}) to scale with $\sim a^{\max(H_x, H_y)}$ instead of the theoretically expected $\sim a^{\min(H_x, H_y)}$. However, this effect should therefore be expected to increase with distance, which is not the case here.

3.6.2.2 Anisotropy

This study is an attempt at objectively quantifying the global structure of the H I distribution in our Milky Way. Lengths and widths of spiral features, varying from 1 kpc and 35 pc (Local arm) to 7 kpc and 220 pc (Outer arm) were analyzed. However, the Local arm is close enough that the sampled scales may be too small to properly study latitudinal behaviors. This may be offset by the finding of Porcel et al. (1998) that the Local arm is more than 70 pc over the plane, probably explaining the similarity of the results shown in Table 3.2. The following relates the findings on the anisotropy to the gravitational theory of spiral structure proposed by Lin & Shu (1964, 1966).

It can be demonstrated that interstellar clouds respond strongly to the imposed spiral potential from a density wave, i.e. Roberts (1972). An eloquent illustration of this effect can be found in Toomre (1977), Figure 7b, where harmonic oscillations are exposed to a traveling sinusoidal force. The gas particles are neatly piled up at positions imposed by the frequency of the traveling wave. A galaxian density wave can thus be seen as an ordering mechanism since the spiral arms are the locus of lower shear and lower tidal forces from the background galaxy as compared to the inter-arms (Elmegreen, 1992). This description falls in line with this paper's results, where the spiral arms are globally the smoother galactic features. In the inter-arms, clouds can be broken apart by the larger shear and tidal forces, giving rise to a more irregular gas distribution. However, as mentioned in §3.6.1, the spiral arms have two types of anisotropic signatures. The arms are smoother along b than along l . In fact, the directional Hurst exponent H_x (along l) is ~ 0.4 whether one considers the arms or the inter-arms. Moreover, the reader should keep in mind that the analysis of the smallest scales ($a \rightarrow 0^+$), which were unavailable here because of the relatively high noise level, would yield similar global Hurst exponents for the arms and inter-arms, i.e. $H = \min(H_x, H_y) \sim 0.4$ instead of $H = \max(H_x, H_y)$.

The rugosity of the spiral arms along l may be explained simply by massive star formation activity and its consequence, supernovae. Indeed, the rugosity of the Perseus arm is larger between $104^\circ \leq l \leq 109^\circ$, where five sites of active star formation are present (S139, S142, S146, S152, and S153) and the supernova CTB 109. Similarly for the Local arm, where the H II regions S185 and S187 and the supernovae G126.2+1.6

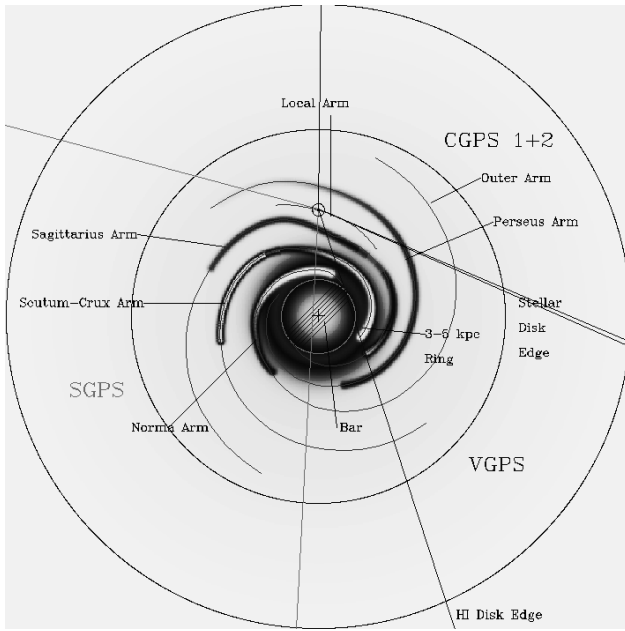


Figure 3.65: Schematic view of the Galactic plane, where one can see the Local, Perseus and Outer arms in the top-right corner. Detailed information of the analyzed subregions ($98^\circ \lesssim l \lesssim 146^\circ$) is presented in §3.2, Table 3.1, and Figure 3.1. (Figure courtesy of S. Gibson.)

and G127.1+0.5 are coeval within $123^\circ \leq l \leq 129^\circ$ ¹². Along l , lines of constant spiral phase are sampled. Therefore, the irregularities in the column density maps are caused either by the “radial” velocity field of galactic rotation or disturbances like supernovae. However, since the galactic rotation velocity field is very smooth, the latter hypothesis is retained as exemplified above. For a schematic view of the plane of the Milky Way and the portion of the CGPS that was analyzed, see Figure 3.65.

The relative smoothness of the arms along b is not easily explained unless the density wave does its ordering role at least up to the scale height of the H I gas (≈ 200 pc) and the kinematic and density disturbances originating in star formation and supernovae are limited to a very thin portion of the disk. The H I layer being so thin, all the gas may follow an identical mean velocity streaming pattern (spiral arms). Lockman (1984) has shown that the mean velocity of the ISM above the plane lies near the circular speed at the corresponding point in the plane for the inner galaxy. Only a process related to

¹²The catalogs of Blitz, Fich & Stark (1982) and Green’s online catalogue (<http://www.mrao.cam.ac.uk/surveys/snrs/>) were consulted.

spiral arms can be invoked to explain the higher H_y value.

In addition to the global processes discussed above, there is a number of phenomena that can act on the vertical extent of the gas.

As mentioned in Dickey & Lockman (1990), the kinetic temperature of H I (3000 – 8000 K) is too low to support it to its observed height against the galactic potential. It could be held up by the photo-levitation of small dusty clouds ($N < 5 \times 10^{20} \text{ cm}^{-2}$) (Franco et al., 1991; Ferrara, 1993). The radiation pressure is provided by the interstellar radiation field and would be stronger near star clusters. Hence, it is argued that this phenomenon is most likely to occur in the inner galaxy. However, the decreasing galactic potential in the outer galaxy may partly offset this segregation. Such a local process would not explain the constancy of H_y along the spiral arms.

Lockman & Gehman (1991) proposed that the random motion of H I clouds, similar to a turbulent pressure, would have enough kinetic energy to rise the H I above the plane. However, this result is not very sensitive to the exact form of the galactic gravitational potential. Again, the high diffusivity associated with this turbulent process cannot be used to explain the arm / inter-arm H_y difference.

Finally, a corrugation effect has been observed in the distribution of H I gas in the spiral arms (Quiroga, 1974, 1977; Spicker & Feitzinger, 1986). This effect is associated only with the arms and is observed along their length. Every young object is affected (OB stars, H II regions, H I) but not molecular clouds. Arms are displaced alternatively to both sides of the galactic plane. The data are somewhat scarce, but Spicker & Feitzinger (1986) estimate wave patterns at scales $1 \text{ kpc} < \lambda < 2 \text{ kpc}$, $4 \text{ kpc} < \lambda < 8 \text{ kpc}$, and $\lambda > 13 \text{ kpc}$. None were found for $\lambda < 1 \text{ kpc}$. The amplitudes range between 145 and 350 pc, they increase with the thickness of the H I distribution. The physical process at the origin of this phenomenon is unknown. Gravitational instabilities of a galactic or extra-galactic nature, the excitation of the galactic warp, magnetic fields have been brought forward but, to our knowledge, no model has been presented. The scale of our observations (1 to 7 kpc in length) is similar to that of the corrugations. It may be the “smoothing factor” we are looking for if spiral arm kinematics have a minor influence on vertical motion.

Unfortunately, the noise level of the DRAO data is too strong to allow a thorough investigation of the smallest scales ($a \rightarrow 0^+$) of the mosaics, where the number of statistics (i.e. the number of WTMM, which behave as $\sim a^{-2}$) are plentiful enough to allow a study of individual sub-regions instead of the averaging methods presented here. With more, cleaner data, one could easily investigate the angle of anisotropy (from the peaks in the pdfs $P_a(\mathcal{A})$) as a function of the galactic longitude (from sub-region to sub-region). Such an analysis could confirm the presence or absence of the corrugation of the H I in the galactic plane.

3.6.2.3 Turbulence

The last step in this discussion is to examine the origin of the anisotropy since so far, only relative comparisons have been made.

Numerous observational and theoretical studies propose the ubiquity of turbulence in the ISM; its signature has been found in all phases of the ISM (Franco & Carramiñana, 1999; Falgarone & Passot, 2003). Recently Wada, Meurer & Norman (2002) have shown through 2D numerical calculations that gravity-driven turbulence in differentially rotating galactic disks reaches a quasi-steady state in a few rotational periods with the energy cascade starting at $\gtrsim 200$ pc. No energy feedback is needed (i.e. supernovae). The inertia range is fitted by $E(k) \sim k^{-1.5}$. For 2D Kolmogorov turbulence, the slope is $-5/3$, while it is -2 for shock dominated turbulence. Hence adding supernovae to the Wada, Meurer & Norman (2002) calculations will change the slope. Interestingly, work by De Avillez & Mac Low (2002) on chemical mixing in a supernova-driven ISM has shown that turbulent mixing dominates at the same large scales as predicted by Wada, Meurer & Norman (2002), i.e., ~ 100 pc. The important point to emphasize is that the turbulence is maintained by a constant supply of energy (gravitational instabilities and energy extracted from the shear field of the galactic rotation) starting at scales of hundreds of parsecs.

Many authors have shown (Miville-Deschénes et al. (2003) and references therein) that the power spectrum of the 3D density field can be determined directly from the power

spectrum of the column density map. However, two conditions have to be satisfied: 1) optical thinness, and 2) the observed spatial scales have to be smaller or equal to the spatial depth of the line of sight. Obviously, only condition 1 cannot be satisfied for every pixel in galactic plane maps such as those used in this paper. The global Hurst exponents derived here for the H I varies from 0.44 – 0.53. However, as mentioned above, having access to the smallest scales would yield global Hurst exponents in the range 0.40 – 0.45 ($\min(H_x, H_y) = H_x$) for arms and inter-arms¹³. The power spectral index of the density fields is thus $\sim 2.8 - 2.9$ (from Eq. 3.28). This value is lower than the predicted 3D Kolmogorov spectrum ($\beta = 11/3$) and thus reflects the variation in optical thickness of the CGPS data. The works of Deshpande, Dwarakanath & Goss (2000) on high optical depth H I regions ($\beta \sim 2.75$) and Bensch, Stutzki & Ossenkopf (2001) on molecular clouds ($\beta \sim 2.65$) show lower slopes and hence the same trend as the H I data presented here. Turbulence thus remains a viable hypothesis as the source of anisotropy for the H I. However, one cannot reject the hypothesis that some other energy injection mechanism is at work.

3.7 CONCLUSION

3.7.1 The Galactic H I

The 2D WTMM method was used to analyze five H I column densities mosaics, corresponding to the Local, Perseus, and Outer spiral arms and the two Inter-arm regions in between.

The formalism was first tested on simulated surfaces. It was shown that the 2D WTMM method can quantitatively characterize isotropic monofractal surfaces, multi-fractal surfaces, as well as anisotropic monofractal surfaces with great accuracy. The

¹³Theoretically, turbulence is multifractal (Arneodo et al., 1995a). However, the multifractality seems to affect the behavior of the $D(h)$ singularity spectrum only if the dissipative scale is reached in the analysis, which is not the case here. Otherwise, the signature is monofractal and $D(h)$ collapses to a single point $D(h = 1/3) = 2$.

characterization of anisotropic structures, by way of the directional Hurst exponents $0 \leq H_x, H_y \leq 1$ is novel.

The results presented in this paper show that the roughness of the H I mosaics, as characterized by the global Hurst exponent, H , is stronger in the inter-arm regions than in the spiral arms. However, having access to the smallest analyzable scales would yield similar global Hurst exponents for both arms and inter-arms. The main difference between arms and inter-arms is the discovery of two types of anisotropic structures. For the spiral arms, the anisotropic signature is scale-dependent while it is scale-independent for the inter-arms. Indeed, the spiral arms have different directional Hurst exponents ($H_x \sim 0.4$ and $H_y \sim 0.5$) while the inter-arms have similar directional Hurst exponents ($H_x \sim H_y \sim 0.43$). The anisotropic signature found in the inter-arms is caused only by the vertical distribution of the H I, which is much more variable than the horizontal distribution. This was also observed for the spiral arms, hence the two types of anisotropic signatures.

In an attempt to explain these quantitative results, several hypotheses have been presented:

- 1) The scale-height gradient could be responsible for the greater variability of the vertical distribution of the H I, and thus the scale-independent anisotropic signature found in all five mosaics (§3.6.2.1).
- 2) The density wave and star formation activity could explain the difference in longitudinal and latitudinal rugosity in the spiral arms.
- 3) The photo-levitation of dusty clouds and the random motion of H I clouds were rejected as responsible candidates for the anisotropic structure.
- 4) Corrugation could be related to the anisotropic signature. Future studies could confirm this hypothesis.
- 5) Finally, interstellar turbulence could be at the origin of the intrinsic roughness of

both arms and inter-arms.

3.7.2 Future Work

The technique used to calculate the individual Hurst exponents, H_x and H_y will be generalized to allow a characterization in any direction, θ and $\theta + \pi/2$. Instead of the relations involving the x and y components of the wavelet transform, i.e. $T_{\psi_1}[f](\mathbf{b}, a) \sim a^{H_x}$ and $T_{\psi_2}[f](\mathbf{b}, a) \sim a^{H_y}$, more general relations will be used. For example, one could have $\mathcal{K}_1[f](\mathbf{b}, a) \sim a^{H_\theta}$ and $\mathcal{K}_2[f](\mathbf{b}, a) \sim a^{H_{\theta+\pi/2}}$, where \mathcal{K}_1 and \mathcal{K}_2 are two general functions depending on both (or a combination of) T_{ψ_1} and T_{ψ_2} .

The “Lockman” scale-height function should be investigated to find out whether or not it can be changed to a more complex version, where $H \in [0, 1]$. Such a new function could, at least partly, explain the anisotropic signature found in the H I mosaics.

An exploration of the recently observed “Cepheus flare” extension of the CGPS will yield very interesting complementary results for high-latitude H I structures ($5^\circ \lesssim b \lesssim 17^\circ$).

3.8 ACKNOWLEDGEMENTS

Many thanks to M.A. Miville-Deschénes for providing us the IDL codes for the “à trous” filtering method. L. Nadeau is acknowledged for the production of the mosaics.

3.9 APPENDICES

This section presents two examples and a numerical implementation algorithm to help the reader appreciate the details of the 2D WTMM methodology. Except for a minor

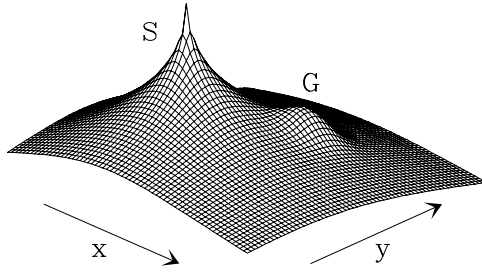


Figure 3.66: Three-dimensional representation of the function $f_1(\mathbf{x}) = Ae^{-(\mathbf{x}-\mathbf{x}_1)^2/2\sigma^2} + B|\mathbf{x}-\mathbf{x}_0|^{0.3}$. The isotropic singularity S is located at $\mathbf{x}_0 = (-256, -256)$. The gaussian localized structure G of width $\sigma = 128$ is located at $\mathbf{x}_1 = (256, 256)$. The parameter values are $A = 1$ and $B = -1$. (Figure taken from Arneodo, Decoster & Roux (2000).)

alteration in step 4 of the description of the numerical algorithm, both following sections were taken from Arneodo, Decoster & Roux (2000).

3.9.1 Examples

In this section are presented two examples to help the reader understand how the 2D wavelet transform behaves on isolated singularities

Example 1: Isotropic singularity interacting with a localized smooth structure.

Let us start by illustrating the definitions above on the function f_1 shown in Figure 3.66:

$$f_1(\mathbf{x}) = Ae^{-(\mathbf{x}-\mathbf{x}_1)^2/2\sigma^2} + B|\mathbf{x}-\mathbf{x}_0|^{0.3}. \quad (3.40)$$

This function is C^∞ everywhere except at $\mathbf{x} = \mathbf{x}_0$ where f_1 is isotropically singular with a Hölder exponent $h(\mathbf{x}_0) = 0.3$. Its 2D wavelet transform (Eq. (3.5)) is shown in Figure 3.67 for a given scale $a = 2^3\sigma_W$, where $\sigma_W = 13$ pixels is the width of the (first-order) analyzing wavelet at the smallest scale where it is still well enough resolved. $T_{\psi_1}[f_1]$ and $T_{\psi_2}[f_1]$ (Eq. 3.6) are shown in Figure 3.67a and 3.67b respectively. The corresponding modulus $\mathcal{M}_\psi[f_1]$ and argument $\mathcal{A}_\psi[f_1]$ are represented in Figures 3.67c and 3.67d. From

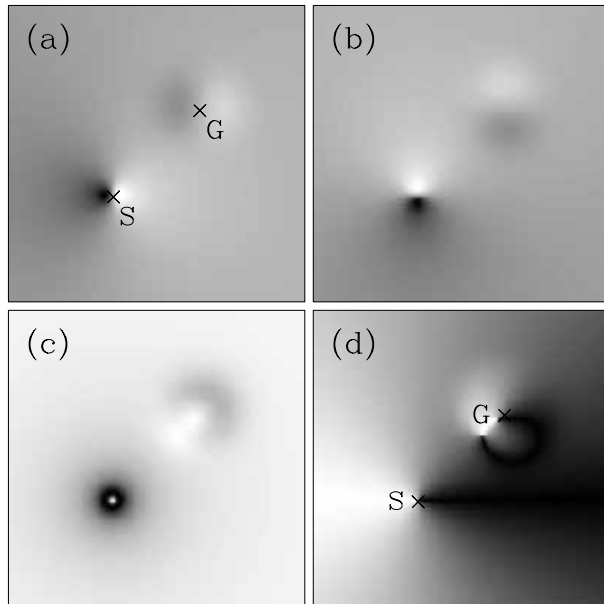


Figure 3.67: Wavelet transform (Eq. (3.6)) of the function f_1 shown in Figure 3.66, with a first-order analyzing wavelet (ϕ is the isotropic gaussian function). (a) $T_{\psi_1}[f_1]$; (b) $T_{\psi_2}[f_1]$ coded using 32 grey levels from white ($\min T_{\psi}$) to black ($\max T_{\psi}$). (c) $\mathcal{M}_{\psi}[f_1]$ coded from white ($\mathcal{M}_{\psi} = 0$) to black ($\max \mathcal{M}_{\psi}$). (d) $|\mathcal{A}_{\psi}[f_1]|$ coded from white ($|\mathcal{A}_{\psi}| = 0$) to black ($|\mathcal{A}_{\psi}| = \pi$). The considered scale is $a = 2^3 \sigma_W$ where $\sigma_W = 13$ (pixels) is the characteristic size of ψ at the smallest resolved scale. (Figure taken from Arneodo, Decoster & Roux (2000).)

a simple visual inspection of Figure 3.67c, one can convince oneself that the modulus is radially symmetric around \mathbf{x}_0 where is located the singularity S. This is confirmed in Figure 3.67d where $\mathcal{A}_\psi[f_1]$ rotates uniformly from 0 to 2π around \mathbf{x}_0 . The WTMM as well as the WTMMM are shown in Figure 3.68 for various values of the scale parameter a ranging from $a = 2^{3.5}\sigma_W$ (Fig. 3.68a) to $a = 2^{7.5}\sigma_W$ (Fig. 3.68f). At small scale, there exist mainly two maxima chains. One is a closed curve around \mathbf{x}_0 where is located the singularity S. The other one is an open curve which partially surrounds G. On each of these maxima chains, one finds only one WTMMM (\bullet) whose corresponding arguments are such that the gradient vector points to S and G respectively. As far as the singularity S is concerned, this means that the direction of largest variation of f_1 around S is given by $\theta_{\mathbf{x}_0} = \mathcal{A}_\psi[f_1] + \pi$, where $\mathcal{A}_\psi[f_1]$ is the argument of the corresponding WTMMM. When increasing the scale parameter, the maxima chains evolve; in particular the closed maxima chain around S swells (its characteristic size behaves like a) until it connects with the maxima chain associated with G (Fig. 3.68d) to form a single closed curve surrounding both S and G (Fig. 3.68f). The topological evolution of the maxima chains in the space-scale half-hyperplane is illustrated in Figure 3.69. This 3-dimensional representation enlightens the existence of two maxima lines obtained by linking the WTMMM step by step (i.e. as continuously as possible) from small to large scales. One of these maxima lines points to the singularity S in the limit $a \rightarrow 0^+$. As shown in Figure 3.70a, along this maxima line ($\mathcal{L}_{\mathbf{x}_0}(a)$), the wavelet transform modulus behaves as (Mallat & Zhong, 1992; Mallat & Hwang, 1992)

$$\mathcal{M}_\psi[f_1](\mathcal{L}_{\mathbf{x}_0}(a)) \sim a^{h(\mathbf{x}_0)}, \quad a \rightarrow 0^+, \quad (3.41)$$

where $h(\mathbf{x}_0) = 0.3$ is the Hölder exponent of S. Moreover, along this maxima line, the wavelet transform argument evolves towards the value (Fig 3.70c):

$$\mathcal{A}_\psi[f_1](\mathcal{L}_{\mathbf{x}_0}(a)) = \pi + \theta_{\mathbf{x}_0}, \quad a \rightarrow 0^+, \quad (3.42)$$

where $\theta_{\mathbf{x}_0}$ is nothing but the direction of the largest variation of f_1 around \mathbf{x}_0 , i.e., the direction to follow from \mathbf{x}_0 to cross the maxima line at a given (small) scale. From the maxima line $\mathcal{L}_{\mathbf{x}_0}(a)$, one thus gets the required amplitude as well as directional information to characterize the local Hölder regularity of f_1 at \mathbf{x}_0 . Note that along the other maxima line $\mathcal{L}_{\mathbf{x}_1}(a)$ which points to \mathbf{x}_1 where is located the smooth localized structure G, the wavelet transform modulus behaves as (Fig. 3.70b):

$$\mathcal{M}_\psi[f_1](\mathcal{L}_{\mathbf{x}_1}(a)) \sim a^{n_\psi}, \quad a \rightarrow 0^+, \quad (3.43)$$

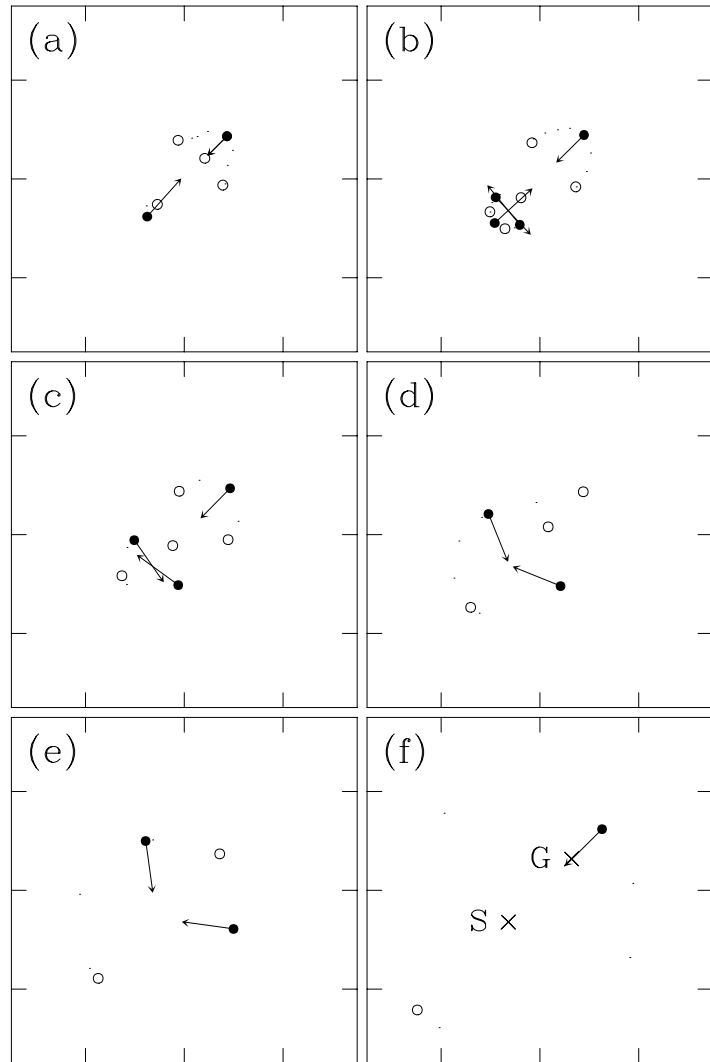


Figure 3.68: Maxima chains (solid line) defined by the WTMM of the function f_1 (Fig. 3.66). The local maxima (resp. minima) along these chains are indicated by (\bullet) (resp. (\circ)) from which originates an arrow whose length is proportional to $\mathcal{M}_\psi[f_1]$ and its direction (with respect to the x -axis) is given by the WTMM argument $\mathcal{A}_\psi[f_1]$. The scale parameter is $a = 2^{3.5}$ (a), $2^{4.7}$ (b), $2^{5.5}$ (c), $2^{6.3}$ (d), $2^{6.8}$ (e) and $2^{7.5}$ (f) in σ_W units. Same first-order analyzing wavelet as in Fig 3.67. (Figure taken from Arneodo, Decoster & Roux (2000).)

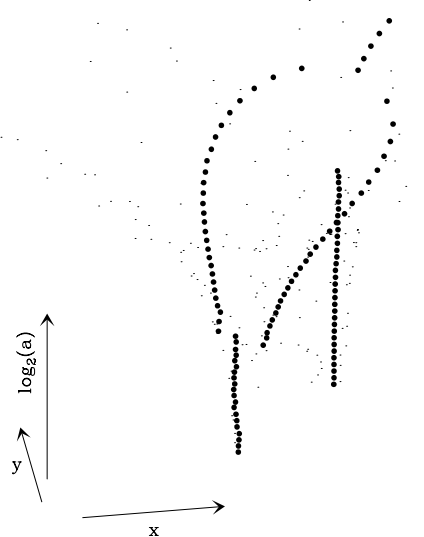


Figure 3.69: Three-dimensional representation of the topological evolution of the WTMM chains of f_1 in the space-scale half-hyperplane. The WTMMMM (\bullet) are disposed on connected curves called maxima lines. These maxima lines are obtained by linking each WTMMMM computed at a given scale to the nearest WTMMMM computed at the scale just above. There exist two maxima lines, $\mathcal{L}_{x_0}(a)$ and $\mathcal{L}_{x_1}(a)$, pointing respectively to the singularity S and to the smooth localized structure G in the limit $a \rightarrow 0^+$. (Figure taken from Arneodo, Decoster & Roux (2000).)

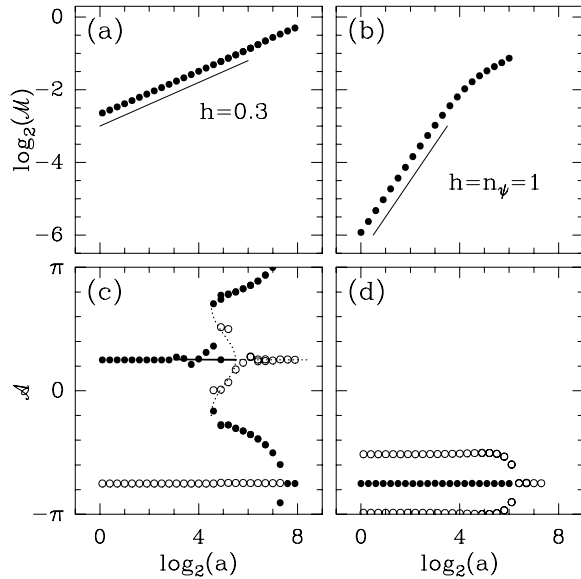


Figure 3.70: Evolution of $\mathcal{M}_\psi[f_1]$ and $\mathcal{A}_\psi[f_1]$ when following, from large scale to small scale, the maxima lines $\mathcal{L}_{\mathbf{x}_0}(a)$ and $\mathcal{L}_{\mathbf{x}_1}(a)$ pointing respectively to the singularity S ((a) and (c) resp.) and to the localized smooth structure G ((b) and (d) resp.). The symbols (●) and (○) have the same meaning as in Figure 3.68. Same first-order analyzing wavelet as in Fig. 3.67. (Figure taken from Arneodo, Decoster & Roux (2000).)

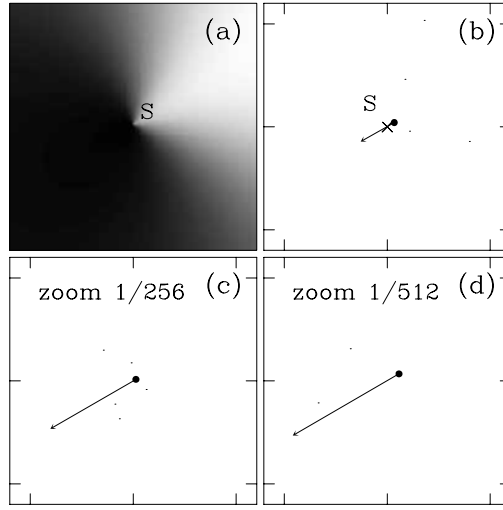


Figure 3.71: WTMM analysis of the function $f_2(\mathbf{x})$ defined in equation (3.44). (a) $f_2(\mathbf{x})$ as coded using 32 grey levels from white (min f_2) to black (max f_2). The maxima chains (solid line) and the WTMM (•) are shown for the following values of the scale parameter $a = 2$ (b), 2^8 (c) and 2^{11} (d) in σ_W units. Same first-order analyzing wavelet as in Fig. 3.67. (Figure taken from Arneodo, Decoster & Roux (2000).)

where $n_\psi = 1$ is the order of the analyzing wavelet. This behavior is to be expected since the smooth localized structure G is infinitely differentiable. More on this topic can be found in Arneodo et al. (1995a); Arneodo, Decoster & Roux (1999, 2000).

Example 2: Anisotropic singularity.

It is possible for a function, $f_2(\mathbf{x})$, to display anisotropic local scale invariance with respect to isotropic dilations. In figure 3.71a is represented the following function:

$$f_2(\mathbf{x}) = f_2(\rho, \theta) = -\rho^{h(\theta)}, \quad (3.44)$$

with

$$h(\theta) = 0.3 \sin(\theta - 2\pi/3) + 0.5. \quad (3.45)$$

The exponent $h(\theta)$ is nothing but the Hölder exponent at $\rho = 0$ of the 1D profile obtained when intersecting the image in Figure 3.71a along the direction θ . Concerning the 2D problem, the Hölder exponent of the singularity S is $h(\mathbf{x}_0) = \min_\theta h(\theta) = 0.2$. It quantifies

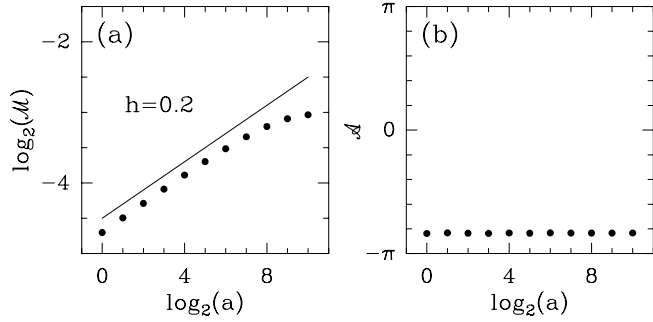


Figure 3.72: Evolution of $\mathcal{M}_\psi[f_2]$ and $\mathcal{A}_\psi[f_2]$ when following, from large to small scales, the maxima line $L_{x_0}(a)$ (\bullet) which points to the singularity S. Same first-order analyzing wavelet as in Figure 3.67. (Figure taken from Arneodo, Decoster & Roux (2000).)

the sharpest variation of $f_2(\mathbf{x})$ which occurs in the direction $\theta_{x_0} = \pi/6$. As shown in Figures 3.71b, c, d for different zooms, there exists at each scale only one WTMM which belongs to a unique maxima line $L_{x_0}(a)$ pointing to the singularity S. Note that this WTMM is located in the direction $\theta_{x_0} = \pi/6$ from the origin. When following $L_{x_0}(a)$ from large to small scales, $\mathcal{M}_\psi[f_2](L_{x_0}(a))$ behaves as a power-law with an exponent $h(x_0) = 0.2$ (Fig. 3.72a) in remarkable agreement with the theoretical prediction for the Hölder exponent of S. Moreover, when investigating $\mathcal{A}_\psi[f_2](L_{x_0}(a))$, one further gets a directional information: $\mathcal{A}_\psi[f_2] = -5\pi/6 = \theta_{x_0} - \pi$, from which one learns about the possible existence of some preferential direction as far as the Hölder regularity properties are concerned.

3.9.2 Numerical Implementation

In this section are presented the main steps of the numerical implementation of the 2D WTMM method as described in Decoster (1999) and Arneodo, Decoster & Roux (2000). Let us consider a $n \times n$ digitized image of a rough surface.

- Step 1: Computation of the 2D wavelet transform. One computes the two components T_{ψ_1} and T_{ψ_2} of the wavelet transform (Eq. (3.5)) in the Fourier domain,

using 2D Fast Fourier Transform (FFT) (Press et al., 1992) and inverse FFT. The analysis begins by choosing the analyzing wavelet among a class of radially isotropic wavelets, here ψ_1 and ψ_2 (Fig. 3.2). To master edge effects only the $n/2 \times n/2$ central part of the image is kept for analysis, where the wavelet coefficients can be shown to be not affected by the boundary of the original image. This means that one must be careful not to increase the scale parameter a above a critical value a_{max} so that the $n/2 \times n/2$ central wavelet coefficients remain safe of finite-size effects. In the opposite limit, one must define a lower bound a_{min} to the accessible range of scales so that the analyzing wavelet be still well resolved at that scale¹⁴. Under those precautions, one can be confident in the wavelet transform microscope as far as the investigation of the scale invariance properties in the range $a \in [a_{min}, a_{max}]$ is concerned.

- Step 2: Computation of the wavelet transform skeleton. At a given scale a , one identifies the wavelet transform modulus maxima (WTMM) as the points where $\mathcal{M}_\psi[f](\mathbf{b}, a)$ (Eq. 3.6) is locally maximum along the gradient direction given by $\mathcal{A}_\psi[f](\mathbf{b}, a)$ (Eq. 3.7). Then the points which are nearest neighbours (which actually have compatible arguments) are chained. Along each of these maxima chains, one locates the local maxima (WTMMM). Note that the two ends of an open maxima chain are not allowed positions for the WTMMM. Once computed the set of WTMMM for a finite number of scales ranging from a_{min} to a_{max} , one proceeds to the connection of these WTMMM from scale to scale. One starts at the smallest scale a_{min} and links each WTMMM to their nearest neighbour found at the next scale just above. This process is done iteratively from scale to scale up to a_{max} . All the WTMMM which then remain isolated are suppressed. All the WTMMM which are connected on a curve across scales which does not originate from the smallest scale a_{min} are also suppressed. One then stores the modulus \mathcal{M}_ψ and the argument \mathcal{A}_ψ of the WTMMM that belong to the so-called maxima lines. Those lines are supposed to converge, in the limit $a \rightarrow 0^+$, to the points where are located the singularities of the image under study. To define the wavelet transform skeleton, one has to select these maxima lines which satisfy equation (3.41) from those which satisfy equation (3.43) and which are wavelet dependent. This is done by increasing

¹⁴The reader is referred to section 1.3.3 of Decoster's PhD thesis manuscript (Decoster, 1999) for a detailed practical definition of the accessible $[a_{min}, a_{max}]$ range of scales

the order of the analyzing wavelet; for n_ψ large enough, the spurious maxima lines are suppressed by a simple thresholding on \mathcal{M}_ψ at the smallest scale a_{min} . Their roots are definitely rejected as misleading singularity locations.

- Step 3: Computation of the multifractal spectrum. According to equation (3.11), one uses the wavelet transform skeleton to compute the partition function $\mathcal{Z}(q, a)$ on the discrete set of considered scales $a_{min} \leq a \leq a_{max}$. Then, for a given value of $q \in [q_{min}, q_{max}]$, one extracts the exponent $\tau(q)$ (Eq. 3.12) from a linear regression fit of $\ln \mathcal{Z}(q, a)$ vs $\ln a$. As a test of the robustness of the measurement, one examines the stability of the estimate of $\tau(q)$ with respect to the range of scales $[a_{min}^*, a_{max}^*] \subset [a_{min}, a_{max}]$ over which the linear regression fit is performed. After estimating the exponent $\tau(q)$ for a discrete set of q -values, the $\tau(q)$ curve is smoothed using standard procedure. Then, one determines the $D(h)$ singularity spectrum by Legendre transforming the $\tau(q)$ curve according to equation (3.13). As a check of the reliability of the results, one uses the alternative strategy defined in equations (3.18) to (3.21) to estimate the $D(h)$ singularity spectrum without performing explicitly the Legendre transform. When dealing specifically with stochastic process, one generally has several images available somehow corresponding to different realizations of this process. In this case, one proceeds to two different averagings corresponding to:

- *Quenched averaging:* One extracts the $\tau(q)$ curve from averaging $\langle \ln \mathcal{Z}(q, a) \rangle$ over the number of images:

$$e^{\langle \ln \mathcal{Z}(q, a) \rangle} \sim a^{\tau(q)}, \quad a \rightarrow 0^+. \quad (3.46)$$

In other words, the $\tau(q)$ spectrum is obtained by averaging over the $\tau(q)$ curves extracted from each individual image.

- *Annealed averaging:* One can alternatively compute the $\tau(q)$ spectrum after averaging the partition functions obtained for each image:

$$\langle \mathcal{Z}(q, a) \rangle \sim a^{\tau(q)}, \quad a \rightarrow 0^+. \quad (3.47)$$

Note that in most of the examples discussed in this work, no significant discrepancy has been observed between the $\tau(q)$ spectra obtained using either one of these averagings. Consequently, in the following the results presented were obtained when estimating the $\tau(q)$ and $D(h)$ multifractal spectra using the annealed averaging.

- Step 4: Computation of the WTMM probability density functions. By representing $\mathcal{M}^q P_a(\mathcal{M})$ as a function of \mathcal{M} , one can objectively define the range of q -values ($q \in [q_{\min}, q_{\max}]$ with $q_{\min} < 0$ and $q_{\max} > 0$) for which the integral in the r.h.s. of equation (3.22) makes sense (Arrault, 1995). Indeed, for a given statistical sample of $n \times n$ images, when considering exaggerated large values of $|q|$, then $\mathcal{M}^q P_a(\mathcal{M})$ is no longer a well defined distribution and the estimate of its integral $\mathcal{Z}(q, a)/\mathcal{Z}(0, a)$ is dramatically affected by a lack of statistical convergence. From the investigation of the shape of $P_a(\mathcal{A})$, and of its possible evolution when varying a , one can then quantify some possible departure from isotropic scaling as well as the existence of possible privileged directions.

Chapitre 4

Conclusion

Deux outils d'analyse d'image ont été utilisés pour caractériser les structures H I du plan de la Galaxie. Comme les conclusions respectives des deux articles sont déjà incluses dans les chapitres 2 et 3, dans ce chapitre nous rappellerons très brièvement les résultats obtenus à l'aide des deux outils avant de discuter des projets futurs et prospectifs qui devraient être entrepris à court, moyen et long terme.

La majorité des contributions de cette thèse sont exclusivement de la part de l'auteur. Hormis celles qui sont plutôt évidentes, surtout dans le chapitre 2 et les choix particuliers des paramètres pour les analyses des surfaces synthétiques présentées dans le chapitre 3, mentionnons notamment:

- 1) L'adaptation des deux méthodologies pour l'analyse des données H I du CGPS.
- 2) La découverte des relations $T_{\psi_1} \sim a^{H_x}$ et $T_{\psi_2} \sim a^{H_y}$ pour les valeurs des exposants de Hurst directionnels tous deux dans l'intervalle $[0, 1]$.
- 3) L'idée de calculer les exposants directionnels β_x et β_y à partir des coupes 1D des images 2D dans le but de les comparer avec les valeurs des exposants de Hurst directionnels H_x et H_y . De plus, aucune étude précédente ne portait sur la relation $\beta = \min(\beta_x + 1, \beta_y + 1)$

(la relation similaire $H = \min(H_x, H_y)$ étant déjà connue).

- 4) La démonstration que les algorithmes fBm 2D standards ne sont pas adéquats pour synthétiser des structures anisotropes (d'où l'utilisation des fBs).

4.1 TECHNIQUE D'ESPACES MÉTRIQUES

Dans le but de poursuivre l'idée originale présentée par Adams en 1992 de faire une analyse multi-facette et objective de données astrophysiques, le formalisme mathématique développé par Adams et Wiseman a été amélioré aux niveaux mathématique et technique et ensuite utilisé pour quantifier la complexité de 28 structures H I associées à des origines connues (régions H II, restes de supernova et étoiles Wolf-Rayet). Les deux résultats les plus importants sont que les supernovae les plus vieilles sont associées à une émission H I plus complexe et que la complexité de l'émission H I photodissocié croît avec le flux de photons ionisants.

4.2 MÉTHODE DES MAXIMA DU MODULE DE LA TRANSFORMÉE EN ONDELETTES

La méthode des Maxima du Module de la Transformée en Ondelettes (MMTO) a été utilisée pour obtenir de l'information quantitative sur la nature fractale / multifractale et sur la structure anisotrope de l'hydrogène neutre de la Galaxie à partir de données provenant du Canadian Galactic Plane Survey. Cinq mosaïques du deuxième quadrant de la Voie Lactée ont été analysées, correspondant aux bras spiraux Local, Persée et Externe, ainsi que les deux milieux "Inter-bras" situés entre ces bras spiraux. Aucune étude objective et quantitative, d'une aussi grande envergure n'avait été effectuée à ce jour pour l'étude du milieu interstellaire. Et de plus, tel que décrit dans le manuscrit, il a été démontré que les méthodes d'analyse dites plus classiques avaient atteint plusieurs de leurs limites, vu la qualité et la quantité sans cesse croissante des données astrophysiques.

Par exemple, nous avons vu que l'utilisation de la pente du spectre de puissance était une technique plutôt limitée car 1) elle ne produit qu'un seul exposant, ce qui la rend inutile pour analyser les structures multifractales (comme la turbulence pleinement développée); et 2) même si la structure analysée est monofractale, l'incertitude sur la pente du spectre de puissance sera toujours plus grande que celle sur le H mesuré à l'aide de la méthode MMTO. Des comparaisons similaires peuvent être faites pour le formalisme multifractal de comptage de boîtes (qui n'est pas adéquat pour caractériser des fonctions, mais plutôt des mesures) et l'approche par fonctions de structure (qui ne peut que caractériser les singularités les plus fortes).

Une signature monofractale est trouvée pour les cinq mosaïques. Une signature anisotrope est détectée: la rugosité des mosaïques est plus grande dans la direction de la longitude que dans la direction de la latitude. Cette anisotropie est indépendante de l'échelle pour les inter-bras tandis qu'elle est dépendante de l'échelle pour les bras spiraux.

Les candidats ou phénomènes pouvant causer la signature anisotrope sont le gradient de distribution en z , l'onde de densité, la formation d'étoiles, la corrugation et la turbulence. Ont été rejetés la photo-lévitation des nuages de poussières et les mouvements aléatoires des nuages H I.

4.3 AUTO-CRITIQUE ET TRAVAUX FUTURS

4.3.1 TEM

Les deux outils d'analyse présentés dans cette thèse devraient être utilisés sur d'autres objets du MIS. À court terme, les directions les plus intéressantes pour la technique d'Espaces Métriques (TEM) sont les récentes extensions du CGPS ainsi que les données du VGPS et du SGPS. De plus, l'ensemble des paramètres physiques (âge, distance, etc.) devrait être homogène pour tous les objets analysés. Une des avenues les plus prometteuse sera l'analyse de régions H I dont le fond (*background*) aura été soustrait.

Ceci est un projet en cours. De plus, il serait intéressant de comparer le classement en complexité des fonctions de sortie dites “géométriques” (densité, volume, composantes et index filamentaires) et celui des fonctions de sortie dites “structurelles” (histogramme et spectre moyenné). Il va sans dire que ces deux familles devraient inclure de nouvelles fonctions de sortie.

La TEM utilise des fonctions de sortie qui caractérisent la complexité des images 2D. Une de ces fonctions, la distribution des index filamentaires (F), doit être améliorée. Tel que mentionné à la section §2.9.1, la définition du diamètre des composantes (composants) doit être modifiée pour pouvoir tenir compte de la convexité de ces objets. Il s’agirait alors de calculer F en forçant le sentier (path) du diamètre à demeurer à l’intérieur des composantes non-convexes (pour les composantes convexes, le diamètre suit un sentier droit).

Les fonctions de sortie de type “géométriques” ne produisent pas d’information spatiale. Par exemple, pour un niveau d’intensité donné, où se trouve la composante ayant le plus grand index filamentaire? Où se trouve(nt) celle(s) étant caractérisée(s) par l’index filamentaire critique $\pi/2$ (rappelons que $F = \pi/2$ peut représenter un carré, une ellipse avec eccentricité $e = 0.77$ ou bien une toute autre structure)? Si le formalisme était amélioré de façon à inclure cette information spatiale et que la définition de l’index filamentaire était revue de telle sorte que les composantes non-convexes puissent être caractérisées adéquatement, alors la coordonnée correspondante, η_f devrait très probablement avoir plus de poids que les autres coordonnées. Tout dépend de l’application (H I, nuages moléculaires, distributions de galaxie) évidemment.

Tel que mentionné à la section 2.9.2, la fondation mathématique soutenant la TEM devrait être entièrement revue et ce, en considérant le simple changement de l’espace des fonctions L^p par l’espace des séquences finies, l^p . Une révision du formalisme de Adams (1992) dans l^p pourrait mener à des améliorations intéressantes du côté mathématique (e.g. simplification et/ou apparition de nouveaux théorèmes).

D’autres fonctions de sortie devraient être utilisées. Entre autres, une analyse par composantes principales (ACP) (Heyer & Schloerb, 1997; Skumanich & López Ariste, 2002) pourrait fournir une information complémentaire aux six fonctions de sortie ex-

istantes. De plus, un nouveau type d'analyse multifractale exploitant les composantes principales vient de voir le jour (Saucier, 2004).

Une des forces de la TEM est son pouvoir d'adaptation. Évidemment, un nouveau contexte scientifique (astrophysique ou non) requiert l'utilisation de fonctions de sortie différentes. Mais, l'importance accordée à chaque fonction de sortie peut être contrôlée. Le schème de classification présenté à la section 2.4.3 pourrait être généralisé de telle sorte que des poids différents soient associés aux fonctions de sortie. Par exemple, on pourrait argumenter que la distribution des filaments (surtout après une révision adéquate, telle que suggéré plus haut) est plus importante que la distribution de la densité. Dans le but de bien calibrer le choix de ces poids, un projet parallèle consisterait alors à construire des surfaces synthétiques ET stochastiques dont les fonctions de sortie seraient connues de façon théorique, ce qui représente un défi technique et mathématique de taille.

4.3.2 Méthode MMTO

Une analyse multifractale des “agrégats” que l'on retrouve dans les inter-bras est requise. Le but serait de vérifier si ces agrégats H I, dont la géométrie fractale semble se rapprocher de celle des microcalcifications dans les seins humains, sont associés à des régions de formation d'étoiles.

Les extensions en longitude et en latitude du CGPS devraient être analysées à l'aide de la méthode MMTO. À plus long terme, les données obtenues à l'aide des futurs relevés (comme le Square Kilometre Array (SKA), par exemple) seront d'une telle résolution que les petites échelles physiques seront accessibles pour la méthode MMTO. L'utilisation de la méthode MMTO pourra même être combinée à la TEM, possiblement comme fonction de sortie.

La technique utilisée pour calculer les exposants de Hurst directionnels, H_x et H_y , devra être généralisée pour permettre la caractérisation d'une anisotropie à n'importe quel angle donné, θ .

Les ondelettes utilisées avec la méthode MMTO sont en fait des dérivées (d'ordres différents) d'une fonction gaussienne. Bien que le formalisme soit construit de telle sorte que l'information directionnelle peut être facilement caractérisée de façon quantitative, d'autres types de "microscopes mathématiques" devraient être considérés. Au-delà des ondelettes, des objets mathématiques comme les *beamlets*, les *ridgelets*, ou bien les *curvelets* devront être investigués. D'ailleurs, les avantages reliés à l'utilisation de "courbelettes" (*curvelets*) au lieu des ondelettes dans les analyses espace-échelle sont présentement démontrés (Candes & Demanet, 2003).

Comme la méthode MMTO n'a pas été exploité à sa pleine puissance (les mosaïques ont beaucoup moins de 32 images 1024×1024 et l'accès aux petites échelles est interdit de par le bruit des données du DRAO), il est difficile d'en faire une critique. Il est toutefois important de rappeler que les fondations purement mathématiques du formalisme 2D ne sont toujours pas élaborées (la méthode repose sur une rigueur mathématique de bonne qualité pour la version 1D). De plus, aux grandes capacités d'analyse de la méthode est associée le besoin d'analyser une (relativement) très grande quantité de données pour produire des résultats statistiquement fiables.

Bibliographie

- Abergel, A., Boulanger, F., Delouis, J. M., Dudziak, G., & Steindling, S. 1996, A&A, 309, 245
- Adams, F.C. 1992, ApJ, 387, 572 (A)
- Adams, F.C., & Wiseman, J. 1994, ApJ, 435, 693 (AW)
- Anselmet, F., Gagne, Y., Hopfinger, E.J., & Antonia, R.A. 1984, J. Fluid Mech., 140, 63
- Arnal, M. 1996, RMxAC, 4, 120
- Argoul, F., Arneodo, A., Elezgaray, J., Grasseau, & G., Murenzi, R. 1990, Phys. Rev. A41, 5537
- Arneodo, A., Bacry, E., & Muzy, J.F. 1991, Wavelet Analysis of Fractal Signals: Direct Determination of the Singularity Spectrum of Fully Developed Turbulence Data (Berlin: Springer Verlag)
- Arneodo, A., Argoul, F., Bacry, E., Muzy, J.F., & Tabard, M. 1992, Phys. Rev. Lett., 68, 3456
- Arneodo, A., Argoul, F., Muzy, J.F., & Tabard, M. 1992, Phys. Lett. A, 171, 31
- Arneodo, A., Argoul, F., Muzy, J.F., & Tabard, M. 1992, Physica A, 188, 217
- Arneodo, A., Argoul, F., Bacry, E., Muzy, J.F., & Tabard, M. 1993, Fractals, 1, 629
- Arneodo, A., Argoul, F., Bacry, E., Elezgaray, J., & Muzy, J.F. 1995 Ondelettes, Multi-fractales et Turbulences: de l'ADN aux croissances cristallines (Paris: Diderot)
- Arneodo, A., Bacry, E., & Muzy, J.F. 1995, Physica A 213, 232

- Arneodo, A., Bacry, E., Graves, P.V., & Muzy, J.F. 1995, Phys. Rev. Lett., 74, 3293
- Arneodo, A. 1996, in Wavelets: Theory and Applications, ed. G. Erlebacher, M.Y. Hussaini, L.M. Jameson (Oxford: Oxford University Press), p. 349
- Arneodo, A., Daubenton-Carafa, Y., Bacry, E., Graves, P.V., & Thermes, C. 1996, Physica D, 96, 291
- Arneodo, A., Bouchaud, J.P., Cont, R., Muzy, J.F., Potters, M., & Sornette, D. 1996, cond-mat/9607120 at xxx.lanl.gov
- Arneodo, A., Muzy, J.F., & Roux, S.G. 1997, J. Phys. II France, 7, 363
- Arneodo, A., Manneville, S., Muzy, J.F., & Roux, S.G. 1998, Eur. Phys. J. B, 1, 129
- Arneodo, A., Audit, B., Bacry, E., Manneville, S., Muzy, J.F., & Roux, S.G. 1998, Physica A, 254, 24
- Arneodo, A., Daubenton-Carafa, Y., Audit, B., Bacry, E., Muzy, J.F., & Thermes, C. 1998, Eur. Phys. J. B, 1, 259
- Arneodo, A., Daubenton-Carafa, Y., Audit, B., Bacry, E., Muzy, J.F., & Thermes, C. 1998, Physica A, 249, 439
- Arneodo, A., Muzy, J.F., Sornette, D. 1998, Eur. Phys. J. B, 2, 277
- Arneodo, A., Bacry, E., & Muzy, J.F. 1998, J. Math. Phys., 39, 4142
- Arneodo, A., Decoster, N., & Roux, S.G. 1999, Phys. Rev. Lett., 83, 1255
- Arneodo, A., Manneville, S., Muzy, J.F., & Roux, S.G. 1999, Phil. Trans. R. Soc. London A, 357, 2415
- Arneodo, A., Decoster, N., & Roux, S.G. 2000, Eur. Phys. J. B, 15, 567
- Arneodo, A., Decoster, N., Kestener, P., & Roux, S.G. 2003, in A Wavelet-Based Method for Multifractal Image Analysis: From Theoretical Concepts to Experimental Applications, ed. P.W. Hawkes, Advances in Imaging and Electron Physics (Academic Press) Vol. 126, p.1
- Arrault, J. 1995, Ph.D. Thesis, Université de Bordeaux I

- Arrault, J., Arneodo, A., Davis, A., &, Marshak, A. 1997, Phys. Rev. Lett., 79, 75
- Audit, B., Bacry, E., Muzy, J.F., & Arneodo, A. 2002, IEEE Trans. on Info. Theory, 48, 2938
- Avedisova, V. S., & Palous, J. 1989, Bull. Astr. Inst. Czech., 40, 42
- Bacry, E., Arneodo, A., Frisch, U., Gagne, Y., & Hopfinger, E. 1991 in Turbulence and Coherent Structures, ed. M. Lesieur, O. Metais (Dordrecht, Kluwer), p.203
- Bacry, E., Muzy, J.F., & Arneodo, A. 1993, J. Stat. Phys., 70, 635
- Badii, R. & Politi, A. 1984, Phys. Rev. Lett., 52, 1661
- Badii, R. & Politi, A. 1985, J. Stat. Phys., 40, 725
- Badii, R. 1987, Ph.D. Thesis, University of Zurich
- Barabási, A.L. & Vicsek, T. 1991, Phys. Rev. A, 44, 2730
- Barabási, A.L., Széfalussy, P., & Vicsek, T. 1991, Physica A, 178, 17
- Barenblatt, G.I., Iooss, G., & Joseph, D.D. 1983, Nonlinear Dynamics and Turbulence (London: Pitman)
- Barnsley, M. F. 1993, Fractals Everywhere (Boston: Academic Press), 2nd edition,
- Batchelor, G.K. & Townsend, A.A. 1949, Proc. Roy. Soc. A, 199, 238
- Bazell, D., & Désert, F.X. 1988, ApJ, 333, 353
- Bensch, F., Stutzki, J., & Ossenkopf, V. 2001, A&A, 366, 636
- Besicovitch, A.S. 1935, Mathematische Annalen, 110, 321
- Binney, J., & Merrifield, M. 1998, Galactic Astronomy (Princeton: Princeton University Press)
- Blitz, L., Fich, M., & Stark, A.A. 1982, ApJS, 49, 183
- Brunt, C.M., Heyer, M.H., Vásquez-Semadeni, E., & Pichardo, B. 2003, ApJ, 595, 2

- Bunde, A. & Havlin, S. (eds) 1991, Fractals and Disordered Systems (Berlin: Springer-Verlag)
- Burton, W.B. 1976, ARA&A, 14, 275
- Campbell, B., & Thompson, R. I. 1984, ApJ, 279, 650
- Candes, E.J. & Demanet, L. 2003, C.R. Math. Acad. Sci. Paris, 336, 395
- Canny, J. 1986, IEEE Trans. on Pattern Analysis and Machine Intelligence, 8, 679
- Caplan, J., Deharveng, L., Peña, M., Costero, R., & Blondel, C. 2000, MNRAS, 311, 317
- Cappa, C.E., Niemela, V.S., Herbstmeier, U., & Koribalski, B. 1996, A&A, 312, 283
- Chappell, D. & Scalo, J. 2001, ApJ, 551, 712
- Chhabra, A.B., Jensen, R.V., & Sreenivasan, K.R. 1989, Phys. Rev. A, 40, 4593
- Chhabra, A.B. & Jensen, R.V. 1989, Phys. Rev. Lett., 62, 1327
- Chhabra, A.B., Meneveau, C., Jensen, R.V., & Sreenivasan, K.R. 1989, Phys. Rev. A, 40, 5284
- Collet, P., Lebowitz, J., & Porzio, A. 1987, J. Stat. Phys., 47, 609
- Combes, J.M., Grossmann, A. & Tchamitchian, P. 1989, Wavelets, (Berlin: Springer-Verlag)
- Chui, C.K. 1992, An Introduction to Wavelets (Boston: Academic Press)
- Crovisier, J. & Dickey, J.M. 1983, A&A, 122, 282
- Cvitanovic, P. 1987, in Proc. Group Theoretical Methods in Physics, ed. R. Gilmore (Singapore, World Scientific)
- Datta, S. 2003, A&A, 401, 193
- Daubechies, I. 1992, Ten Lectures on Wavelets, CBMS-NSF Regional Conference Series in Applied Mathematics (Philadelphia: SIAM)
- De Avillez, M.A. & Mac Low, M.M. 2002, ApJ, 581, 1047

- Decoster, N. 1999, Ph.D. Thesis, Université Bordeaux I
- Decoster, N., Roux, S.G., & Arneodo, A. 2000, Eur. Phys. J. B, 15, 739
- Deshpande, A.A., Dwarakanath, K.S., & Goss, W.M. 2000, ApJ, 543, 227
- Dickey, J.M. & Lockman, F.J. 1990, ARA&A, 28, 215
- Dickey, J.M., McClure-Griffiths, N.M., Stanimirovic, S., Gaensler, B.M., & Green, A.J. 2001, ApJ, 561, 264
- Dickman, R.L., Horwath, M.A., & Margulis, M. 1990, ApJ, 365, 586
- Dobashi, K., Bernard, J.P., Yonekura, Y., & Fukui, Y. 1994, BAAS, 95, 419
- Du, Y. & Ott, E. 1993, Physica D, 67, 387
- Elmegreen, B.G. 1992, in The Galactic Interstellar Medium, ed D. Pfenniger & P. Bartholdi (Berlin: Springer), 157
- Elmegreen, B.G., & Falgarone, E. 1996, ApJ, 471, 816
- Erlebacher, G., Hussaini, M.Y., & Jameson, L.M. 1996 Wavelets: Theory and Applications (Oxford: Oxford University Press)
- Falconer, K.J. 1990, Fractal Geometry: Mathematical Foundations and Applications (New York: John Wiley and Sons)
- Falconer, K.J. 1997, Techniques in Fractal Geometry (New York: John Wiley and Sons)
- Falgarone, E. 1989, in Structure and Dynamics of the Interstellar Medium, ed G. Tenorio-Tagle, M. Moles, & J. Melnick (Berlin: Springer), 68
- Falgarone, E., & Phillips, T.G. 1990, ApJ, 359, 399
- Falgarone, E., Phillips, T.G., & Walker, C.K. 1991, ApJ, 378, 186
- Falgarone, E. & Passot, J. 2003, Turbulence and Magnetic Fields in Astrophysics (Berlin: Springer)
- Family, F., Meakin, P., Sapoval, B., & Wool, R. (eds) 1995 Fractal Aspects of Materials, Material Research Society Symposium Proceedings, Vol. 367 (Pittsburgh)

- Feder, J. 1988, Fractals, (New York: Plenum Press)
- Feigenbaum, M.J., Jensen, M.H., & Procaccia, I. 1986, Phys. Rev. Lett., 57, 1503
- Feitzinger, J.V., & Spicker, J. 1986, PASJ, 38, 485
- Felli, M., Churchwell, E., & Massi, M. 1984, A&A, 136, 53
- Ferrara, A. 1993, ApJ, 407, 157
- Fich, M., & Blitz, L. 1984, ApJ, 279, 125
- Fich, M., Treffers, R. R., & Dahl, G.P. 1990, AJ, 99, 622
- Fich, M. 1993, ApJS, 86, 475
- Flandrin, P. 1998, Temps-Fréquence, 2e édition (Paris: Hermès)
- Flandrin, P., Abry, P., & Goncalvès, P. 2002, in Lois d'échelle, fractales et ondelettes, ed. P. Abry, P. Goncalvès, & J. Lévy-Véhel (Paris: Hermès)
- Fogel, M.E. & Leung, C.M. 1998, ApJ, 570, 379
- Franco, J., Ferrini, F., Ferrara, A. & Barsella, B. 1991, ApJ, 366, 443
- Franco, J. & Carramiñana, A. 1999, Interstellar Turbulence (Cambridge: Cambridge University Press)
- Freund, J. E. 1992, Mathematical Statistics, 5th edition, (Englewood Cliffs, NJ: Prentice-Hall)
- Frisch, U. 1995, Turbulence (Cambridge: Cambridge University Press)
- Gaite, J. & Maurubia, S.C. 2002, MNRAS, 335, 977
- Gautier, T.N., Boulanger, F., Péault, M., & Puget, J.L. 1992, AJ, 103, 4
- Geller, S. 1975, Abrégé de statistique, 2e édition, (Paris: Masson)
- Gill, A.G. & Henriksen, R.N. 1990, ApJ, 365, 27
- Gill, A.G. 1993, Ph.D. Thesis, Queens University, Kingston, Ontario, Canada

- Goldman, I. 2000, ApJ, 541, 701
- Grassberger, G., Badii, R., & Politi, A. 1988 J. Stat. Phys. 51, 135
- Grasseau, G. & Proccacia, I. 1983, Phys. Rev. Lett., 50, 346
- Grasseau, G. & Proccacia, I. 1983, Physica D 9, 189
- Grasseau, G. 1989, Ph.D. Thesis, Université de Bordeaux I
- Green, D.A. 1993, MNRAS, 262, 327
- Grossmann, A. & Morlet, J. 1984, SIAM J. Math. Anal. 15, 723
- Grossmann, A. & Morlet, J. 1985, in Mathematics and Physics, Lectures on Recent Results, ed. L. Streit (Singapour: World Scientific), 135
- Goupillaud, P., Grossmann, A., & Morlet, J. 1984 Geoexploration 23, 85
- Halsey, T.C., Jensen, M.H., Kadanoff, L.P., Procaccia, I., & Shraiman, B.I. 1986, Phys. Rev. A, 33, 1141
- Hausdorff, F. 1919, Mathematische Annalen, 79, 157
- Hentschel, H. & Procaccia, I. 1983, Physica D, 8, 435
- Hatem, A. & Lépine, J.R.D. 1993, A&A, 270, 451
- Heyer, M.H. & Schloerb, F.P. 1997, ApJ, 475, 173
- Heyer, M.H. & Terebey, S. 1998, ApJ, 502, 265
- Heyer, M.H., Brunt, C., Snell, R.L., Howe, J.E., Schloerb, F.P., & Carpenter, J.M. 1998, ApJS, 115, 241
- Holsneider, M. 1996, Wavelets: An Analysis Tool (Oxford: Oxford University Press)
- Houlihan, P. & Scalo, J. 1990, ApJS, 72, 133
- Houlihan, P. & Scalo, J. 1992, ApJ, 393, 172
- Hunter, D., Thronson, H.A., & Wilton, C. 1990, AJ, 100, 1915

- Hunter, D.A., & Massey, P. 1990, AJ, 99, 846
- Jaffard, S. 1991, Publication mathématiques, 35, 155
- Jaffard, S. 1998, C. R. Acad. Sci. Paris, Serie I: Math., 326, 555
- Jensen, M.H., Kadanoff, L.P., & Procaccia, I. 1987, Phys. Rev. A, 40, 4593
- Johnstone, D., Wilson, C. D., Moriarty-Schieven, G., Joncas, G., Smith, G., Gregersen, E., & Fich, M. 2000, ApJ, 545, 327
- Joncas, G., & Mashchenko 1999, New Perspectives on the Interstellar Medium, ed. A. R. Taylor, T. L. Landecker, & G. Joncas (San Francisco:PASP), 363
- Kestener, P., Lina, J.M., Saint-Jean, P., & Arneodo, A. 2001, Image Anal. Stereol., 20, 169
- Kestener, P. & Arneodo, A. 2003, in Proceedings of the 4th Pacific Symposium on Flow Visualization and Image Processing, ed. J. Prenel & Y. Bailly
- Kestener, P. & Arneodo, A. 2003, Phys. Rev. Lett., in press
- Kestener, P. 2003, Ph.D. Thesis, Université de Bordeaux I.
- Khalil, A. 1998, Exploration of the Fractal Dimension, Thèse de maîtrise, Université Concordia
- Khalil, A., Joncas, G., & Nekka, F. 2004, ApJ, 601, 352
- Khalil, A., Joncas, G., Kestener, P. , Nekka, F., & Arneodo, A. 2004, soumission à ApJ en septembre 2004
- Khun, A., Argoul, F., Muzy, J.F., Arneodo, A. 1994, Phys. Rev. Lett., 73, 2998
- Klein, R. I., McKee, C. F., & Colella, P. 1994, ApJ, 420, 213
- Kolmogorov, A.N. 1941, C.R. Acad. Sci. USSR, 30, 301
- Koo, B.C., Rho, J., Reach, W.T., Jung, J., & Mangum, J.G. 2001, ApJ, 552, 175
- Kothes, R., Landecker, T.L., Foster, T., & Leahy, D.A. 2001, A&A, 376, 641

- Kothes, R., Uyaniker, B., & Yar, A. 2002, ApJ, 576, 169
- Lahulla, J. F. 1985, BAAS, 61, 537
- Landecker, T.L., Anderson, M.D., Routledge, D., & Vaneldik, J.F. 1992, A&A, 258, 495
- Landecker, T. L., Dewdney, P. E., Burgess, T. A., et al. 2000, BAAS, 145, 509
- Langer, W.D., Wilson, R.W., & Anderson, C.H. 1993, ApJ, 408, 45
- Lea-Cox, B. & Wang, J.S.Y. 1993, Fractals, 1, 87
- Lebron, M. E., Rodriguez, L. F., & Lizano, S. 2001, ApJ, 560, 806
- Lemarié, P.G. 1990, Les ondelettes en 1989 (Berlin: Springer-Verlag)
- Lequeux, J. 2002, Le milieu interstellaire (Paris: CNRS Éditions)
- Lévy, P. 1965, Processus stochastiques et mouvements Browniens (Paris: Gauthiers-Villars)
- Li, J., Arneodo, A., & Nekka, F. 2004, Chaos and Solitons, submitted
- Lin, C.C. & Shu, F.H. 1964, ApJ, 140, 646
- Lin, C.C. & Shu, F.H. 1966, Proc. Nat. Acad. Sci. USA, 55
- Lockman, F.J. 1984, ApJ, 283, 90
- Lockman, F.J. 1989, ApJS, 71, 469
- Lockman, F.J. & Gehman, C.S. 1991, ApJ, 382, 182
- Lovejoy, S. 1982, Science, 216, 185
- Maisinger, K., Hobson, M.P., & Lasenby, A.N. 2003, MNRAS, 347, 339
- Makse, H.A., Havlin, S., Schwartz, M., & Stanley, H.E. 1996, Phys. Rev. E, 53, 5445
- Mallat, S. & Zhong, S. 1992, IEEE Trans. on Pattern Analysis and Machine Intelligence, 14, 710
- Mallat, S. & Hwang, W.L. 1992, IEEE Trans. on Information Theory, 38, 617

- Mallat, S. 1998 A Wavelet Tour of Signal Processing (New York: Academic Press)
- Mandelbrot, B.B. & Van Ness, J.W. 1968, SIAM Rev., 10, 422
- Mandelbrot, B.B. 1974, C. R. Acad. Sci. Paris Ser. A, 278, 289, 355
- Mandelbrot, B.B. 1974, J. Fluid Mech., 62, 331
- Mandelbrot, B.B. 1977, Fractals: Form, Chance and Dimensions (Freeman: San Francisco)
- Mandelbrot, B.B. 1982, The Fractal Geometry of Nature, (Freeman: San Francisco)
- Mandelbrot, B.B. 1989, Fractals and Multifractals: Noise, Turbulence and Galaxies, Vol. 1 of Selecta (Berlin, Springer-Verlag)
- Meneveau, C. & Sreenivasan, K.R. 1987, Phys. Rev. Lett., 59, 1424
- Meyer, Y. 1990, Ondelettes, (Paris: Herman)
- Meyer, Y. 1992, Wavelets and Applications, (Berlin: Springer-Verlag)
- Meyer, Y. & Roques, S. 1993 Progress in Wavelets Analysis and Applications (Gif-sur-Yvette: Éditions frontières)
- Miville-Deschénes, M.A., Joncas, G., Falgarone, E., & Boulanger, F. 2003, A&A, 411, 109
- Miville-Deschénes, M.A., Levrier, F., & Falgarone, E. 2003, ApJ, 593, 831
- Monin, A.S. & Yaglom, A.M. 1975, Statistical Fluid Mechanics, Vol. 2 (Cambridge, MA: MIT Press)
- Montseny, G. 2004, in preparation
- Moreno, M.A., & Chavarria-K., C. 1986, A&A, 161, 130
- Muzy, J.F., Bacry, E., & Arneodo, A. 1991 Phys. Rev. Lett., 67, 3515
- Muzy, J.F., Bacry, E., & Arneodo, A. 1993 Phys. Rev. E, 47, 875
- Muzy, J.F., Bacry, E., & Arneodo, A. 1994 Int. J. of Bifurcation and Chaos 4, 245

- Normandeau, M., Taylor, A. R., & Dewdney, P. E. 1997, ApJS, 108, 279
- Ott, E., Yunson, D., Sreenivasan, K.R., Juneja, A., & Suri, A.K. 1992, Phys. Rev. Lett., 69, 2654
- Padoan, P., Boldyrev, S., Langer, W., & Nordlund, A 2003, ApJ, 583, 308
- Palandin, G. & Vulpiani, A. 1987, Phys. Rep., 156, 148
- Panagia, N. 1973, AJ, 78, 929
- Parisi, G. & Frisch, U. 1985, in Turbulence and Predictability in Geophysical Fluid Dynamics and Climate Dynamics, Proc. of Int. School, ed. M. Ghil, R. Benzi, & G. Parisi (Amsterdam: North-Holland), p.84
- Peitgen, H.O. & Saupe, D. (eds) 1988, The Science of Fractal Images (New York: Springer-Verlag)
- Pesquet-Popescu, B. & Lvy Vhel, J. 2002, IEEE Signal Processing Magazine Sept. 2002, 48
- Piepenbrink, A., & Wendker, H. J. 1988, A&A, 191, 313
- Pismis, P., Moreno, M.A., & Hasse, I. 1983, RMAA, 8, 51
- Pontrjagin, L. & Schnirelman, L. 1932, Annals of Math., 33, 156
- Porcel, C., Garzon, F., Jimenez-Vicente, J., & Battavier, E. 1998, A&A, 332, 71
- Press, W.H., Flannery, B.P., Teukolsky, S.A., & Vetterling, W.T. 1992, Numerical Recipes (Cambridge: Cambridge University Press)
- Quiroga, R.J. 1974, Ap&SS, 27, 323
- Quiroga, R.J. 1977, Ap&SS, 50, 281
- Rand, D. 1989, Ergod. Th. and Dyn. Sys., 9, 527
- Richardson, L.F. 1922, Weather Prediction by Numerical Process, (Cambridge: Cambridge University Press)
- Roberts, W.W. 1972, ApJ, 173, 259

- Roger, R. S., & Dewdney, P. E. 1992, ApJ, 385, 536
- Rohlfs, K. 1974, A&A, 35, 177
- Roux, S.G., Muzy, J.F., & Arneodo, A. 1999, Eur. Phys. J. B, 8, 301
- Roux, S.G., Arneodo, A., & Decoster, N. 2000, Eur. Phys. J. B, 15, 765
- Ruskai, M.B., Beylkin, G., Coifman, R., Daubechies, I., Mallat, S., Meyer, Y., & Raphael, L. 1992, Wavelets and Their Applications (Boston: Jones and Barlett)
- Rys, F.S. & Waldvogel, A. 1986, in Fractals in Physics, ed. L. Pietronero & G. Tosatti (Amsterdam: Elsevier Science Publications), 461
- Salpeter, E.E. 1955, ApJ, 121, 161
- Sargent, A.I. 1977, ApJ, 218, 736
- Sargent, A.I. 1998, AJ, 115, 2009
- Saucier, A. 2004, en préparation
- Scalo, J. 1987, in Interstellar Processes, ed. D. J. Hollenbach & H. A. Thronson (Dordrecht: Kluwer), 349
- Scalo, J. 1990, in Physical Processes in Fragmentation and Star Formation, ed. R. Capuzzo-Dolcetta, C. Chiosi, & A. DiFazio (Dordrecht: Kluwer), 151
- Schertzer, D. & Lovejoy, S. 1985, Phys. Chem. Hyd. J., 6, 623
- Schertzer, D. & Lovejoy, S. 1987, J. Geophys. Res., 92, 9693
- Schertzer, D. & Lovejoy, S., Schmitt, F., Ghigisinskaya, Y., & Marsan, D. 1997, Fractals, 5, 427
- Schmittbuhl, J., Violette, J.P., & Roux, S.G. 1995, Phys. Rev. E, 51, 131
- Simonson, S.C. 1976, A&A, 46, 261
- Skumanich, A. & López Ariste 2002, ApJ, 570, 379

- Sornette, D. 2000, in Critical Phenomena in Natural Sciences. Chaos, Fractals, Self-Organization and Disorder: Concepts and Tools, Series in Synergetics, ed. H. Haken (Berlin: Springer-Verlag)
- Spicker, J., & Feitzinger, J.V. 1986, A&A, 163, 43
- Spivak, M. 1994, Calculus, Third Edition, (Houston: Publish or Perish)
- Stanimirovic, S., Staveley-Smith, L., Sault, R.J., Dickey, J., & Snowden, S. 1998, IAUS, 190, 61
- Stutzki, J., Bensch, F., Heithausen, A., Ossenkopf, V., & Zielinsky, M. 1998, A&A, 336, 697
- Tatematsu, K., Fukui, Y., Nakano, M., Kogure, T., Ogawa, H., & Kawabata, K. 1987, A&A, 184, 279
- Taylor, A.R. et al. 2003, AJ, 125, 3145
- Tenman, R. 1976, Turbulence and the Navier-Stokes Equations (Lecture Notes in Mathematics, 565), (New York: Springer)
- Toomre, A. 1977, ARA&A, 15, 437
- Torresani, B. 1998 Analyse continue par ondelettes (Les Ulis: Éditions de Physique)
- Uchiyama, Y., Takahashi, T., Aharonian, F.A., & Mattox, J.R. 2002, ApJ, 571, 866
- van der Hucht, K.A. 2001, New Astronomy Reviews, 45, 135
- Vergassola, M., Benzi, R., Biferale, L., & Pisarenko, D. 1993, J. Phys. A, 26, 6093
- Vicsek, T. 1989, Fractal Growth Phenomena (Singapour: World Scientific)
- Vicsek, T., Schlesinger, M., Matsushita, M. (eds) 1994, Fractals in Natural Science (Singapour: World Scientific)
- Vogelaar, M.G.R., & Wakker, B.P. 1994, A&A, 291, 557
- Wada, K., Meurer, G., & Norman, C.A. 2002, ApJ, 577, 197

- Weikand, H., Wouterloot, J.G.A., Castets, A., Winnewisser, G., & Sugitani, K. 1996, A&A, 309, 581
- West, B.J. 1990, Fractal Physiology and Chaos in Medicine (Singapour: World Scientific)
- Westpfahl, D.J., Coleman, P.H., Alexander, J., & Tongue, T. 1999, AJ, 117, 868
- Wilkinson, G.G., Kanellopoulos, J., & Megier, J. (eds) 1995, Fractals in Geoscience and Remote Sensing, Image Understanding Research Series, Vol. 1, ECSC-EC-EAAC (Luxembourg: Bruxelles)
- Williams, P.M., Dougherty, S.M., Davis, R.J., van der Hucht, K.A., Bode, M.F., & Setia Gunawan, D.Y.A. 1997, MNRAS, 289, 10
- Wiseman, J., & Adams, F.C. 1994, ApJ, 435, 708 (WA)
- Wynn-Williams, G. 1992, The Fullness of Space (Cambridge: Cambridge University Press)
- Xu, J., & Stone, J. M. 1995, ApJ, 454, 172